



**HAL**  
open science

# Development of microfluidic platform for continuous monitoring of aquatic contaminants in freshwater

Ngoc Mai Duong

► **To cite this version:**

Ngoc Mai Duong. Development of microfluidic platform for continuous monitoring of aquatic contaminants in freshwater. Other [cond-mat.other]. Université Paris Cité, 2022. English. NNT : 2022UNIP7084 . tel-04223101

**HAL Id: tel-04223101**

**<https://theses.hal.science/tel-04223101>**

Submitted on 29 Sep 2023

**HAL** is a multi-disciplinary open access archive for the deposit and dissemination of scientific research documents, whether they are published or not. The documents may come from teaching and research institutions in France or abroad, or from public or private research centers.

L'archive ouverte pluridisciplinaire **HAL**, est destinée au dépôt et à la diffusion de documents scientifiques de niveau recherche, publiés ou non, émanant des établissements d'enseignement et de recherche français ou étrangers, des laboratoires publics ou privés.

Université Paris Cité  
École doctorale Physique en Île-de-France (564)  
*Laboratoire Matière et Système Complexes (UMR 7057)*

# **Development of microfluidic platform for continuous monitoring of aquatic contaminants in freshwater**

Par Ngoc Mai DUONG

Thèse de doctorat de Physique

Dirigée par Gaëlle CHARRON  
Et par Pascal HERSEN

Présentée et soutenue publiquement le 07/09/2022

Devant un jury composé de :

Hynd REMITA, professeur, Université Paris-Saclay, Rapportrice  
Christophe VIEU, professeur, Université de Toulouse, Rapporteur  
Janina KNEIPP, professeur, Université Humboldt de Berlin, Examinatrice  
Julien BOUCHEZ, CR CNRS, Institut de Physique du Globe de Paris, Examineur  
Pascal HERSEN, DR CNRS, Institut Curie, Co-directeur de thèse  
Gaëlle CHARRON, Maître de conférences, Université Paris Cité, Directrice de thèse



## Acknowledgments

There have been many people who have contributed directly or indirectly in this thesis, to whom I am extremely grateful for their help and support. It is not possible to express my appreciation in simple words, but still, I hope they all feel that some part of this work is theirs.

In particular, I would like to thank Gaëlle Charron for being my advisor and helping me learn advanced techniques in chemistry, especially in Surface-enhanced Raman spectroscopy. I would like to thank my co-advisor, Pascal Hersen, for supporting me in applying microfluidics to a real-world application. A special acknowledgement to my colleagues Victoria Reichel and Angéline Noclain, the members of Pascal's group and laboratory MSC at the University Paris Cité.

This thesis would not have been possible without the funding of the ANR-17-CE04-0009-01 (UnivSERS).

## **Titre: Développement d'une plateforme microfluidique pour la surveillance continue des contaminants aquatiques dans l'eau douce**

**Résumé:** Dans le contexte de la pollution environnementale mondiale, l'eau est l'un des principaux vecteurs qui stocke et transmet les contaminants entre les régions et vers la vie humaine. Par conséquent, l'identification des sources de polluants et l'évaluation de l'état de la pollution nécessitent des mesures de la qualité de l'eau à une fréquence et à une résolution spatiale pertinentes. Cette collecte de données peut aider à appliquer de meilleures politiques de gestion et des actions de prévention. Cependant, les méthodes de surveillance actuelles sont coûteuses et principalement basées sur la manipulation d'analystes bien formés, ce qui les rend inappropriées pour des mesures sur le terrain à grande échelle et à haute fréquence. Pour cette raison et l'aggravation du statut de polluant, les agences internationales telles que l'ONU, l'Unicef et l'OMS appellent à développer de nouveaux outils de surveillance de la qualité de l'eau. Dans ce travail, nous avons développé une plateforme microfluidique automatisée intégrant la spectroscopie Raman exaltée de surface (SERS) pour la surveillance des ions métalliques dans les eaux douces. Dans la première partie, nous avons examiné une stratégie pour effectuer une analyse quantitative basée sur SERS sans avoir besoin d'étalonnage, qui est la partie de l'analyse la plus longue et la plus coûteuse. La méthode réinvestit une procédure de titrage colorimétrique pour déterminer la dureté de l'eau mais implique de surveiller la progression du titrage à travers le signal SERS d'un indicateur complexométrique. Trois eaux minérales dont les concentrations en métaux divalents varient d'un facteur 25 ont été titrées avec succès de cette manière, avec une justesse moyenne de 93 % et une précision moyenne de 2%. Dans la deuxième partie, nous avons développé une plateforme microfluidique qui automatise le précédent titrage complexométrique basé sur SERS. La plateforme a généré une chaîne de gouttelettes SERS actives avec des conditions de titrage bien contrôlées et a collecté les signaux SERS. En utilisant les trois mêmes eaux minérales que précédemment, la plateforme a fourni des résultats comparables au protocole manuel précédent, avec une justesse moyenne inférieure de 82 % et une précision moyenne supérieure de 7 %. En contrepartie, cette plateforme a permis de réduire le travail humain grâce à l'automatisation, de diviser par quatre au moins le temps d'acquisition des données, d'avoir un coût instrumental modéré et de consommer moins de réactifs de près de deux ordres de grandeur. En plus, avec sa convivialité et sa robustesse, la plateforme microfluidique développée peut être considérée comme une base solide pour une station de surveillance environnementale sur le terrain.

**Keywords:** Environnements Aquatiques, SERS, microfluidique, dureté de l'eau, Nanoparticules

## **Title: Development of microfluidic platform for continuous monitoring of aquatic contaminants in fresh water**

**Abstract:** In the context of global environmental pollution, water is one of the principal vectors that stores and transmits contaminants between regions and into human life. Consequently, identifying pollutant sources and evaluating pollution status requires water quality measurements at relevant frequency and spatial resolutions. This data collection can help enforce better management policies and prevention actions. However, current monitoring methods are high cost and mainly based on well-trained analyst manipulation, making them inappropriate for in-field measurement at large-scale and high frequency. For this reason and the worsening of the pollutant status, international agencies such as the UN, Unicef, and WHO are calling to develop new tools for monitoring water quality. In this work, we developed an automated microfluidic platform integrating with Surface-enhanced Raman spectroscopy (SERS) for monitoring metal ions in freshwaters. In the first part, we examined a strategy to perform SERS quantitative analysis without the need for calibration, which is the most time-consuming and high-cost analysis part. The method reinvests a colorimetric titration procedure to determine water hardness but involves monitoring the progression of the titration through the SERS signal of a complexometric indicator. Three mineral waters spanning divalent metal concentrations varying by a factor of 25 were successfully titrated in this way, with mean trueness of 93 % and mean precision of 2 %. In the second part, we developed a microfluidic platform that automated the previous SERS-based complexometric titration. The platform generated a chain of SERS-active droplets with well-controlled titration conditions and collected the SERS signals. Using the same three mineral waters as before, the platform provided comparable results to the previous manual protocol with a lower mean trueness of 82 % and a larger mean precision of 7 %. In exchange, this platform reduced human labour work through automation, reduced data acquisition time by at least four times, has a moderate instrumental cost and consumed less reagent by almost two orders of magnitude. In addition, with its user-friendliness and robustness, the developed microfluidic platform can be considered a solid foundation for an on-field environmental monitoring station.

**Keywords:** aquatic environments, SERS, microfluidics, water hardness measurement, Nanoparticles



## Résumé substantiel

### Introduction

En raison de la révolution industrielle et de la croissance démographique, les ressources en eau sont continuellement contaminées par des métaux lourds, des composés organiques synthétiques, des organismes pathogènes provenant des établissements humains, des activités industrielles et des eaux de ruissellement humaines. Dans les pays en développement, 80 à 90 % des eaux usées des villages artisanaux, des usines industrielles et des eaux usées domestiques se déversent encore directement dans la nature. Dans les pays développés, des lois et des politiques environnementales ont été établies depuis les années 1970s mais n'ont pas été appliquées de manière adéquate en raison d'un financement insuffisant, d'une mauvaise exécution et d'une intégration inadéquate des objectifs environnementaux dans la politique sectorielle. En réalité, selon une étude réalisée par une association française de consommateurs, "dans la moitié du territoire français, les pesticides sont présents dans les cours d'eau à des doses supérieures à la norme autorisée dans l'eau potable". La consommation d'eau contaminée directement via l'eau potable et l'hygiène de l'eau, ou indirectement via les cultures et le bétail, peut provoquer des problèmes de santé aigus ou chroniques tels que le choléra, la fièvre typhoïde ou des cancers.

L'eau est l'une des principales voies, outre l'air et le sol, qui transmet les polluants rapidement et géographiquement à grande échelle en raison de sa haute mobilité et de sa popularité sur Terre. Par conséquent, l'identification de la source polluante et l'évaluation de l'état de la pollution nécessitent des mesures massives de la qualité de l'eau à une fréquence et une résolution spatiale pertinentes. À titre d'illustration, il a été montré que les concentrations de  $Zn^{2+}$  et de  $Cu^{2+}$  dissous dans les rivières varient au sein d'un cycle journalier (24 - h), la plus grande variation enregistrée étant de  $5,5 \mu M$ . Par conséquent, des données de surveillance massives permettraient de cartographier les flux de contaminants à des échelles temporaires et spatiales appropriées pour établir la ligne de base, la saisonnalité et les tendances. Cela aiderait également à comprendre, anticiper et communiquer sur la pression des contaminants dans le processus de la terre vitale. Ainsi, de meilleures politiques de gestion pourraient être appliquées et des actions de prévention telles que l'alerte précoce et la réaction rapide peuvent être renforcées.

Cependant, les méthodes de surveillance actuelles impliquent à la fois du temps et des ressources humaines à chaque étape, de l'échantillonnage, du transport à l'analyse, ce qui entraîne un coût élevé par mesure et devient problématique lors de l'augmentation du nombre d'analyses. Par exemple, la surveillance mensuelle de la qualité de l'eau d'une rivière urbaine à un endroit spécifique pour quatre métaux lourds (par exemple Zn, Cd, Hg, Pb), deux composés organiques synthétiques (par exemple phtalate, DDT) et une bactérie commune (*E. Coli*) coûterait environ 10 k€/an. Ces données suggèrent que l'extension de la surveillance de la qualité de l'eau à des bassins fluviaux entiers entraînera des coûts substantiels, même pour les pays développés. Pour les pays en développement, cela est très difficile en raison d'une pénurie d'équipements et de travailleurs bien formés. Par conséquent, les don-

nées fiables sur la qualité de l'eau dans le monde restent insuffisantes, partielles ou indisponibles. C'est pourquoi les agences internationales de développement (ONU, Unicef, OMS) ont demandé à plusieurs reprises le développement de nouvelles méthodes de surveillance de la qualité de l'eau. Par conséquent, il facilite la collecte de données de meilleure qualité et en plus grande quantité, améliorant ainsi la gestion de l'eau et les programmes de développement.

Pour développer de nouveaux outils de surveillance environnementale, nous avons sélectionné certaines propriétés ciblées telles que la mesure *in situ*, le coût raisonnable des instruments et l'automatisation. En effet, la mesure *in situ* éviterait le conditionnement, le transfert et le suivi des échantillons ; par conséquent, cela réduirait la charge de travail et le temps de mesure, et accélérerait le rythme de collecte des données. Cette propriété peut être obtenue en visant un instrument compact à apporter sur le site ou à installer sur site. L'instrument doit également être accessible à un large éventail d'utilisateurs en maximisant son automatisation ou entièrement automatisé pour une surveillance continue. En plus de cela, une sensibilité et une sélectivité appropriées aux contaminants à l'état de traces dans les eaux douces à matrice complexe doivent également être satisfaites.

## **Partie I. Titrage complexométrique basé sur SERS pour la dureté de l'eau**

La spectroscopie Raman exaltée de surface (SERS) est une technique analytique très sensible qui a attiré beaucoup d'attention pour les applications d'analyse environnementale depuis 30 ans. En utilisant des nanostructures métalliques pour générer des résonances plasmoniques, SERS peut amplifier le signal vibrationnel Raman de 6 à 8 ordres de grandeur. Le SERS peut détecter des analytes moléculaires à des niveaux de trace inférieurs au  $\mu\text{M}$  ou même une seule molécule. Par conséquent, SERS pourrait permettre la détection de contaminants dans les eaux douces à des niveaux de trace (sub- $\mu\text{M}$ ). De plus, SERS fournit un spectre avec de nombreuses caractéristiques qui est généralement considéré comme une empreinte digitale de l'analyte. Par conséquent, SERS convient à l'identification d'un analyte spécifique dans des échantillons de matrice complexes comme les eaux douces. La sensibilité et la spécificité élevées de SERS peuvent alléger certaines étapes de prétraitement telles que la séparation et l'amplification. Cependant, l'utilisation en routine du SERS comme technique d'analyse a été entravée par des considérations pratiques parmi lesquelles l'irreproductibilité du signal SERS et le manque de robustesse de leur étalonnage.

Dans la première partie, nous avons examiné une stratégie pour effectuer une analyse quantitative SERS sans avoir besoin d'étalonnage. Nous avons réinvesti une procédure de titrage volumétrique complexométrique pour la mesure de la dureté de l'eau mais impliqué le suivi de la progression du titrage à travers le signal SERS d'un indicateur complexométrique.

Un titrage volumétrique complexométrique général se base sur trois protagonistes chimiques : l'ion métallique cible en tant qu'analyte, un chélateur ayant une forte affinité pour l'analyte en tant que titrant, et un indicateur coloré ayant une

affinité un peu plus faible pour l'analyte que le titrant et deux couleurs distinctes dans ses états libres et liés au métal. Un titrage volumétrique complexométrique se déroule comme suit. L'indicateur est introduit dans l'échantillon en défaut, typiquement quelques pourcents, par rapport à une estimation brute de la concentration de l'analyte ; il se lie quantitativement à l'analyte et transmet sa couleur d'état lié à la solution. Le titrant est introduit par portions dans le mélange au moyen d'une burette ; il se lie aux ions métalliques libres. Une fois que pratiquement tous les ions métalliques libres ont été consommés, tout nouvel ajout de titrant vole les analytes de la cavité de liaison de l'indicateur, libérant ainsi des molécules indicatrices libres qui apportent leur couleur d'état libre à la solution. Le passage entre les couleurs d'état lié et à d'état libre de l'indicateur dans le mélange réactionnel se produit autour du point d'équivalence et sert donc de marqueur de point final de tirage.

Nous avons réexploité cette procédure de titrage en utilisant le signal SERS de l'indicateur comme marqueur de point final au lieu de compter sur le commutateur de couleur classique sondé à l'œil nu. Pour ce faire, nous avons effectué le titrage en présence de billes micrométriques SERS-actives assemblées in situ à partir de nanoparticules sphériques d'argent (Ag NPs) et d'une polyamine visant à relier les NPs entre elles. Pratiquement, en plus des produits chimiques nécessaires pour effectuer le titrage colorimétrique classique, à savoir l'indicateur et le titrant, l'échantillon d'eau a également été mélangé avec des précurseurs des billes actives SERS : Ag NPs, polyéthylèneimine (PEI) comme réticulant polyamine et un filtre polymérique (polyéthylène glycol, PEG). L'agent de filtrage a servi à ralentir la cinétique d'agrégation des nanoparticules pour aider à obtenir des agrégats sphériques reproductibles et une insertion reproductible de l'indicateur dans les agrégats.

Trois eaux minérales couvrant des concentrations en ions alcalino-terreux variant d'un facteur 25 (de 0,6 mM à 15 mM) ont ainsi été titrées avec succès. Lors du titrage des ions alcalino-terreux (i.e.  $\text{Ca}^{2+}$ ,  $\text{Mg}^{2+}$  dans ces eaux) avec un titrant chélatant l'acide éthylènediaminetétraacétique (EDTA), le signal SERS du noir d'ériochrome T (EBT) saute brusquement lors du passage de la forme complexe à la forme libre. Ce comportement a été utilisé comme marqueur de point final. Cette méthode fournit une justesse moyenne satisfaisante de 93 % et une précision moyenne de 2 %. Pour chaque mesure en triple, la justesse varie de 78 % à 111%, avec leur écart-type relatif de 12 %. Une estimation de la concentration peut être obtenue à partir de mesures en triple en environ deux heures, et environ 30 minutes pour une seule mesure sans avoir besoin d'étalonnage.

Dans cette méthode, étant donné que le saut brusque de la courbe de titrage domine la fluctuation du signal SERS, il n'est pas nécessaire de construire une courbe d'étalonnage. Par conséquent, cette méthode a considérablement réduit le temps de mesure, la consommation de matériaux et le travail par rapport à nos analyses quantitatives SERS précédentes basées sur des courbes d'étalonnage. Ces réductions ont rapproché le SERS des utilisations courantes et pratiques.

Ce protocole manuel basé sur SERS peut être acceptable pour des mesures ponctuelles. Cependant, cela reste un défi pour la surveillance environnementale qui nécessite une fréquence élevée et des mesures de grandes bibliothèques

d'échantillons. Une amélioration spectaculaire de l'aspect pratique pourrait être obtenue en automatisant la procédure d'analyse. Il s'agit de la deuxième partie de cette thèse.

## **Partie II. Plateforme microfluidique automatisée**

La microfluidique, en bref, est la science de la manipulation de fluides dans un réseau de microcanaux fabriqués. Depuis les années 1990, la microfluidique a continuellement contribué à l'amélioration des sciences de la vie et de la chimie en permettant une manipulation précise des fluides à des échelles micrométriques et une réduction significative de la consommation de réactifs. Les analyses basées sur SERS peuvent également bénéficier des technologies microfluidiques car la microfluidique peut réduire la consommation de nanomatériaux plasmoniques et permettre d'automatiser la préparation et l'analyse des échantillons, réduisant ainsi le travail de la main-d'œuvre. De plus, la réduction de la consommation de matière dans les dispositifs microfluidiques profite également à la surveillance environnementale à grande échelle car on n'aurait pas à recharger régulièrement les réservoirs de réactifs.

Dans cette deuxième partie, nous avons développé la plateforme microfluidique automatisée pour l'analyse basée sur SERS qui a automatisé la procédure de titrage précédente basée sur SERS. Le prototype de titreur se compose de trois blocs fonctionnels : (i) une puce microfluidique conçue pour préparer des échantillons de mesure indépendants sous forme de gouttelettes d'eau dans l'huile à partir de toutes les matières premières nécessaires, (ii) une chambre de mesure optique configurée pour acquérir les spectres SERS de gouttelettes en ligne, et (iii) un système d'injection contrôlable pour contrôler et varier les proportions de l'échantillon et du réactif pour effectuer un titrage. De plus, nous avons développé un programme python qui contrôle les différents instruments impliqués dans la préparation des gouttelettes et le spectromètre Raman afin d'effectuer des titrages de manière autonome. Après assemblage, la plateforme est capable d'effectuer trois tâches principales : (i) préparer de manière autonome des échantillons de mesure complexes contenant des portions d'essai de l'échantillon d'eau, les précurseurs nécessaires des agrégats SERS-actifs, le titrant et l'indicateur ; (ii) faire varier le rapport analyte/titrant afin de localiser la fin de la réaction et (iii) acquérir les spectres SERS des mélanges résultants.

La plateforme a mis en œuvre avec succès des titrages continus de la dureté de l'eau jusqu'à 2,5 heures sur quatre jours différents sans aucune intervention humaine. Trois eaux minérales, identiques à celles du protocole manuel, ont été titrées en 8 lancements indépendants, donnant une justesse et une précision moyennes comparables à celles du protocole manuel, respectivement 82 % et 7 %. Pour chaque lancement, la justesse varie de 64 % à 111 % avec leur écart-type relatif de 17 %. Grâce à l'automatisation et à la manipulation fluidique à petite échelle, la plateforme a réduit le temps de mesure d'au moins 4 fois et la consommation de réactifs d'un facteur 82.

La plateforme ne nécessite que 30 minutes de travail manuel pour la configuration initiale ; puis il exécute les titrages automatiquement. Par conséquent,

plus la plate-forme est utilisée longtemps, plus elle apporte d'avantages en termes de main-d'œuvre, qui est la partie analyse qui domine le coût consolidé dans le protocole manuel. De plus, avec une faible consommation de réactifs ( $25 \mu\text{L}/\text{min}$ ), la plateforme est tout à fait appropriée pour la surveillance environnementale à grande échelle et à haute fréquence. Par exemple, un lot de 50 ml de NP suffit pour 33 heures de surveillance continue, produisant 8 000 spectres, alors que cette quantité est juste suffisante pour produire 66 spectres dans le protocole manuel. De plus, le fonctionnement de la plateforme est convivial pour les non-experts après seulement quelques heures de formation. Cette fonctionnalité est essentielle pour apporter l'analyse SERS aux applications du monde réel où les utilisateurs n'ont aucune formation en chimie et n'ont pas le temps de préparer les échantillons. Le coût instrumental total est de 35 k€, soit 30 - 50% du prix d'un spectromètre ICP-AES habituellement utilisé pour analyser la teneur en alcalino-terreux. En résumé, ce travail a établi une base solide pour une station de surveillance environnementale sur le terrain.

### **Conclusions et perspectives**

Ce projet de thèse visait à développer une plateforme de terrain pour le suivi de la qualité de l'eau douce. Nous avons atteint cet objectif en deux parties : (i) établir un protocole pour effectuer un titrage complexométrique basé sur SERS, et (ii) développer une plateforme microfluidique pour automatiser la méthode chimique précédente. Le principe de fonctionnement du titrage complexométrique basé sur SERS a d'abord été validé pour déterminer la dureté de l'eau dans une procédure manuelle. L'exploration de la méthode pour la détermination d'autres ions métalliques devrait être faisable car le titrage complexométrique a été établi pour pratiquement tous les cations métalliques. De plus, comme la SERS est une technique très sensible, cette méthode est prometteuse pour la détermination des métaux lourds qui est généralement affichée à moins de  $\mu\text{M}$  dans les eaux douces. La plateforme microfluidique a ensuite été développée pour automatiser le précédent titrage complexométrique basé sur SERS, affichant sa forte automatisation, sa convivialité et sa robustesse. La plateforme est prête à tester avec des eaux douces inconnues pour la mesure de la dureté de l'eau et à s'appliquer aux mesures à grande échelle. Avec les principales fonctions de génération automatique de gradient de concentration et d'acquisition de spectres, la plateforme actuelle peut facilement mettre en œuvre d'autres déterminations d'ions métalliques en changeant simplement les réservoirs. Elle devrait également s'appliquer aux méthodes d'étalonnage. Avec des possibilités ouvertes de mise à niveau vers une automatisation complète et une analyse multi-analyte, la plateforme microfluidique développée est une base solide pour développer un instrument de surveillance environnementale polyvalent.



# Contents

<b>Introduction</b>	<b>1</b>
0.1 Water pollution: status and impact . . . . .	1
0.2 Need for massive environmental data . . . . .	2
0.3 Contaminants in surface water . . . . .	3
0.4 Procedure of water quality analysis. Methods for metal determination	3
0.5 Demanding for new tools . . . . .	5
0.6 Our strategy and thesis structure . . . . .	5
<b>1 Surface Enhanced Raman Scattering Methods</b>	<b>7</b>
1.1 Raman scattering . . . . .	7
1.2 Surface enhanced Raman scattering (SERS) . . . . .	9
1.2.1 Plasmons and plasmon resonance . . . . .	9
1.2.2 Electric field enhancement in the vicinity of NPs . . . . .	11
1.2.3 Surface-enhanced Raman scattering . . . . .	12
1.3 Practical implementation of SERS . . . . .	14
1.3.1 SERS substrates . . . . .	14
1.3.2 Quantification methods . . . . .	16
1.3.3 SERS irreproducibility and solutions . . . . .	16
1.4 Our strategic choices . . . . .	19
<b>2 SERS-complexometric titration: water hardness measurement</b>	<b>23</b>
2.1 <i>Pre-print</i> : A new look at an old classic: implementation of a SERS- based water hardness titration . . . . .	23
<b>Supplementary information</b>	<b>25</b>
2.2 Supplementary information of the pre-print: A new look at an old classic: implementation of a SERS-based water hardness titration . . .	25
<b>3 Microfluidic Methods</b>	<b>27</b>
3.1 SERS and microfluidics . . . . .	28
3.2 A typical microfluidic system . . . . .	30
3.2.1 Fabrication of a microfluidic chip . . . . .	30
3.2.2 Flow control instruments . . . . .	32
3.3 Droplet-based microfluidics . . . . .	34
3.4 Mixing in microfluidic systems . . . . .	37
3.5 Generation of concentration gradients . . . . .	37
<b>4 Microfluidic platform for SERS-complexometric titration</b>	<b>41</b>
4.1 Introduction . . . . .	41
4.2 Results and discussion . . . . .	43

---

4.2.1	Chemical principle of the SERS-based titration of water hardness . . . . .	43
4.2.2	Overview of the automated SERS titrator . . . . .	45
4.2.3	Microfluidic set-up . . . . .	45
4.2.4	SERS readout . . . . .	47
4.2.5	Injection system for controlling the progression of the titration . . . . .	48
4.2.6	Operation of the platform python program . . . . .	50
4.2.7	Evian titration . . . . .	51
4.2.8	Volvic and contrex titrations . . . . .	54
4.2.9	Critical reviewing of the analytical performances of platform . . . . .	55
4.2.10	Operating cost . . . . .	56
4.3	Conclusion . . . . .	57
4.4	Experimental section . . . . .	58
	<b>Supplementary information</b> . . . . .	<b>61</b>
4.5	Feedstock preparation . . . . .	62
4.5.1	Chemicals . . . . .	62
4.5.2	Protocol for stock preparation . . . . .	62
4.5.3	Stock selection for microfluidic launches . . . . .	64
4.6	Microfluidic chip fabrication . . . . .	64
4.7	Full microfluidic platform set-up . . . . .	67
4.8	Imaging the flows in the microfluidic chip . . . . .	70
4.9	Droplet characterization . . . . .	72
4.9.1	Droplet volume . . . . .	72
4.9.2	Droplet speed . . . . .	73
4.9.3	Aqueous/oil segment ratio . . . . .	73
4.10	SERS measurement set-up . . . . .	74
4.11	Comparison between spectra acquired in cuvettes and in-line in droplets . . . . .	76
4.11.1	Preparation of test cuvettes and microfluidic set-up for spectral and pH check. . . . .	76
4.12	SERS signal reproducibility . . . . .	78
4.13	Python program & automated experiment procedure description . . . . .	78
4.14	Estimation of lag time from fluidic circuit . . . . .	81
4.15	Data processing . . . . .	84
4.15.1	The raw data structure . . . . .	84
4.15.2	Baseline correction . . . . .	84
4.15.3	Lag time estimation by metrical calibration method . . . . .	85
4.15.4	Lag time correction for spectral data . . . . .	88
4.15.5	Endpoint identification . . . . .	88
4.16	Comparison between the microfluidic system and manual protocol . . . . .	89
4.17	Evian titrations . . . . .	90
4.18	Volvic titrations . . . . .	95
4.19	Contrex titrations . . . . .	99
4.20	Estimation of cost of the platform . . . . .	103

---

4.20.1	Cost per liter of chemical stock solutions . . . . .	103
4.20.2	Labour for the preparation of the stock solutions . . . . .	103
4.20.3	Reagent cost per spectrum . . . . .	104
4.20.4	Cost for microfluidic chip fabrication . . . . .	104
4.20.5	Time and costs of preparation of measurement samples and acquisition of spectra . . . . .	105
4.20.6	Total cost per spectrum . . . . .	105
4.20.7	Instrument cost for the microfluidic platform . . . . .	106
<b>5</b>	<b>Conclusions and perspectives</b>	<b>107</b>
	<b>Bibliography</b>	<b>113</b>



# Introduction

## Contents

---

<b>0.1</b>	<b>Water pollution: status and impact</b>	<b>1</b>
<b>0.2</b>	<b>Need for massive environmental data</b>	<b>2</b>
<b>0.3</b>	<b>Contaminants in surface water</b>	<b>3</b>
<b>0.4</b>	<b>Procedure of water quality analysis. Methods for metal determination</b>	<b>3</b>
<b>0.5</b>	<b>Demanding for new tools</b>	<b>5</b>
<b>0.6</b>	<b>Our strategy and thesis structure</b>	<b>5</b>

---

## 0.1 Water pollution: status and impact

As a result of the industrial revolution and population growth, the human impact accumulated on Earth has been significant enough to alter the stratigraphic compositions. Namely, human products like concrete, plastics, and aluminium have been globally widespread since the 1950s and have become new components in geological deposits nominated as “techno-fossils” [1]. Moreover, water resources are continuously contaminated with heavy metals, synthetic organic compounds, pathogenic organisms from human settlements, industrial activities, and human runoffs [2]. In developing countries, 80 – 90% of wastewater from craft villages, industrial factories, and domestic wastewater is still discharging directly to nature [3]. In developed countries, environmental laws and policies have been established since the 1970s but have not been enforced adequately due to a lack of will and capacity. The European water framework directive aimed to restore natural water bodies to their natural geochemical levels in quantity and quality by 2020, but it failed due to inadequate finance, poor execution, and inadequate integration of environmental objectives into sectoral policy [4]. In reality, according to a study put together by a French consumer association, “pesticides are currently present in waterways at doses higher than the standard authorized in drinking water in half of France territory”<sup>1</sup> [5]. In Guadeloupe, an overseas region of France in the Caribbean, “a third of the agricultural surface is poisoned with chlordecone”, an insecticide widely used against the weevil<sup>2</sup> [6].

Human-made water pollution impacts human health directly through drinking water and water hygiene, and indirectly through the food chain such as through crop

---

<sup>1</sup>« Dans la moitié du territoire français, les pesticides sont présents dans les cours d’eau à des doses supérieures à la norme autorisée dans l’eau potable. »

<sup>2</sup>« Un tiers de la surface agricole guadeloupéenne est empoisonné au chlordécone. »

and livestock contamination [7]. Depending on the pollutant concentration and the exposure duration time, the effects of water pollution can be acute or chronic. Consumption of water contaminated by microbial pollutants from sewage can cause acute diarrheal diseases such as cholera and typhoid fever [8]. Those are the primary causes of infant mortality in developing countries, more than deaths from malaria or HIV [8]. Exposure to heavy metals in the long term can cause scores of health issues, including neurodegenerative conditions, disruption of the endocrine system, and cancers [9]. Many pesticides can cause congenital disabilities, reproductive disorders, hormone disruption and cancers [10]. For example, the insecticide pollution in Guadeloupe has been causing 500 cases of prostate cancer every year out of a population of 395.000 population [6]. This means one of every 1000 people in Guadeloupe will be diagnosed with prostate cancer every year, becoming the most frequent cancer, far ahead of other cancers in this archipelago [6].

## 0.2 Need for massive environmental data

Water is one of the principal pathways besides air and soil that transmits pollutants fast and geographically large due to its high mobility and popularity on Earth. Consequently, identifying the pollutant source and evaluating pollution status requires massive water quality measurements at a relevant frequency and spatial resolution. For example, the work of Borrok, D. M. et al. 2008 [11] shows that dissolved Zn and Cu concentrations in rivers vary even within a diel ( $24 - h$ ) cycle, with the largest variation recorded is of  $5.5 \mu M$ . This variation is supposed to link to photocycle-controlled processes. Another example for the need for spatial data is the work of Kelsey J. Pieper et al. 2018 [12]. In this work, the impact of road salt used for de-icing highway roads on water quality in private wells was studied by analyzing 95 water samples in a whole town. The work established the spatial chloride-level map showing the areas affected by road salt. This reliable data is needed and helpful in future discussions for better road salt management.

The Flint water crisis is another example demonstrating the importance of massive water quality monitoring both spatially and temporally. In April 2014, switching the drinking water source in Flint, Michigan without adding corrosion inhibitors led to lead leaching from plumbing. This leaching affected 20.000 children, who are the most vulnerable to lead exposure. To evaluate the system-wide contamination situation and track lead reductions in water lines after multiple interventions, four subsequent sampling efforts were conducted for two years, collecting samples of hundreds homes in the city each time [13].

As illustrated through the examples above, massive monitoring data enables mapping contaminant fluxes at temporary and spatial scales appropriate to establish baseline, seasonality, and trends. It would also help understand, anticipate, and communicate about the pressure of contaminants in the vital earth process. Thus,

better management policies could be enforced, and prevention actions such as early warning and prompt reaction can be empowered [14].

### 0.3 Contaminants in surface water

The contaminants in water are diverse, including inorganic substances (e.g. chloride, nitrate, metal ions), organic substances (pesticides, herbicides, compounds from personal hygiene and cosmetic) and biological pathogens (e.g. E. coli, Coliform). Their typical concentration range together with their analysis characteristics are listed in Table 1, they vary from trace level to a high concentration (Tab. 1). A comprehensive summary of each composition in surface water can be found in table A.1 of the ref.[15].

Contaminant	Heavy metal	Organic compound	Bacteria
Typical concentration range	10 $pM$ to 1 $\mu M$	1 $\mu g/L$ to 1000 $g/L$	$10^1 - 10^7$ CFU[b]/L
Analytical method	ICP-OES ICP-MS	LC-MS	Colony counting
Availability on field	No	No	No
Sample pre-treatment (duration)	Acidic digestion (a few hours)	Extraction (a few hours)	Culture (24h)
Overall processing time	20 <i>min</i>	30 <i>min</i>	1 – 20 <i>min</i>
Instrument price (k€)	50 – 100	50 – 100	10
Price per analysis (€)	23 [a]	100 [b]	90 [c]

Table 1: Characteristics of standard analytical methods for heavy metals, organic compounds, and bacteria. [a] CNRS analysis service; [b] colony forming units; [c] private certified analytical labs. (Adapted from ANR-17-CE04-0009-01 (UnivSERS) project proposal).

### 0.4 Procedure of water quality analysis. Methods for metal determination

A general procedure for water quality analysis consists of several steps: sampling on-site, sample storage, sample transport to a measurement site, and finally analyzing it. First, sampling for water environmental monitoring is designed to ensure the taken samples represent the whole target system to provide meaningful analytical results for environmental assessment. Spatial aspects like currents of flows, suspicious contaminant sources or depth stratification need to be considered to decide the location and resolution of sampling sites [16]. An efficient water quality monitoring over time also requires choosing an appropriate sampling rate to reflect a periodic evaluation, a trend or capture an unpredictable event. Although sampling is the first step of the whole process, it is crucial to deciding the later

efforts worth it. In the Flint water crisis, one of the factors that contributed to its happening was the improper sampling method [13]. The Lead and Copper Rule (LCR) established by the U.S. Environmental Protection Agency (USEPA) requires at least 50% of samples from high-risk sites, but not enough required number of samples was conducted before discovering the water crisis in Flint [13, 17]. In addition, the practise of flushing out water lines before testing [17] also contributed to the failure of lead contamination detection.

Many analyses, such as heavy metal and biological analysis, require equipment and staff in qualified laboratories. Therefore, the collected samples on site are stored and conditioned correctly to conserve the concentrations of determinants of interest before analyzing in a laboratory. Appropriate containers are selected not only to avoid additional contaminants but also minimize the sorption of target analyte onto the container walls. For example, the adsorption of Cypermethrin pesticide on the Duran glass surface is four times higher than on the PTFE surface. In contrast, with permethrin pesticide, the Duran glass surface absorbs two times less than PTFE surface [18]. Sample conditioning can be required, for example, cooling or freezing to reduce the bacterial activity or acidification to pH 1 – 2 to prevent hydrolysis and precipitation [16].

Sampling and sample conditioning can be carried out by trained employees coming directly to the sampling sites, which can be in a rural region or underground. In urban areas, sampling can be carried out by habitants through distributed sampling kits with sampling guide instructions. The collected samples are then transported or sent by post to a measuring laboratory for analysis.

When samples arrive in a laboratory, before analyzing the samples, pretreatment may be necessary, such as filtration or digestion, to remove or dissolve colloids and suspended particulate matters. Then according to the type of substance to analyze, an analytical method is selected among the techniques available. Their procedure can be simple to highly sophisticated, fast to time-consuming, and provide different detection limits. Following is a brief summary of the main analytical procedures that can be used to determine metal concentrations in aquatic samples.

Metal determination can be carried out by classical or modern techniques. The classical analysis for metal ions is based on titrimetric techniques that involve monitoring a chemical reaction between a controlled concentration of a reagent or titrant and a precisely known sample volume. Complexometric titration by forming complexes between metal ions and titrant is the most commonly used method for metal determination. To signify the equivalence point, it requires an indicator that displays different colours before and after the equivalence. The advantages of this method are that it is cheap and can be established for virtually every metal ion. However, those methods are often limited to concentrations in the  $\mu M$  to  $mM$  range and are difficult to validate for turbid solutions.

On the other hand, modern methods show significant improvement in sensitivity and accuracy through using modern instruments [19]. They are applicable to almost any metal analytes and appropriate to their typical range in aquatic waters. Inductively coupled plasma optical emission spectroscopy (ICP-OES) can measure from minor to trace levels (ppm to ppb) and show simultaneous multi-element analysis capability. Graphite furnace atomic absorption (GFAA) is more sensitive than ICP-OES that its detection limits are down to ultra-trace levels (sub-ppb). However, GFAA is slow and expensive to operate. Combining the advantages of the two above methods, inductively coupled plasma mass spectrometry (ICP-MS) is currently considered the golden technique but is the most expensive. In general, those instruments are bulky and immobilized in the lab. They are expensive for the instruments themselves and maintenance.

## 0.5 Demanding for new tools

As presented previously in section 0.2 (Need for massive monitoring data), massive water quality measurement at relevant frequency and spatial resolution is important for environmental monitoring, especially in the current context of global pollutant widespread. However, the current monitoring methods involve both the time and human resources in every step, from sampling, transporting to analysing, leading to a high cost per measurement. The golden standard methods using Inductively Coupled Plasma Mass Spectrometry (ICP-MS), Liquid Chromatography coupled to Mass Spectrometry (LC-MS) cost about 20 to 100 € per analysis (Tab. 1). This price considerably becomes problematic when scaling up the number of analyses. For example, menstrual monitoring the water quality in an urban river at a specific spot for four heavy metals (e.g. Zn, Cd, Hg, Pb), two synthetic organic compounds (e.g. phthalate, DDT), and one common bacteria (E. Coli) would cost about 10 k€/year. This data suggests that expanding water quality monitoring to whole river basins will incur substantial costs even for developed countries. For developing countries, this is highly challenging due to a shortage of equipment and well-trained workers [20]. Therefore, reliable water quality data worldwide remains inadequate, partial, or unavailable [21]. For this reason, the international development agencies (UN, Unicef, WHO) have repeatedly urged the development of new monitoring methods for water quality. Consequently, it facilitates the collection of higher quality and larger quantity data, thereby enhancing water management and development programs.

## 0.6 Our strategy and thesis structure

We selected some targeted properties such as in-situ measurement, reasonable instrument cost, and automation to develop new environmental monitoring tools. We attempted to lower the instrument cost in the ICP-MS method by two orders of

magnitude per analysis. In addition, measuring the sample directly on-site would avoid conditioning, transferring, and tracking samples, which are three steps that increase the measurement duration and cost. In consequence, it would accelerate the rate of data collecting. This property can be achieved by aiming for a compact instrument to bring to the site or can be installed on-site. The instrument should also be accessible to a broad range of users by maximizing its automation or fully automated for continuous monitoring. On top of those, appropriate sensitivity and selectivity at trace-level contaminants in complex-matrix freshwaters should also be satisfied.

Surface-enhanced Raman spectroscopy (SERS) is a highly sensitive analytical technique that has attracted much attention for environmental analysis applications for 30 years [22]. Using metallic nanostructures to generate plasmonic resonances, SERS can amplify the Raman vibrational signal by 6 - 8 orders of magnitude [23]. SERS can detect molecular analytes at trace levels of sub  $\mu M$  or even a single molecule [24, 25]. Therefore, SERS could empower the detection of contaminants in freshwaters at trace levels. In addition, SERS provides a spectrum with numerous features which is usually regarded as a fingerprint of the analyte. Therefore, SERS is suitable for identifying a specific analyte in complex matrix samples [26, 27] like freshwaters. SERS' high sensitivity and specificity can alleviate some pre-treatment steps such as separation and amplification.

However, practical implementation of SERS is often hindered by the irreproducibility of SERS signals [28] and impractical sample preparation procedure [29]. The group has been working on practical implementation of SERS for some years. The thesis of Gwennhael Brackx (2017) was dedicated to the prototyping of a SERS sensor of  $Zn^{2+}$ . In his thesis work, he quantitatively demonstrated that the irreproducibility of SERS signals is a strong limitation bringing SERS to become a practical application. Because of this, large datasets must be acquired to build calibration models with satisfactory predictive powers. This is highly time-consuming and labor intensive.

In this work, we developed a method to overcome the lack of reproducibility of SERS signal when performing quantitative analysis, on the specific case of water hardness determination. This work is the topic of chapter 2. All scientific background needed to understand the fundamentals and limitations of SERS is in chapter 1.

To minimize the time and labor load, automation of the quantitative SERS-based analysis procedure was investigated. Building of a custom microfluidic platform for the method presented in chapter 1 is the topic of chapter 4. All scientific background to understand the fundamentals of microfluidics is in chapter 3. Finally, the perspectives of this work are discussed in chapter 5.

# Surface Enhanced Raman Scattering Methods

---

## Contents

---

<b>1.1 Raman scattering</b> . . . . .	<b>7</b>
<b>1.2 Surface enhanced Raman scattering (SERS)</b> . . . . .	<b>9</b>
1.2.1 Plasmons and plasmon resonance . . . . .	9
1.2.2 Electric field enhancement in the vicinity of NPs . . . . .	11
1.2.3 Surface-enhanced Raman scattering . . . . .	12
<b>1.3 Practical implementation of SERS</b> . . . . .	<b>14</b>
1.3.1 SERS substrates . . . . .	14
1.3.2 Quantification methods . . . . .	16
1.3.3 SERS irreproducibility and solutions . . . . .	16
<b>1.4 Our strategic choices</b> . . . . .	<b>19</b>

---

Surface enhanced Raman scattering (SERS) is a highly sensitive technique that amplifies Raman scattering by several orders of magnitude by using metallic nanostructure substrates [30, 31]. SERS results from the combination of two effects: Raman scattering and plasmonic enhancement of the local electric field. In this chapter, the basics of these two phenomena are presented. For more details, see [32, 2].

## 1.1 Raman scattering

Raman scattering is a vibrational spectroscopic process that happens when an incoming excitation light which is often near-infrared or visible light (NIR-Vis) made of photons with energy  $E_0$ , interacts with the molecules of a sample. This light beam excites the molecules to a short-lived state, often called a virtual state. Then the excited molecules immediately relax to their initial electronic state. However, the molecule can relax to the same or different vibrational state. If it relaxes to a different vibrational state, scattered photons have an energy  $E_s$  different from  $E_0$  (Fig. 1.1). This inelastic scattering process is called Raman scattering. During the scattering process, most of the scattered photons have the same energy as the incident photons  $E_0$ , which is called elastic scattering or

Rayleigh scattering (Fig. 1.1). Only a small fraction of scattered photons (i.e. one in every  $10^6 - 10^8$ ) undergo Raman scattering with an energy change. Depending on whether the scattered photons gain or lose energy during the process, Raman scattering is termed as Stokes or anti-Stokes transitions, respectively (Fig. 1.1).

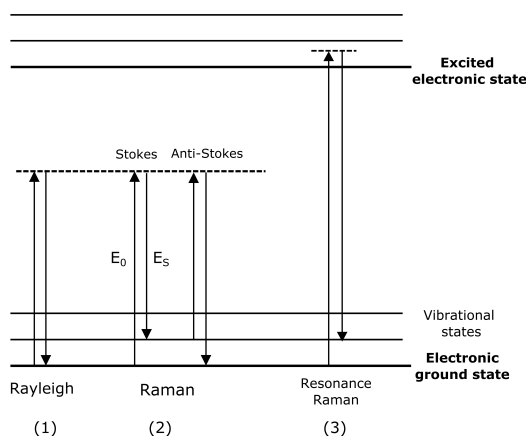


Figure 1.1: Raman and Rayleigh scattering processes.  $E_s$ : emitted energy of scattered photons, and  $E_0$ : absorbed energy of the excited photons.

The difference in energy between the incident and scattered photons is recorded as Raman spectrum. It usually encompasses a rich collection of spectral features having narrow linewidth that reflects the vibrational modes of chemical bonds of the molecules. Thus, Raman spectrum is specific and can be regarded as a fingerprint of the molecule. Raman spectra are expressed in Raman shifts

$$\text{Raman shift} = \frac{10^7}{\lambda_{ex}} - \frac{10^7}{\lambda_s} \quad (1.1)$$

where,  $\lambda_{ex}$  is the wavelength of the excitation radiation of unit  $nm$ ,  $\lambda_s$  is the wavelength of the scattered beam of unit  $nm$ , and Raman shift is of unit  $cm^{-1}$ . The typical range of Raman shifts is from  $200\text{ }cm^{-1}$  to  $4000\text{ }cm^{-1}$ . It can be divided into two regions. The region above  $1500\text{ }cm^{-1}$  is known as the functional group region that indicates the presence of certain chemical groups. For example, the stretching vibration of the carbonyl group ( $C=O$ ) in an aldehyde ( $-C(H)=O$ ) is always in the range of  $1730\text{ }cm^{-1}$  to  $1700\text{ }cm^{-1}$  [33]. The region below  $1500\text{ }cm^{-1}$  is known as the fingerprint region. This region contains characteristic features reflecting vibrational modes of the whole molecular scaffolding. This region is highly specific to a given molecule and is the most important part of the spectrum for identification purposes.

Therefore, the spectrum of a specific analyte in a complex mixture can be extracted from the spectrum of the whole mixture. Thus, Raman spectroscopy is highly appropriate for determining a molecular analyte in a mixture. For example,

it has been reported for quantitative analysis of cocaine in solid mixtures with caffeine and glucose [34]. Raman highly specificity can even discriminate difference edible vegetable oils [35].

For a vibrational transition to be Raman active, it must involve a change in the polarizability, which refers to the ease of distorting the electron cloud under an external electric field. Thus, the molecules having symmetric bonds such as S-S, C-C tend to have higher Raman scattering cross-sections, whereas, molecules having asymmetric vibrations, such as C-H, O-H tend to have lower Raman scattering cross-sections.

Raman scattering is a weak process. As mentioned above, only one photon in every  $10^6 - 10^8$  photons undergoes Raman scattering. This weak effect is because the incident photon does not resonate with any electronic transition of the molecule, so the light-material interaction is inefficient. Raman spectroscopy is usually employed for pure compounds or solutions in the high concentration range ( $mM, M$ ). It is unsuitable for dilute solutions and even not considered for trace analysis.

When the incident energy coincides with an electronic energy transition of the analyte, the intensities of the Raman effect can be about three orders of magnitude stronger than normal Raman. The technique is known as resonant Raman. That is usually the case of colored molecules, such as dyes, pigments made from phthalocyanines, polyacetylenes, or enzymes carrying porphyrin rings [32]. They have a high chance to undergo resonant Raman, thus benefiting from a higher sensitive analysis technique.

## 1.2 Surface enhanced Raman scattering (SERS)

The weak Raman scattering can be amplified by a giant factor by using metallic nanostructured substrates. This technique is known as Surface enhanced Raman scattering. This section explains qualitatively the mechanisms of this enhancement, and then demonstrates the square dependency showing Raman signal enhancement gained in both excitation and deexcitation scattering processes.

### 1.2.1 Plasmons and plasmon resonance

We first examine the behaviour of the electron cloud within a spherical metallic nanoparticle (NP) of  $1 - 10 \text{ nm}$  in diameter under an irradiation. It can be described as a free electron gas bathed in a fixed nuclei framework. The NP is irradiated by a light in the NIR-Vis range, which is an electromagnetic wave with a wavelength of one order of magnitude larger than the size of the NP. Under this irradiation, the electron cloud oscillates collectively according to the electric field (Fig. 1.2). Meanwhile, an induced dipole is created due to the redistribution of the

electron cloud (Fig. 1.2).

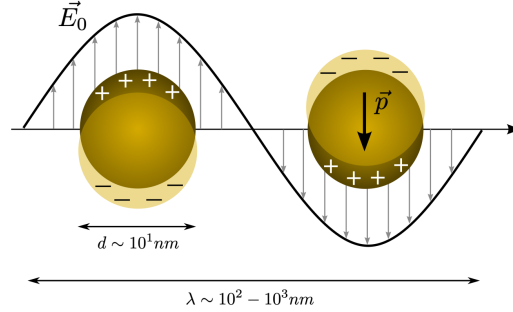


Figure 1.2: Electronic clouds are shifted according to the external electric field. Spherical metallic NPs, typically made of gold, with an typical size of  $d = 1 - 10 \text{ nm}$ . The external electric field  $\vec{E}_0$  induces a redistribution of electrons that generates an internal dipole  $\vec{p}$ . The typical wavelength  $\lambda$  of the external electric field is in the  $10^2 - 10^3 \text{ nm}$  range. (Adapted from [2]).

Because the electron cloud is tied to the fixed nuclei framework, their oscillation is constrained, and its amplitude can be maximized at a certain resonance frequency, i.e., eigenfrequency or natural frequency. The general collective oscillation of free electrons is a plasmon, and the oscillation at the natural frequency is the plasmon resonance. The high absorption band in the extinction spectrum is often used to indicate the resonant frequency of the plasmon.

Each metallic material exhibits different strength of the bonding between electrons and its cation network. Thus, their resonant frequency is different. Plasmon resonant frequency of silver and gold NPs is in the visible range (Fig. 1.3a). Aluminium NPs display resonance plasmon in the UV range. Because electrons are confined within metallic particles, their shape and size also affect the resonant frequency. It goes to a higher frequency with larger NPs. Anisotropic NPs can display more than one plasmon resonance. For instance, nanorods present two plasmonic modes in their spectrum, corresponding to the electron oscillations in the transverse and longitudinal directions (Fig. 1.3b).

When two NPs are brought close enough to each other to form a dimer of NPs, the induced dipoles generated in each NP interact with each other. Besides the external field, electrons in each NP are also regulated according to the local electric field generated from the adjacent NP's dipole. Therefore, the resonant energy is shifted into two plasmonic modes at lower energy and higher energy. They correspond to the arrangements of dipoles in the same and opposite directions (Fig. 1.4a). Only one of these coupled oscillations satisfies the electronic absorption rule of an electric dipole that varies over the transition: the in-phase or “bonding” one. Multimeric aggregates of NPs display complex coupled plasmonic modes with the resonant

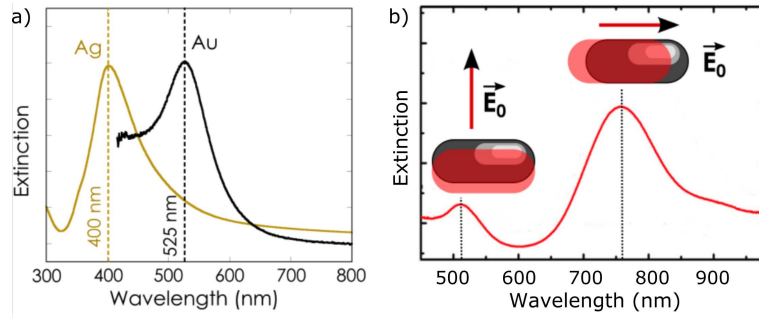


Figure 1.3: a) Normalized extinction spectra of gold and silver nanospheres 50 nm in diameter (adapted from [2]). b) Extinction spectrum of gold nanorods with the corresponding plasmon mode depicted as insets. Red arrows denoted the direction of the external electric field  $\vec{E}_0$ . (Adapted from [36]).

frequency shifted to lower energy (Fig. 1.4b).

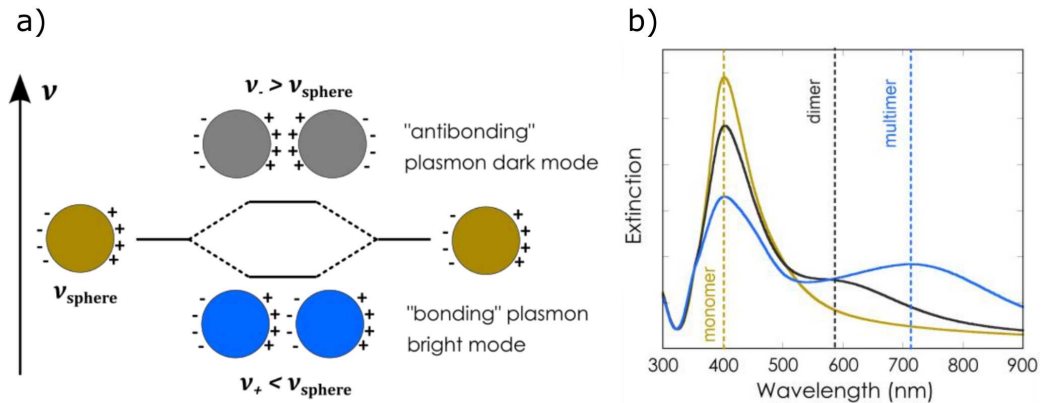


Figure 1.4: a) Coupling of the plasmon modes of two adjacent nanospheres. The characteristic energy levels are denoted by  $\nu$ . b) Extinction spectrum of a mixture of monomers, dimers and multimers of 50 nm Ag NPs. (Adapted from [2]).

### 1.2.2 Electric field enhancement in the vicinity of NPs

Reconsidering the case of a spherical metallic NP under irradiation at its plasmon resonance, the induced dipole generates an electric field ( $\vec{E}_{ind}$ ) (Fig. 1.5b). This field is particularly intense at the point near the NP, where the induced field and the external field add up constructively (point A in Fig. 1.5a). The total electric field at this point is the superposition of the external electric field  $\vec{E}_0$  and the induced electric field,  $\vec{E}_{total} = \vec{E}_0 + \vec{E}_{ind}$ . The local field intensity enhancement factor (LFI-EF) at a point is defined as the ratio of the square amplitude of the total electric

field at this point with and without the presence of the NP

$$\text{LFI-EF} = \frac{E_{total}^2}{E_0^2} \quad (1.2)$$

For gold and silver NPs, LFI-EFs at the most intense point (point A in Fig. 1.5a) are expected to be 20 and  $2 \cdot 10^3$ , respectively.

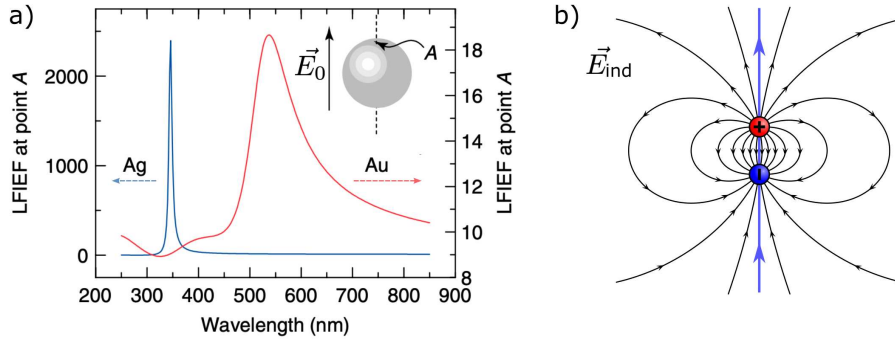


Figure 1.5: a) Local field enhancement factors at point A for gold (Au) and silver (Ag) NPs (Adapted from [30]). Inset: Schematic of a NP with the incident field  $\vec{E}_0$  and the position of point A. b) Induced electric field  $\vec{E}_{ind}$  from the induced dipole created by a metallic sphere under an external field  $\vec{E}_0$ . The blue line corresponds to the direction of  $\vec{E}_0$  and demonstrates the constructive superposition of the external  $\vec{E}_0$  and induced  $\vec{E}_{ind}$  electric fields.

For NP dimers, LFI-EFs can be stronger within their gap. The magnitude of LFI-EFs strongly depends on the distance between NPs. The closer they are, the higher LFI-EF is. Considering a dimer of two identical  $50 \text{ nm}$  Ag nanospheres at the resonance plasmon mode, the LFI-EF in the middle of the  $20 \text{ nm}$ -gap is about a factor  $7 \cdot 10^3$  (Fig. 1.6a). Then each time the distance reduces to  $10 \text{ nm}$ ,  $5 \text{ nm}$ , and down to  $1 \text{ nm}$ , LFI-EF gains approximately one order of magnitude and can reach values up to  $5 \cdot 10^5$  [30]. This electric enhancement is highly localized only in volumes on the order of a few of  $\sim \text{nm}^3$  in the interparticle junction. When moving away from this region, the LFI-EF drops dramatically (Fig. 1.6b).

Hot spots are the particular points near the NPs surface at which the LFI-EF is enhanced by  $10^5$  to higher. Therefore, the molecules located at the hot spots are under extremely intense irradiation. Thus, all spectroscopic processes would benefit from this enhancement, especially Raman scattering.

### 1.2.3 Surface-enhanced Raman scattering

Surface enhanced Raman scattering (SERS) is the amplified Raman scattering of molecules that is gained from the giant electric field enhancement in hot spots. Remarkably, Raman scattering benefits twice from this enhancement, during its

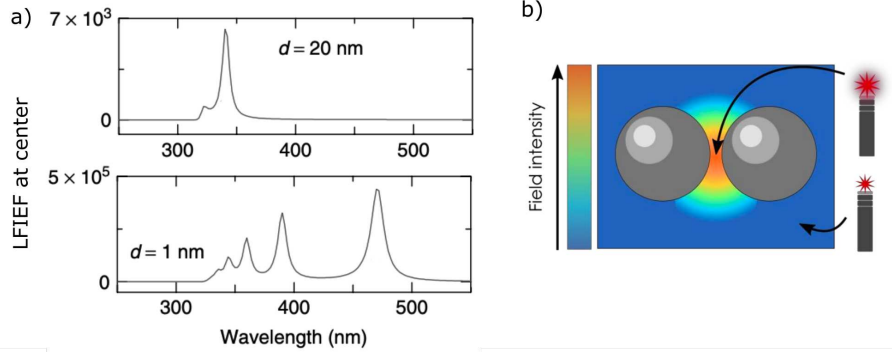


Figure 1.6: a) Local field intensity enhancement factors (LFI-EF) at the center of the nanogap formed by two identical  $50 \text{ nm}$ -radius silver NPs separated by a gap of  $d = 20 \text{ nm}$  (top) and  $d = 1 \text{ nm}$  (bottom) (adapted from [30]). b) Qualitative heat map of the LFI-EF distribution from a NP dimer (adapted from [2]).

excitation and de-excitation processes.

During the excitation process, the interaction probability of a photon with a molecule is proportional to the intensity of the incident electric field at frequency  $\nu_L$  (Eq. 1.3). The probability for deexcitation of a photon through Raman scattering is proportional to the intensity of the scattered field at frequency  $\nu_S$  (Eq. 1.4). Therefore, the probability of a Raman transition is proportional to both the intensity of the incident field and the scattered field (Eq. 1.5).

$$\sigma_{\text{excitation}} \sim |E_0(\nu_L)|^2 \quad (1.3)$$

$$\sigma_{\text{deexcitation}} \sim |E_0(\nu_S)|^2 \quad (1.4)$$

$$\sigma_{\text{Raman scattering}} = |E_0(\nu_L)|^2 \times |E_0(\nu_S)|^2 \quad (1.5)$$

When these processes happen in a hot spot, both incident and scattered fields are enhanced by an amount related to the LFI-EF. This leads to an enhancement factor for SERS (SERS-EF) of the form

$$\text{SERS-EF} = \text{LFI-EF}(\nu_L) \times \text{LFI-EF}(\nu_S) = \frac{|E(\nu_L)|^2}{|E_0(\nu_L)|^2} \times \frac{|E(\nu_S)|^2}{|E_0(\nu_S)|^2} \quad (1.6)$$

In general, the difference between the LFI-EF at  $\nu_L$  and  $\nu_S$  is ignored, leading to a simplified formula for SERS-EF

$$\text{SERS-EF} \sim \text{LFI-EF}(\nu_L)^2 = \frac{|E(\nu_L)|^4}{|E_0(\nu_L)|^4} \quad (1.7)$$

This equation illustrates that Raman scattering is expected to be enhanced by the square of the LFI-EF at the excitation wavelength in the hotspot. In other words, when the field is locally enhanced by  $n$  orders of magnitude, the Raman signal is

enhanced by  $2n$  orders of magnitude. This square dependency enables acquiring Raman spectra from solutions of dilute analytes. Thus, SERS becomes particularly interesting for trace analysis.

### 1.3 Practical implementation of SERS

Surface-enhanced Raman scattering (SERS) has been highlighted as a potentially ground-breaking tool for chemical analysis for more than a decade, thanks to its extreme sensitivity and fingerprint-like spectra [28, 37, 38, 23]. Indeed, SERS has been reported to be able to detect a single molecule [39, 40]. However, several practical applications have hindered the routine use of SERS as an analytical technique, namely, the SERS signal dispersion caused by irreproducible substrates and the time-consuming measurement procedure. This section discusses some practical implementations for SERS analysis, including a short review of SERS substrates, some main quantification methods, and solutions to overcome SERS signal irreproducibility. We end up with our strategic approaches for this thesis project.

#### 1.3.1 SERS substrates

SERS substrates can be classified into three groups: metallic NPs in suspension, metal NPs immobilized on solid substrates; and nanostructures fabricated directly on solid substrates [41]. Among them, metal NPs in suspension are popularly known for its ease in fabrication through regular wet chemistry. In addition, SERS enhancement can be easily improved through aggregating the NPs directly in suspension. However, their application in quantitative analysis is limited due to the poor signal reproducibility. The latter two solid substrates are known for providing better reproducibility than NPs in suspension, however they are more complicated to fabricate. A popular principle for immobilizing NPs on a solid support is to have the NPs interacting with wafers functionalised with thiol or amine coordinating groups. The procedure requires some further steps after synthesizing NPs in suspension, for instance, polymerising functional silanes or by a simple non-covalent adsorption of polyamines such as polyethyleneimine or polylysine onto a glass slide [36], then incubating for NPs deposition and self-assembly [41]. This leads to an increase in complexity and fabrication time in compared to NPs in suspension. The second type of the solid substrates, metallic nanostructures fabricated directly on the solid support, for example using electron beams to generate nano-patterns. This type of substrate can accurately control NPs size, shape and interparticle nanogaps. Thus, they provide high SERS enhancement factor and great reproducibility. However, these methods require specific instruments to generate beams of electrons or ions, in addition to several intermediate steps such as material deposition and removal. Thus, they have long-time fabrication and are not scalable.

Metallic NPs in suspension used as SERS substrates are diverse in shape such as spherical NPs, triangle or star NPs with different enhancement magnitudes,

Fig. 1.7 [42]. Nano stars and nano triangles can give very high enhancement thanks to their sharp tips. However, they are more complicated to fabricate and scale up than spherical particles.

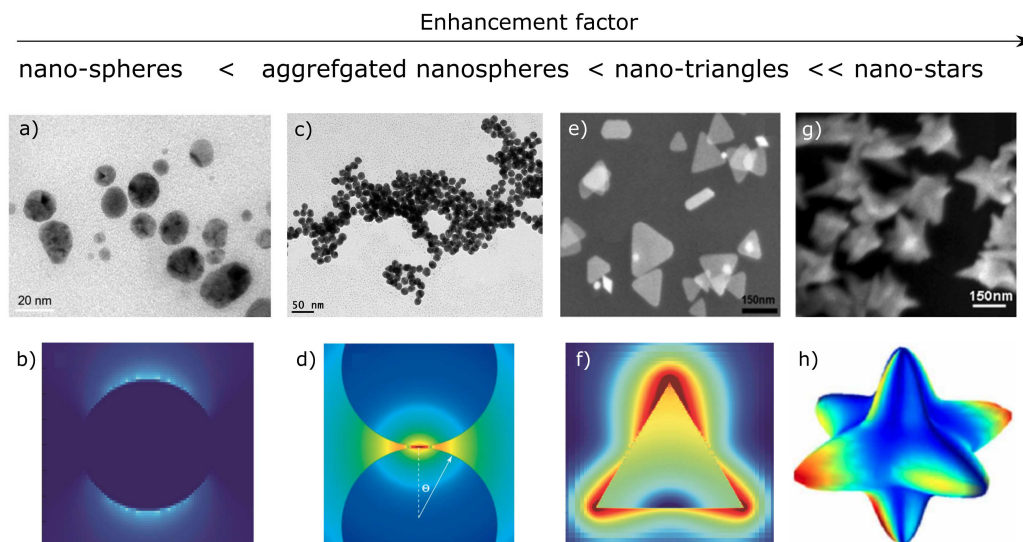


Figure 1.7: SERS substrates: Metal NPs in suspensions. a) TEM image of nano-spheres, b) TEM image of aggregated nano-spheres, c) SEM image of nano-triangles, d) SEM image of nano-stars, e-h) and their local electric field distribution respectively. (Adapted from Refs. [43, 44, 45, 46, 47, 48]).

The synthesis methods for metal NPs in suspensions, nonetheless, have common steps. First, silver or gold ions in solution are reduced by reducing agents, for examples: citrate, sodium borohydrate, hydrazine, etc. Nucleation process starts from the first reduced metal molecules and grow up to form NPs. Meanwhile, capping agents such as Polyvinylpyrrolidone (PVP), Polyethylene glycol (PEG), Cetrimonium bromide (CTAB), tannic acid, etc. are used to bind to the surface of the NPs to prevent the aggregation by repulsive forces [42]. The NPs size is modulated by selecting the strength and concentration of reducing agent. The stronger reducing agents often give smaller NPs. Whereas the shape of particle is affected by the surfactant and particle materials [42]. Moreover, temperature can also influence the size distribution [49].

In this thesis project, we used Lee-Meisel NPs, which are historical spherical NPs synthesized according to the protocol of P. C. Lee and D. Meisel published in 1982 [50]. Compared to other NPs shapes, spherical NPs are stable over time as its shape. A Lee-Meisel NPs batch can be synthesized at large scale, generally 500 mL which is worth at least 5000 acquisitions and can be stored for months in the fridge before use. To increase the SERS enhancement, in the work described in

chapter 2, we implemented a protocol to aggregate these spherical NPs into micrometric spheroids rich in hot spots. The detail of the NPs synthesis and aggregation are presented in chapter 2.

### 1.3.2 Quantification methods

For SERS quantitative analysis, the general method is to build a calibration curve that relates the spectral intensity to the analyte concentration, then the intensity from measurement samples is projected on this calibration curve to read the unknown concentration. In direct sensing, the analyte concentration is related directly to the spectral intensity of itself. Within a certain concentration, the higher concentration, the stronger spectral intensity, and linear calibration curves are usually established, Fig. 1.8a. However, in a broad range, when the concentration of the analyte is high enough to saturate the NPs surface, the SERS intensity reaches to a plateau, a non-linear calibration curve is obtained, Fig. 1.8b [51]. Another shape of calibration curves was also obtained from pH-sensitive molecule, 4-mercaptobenzoic acid (4-MBA) [52]. In this work, the spectral peaks generated from COO<sup>-</sup>, C=O groups were investigated to build the calibration curve in which there was a high/low intensity switching between basic and acidic pH ranges, Fig. 1.8c. This calibration curve was used to discriminate cancer cells from normal ones because cancer cells have a more acidic extracellular milieu.

Indirect sensing is usually applied when the analyte itself does not provide a specific enough or intense enough signal. Metal ions are representative cases that need indirect sensing method because they do not have any chemical bonds to generate Raman signal. The strategy is to use a very strong Raman reporter that binds to the analyte or is displaced by the analyte to translate analyte presence into a strong and distinctive SERS signal. The calibration curve is linked to this Raman reporter. For example, in Zamarion, Vitor M., et al 2008 [54], the authors used 2,4,6-trimercapto-1,3,5-triazine species (TMT) to bind to mercury ion Hg<sup>2+</sup>, Fig. 1.9a. Mercury ion binding to the thiol group of TMT decreased the stretching  $\nu$ C-S peaks at 432  $cm^{-1}$  and 485  $cm^{-1}$ . In parallel, Hg<sup>2+</sup> bound to the nitrogen ring increased the ring N atoms peak at 973  $cm^{-1}$ . Their intensity ratio in relation with mercury concentration were used to build the calibration curve, Fig. 1.9b.

### 1.3.3 SERS irreproducibility and solutions

The reproducibility of SERS enhancement between different batches is difficult to achieve because there are many factors evolved in the NPs formation, for instance, even a small variation in precursor ingredient concentration prone to human manipulation or random nucleation process. The SERS enhancement factor is also altered by the ageing of the NPs. For aggregation NPs substrates, even using the same NPs batch, the SERS signal intensity is still varied due to random aggregation process, mixing conditions and aggregation age [55, 56]. Additionally,

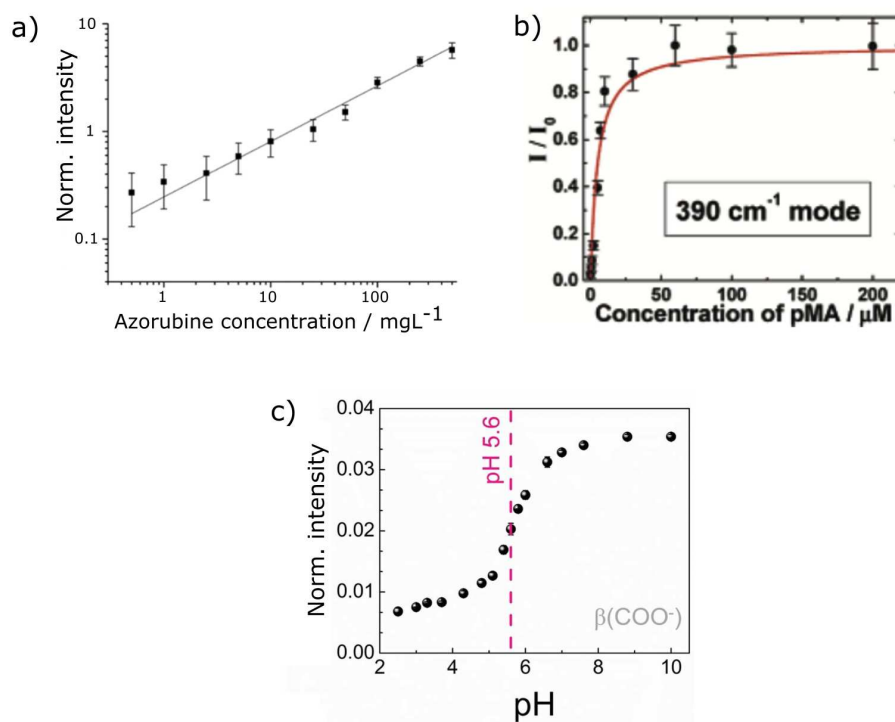


Figure 1.8: Different examples of SERS calibration curves. a) Linear calibration curve, b) non-linear calibration curve, c) pH titration curve. (Adapted from refs [53, 51, 52]).

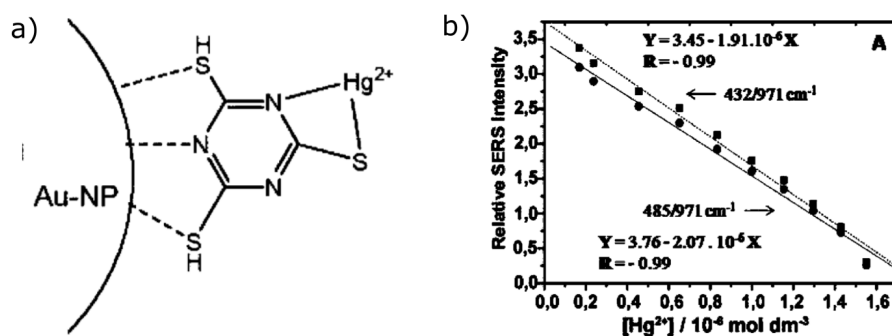


Figure 1.9: a) Schematic illustration showing the TMT stabilized on the AuNP surface binding to mercury ion  $\text{Hg}^{2+}$ . b) Calibration curves based on the intensity ratios at 432/971 (squares) and 485/971  $\text{cm}^{-1}$  (circles) versus the  $\text{Hg}^{2+}$  concentration. Adapted from [54].

the fluctuation of the laser power, electric source, and the distance between sample and laser source combined with high SERS sensitivity also contribute to the intensity fluctuation [57]. Unfortunately, SERS irreproducibility has been not well concerned and thoroughly investigated in analytical measurements. Many published works usually use just a few NPs batches for their measurements, from

which the reproducibility is challenging to estimate and often ignored. Therefore, on the whole, irreproducibility is still one of the biggest challenges preventing SERS from becoming a routine quantitative analysis and applied in real-world applications.

Many efforts have been made to improve the SERS reproducibility, like optimizing the substrates fabrication method to get the lowest variation possible. 5 – 10% variation has been reported on solid-supported metal NPs [58]. For lower reproducible substrates like NPs in suspensions or NPs films, another approach is to use internal intensity standards [59, 56]. In this method, the SERS signal from the target analyte is normalized to the signal from a close-by source. For example, Vlastimil Peksa et al. 2015 [53] used the Raman signal from silicon support of the NP film as an internal standard to normalize the SERS signal of the target molecule, Fig. 1.10a. This way can eliminate the signal fluctuations from laser power or sample-laser distance, but it does not access the SERS signal irreproducibility. For that, using a molecule with a similar chemical structure to the target molecule is more effective. This molecule provides the same relative enhancement factors to the target molecule but a different spectral feature to be able to differentiate from the spectrum of the target molecules [59, 56], Fig. 1.10b. Therefore, normalizing the SERS signal to the spectral feature from the added molecule can reduce the irreproducibility of SERS. However, it is challenging to find an appropriate internal standard molecule. An additional approach is to produce large replicates to improve the precision or to use statistic tools known as chemometrics to extract the information from informative Raman spectra [60, 29, 61].

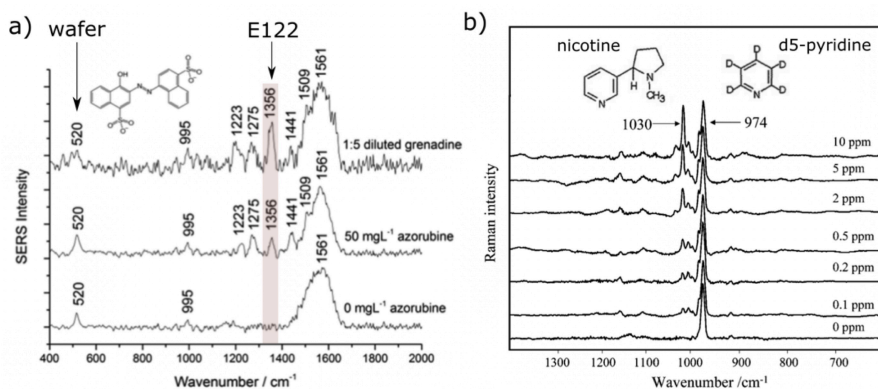


Figure 1.10: Quantitative SERS analysis using internal standards. a) The band intensity from target analyte E122 is normalized to the band intensity from silicon wafer (adapted from ref. [53]), b) using d5-pyridine internal standard to quantify analyte nicotine (adapted from ref. [59]).

## 1.4 Our strategic choices

In this thesis, we aim at developing an environmental monitoring method for metallic ion determination that will ultimately be implemented in real world. Our SERS-based method should satisfy several needs such as: large-scale measurements, ease in analytical sample preparation on field or in an automated device. It should also have lower cost compared to the current popular methods such as ICP or ion chromatography. Therefore, the SERS substrates should be easy to fabricate in large quantity and stable over time. Thus, working with spherical NPs in suspension are our first choice.

Our group has been working with the spherical Lee-Meisel NPs for several years. Their fabrication and properties such high stability and scaling-up ability have been well studied and confirmed. By reducing silver nitrate at boiling temperatures for an hour, we obtained spherical NPs with negative surface charge coming from the reducing agent, citrate. These suspensions were stable after several months stored in darkness at  $5^{\circ}\text{C}$ . For quantifying metal ions in water sample, we need a further step that removes residual citrate because citrate is an interference ligand binding to metal ions.

To increase the SERS enhancement, our ancient post-doc researcher established a protocol to aggregate NPs under electro-steric control. She used positive charge polymers, Polyethylenimine, to assemble the NPs with negative-surface-charge through electrostatic interaction. To control the NPs distribution and the size of NP aggregates, this reaction was carried out under a sufficient high viscosity generated by the screening agent, Polyethylene glycol. The proportion of these components was scanned to find the combination at which the resulted NP aggregates, so-called SERS beads, had a high absorption at our wavelength lasers. This method is easy and straight forward to apply. It provides SERS beads with a very good SERS enhancement when tested with Raman reporter. Since then, the method was then popularly used in our group to develop to quantify aquatic contaminants which is more relevant and challenging in real-world.

For metal ion determination, our previous PhD student worked on an indirect SERS sensing method for  $\text{Zn}^{2+}$  ions [29]. In this work,  $\text{Zn}^{2+}$  formed complexes with the receptor Xylenol orange (XO) which was trapped in NPs aggregates, Fig. 1.11a. XO displays a rich Raman spectrum thanks to its extended  $\pi$  system and multiple electron-rich centers (Fig. 1.11b). When it binds to  $\text{Zn}^{2+}$ , the intensity variation of the  $442\text{ cm}^{-1}$  peak was used to build the calibration curve, Fig. 1.11c. However, even after normalizing the signal to an internal standard, there was still a visible intensity variation between different replicates, Fig. 1.11c. Due to the SERS signal irreproducibility, building a reliable calibration curve requires a sufficient number of replicates to take average of them. His work also shown that the labour involved in acquiring such large data sets dominating the consolidated cost per analysis.

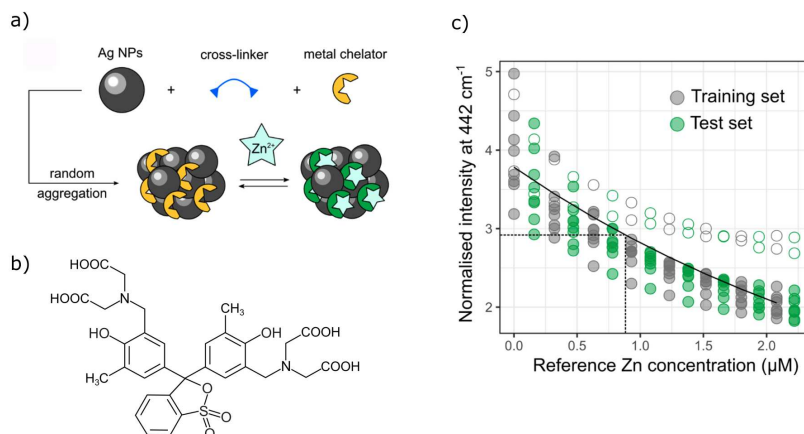


Figure 1.11: a) Chemical sensing scheme of  $Zn^{2+}$  ions. b) structure of the metal chelator Xylenol Orange. c) Evolution of the normalized XO-specific  $442\text{ cm}^{-1}$  peak as a function of added  $Zn^{2+}$  concentration (circle data points) and the built-in titration curve (black line). (adapted from [29]).

In this thesis work, we would like to overcome the limitation of the laborious SERS measurement procedure for building a calibration curve. We keep taking advantage of metal receptors that potentially display a high Raman cross-section, which is Eriochrome black (EBT) in this project. Indeed, EBT displays a strong SERS/Raman band around  $1300\text{ cm}^{-1}$  corresponding to the CC asymmetric stretching vibrations of the naphthalene ring that binds to sulfur and nitrogen atoms [62], Fig. 1.12. However, we explored the use of EBT not in a calibration mode but as an indicator for a complexometric titration. The analyte concentration will be determined straight away at the interrupt point on the titration curve. Chapter 2 will describe how these building blocks have been successfully implemented to quantify calcium and magnesium ions in mineral waters.

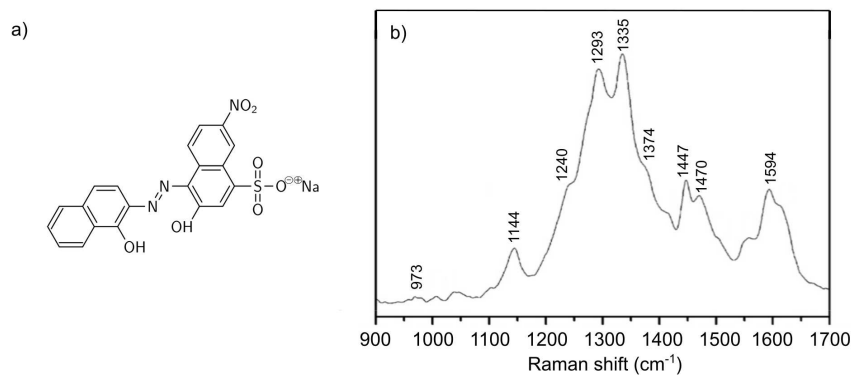


Figure 1.12: a) Chemical structure of EBT and b) EBT SERS spectra using 532 *nm* laser source. The wavelength associated to intensity peaks are denoted in the panel. (adapted from [62]).



# SERS-complexometric titration: water hardness measurement

---

## Contents

---

<b>2.1</b>	<b><i>Pre-print: A new look at an old classic: implementation of a SERS-based water hardness titration</i></b> . . . . .	<b>23</b>
------------	--	-----------

---

## **2.1** *Pre-print: A new look at an old classic: implementation of a SERS-based water hardness titration*

In this chapter, we will include the pdf of the pre-print corresponding to the method of SERS-based titration for water hardness determination. The pdf of the supplementary information associated to this pre-print is included in Appendix 2.1. Note that the labels of the supplementary figures in the pre-print correspond to the figures in Appendix 2.1.

# A new look at an old classic: implementation of a SERS-based water hardness titration

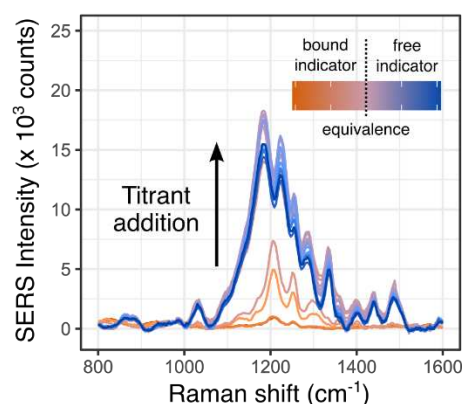
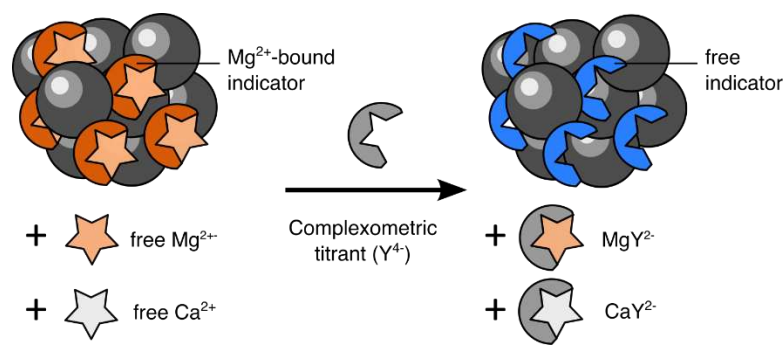
Ngoc Mai Duong,<sup>a</sup> Victoria E. Reichel,<sup>a</sup> Angelina Noclain,<sup>a</sup> Jean-Marc Di Meglio,<sup>a</sup> Pascal Hersen<sup>b</sup>  
and Gaëlle Charron (ORCID 0000-0002-9501-6376)<sup>a,\*</sup>

- a) Laboratoire Matière et Systèmes Complexes, UMR 7057, Université de Paris, CNRS, 10 rue Alice Domon et Léonie Duquet, 75205, Paris, cedex 13, France
- b) Institut Curie, Université PSL, Sorbonne Université, CNRS UMR168, Laboratoire Physico Chimie Curie, 75005 Paris, France

## Abstract

The routine use of SERS as an analytical technique has been hindered by practical considerations among which the irreproducibility of its signals and the lack of robustness of their calibration. In the present work, we examine a strategy to perform quantitative SERS without the need for calibration. The method reinvests a colorimetric volumetric titration procedure to determine water hardness but involves monitoring the progression of the titration through the SERS signal of a complexometric indicator. Upon reaching the equivalence between the chelating titrant and the metal analytes, the SERS signal abruptly jumps, which conveniently serves as an endpoint marker. Three mineral waters spanning divalent metal concentrations varying by a factor of 25 were successfully titrated in this way, with satisfactory accuracy, using a practical procedure that can be run in less than an hour.

## Table of contents graphic



To alleviate the need for calibration in SERS quantitative analysis, a complexometric indicator-based titration method has been implemented on the case of water hardness determination. The SERS signal abruptly switches about the equivalence, enabling accurate quantification without any calibration.

## Keywords

Complexometric titration - **Raman spectroscopy** - **Sensors** – SERS (2 mandatory from core keyword list)

## Introduction

Owing to its extreme sensitivity, down to the single molecule level, and to the fingerprint-like character of its spectra, surface-enhanced Raman scattering (SERS) has been highlighted as a potentially ground-breaking tool for chemical analysis for more than 10 years.<sup>1-4</sup> However, the necessary conditions to improve inter-laboratory comparability of experimental SERS results were still being discussed in a recent review by an international team of scientists with long-standing expertise in SERS.<sup>5</sup> Due to a complex interplay of electromagnetic and physico-chemical effects in the mechanism of SERS, it is a phenomenon intrinsically hard to control and results can differ significantly between laboratories, between days or even between nanoparticle (NP) batches or nanostructured substrates.<sup>5,6</sup>

As a quantification technique, SERS has been mostly used in spectrophotometric mode, the simplest implementation of which involves an analyte generating a distinctive SERS signal that gradually builds up as the concentration grows, much as in the direct sensing involved in HPLC or flame spectroscopy. Analytes that do not give rise to a sufficient signal, or to no SERS signal at all, can alternatively be tracked through their interaction with a chromogenic receptor giving rise to strong SERS signals or with a receptor bound to a SERS tag, thereby leading to turn-on or turn-off sensors (**Figure S0**). One typical case is that of a metal ion interacting with a ligand that acts as a loud SERS proxy for an otherwise silent analyte.<sup>7-13</sup> In both cases, direct sensing or through interaction with a receptor, the quantification capability exploits the dependence of the signal on the concentration through a calibration model, generally in a linear regime. However, owing to inhomogeneities at the nanoscale of the SERS-active material, to ageing of the material or to variations in the concentrations in the stocks (over time or from one batch to another), the validity of the calibration model is short-lived. Any new SERS material batch or any new day will most likely require a new calibration step to be performed. This can consume precious SERS-active materials and is time-consuming. We recently demonstrated that calibration is actually the largest driver of the consolidated cost of a metal ion analysis by SERS.<sup>14</sup>

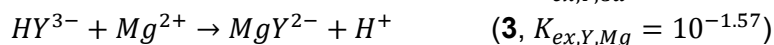
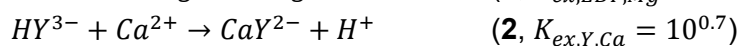
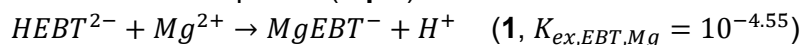
Before the advent of spectrophotometric techniques, concentrations of metal ions in samples were measured by means of complexometric volumetric titrations.<sup>15</sup> Briefly, these methods rely on three chemical protagonists: the target metal ion as the analyte, a chelator having a strong affinity for it as the titrant, and a highly absorbing chelating dye having a somewhat weaker affinity for the analyte than the titrant and two distinct colours in its free and

metal-bound states. A complexometric volumetric titration proceeds as follows. The indicator is introduced in the sample in default, typically a few percents, with regards to a gross estimation of the concentration of the analyte; it binds to the analyte quantitatively and imparts its bound-state colour to the medium. The titrant is introduced portion-wise into the mixture by mean of a burette; it binds to free metal ions. Once virtually all free metal ions have been consumed, any new addition of the titrant steals analytes from the binding cavity of the indicator, thereby releasing free indicator molecules that bring their free-state colour to the solution. The switch between bound and free-state colours of the indicator in the reaction mixture occurs about the equivalence point and therefore serves as an end-point marker. Complexometric methods have been documented for the titration of virtually every metallic ion.<sup>16</sup> Selectivity is often achieved by playing on the pH or through the use of masking agents. However, due to the colorimetric (absorption) nature of the visualisation of the end-point, those methods are often limited to concentrations in the mid- $\mu\text{M}$  to mM range.

Complexometric indicators often bear highly Raman-active chromophores. Revisiting those molecules as end-point markers in SERS-transduced titration could extend their usefulness to lower concentrations ranges due to the giant nature of SERS signals compared to their absorption features, while at the same time alleviating the need to build a reliable, robust calibration model. Indeed in complexometric titrations, calibration is enacted through the use of a standardised titrant. Here we examine the possibility of implementing an indicator-based metal complexometric titration in SERS on a well-known case example: the determination of water hardness. The developed method is successfully applied to three commercial mineral waters – Evian, Volvic and Contrex - having alkaline earth metal ion concentrations spanning one and a half order of magnitude.

## Results

Water hardness refers to the total concentration of calcium and magnesium ions in a water sample. The standard complexometric method for measuring it consists in titrating  $\text{Ca}^{2+}$  and  $\text{Mg}^{2+}$  ions with EDTA, an hexadentate ligand, in the presence of the complexometric indicator Eriochrome Black T (EBT, **Figure S1**).<sup>17</sup> The titration is conducted at pH 10 to ensure quantitative complexation. On first approximation, the titration can be considered to proceed as follows. Before titration begins, EBT is added to the sample in default compared to the divalent metal content and binds to a fraction of  $\text{Mg}^{2+}$  ions (**eq. 1**), thereby turning pink. As the first drop of titrant is added, EDTA binds to free calcium ions (**eq. 2**). Once all  $\text{Ca}^{2+}$  ions have been consumed, EDTA binds to free  $\text{Mg}^{2+}$  ions (**eq. 3**). When the reservoir of free  $\text{Mg}^{2+}$  ions is exhausted, newly added EDTA displaces  $\text{Mg}^{2+}$  ions from the EBT chelating cavity, which then retrieves its characteristic blue colour as a free species (**eq. 4**).



(Y refers to EDTA. Note that exchange constants were calculated from thermodynamic constants in ref. 16)

To visualize the end-point of this classic titration in SERS, we entrapped EBT into SERS-active aggregates made of hundreds of Ag nanoparticles (NPs) that were directly formed in the presence of the water sample and added titrant (**Figure 1**).

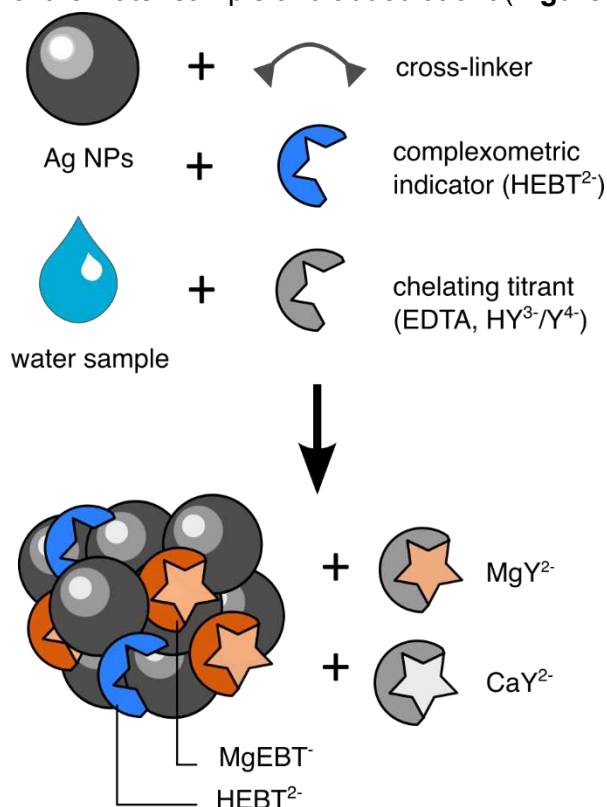


**Figure 1:** Scheme of the assembly of SERS active aggregates entrapping EBT in the presence of Ca<sup>2+</sup>, Mg<sup>2+</sup> and EDTA.

**SERS aggregates.** The SERS-active material was designed from simple building blocks so as to avoid being limited in our SERS measurements by the synthesis of the plasmonic aggregates. Details can be found in Supporting Information. Briefly, Ag nanoparticles were directly aggregated into water samples supplemented with EBT using a polyamine cross-linker (**Figure 1**). The Ag NPs were synthesised according to the Lee-Meisel method on a scale of 100 mL and 120  $\mu$ moles of Ag. The as-synthesised colloidal solution contains about 88  $\mu$ M residual citrate ligands, a fraction of which on their surface (see ESI).<sup>18</sup> Those strongly coordinate to Mg<sup>2+</sup> and Ca<sup>2+</sup> ions and therefore interfere with their titration. Hence we attempted to replace the native surface ligands with chloride ions after synthesis using a simple precipitation-redispersion protocol.<sup>19</sup> This procedure removes 95% of the total citrates, most likely the unbound ones, but we had no mean to characterize a full removal of the surface-bound ones. The Cl-derived NPs have a diameter of  $80 \pm 23$  nm (**Figure S2**). The chloride derived NPs are significantly larger than what is traditionally observed for Lee-Meisel NPs. This is due to the purification process which tends to discard

smaller NPs. Aggregation of NPs is then launched through addition of polyethyleneimine (PEI) as a cross-linking agent and PEG as a screening agent. The incorporation of PEG (20 kDa) slows down the aggregation through increased medium viscosity and steric crowding of the NP surface. It enables the formation of discrete, spherical, sub-micrometric ( $406 \pm 87$  nm in diameter according to optical microscopy) NP aggregates, hereafter referred to as SERS-beads, instead of large objects that precipitate out of the solution (**Figure S3**). To monitor the plasmonic properties of the SERS-active aggregates, we recorded the extinction spectra of SERS beads that were assembled without EBT. The extinction spectrum of the SERS-beads features a broad resonance with a maximum at 650 nm that overlaps well with the 638 nm and 785 nm excitation wavelengths of the lasers at our disposal and should therefore warrant acquisition of good quality SERS spectra (**Figure S4**).

### SERS spectra of aggregate-entrapped EBT.

The SERS spectrum of a blank sample of pure water supplemented with EBT was recorded under 638 nm irradiation, the final pH of the cuvette being buffered close to 10 (**Figure 2, solid orange trace and Figure S5**). The EBT concentration in the cuvette was  $3.7 \mu\text{M}$ . According to speciation analysis, under those conditions, EBT is present as the free monoprotated  $\text{HEBT}^{2-}$  species only. Entrapment of EBT within the aggregates is evidenced by the display of very intense features at Raman shifts. We were unable to link them to spectra from previous literature since the spectral features are highly dependent on the pH and pH was not reported in said studies.<sup>20–22</sup> At the same concentration and under the same acquisition conditions, the normal Raman spectrum is flat (**Fig. S6**). Likewise, these intense features do not stem from the ligands of the NPs or the crosslinker since EBT-free beads give rise to a comparatively flat SERS spectrum.

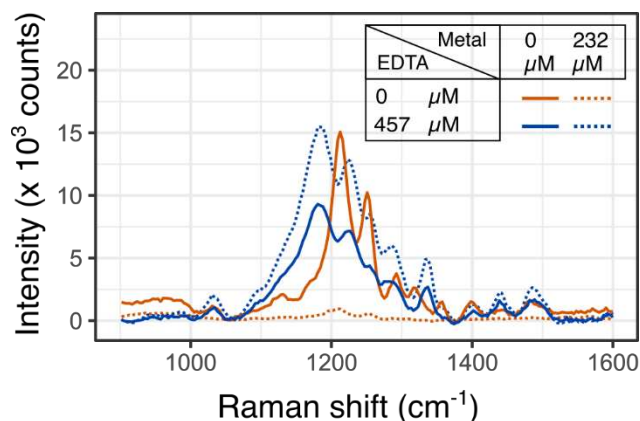


**Figure 2:** SERS spectra of free and bound EBT, in the presence or absence of an excess of EDTA, acquired under 638 nm irradiation. The analytical concentration of EBT is  $3.7 \mu\text{M}$  in each condition. Complexation of the indicator occurs in the presence of  $82 \mu\text{M}$   $\text{Mg}^{2+}$  (and  $150 \mu\text{M}$  of  $\text{Ca}^{2+}$ ).

A sample of Evian water was substituted for pure water to give rise to  $232 \mu\text{M}$  of divalent cations ( $\text{Ca}^{2+}$  and  $\text{Mg}^{2+}$ ) in the cuvette (**Figure 2, dashed orange trace**). Under those conditions, speciation analysis indicates that 87.5% of EBT is bound to  $\text{Mg}^{2+}$  (92% of EBT is metal-bound).

Compared to free EBT, the maximum intensity of the spectrum of bound EBT dramatically drops, by a factor of about 15. This is consistent with the absorption properties of EBT at pH=10 in the visible range (**Figure S7**). At 638 nm irradiation, the excitation source is almost in perfect resonance with the main electronic absorption band of free EBT. In the case of MgEBT<sup>-</sup>, the electronic match between the extinction spectrum and the laser source is poorer since the excitation wavelength falls in between the main and secondary absorption bands and the extinction coefficient of the complex at that wavelength is about half that of the free species. Schematically, the SERS signal could be damped when EBT binds to Mg<sup>2+</sup> because its electronic resonance with the laser is damped too, although a change of entrapment efficiency of the indicator in the aggregates between the free and bound states cannot be ruled out. Upon addition of an excess of EDTA compared to the total metal content, speciation analysis predicts that Mg<sup>2+</sup> should be released from the EBT cavity and this is indeed what is observed in the absorption spectrum with the restoration of the spectrum of free EBT (**Figure S7**). Note that due to constraints on the optical path length, the EBT concentration in absorption measurements was 33 μM. However, in SERS, the demetalation of EBT by EDTA does not lead to the recovery of the free EBT spectrum: upon addition of about 2 eq. of EDTA vs. metal (**Figure 2, dashed blue trace**), the obtained spectrum has a comparable maximum intensity compared to the free EBT spectrum but the spectral features are different. Identical spectral features are observed when the same amount of EDTA is added to the blank, free EBT sample (**Figure 2, solid blue trace**). This suggests an interaction between excess EDTA and EBT on the surface of the nanoparticles. A deeper investigation of the exact speciation of EBT adsorbed onto the SERS-active beads would be needed but was beyond the scope of the present study, in the frame of which we got satisfied with the spectra of EBT being markedly different when bound or unbound to Mg<sup>2+</sup>. A tentative link between these spectral features and speciation is nonetheless discussed in supporting information (**Figure S8**).

Under 785 nm irradiation, the excitation wavelength falls into the tail of the electronic absorption bands of free EBT (**Figure S7**). As the molar extinction coefficient of MgEBT<sup>-</sup> is about 75% that of HEBT<sup>2-</sup>, a change in SERS intensity of smaller magnitude than at 638 nm is expected upon complexation. However, the maximum SERS intensity drops, but by a factor of at least 70, suggesting that a weaker adsorption of EBT on the surface of the NPs upon complexation might also account for the drop in SERS intensity, on top of the change in resonance condition (**Figure S9**). The Raman shifts of the spectral features remain however largely unaffected by the complexation. At this wavelength, the free EBT spectrum is mostly restored through quantitative complexation of the metal cations upon adding EDTA.

### **SERS-titration of water hardness by EDTA using EBT as an end-point indicator.**

The switching *on* and *off* of the SERS signal of EBT upon demetalation and complexation respectively can be used as a proxy for visualising the equivalence of a complexometric titration. The general procedure to conduct the titration involves preparing a set of spectrophotometric cuvettes containing precursors of the SERS active aggregates, a fixed volume of water sample and a varying volume of titrant so as to sweep the ratio of titrant to divalent metal ions from 0 to 2 while maintaining the total volume constant through appropriate addition of a buffer (**Figure S5**). Evian, Volvic and Contrex mineral waters, which have total alkaline earth metal concentrations

differing by a factor of 23 and total mineral contents differing by one order of magnitude, were titrated in this way (**Table 1**). The molarity of the titrant was adapted for each mineral water to offer the same resolution about the equivalence. The buffer used was Britton & Robinson, an equimolar mixture of sodium acetate, potassium hydrogenophosphate and boric acid.<sup>23</sup> To maintain a pH constant at ~9.8 across the whole set of samples, the buffer molarity in the cuvette had to be increased from about 2.2 mM boron for Evian and Volvic to 4.6 mM boron for Contrex. For each water sample, the titration series were conducted in triplicates using two independent batches of Ag NPs (for a total of 6 titrations per mineral water sample). An additional blank titration was conducted for each target mineral water in which ultrapure water was substituted for the mineral water fraction.

Mineral water brand	Mg <sup>2+</sup> (mM)	Ca <sup>2+</sup> (mM)	Total divalent metal concentration (mM)	Bicarbonate (mM)	Dry residue (mg/L)
Evian	1.1	2.0	3.1	5.90	345
Volvic	0.3	0.3	0.6	1.2	130
Contrex	3.07	11.7	14.7	6.10	1121

**Table 1:** Composition of Evian, Volvic and Contrex water according to bottle labels.

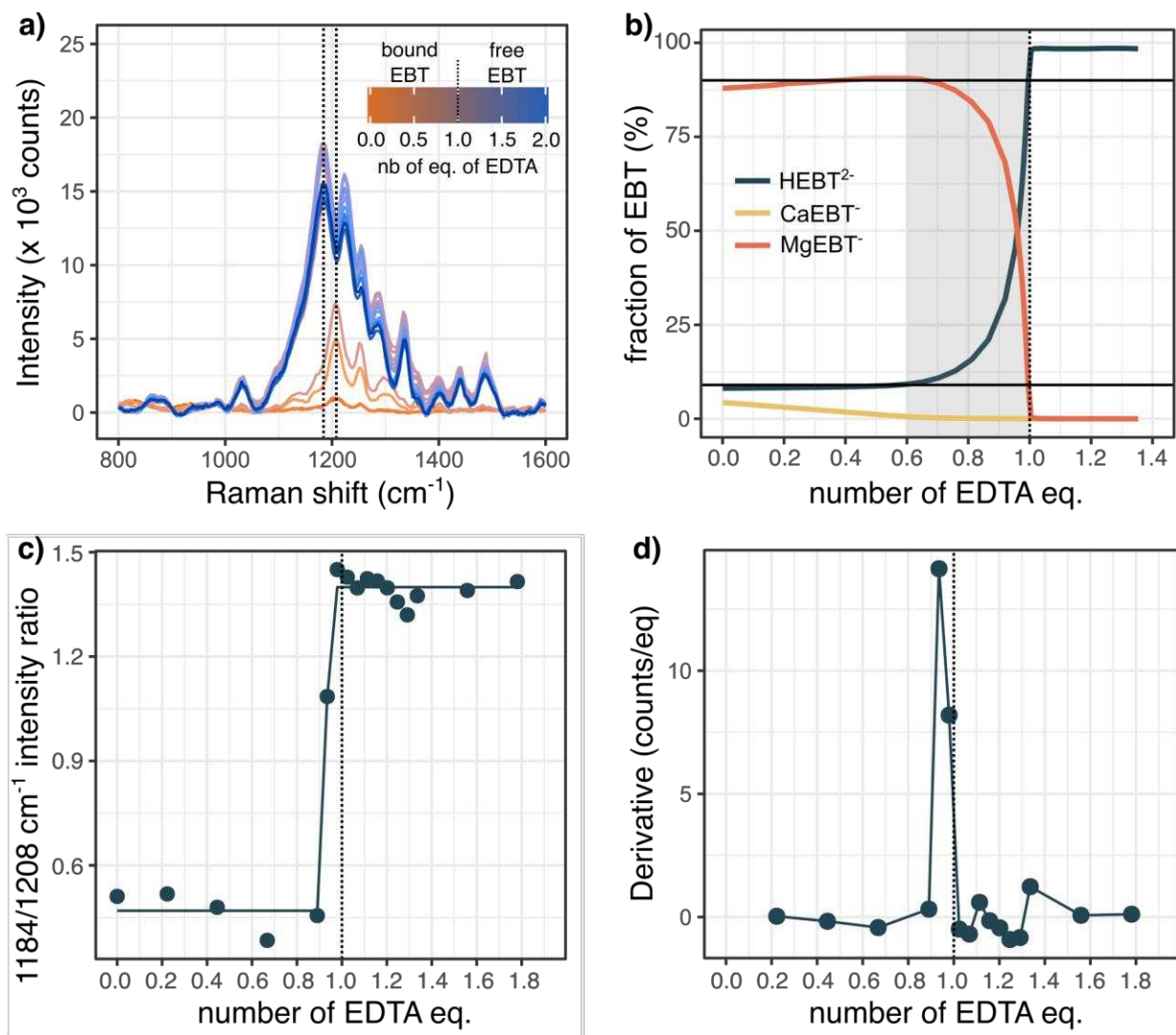


**Figure 3:** Baselined-corrected SERS spectra acquired under 638 nm irradiation over the course of one representative titration of Evian (a), corresponding speciation analysis (the calculations have been run without inclusion of the SERS aggregates) (b), intensity ratio of the 1184 and 1208 cm<sup>-1</sup> peaks as a function of added EDTA (c), and derivative of that ratio (d). The dashed lines in speciation, titration and derivative plots serve as visual guides of the theoretical equivalence according to metal concentrations indicated on the bottle label. The shaded area in (b) corresponds to the switching range of the indicator when exploiting it in classic colorimetric titration.

**Titration of Evian.** Figure 3a displays the evolution of the SERS spectra acquired under 638 nm across one typical titration series of Evian water. The spectra neatly aggregate into two groups of distinct shapes before and after equivalence: the first one having its maximum intensity at 1208 cm<sup>-1</sup> and the second one having its maximum at 1184 cm<sup>-1</sup> (see also replicate measurements in Fig. S10) The evolutions with titrant addition of those peaks mirror the sigmoidal one of the molar fraction of HEBT<sup>2-</sup> calculated by speciation simulation (Figures 3b, S11 & S12), albeit with a

significant lag in the case of the  $1208\text{ cm}^{-1}$  peak tracking. When tracking the ratio of both peaks, an abrupt sigmoid was obtained for each of the titration replicates (**Figures 3c & S13**), in which the height of the jump was maximised compared to the intensity variations observed throughout the blank titration. To read the equivalence from the SERS titration curve, the derivative can be calculated with regards to the number of equivalents of added titrant (**Fig. 3d**). Alternatively, the experimental points can be fitted to a sigmoid.

The number of titrant equivalents at which the endpoint of the reaction is experimentally read relatively to the theoretical equivalence inferred from the knowledge of the reference analyte concentration gives an estimate of the trueness of the quantification method. While speciation analysis predicts an abrupt increase in  $\text{HEBT}^{2-}$  molar fraction with an inflexion point at 95% of equivalence (**Fig. 3b**), the sigmoidal fit of the ratio displays its inflexion point at 94% of the theoretical equivalence on average over the intra and inter-batch replicates. This indicates that the interaction of the indicator with the surface of the NPs does not introduce a prohibitive bias; the SERS-derived endpoint is almost as good as the chemical speciation allows it. When monitoring the titration under 785 nm irradiation in SERS, similar results are obtained. Monitoring the maximum peak at  $1279\text{ cm}^{-1}$  yields sigmoidal titration curve with a mean inflexion point at 90% of equivalence (**Fig. S14 & S15**). Both irradiation wavelengths are therefore suitable to monitor the titration, on the condition of accounting for the observed difference in trueness. Remarkably, the SERS-based titrations are 90 to 94 % true without any calibration of the signal.

**Comparison of SERS-based and classic water hardness titrations.** When performing the classic colorimetric water hardness titration monitored by eye, the end point is pinpointed by means of the colour transition from pink to blue. That transition actually occurs over a range of numbers of titrant equivalent, which is formalized as the range over which the concentration ratio of the two species of the indicator changes from 0.1 to 10 (shaded area in **Fig. 3b**).<sup>15</sup> That range depends on the ratio of indicator to metal within the titration medium: the larger that ratio, the more progressive that transition (**Fig. S16**). To ensure a sharp colour switch, it is therefore recommended to work with indicator concentrations within a few % of the target metal concentration in the reaction vessel. However, there is a trade-off to consider because at low concentrations, colours are very faint. In the conditions in which the Evian SERS titrations were run, the EBT concentration was  $3.8\text{ }\mu\text{M}$  or 1.7% of the reference metal concentration in the cuvette mix. Not only would the transition range have extended over  $\sim 0.35$  eq. of EDTA vs. metal, making for an unprecise equivalence determination, EBT would have contributed only  $\sim 0.05$  to the absorption of the cuvette, altogether precluding naked eye inspection of the colour switch. Spectrophotometric monitoring would have been needed.

On the basis of the molar extinction coefficients determined in **Fig. S7**, we simulated the titration curve that would be obtained when tracking the absorption bands having maxima at 550 and 600 nm respectively or their ratio (**Fig. S17**). They display slopes and inflexion points at values comparable to those observed in the  $1184\text{ cm}^{-1}$  peak or 1184/1208 ratio-based SERS titration curves (97% trueness, 90 % switch achieved over 0.23 eq. of titrant in the case of absorption vs. 94 % trueness and 90% switch achieved over just under 0.1 eq. of titrant in the case of the ratiometric SERS monitoring). This evidences that EBT is about as good an indicator in SERS as

it is in absorption spectrometry and proves the feasibility of using colorimetric indicators to implement SERS-monitored complexometric titrations.

The determination of Evian hardness could hardly be seen as an unresolved issue since it can be easily done, if not by colorimetric means, with the assistance of an absorption spectrometer. However, the projected absorbance range spanned over the titration deserves a comment. The simulated titration curves (**Fig. S17**) imply that absorbances on the order of 0.04 and varying by just 0.007 absorbance units can be instrumentally resolved. At those absorbance levels, a signal-to-noise ratio of 100, which is commonly provided by entry-level absorption spectrometers, is enough to distinguish between the bound and free states of the indicator. However, disposable cuvettes, which were used in our protocol, have intrinsic absorbances that typically vary by 0.005 absorbance units. Given this cuvette-to-cuvette variability, a sharp titration curve could not have been obtained from absorption readings with our sample preparation protocol. Yet it was when monitoring the titration in SERS. Knowing that dyes can be detected in SERS at concentration much lower than the  $\mu\text{M}$  range, this gives a taste of the reservoir of sensibility that could be tapped when reinvestigating complexometric titrations at lower indicator and metal concentrations in SERS.

**Titration of Volvic.** The main advantage of running a complexometric titration with an indicator is that there is no need to recalibrate the spectroscopic signal when the target analyte concentration changes order of magnitude. One just needs to adjust the molarity of the titrant. We checked that this was indeed still the case when monitoring its progression in SERS by titrating Volvic which has a total divalent metal contents  $1/5^{\text{th}}$  that of Evian. This time, the SERS spectra acquired under 638 nm irradiation over titration aggregate into 3 groups (**Fig. S18**): one with a maximum intensity at  $1208\text{ cm}^{-1}$  and overall low intensity (before equivalence), one with a maximum intensity at  $1208\text{ cm}^{-1}$  and overall high intensity (about equivalence) and one with a maximum intensity at  $1184\text{ cm}^{-1}$  and overall high intensity (after equivalence). Again, the ratio of intensities at  $1184$  and  $1208\text{ cm}^{-1}$  was exploited to track the progress of the titration (**Fig. S19**). The evolution of the ratio closely mirrors the build-up of free EBT as  $\text{HEBT}^{2-}$  (see speciation analysis in **Fig. S16**), albeit with an inflexion point shifted beyond the theoretical equivalence point. For both batches of NPs, estimates of trueness were 113 and 102 % respectively, suggesting, by comparison with the Evian results, that some of the titrant could be consumed by adsorption to the surface of NPs. However, when monitoring the titration under 785 nm, the trueness estimates fall at 97 and 88 % depending on the NP batch, in closer agreement with speciation analysis (**Fig. S20 & S21**). This disqualifies adsorption of EDTA on the surface of the NPs as a source of positive bias in the 638 nm-monitored titration.

**Titration of Contrex.** We checked that the method was also capable of accurately titrating water being significantly harder than Evian by titrating Contrex, which has a divalent cation concentration 5 times that of Evian. Under 638 nm irradiation, the spectral evolution is similar to that observed for Volvic, with a transitory spectral contribution of high intensity arising about the equivalence (**Fig. S22**). Monitoring the ratio of  $1184$  and  $1208\text{ cm}^{-1}$  peaks give rise to sigmoidal titration curves, in line with speciation analysis, with positively biased trueness estimates of 103 and 117% respectively (**Fig. S23**). Under 785 nm, the spectral evolution is exactly similar to those

observed for Evian and Volvic, with trueness estimates of 105 and 96% depending on the NP batch (**Fig. S24 & S25**).

### **Discussion.**

SERS titrations have been successfully implemented for mineral waters having hardnesses spanning almost 2 orders of magnitude (differing 25 fold in total divalent metal cation content). **Figure 4** displays the observed analytical performances aggregated per batch of NP. Through monitoring the ratio of peaks at 1184 and 1208  $\text{cm}^{-1}$  under 638 nm irradiation or monitoring the sole peak at 1279  $\text{cm}^{-1}$  under 785 nm irradiation, the trueness never falls below 89% and never exceeds 117 %. The relative standard deviation of trueness, which we use here as a proxy for precision, does not exceed 2% when using a single batch of NPs (over 3 replicate titrations), or at most 7% over 6 titrations performed using two batches of NPs. These worst-case figures of merit are similar to the best ones we obtained in a similar study from the same chemical components (Lee Meisel NPs, a polyamine cross-linker) but using the complexometric metal probe in spectrophotometric mode, *ie.* through building a signal calibration model. The significant difference is, however, that it took much less time to achieve them using the complexometric probe in indicator mode: where it took 80 samples to build the calibration model and 6 replicate measurements to achieve 5% precision in spectrophotometric mode, one water hardness titration required only 18 samples. Moreover, the calibration model in the previous study was valid over just one decade of metal analyte concentration, whereas the present detection scheme works over a concentration range extended 2.5 folds. Practically, the titrations can be run in triplicate in a little less than two hours, from a batch of NPs that can be synthesised easily on a scale of 18 titrations. We see no limitation to the preparation and measurement of titration samples outside of conventional laboratory settings as the preparation steps involve only pipetting and mixing in hemolysis tubes, and measurements were run on two portable Raman spectrometers. The combined advantages of this practicality, of the inferred analytical figures of merit and of their robustness across about one decade and a half of concentrations demonstrate the merit of the complexometric volumetric titration strategy to turn SERS into a practical and reliable analytical technique.

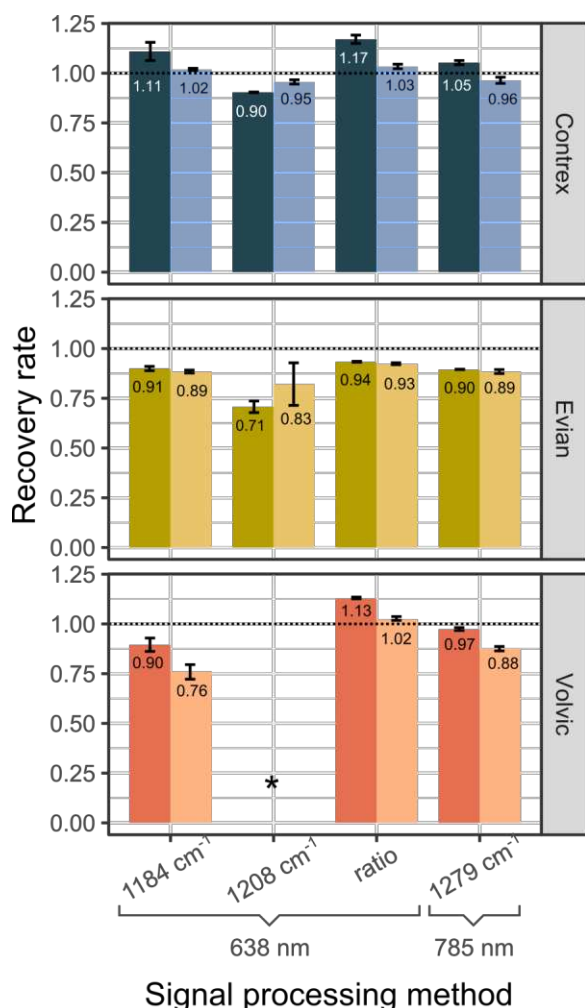


**Figure 4:** Overview of mean trueness estimates and their standard deviation per NP batch given as an estimation of precision. (\*) Sigmoidal fitting of intensities at 1208 cm<sup>-1</sup> under 638 nm over the course of the titration of Volvic was inappropriate for the data.

## Conclusion

Practical implementation of SERS in routine analytical chemistry has been hindered by the need to calibrate SERS signals. To alleviate this problem in the case of metal cation analyte, we suggested reinvesting tried and tested complexometric volumetric methods which were popular before the advent of modern instrumental analysis. We successfully implemented a SERS-monitored complexometric titration of water hardness, in which the calibration is built-in through the use of a standardised titrant and the SERS signal abruptly switches when the equivalence is reached. The full titration in triplicates can be run in a little less than two hours, with nothing more than pipettes, tubes and a portable Raman spectrometer. Mean trueness estimates between 88 and 117 % were obtained, with a precision of maximum 2%, without any external calibration, and for mineral waters having hardnesses differing by a factor of 25, from 0.6 mM to 15 mM. Given the breadth of complexometric methods and indicators that were employed in the past for titrating

virtually every metal cation, but also many anions, and the notorious sensitivity of SERS, we hope that these results will pave the way for implementing practical SERS-based titrations at trace levels.

## Acknowledgements

We graciously acknowledge the support of the Agence Nationale de la Recherche under the grant ANR-17-CE04-0009-01 (UnivSERS), that of Ville de Paris under the grant Emergences Métal'Eau and of Région Île de France under the grant 13012334 (Scorpions).

## Disclaimer

The authors declare no conflict of interest.

## Supporting information

Detailed chemical protocols, descriptions of instrumental set-ups and spectral processing, and additional SERS results as figures and raw data can be found in supporting information.

## References

1. Cialla, D. *et al.* Surface-enhanced Raman spectroscopy (SERS): progress and trends. *Anal. Bioanal. Chem.* **403**, 27–54 (2011).
2. Alvarez-Puebla, R. A. & Liz-Marzán, L. M. Traps and cages for universal SERS detection. *Chem Soc Rev* **41**, 43–51 (2011).
3. Golightly, R. S., Doering, W. E. & Natan, M. J. Surface-Enhanced Raman Spectroscopy and Homeland Security: A Perfect Match? *ACS Nano* **3**, 2859–2869 (2009).
4. Halvorson, R. A. & Vikesland, P. J. Surface-Enhanced Raman Spectroscopy (SERS) for Environmental Analyses. *Environ. Sci. Technol.* **44**, 7749–7755 (2010).
5. Le Ru, E. C. & Etchegoin, P. G. Basic Electromagnetic Theory of SERS. in *Surface Enhanced Raman Spectroscopy* (ed. Schlücker, S.) 1–37 (Wiley-VCH, 2011).

6. Bell, S. E. J. *et al.* Towards Reliable and Quantitative Surface-Enhanced Raman Scattering (SERS): From Key Parameters to Good Analytical Practice. *Angew. Chem. Int. Ed.* **59**, 5454–5462 (2020).
7. Jimenez de Aberasturi, D. *et al.* Optical Sensing of Small Ions with Colloidal Nanoparticles. *Chem. Mater.* **24**, 738–745 (2012).
8. Zamarion, V. M., Timm, R. A., Araki, K. & Toma, H. E. Ultrasensitive SERS Nanoprobes for Hazardous Metal Ions Based on Trimercaptotriazine-Modified Gold Nanoparticles. *Inorg. Chem.* **47**, 2934–2936 (2008).
9. Sarkar, S., Pradhan, M., Sinha, A. K., Basu, M. & Pal, T. Selective and Sensitive Recognition of Cu<sup>2+</sup> in an Aqueous Medium: A Surface-Enhanced Raman Scattering (SERS)-Based Analysis with a Low-Cost Raman Reporter. *Chem. – Eur. J.* **18**, 6335–6342 (2012).
10. Tsoutsis, D. *et al.* Simultaneous SERS detection of copper and cobalt at ultratrace levels. *Nanoscale* **5**, 5841–5846 (2013).
11. Guerrini, L. *et al.* Chemical speciation of heavy metals by surface-enhanced Raman scattering spectroscopy: identification and quantification of inorganic- and methyl-mercury in water. *Nanoscale* **6**, 8368–8375 (2014).
12. Tang, W., Chase, D. B., Sparks, D. L. & Rabolt, J. F. Selective and Quantitative Detection of Trace Amounts of Mercury(II) Ion (Hg<sup>2+</sup>) and Copper(II) Ion (Cu<sup>2+</sup>) Using Surface-Enhanced Raman Scattering (SERS). *Appl. Spectrosc.* **69**, 843–849 (2015).
13. Xu, G., Song, P. & Xia, L. Examples in the detection of heavy metal ions based on surface-enhanced Raman scattering spectroscopy. *Nanophotonics* (2021) doi:10.1515/nanoph-2021-0363.
14. Brackx, G. *et al.* A frugal implementation of Surface Enhanced Raman Scattering for sensing Zn<sup>2+</sup> in freshwaters – In depth investigation of the analytical performances. *Sci. Rep.* **10**, 1–11 (2020).

15. Skoog, D. A., West, D. M., Holler, F. J. & Crouch, S. R. *Fundamentals of Analytical Chemistry*. (Brooks Cole, 2003).
16. Cheng, K. L., Ueno, K. & Imamura, T. *CRC Handbook of Organic Analytical Reagents, Second Edition*. (CRC Press, 1992).
17. Harvey, A. E., Komarmy, J. M. & Wyatt, G. M. Colorimetric Determination of Magnesium with Eriochrome Black T. *Anal. Chem.* **25**, 498–500 (1953).
18. Munro, C. H., Smith, W. E., Garner, M., Clarkson, J. & White, P. C. Characterization of the Surface of a Citrate-Reduced Colloid Optimized for Use as a Substrate for Surface-Enhanced Resonance Raman Scattering. *Langmuir* **11**, 3712–3720 (1995).
19. Stewart, A., Murray, S. & Bell, S. E. J. Simple preparation of positively charged silver nanoparticles for detection of anions by surface-enhanced Raman spectroscopy. *Analyst* **140**, 2988–2994 (2015).
20. Carron, K., Mullen, K., Lanouette, M. & Angersbach, H. Selective-Ultratrace Detection of Metal Ions with SERS. *Appl. Spectrosc.* **45**, 420–423 (1991).
21. Gauldie, R. W., Xi, K. & Sharma, S. K. Developing a Raman Spectral Method for Measuring the Strontium and Calcium Concentrations of Fish Otoliths. *Can. J. Fish. Aquat. Sci.* **51**, 545–551 (1994).
22. Szabó, L., Herman, K., Leopold, N., Buzumurgă, C. & Chiş, V. Surface-enhanced Raman scattering and DFT investigation of Eriochrome Black T metal chelating compound. *Spectrochim. Acta. A. Mol. Biomol. Spectrosc.* **79**, 226–231 (2011).
23. Britton, H. T. S. & Robinson, R. A. CXCVIII.—Universal buffer solutions and the dissociation constant of veronal. *J. Chem. Soc. Resumed* 1456–1462 (1931)  
doi:10.1039/JR9310001456.

# Supplementary information for chapter 2

## Contents

---

2.2	Supplementary information of the pre-print: A new look at an old classic: implementation of a SERS-based water hardness titration . . . . .	25
-----	---	----

---

2.2	Supplementary information of the pre-print: A new look at an old classic: implementation of a SERS-based water hardness titration	
-----	---	--

# Supporting information to “A new look at an old classic: implementation of a SERS-based water hardness titration”

Ngoc Mai Duong,<sup>a</sup> Victoria E. Reichel,<sup>a</sup> Angelina Noclain,<sup>a</sup> Jean-Marc Di Meglio,<sup>a</sup> Pascal Hersen<sup>b</sup> and Gaëlle Charron (ORCID 0000-0002-9501-6376)<sup>a,\*</sup>

- a) Laboratoire Matière et Systèmes Complexes, UMR 7057, Université de Paris, CNRS, 10 rue Alice Domon et Léonie Duquet, 75205, Paris, cedex 13, France
- b) Institut Curie, Université PSL, Sorbonne Université, CNRS UMR168, Laboratoire Physico Chimie Curie, 75005 Paris, France

## Detailed chemical protocols

### Chemicals

**Ethylenediamine tetraacetic acid, di sodium salt dihydrate** (99% purity as per titration, CAS 6381-92-6r), **Eriochrome Black T** (Reagent specification as per European Pharmacopoeia, #CAS 1787-61-7), **polyethylene glycol** (MW ~20 kDa, BioUltra grade, CAS 25322-68-3), polyethyleneimine (branched, MW ~25 kDa by light scattering, 13000 – 18000 mPa.s viscosity, CAS 9002-98-6), **silver nitrate** (ACS reagent, >99.0%, CAS 7761-88-8), sodium citrate tribasic dihydrate (p.a., ≥99.0%, CAS 6132-04-3) and tetrasodium borate (99%, BioUltra, CAS1330-43-4) were purchased from Aldrich. Glacial acetic acid (100%, NormaPur, CAS 64-19-7) and disodium hydrogen phosphate dodecahydrate (102% assay, NormaPur, CAS 7558-79-4) were purchased from VWR. All pH adjustments were performed using a 1N sodium hydroxide standardised solution from Aldrich. All chemicals were used as received without further purification. Evian, Volvic and Contrex water were stocked as 1.5 L bottles from a supermarket.

### Synthesis of Lee-Meisel silver nanoparticles.

*Apparatus for the synthesis process.* A 250 mL triple-neck round bottom flask was washed using 100 mL (1 volume) aqua regia (a mixture of 80 mL hydrochloric acid (37%wt) and 20 mL nitric acid (69%wt)) prior to synthesis, rinsed with 10 equivalent volumes of milliQ water, then with 0.5 volume of 70% ethanol afterwards and finally dried overnight in a 55°C stove. The flask was nested within a silicon oil bath on top of a magnetic heating plate. The temperature was controlled through a thermocouple inserted in the oil bath and a temperature controller. The flask was equipped with an oval stir bar and a condenser.

*Synthesis.* To synthesize 100 mL of silver nanoparticle solution, 20 mg silver nitrate were inserted into the flask along with 100 mL ultrapure water. The solution was brought to reflux under stirring

using a 130°C set point for the oil bath. 2 mL of trisodium citrate 34.0 mM were quickly injected using a syringe into the reaction mixture through one of the side necks. The temperature was set and maintained at 100°C for 1 hour. Over time, the solution turns yellow then grey to reach a final milky green-grey colour. After cooling, the solution is stored in a closed glass bottle at 2-5°C.

Munro *et al.* have proposed on the basis of NMR data that the one-electron reduction of Ag(I) combines with a two-electron oxidation of citrate as acetonedicarboxylic acid and CO<sub>2</sub> (through formate).<sup>1</sup> The balanced chemical equation for the reduction of Ag(I) by citrate then writes as



Given this stoichiometry, silver is the limiting reagent of the reaction in our conditions. Assuming again that the reaction is quantitative, the as-synthesised solution has a 1.2 mM Ag concentration as colloidal nanoparticles and contains 88 µM residual citrate.

*Removal of surface citrates.* In order to achieve more reactive surfaces, the residual citrates in the previously synthesized Lee-Meisel silver NPs were displaced by supplementing the reaction mixture with sodium chloride at a final concentration of 0.2 mM, according to a protocol by Stewart *et al.*<sup>2</sup> The mixture was shaken via vortex mixing and incubated for 10 minutes. The solution was then aliquoted as 12.5 ml fractions into 15 mL Falcon tubes, centrifuged at 6000 rpm for 25 min on a Hettich EBA 21 centrifuge. The supernatant was discarded to leave a 600 µL NP-rich fraction which was resuspended in ultrapure water to reach back the initial volume, and homogenized using a vortex mixer and then by ultrasonication for 4 min. All aliquots were then merged into a single stock which was stored in a closed glass bottle at 2-5°C. The assumed Ag concentration as colloidal nanoparticles is 1.2 mM. At most, the residual citrate concentration is 4.2 µM and the chloride concentration is 0.01 mM. The NPs are ready to be used after one night of aging and remain functional for at least 5 days under these storing conditions.

## **Bead assembly and cuvette preparation for SERS measurements (synthesis of beads)**

### ***Stock solutions***

All stock solutions were prepared using volumetric glassware (glass pipettes and flask) and scales with a 1 mg or 0.1 mg precision under our experimental conditions.

*Britton and Robinson buffer (BRB).* An equimolar mixture of acetic, phosphoric and boric acid) 40 mM in boron at pH 8 was prepared from glacial acetic acid, disodium hydrogen phosphate and sodium tetraborate. This mother buffer was then diluted to give rise to BRB 4 mM in boron at pH 8 and BRB 4 mM in boron at pH 10.5 (pH adjustment was performed using NaOH 1N ).

*PEI solution.* A 10 mM (monomeric unit) mother solution was prepared by mixing 43 mg of PEI with 10 mL BRB 4 mM pH8. The solution was diluted to a 1 mM stock solution using BRB 4 mM pH 8 as the solvent.

*PEG solution.* A 17%wt PEG stock was prepared by dissolving 80 g of PEG in 400 g of BRB 4 mM pH 10.5.

*EBT solution.* 23.3 mg of EBT were dissolved in 10 mL ultrapure water to give a 5.05 mM stock.

*EDTA solutions.* 379 mg EDTA disodium salt were introduced in a volumetric flask and dissolved in approximately 100 mL BRB 4 mM pH 10.5. The pH was monitored and adjusted to 10.5 through addition of approximately 1.7 mL NaOH 1 N. The flask was topped up to the mark using BRB 4 mM pH 10.5. The pH can drift by ~2% overnight. On the day of SERS acquisition, the pH was adjusted to 10.5 using NaOH 1N. The final EDTA titer was 4.06 mM. Following the same protocol, 1861 mg of EDTA disodium salt were introduced in a 250 mL volumetric flask along with 100 mL BRB 4 mM pH 10.5 and approximately 8 mL of a NaOH 1N. The pH was measured and adjusted to 10.5 before topping up the flask to the mark with BRB 4 mM pH 10.5. Overnight, the pH had dropped to 10.35 and was adjusted back to 10.5 to give a 19.97 mM stock. The 4.06 mM solution was diluted 5 times with BRB 4 mM pH 10.5 to give a 0.81 mM solution.

#### ***Preparation of plain beads for absorption measurements***

In a disposable hemolysis tube, 1.5 mL of chloride-derived Ag NP solution were inserted along 1.5 mL of PEG stock. The mixture was homogenized by vortex mixing. Next, 26  $\mu$ L of PEI stock were added and the mixture was again homogenized by vortexing. The solution was transferred to a disposable PMMA spectrophotometric cuvette and left to mature 1 hour before acquiring its UV-vis absorption spectrum.

#### ***Preparation of samples for SERS-based titrations***

Samples for SERS-based titrations (of mineral water or of blank) were prepared according to the protocol depicted in **Fig. S5** using the stock solutions described above. The procedure involves adding into hemolysis tubes a constant volume of sample supplemented with EBT, a variable volume of appropriate buffer, a variable volume of appropriate EDTA stock such that the total of buffer and EDTA fractions remains at 600  $\mu$ L, a fix volume of chloride derived Ag NP solution, a fix volume of PEG stock and a fix volume of PEI to initiate bead formation, in that order. The content of the tubes is homogenized using a vortex mixer after addition of the EDTA, NP, PEG and PEI fractions. The full mineral water titrations series in triplicate plus the blank titration series have been prepared at once, adding each reagents into the 4x18 tubes and then moving to the next one. The water samples supplemented with EBT were obtained by mixing 1 volume of EBT 5.05 mM stock (250  $\mu$ L or 500  $\mu$ L using a 1 mL graduated glass pipette) with 100 volumes of mineral water or ultrapure water (volumetric pipette).

The mixtures were aged for 1 hour before launching the spectral acquisitions. Two operators were required to run the optical measurements so that acquisitions under the two excitation wavelengths were run at similar aging time. Operator A measured two titrations series under 638 nm excitation while operator B measured the two remaining series under 785 nm. They then swapped sample trays.

#### ***Preparation of plain beads for SERS control measurements***

Plain beads having the same Ag concentration as those assembled in the SERS-titration sample were prepared by substituting ultrapure water for the fraction of sample water supplemented with EBT, all other components being the same.

***Preparation of cuvette for normal Raman measurement of EBT.***

1,826  $\mu\text{L}$  of ultrapure water were mixed with 2,100  $\mu\text{L}$  BRB 4 mM pH 10.5 and 3  $\mu\text{L}$  of 4.8 mM EBT solution to give rise to a 3.7  $\mu\text{M}$  EBT solution at pH 9.90.

## Instrumental set-ups

***SERS measurements: 638 nm & 785 nm set-up***

Spectra under 638 nm excitation were acquired using an optical fiber-based set-up from Ocean Optics comprising a QE Pro spectrometer, a 638 nm laser module (I0638SL0050MA) and a coaxial Raman probe for measurement in backscattering configuration. The laser power was within 50-100 mW. PMMA spectrophotometric cuvettes were nested into a 4-window sample holder which had 3 windows obliterated. The integration time was 15 s and the spectra were recorded without averaging.

Spectra under 785 nm excitation were acquired on an integrated BWTEK *iRaman Plus* portable spectrometer equipped with a 785 nm laser having a maximal power of 420 mW and a laser spot size at the sample surface of 85  $\mu\text{m}$ . Excitation and collection were performed in backscattering configuration using a coaxial optical fibre Raman probe. The spectrometer resolution is  $\sim 4.5 \text{ cm}^{-1}$ . The spectral acquisition range was set to 300–2000  $\text{cm}^{-1}$ . The acquisition time was set to 2 s and the laser power to 20%, or 15% in the few instances where the signal was saturated. Each spectrum was averaged over 3 spectral recordings.

***UV-vis measurements***

UV-vis absorption spectra were acquired on a Jasco V-630 UV-vis spectrophotometer in PMMA disposable cuvettes.

***Optical imaging of SERS active aggregates***

Optical imaging of SERS aggregates was performed on an Olympus inverted microscope mounted with a 100 X objective. A Gene Frame (65  $\mu\text{L}$  [1.5 x 1.6 cm]) was placed onto a microscopy slide and 50  $\mu\text{L}$  of active aggregate solution (non-diluted) was inserted within the frame. The filled Gene Frame was closed using a glass cover slip. Care was taken to avoid any air bubbles within the reservoir.

***TEM imaging.***

TEM imaging of chloride derived nanoparticles was performed on a Tecnai12 transmission electron microscope (ThermoFischer Scientific) equipped with a 4K $\times$ 4K Oneview camera (Gatan), under 120KV voltage. The Cl-NP mother solution (assumed Ag concentration of 1.2 mM) was diluted 2.6 fold to limit aggregation onto the grid. Carbon coated copper grids (400 mesh) were used. Parafilm was stucked to the laboratory desk and a drop of 10  $\mu\text{L}$  nanoparticle solution was placed on top of the parafilm surface. The carbon coated copper grid was placed upside down

onto the drop (shiny side of the grid in touch with the solution). The carbon coated copper grid was incubated for 5 minutes. Afterwards, a Kimwipe filter paper was used to remove residues of the drop on the edge of the carbon coated copper grid. The carbon coated copper grid is placed within a half open petri dish on a filter paper to dry. After 10 minutes the dry carbon coated copper grid can be inserted within the TEM sample holder.

### **Speciation analysis**

Speciation analysis was conducted using Visual MINTEQ software with the speciation constants given provided in Cheng, Ueno and Imamura.<sup>3</sup>

## **SERS and Raman spectral processing**

### **Softwares, packages and algorithms**

Spectral data were processed independently by the lead and corresponding authors using the open-source software R or Python.<sup>4,5</sup> Baseline corrections were performed using either asymmetric least squares smoothing in Python or polynomial fitting (*modpolyfit()* function of the baseline package in R).<sup>6,7</sup> Both spectral processing gave identical results. The data presented in the figures were treated in R.

### **SERS spectral processing, description of aggregated data set, packages and parameters for baseline subtraction**

*Laser 638 nm.* The raw data contains 1044 data points with Raman shift ranging from 99.943 to 3309.417  $\text{cm}^{-1}$ . Then they are truncated to keep the Raman shift range from 164.32 to 3267.65  $\text{cm}^{-1}$  corresponding to 1010 data points, before doing baseline correction.

*Laser 785 nm.* The raw data contains 1803 data points with Raman shift ranging from 296.86 to 3294.32  $\text{cm}^{-1}$ . Then they are truncated to keep Raman shift range from 331.77 to 3200.76  $\text{cm}^{-1}$  corresponding to 1746 data points before doing baseline correction.

### **Structure of aggregated titration dataset**

For each water brand analyzed, two independent experiments were performed using two distinct batches of NPs. Each experiments contained 3 titration series replicates and one blank titration series. A titration series contains 18 points. Therefore, there are  $2 \times (3 + 1) \times 18 = 144$  spectra per analysed water brand at any given excitation wavelength. The two sets of  $3 \times 144 = 432$  spectra acquired under 638 nm and 785 nm respectively were aggregated into two dedicated files.

In those files, the spectra were ordered as row vectors, the 17 first columns of which give the chemical composition and settings of optical measurements. The remaining columns are the Raman intensities at the Raman shift given as headers.

## **Supporting Figures**

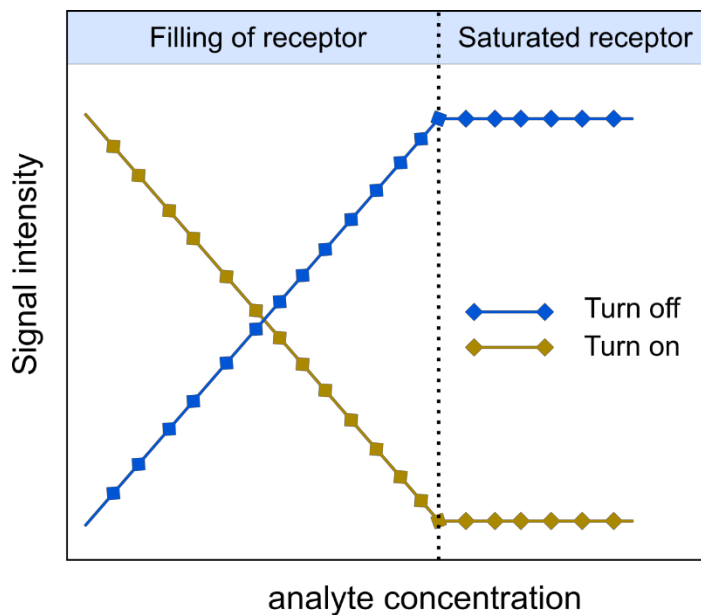


**Figure S0:** Schematic depiction of calibration models when detecting an analyte in spectrophotometric mode through its interaction with a receptor.

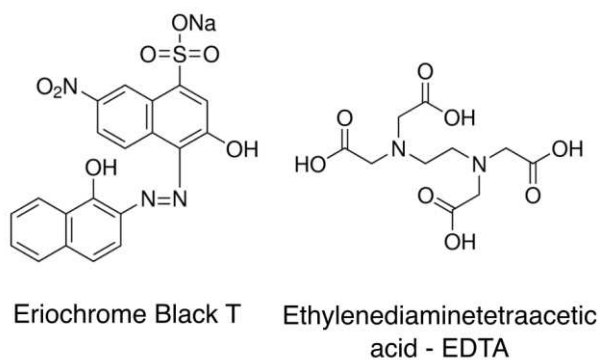


**Figure S1:** structures of the indicator (EBT) and chelator (EDTA) used in the water hardness titration.

(a)

(b)

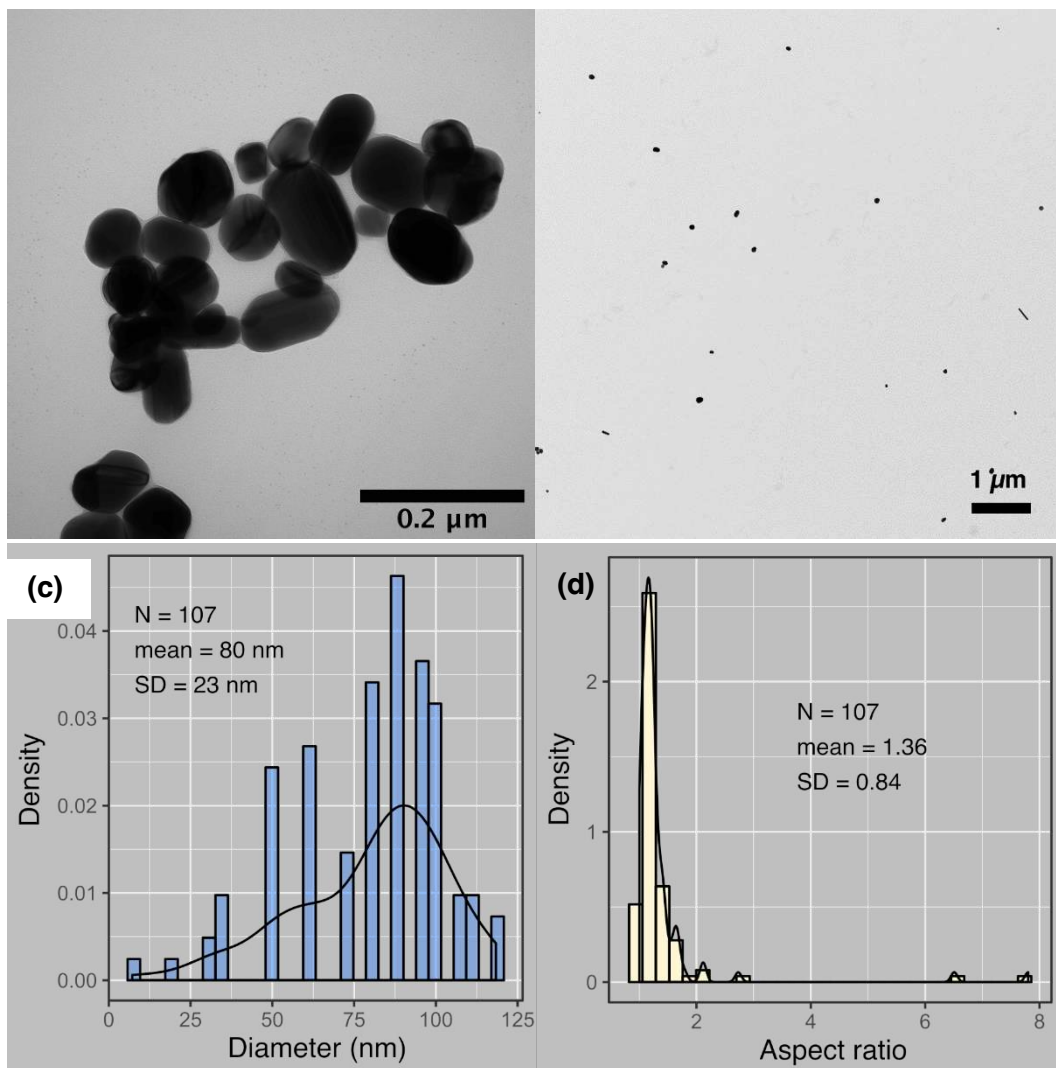


**Figure S2:** TEM micrograph of chloride derived NPs at high (a) and low magnification (b). The diameter distribution, (c), was determined from manually measuring the area of NPs on micrographs having the same magnification as (b) and assuming that the particles were spherical. The NPs have in fact an aspect ratio of  $1.36 \pm 0.84$  (d).

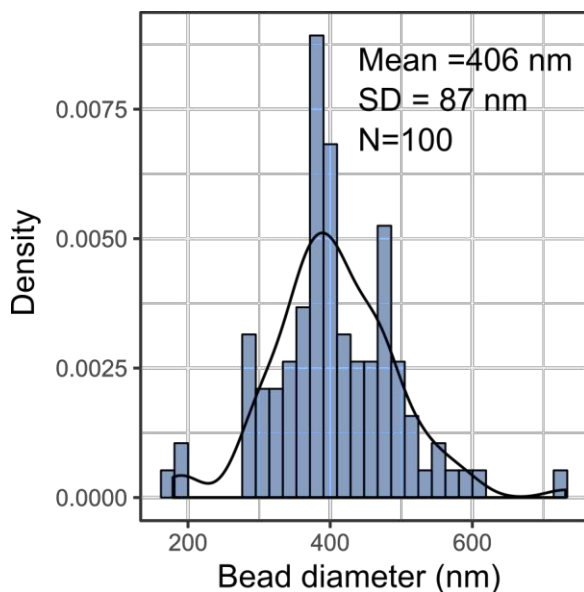
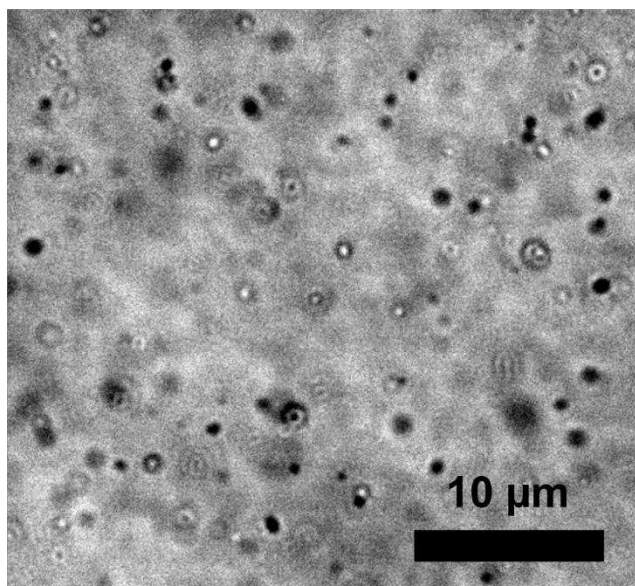


**Figure S3:** optical imaging of SERS aggregates (100X objective) and corresponding size distribution.

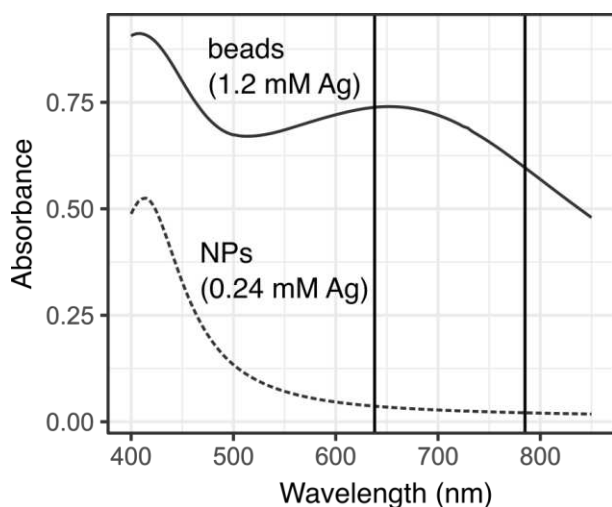
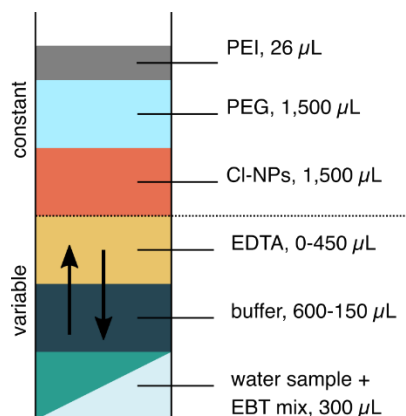


**Figure S4:** Extinction spectra of Cl-exchanged NPs and plain beads (synthesised without incorporated EBT). The vertical lines indicate the excitation wavelengths of the Raman spectrometers used for SERS acquisition (638 and 785 nm).

# Practical running of titration

## Cuvette preparation



	Evian	Volvic	Contrex
$C_{Metal}$	3.1 mM	0.6 mM	14.7 mM
$C_{EDTA}$	4.06 mM	0.81 mM	19.97 mM
pH	$9.73 \pm 0.10$	$9.78 \pm 0.08$	$9.78 \pm 0.09$

Each titration series contains 18 points. The points are spread closer to one another close to the equivalence.

## Stock solutions

	Evian	Volvic	Contrex
<b>PEI</b>	PEI 10 kDa, 1 mM (monomer), in BRB 4 mM, pH 10.4	PEI 10 kDa, 1 mM (monomer), in BRB 4 mM, pH 10.5	PEI 10 kDa, 1 mM (monomer), in BRB 4 mM, pH 10.5
<b>PEG</b>	PEG 20 kDa, 17% wt, in BRB 4 mM, pH 10.5	PEG 20 kDa, 17% wt, in BRB 4 mM, pH 10.5	PEG 20 kDa, 17% wt, in BRB 4 mM, pH 10.5
<b>Cl-NPs</b>	Cl-NPs, 1.2 mM Ag	Cl-NPs, 1.2 mM Ag	Cl-NPs, 1.2 mM Ag
<b>EDTA</b>	EDTA, 4.06 mM, in BRB 4 mM, pH 10.5	EDTA, 0.81 mM, in BRB 4 mM, pH 10.5	EDTA, 19.97 mM, in BRB 4 mM, pH 10.5
<b>buffer</b>	BRB, 4 mM in boron, pH 10.5	BRB, 4 mM in boron, pH 10.5	BRB, 20 mM in boron, pH 10.5
<b>water sample + indicator</b>	Evian/ultrapure water + EBT 5.05 mM, 100:1 in volume	Volvic/ultrapure water + EBT 5.05 mM, 100:1 in volume	Contrex/ultrapure water + EBT 5.05 mM, 100:1 in volume

Evian

Volvic

Contrex

## Titration series

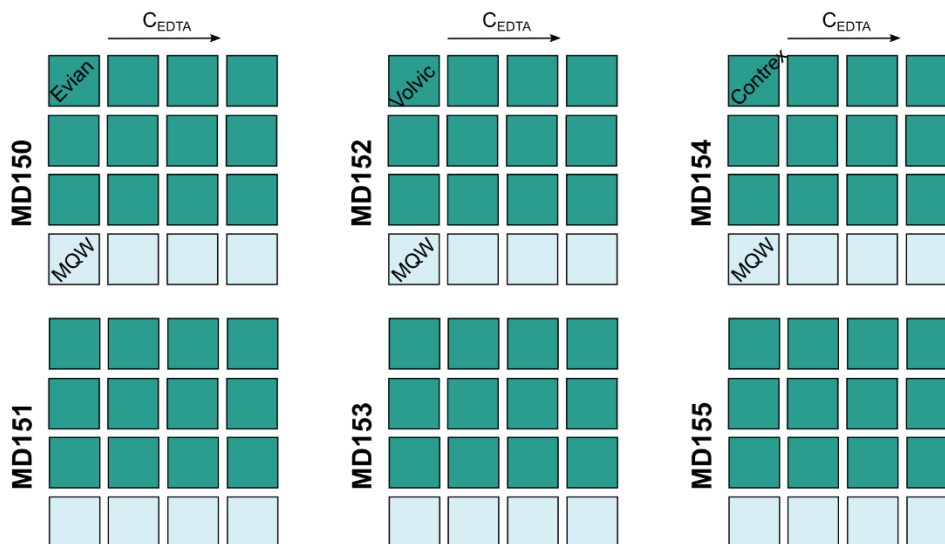


**Figure S5:** Graphical depiction of reagent addition to prepare the cuvettes for SERS acquisition. The reagents were added stepwise into a hemolysis tube and then transferred to a spectrophotometric cuvette. The EDTA, PEG and PEI solutions were buffered using Britton & Robinson buffer 4 mM in boron. The final pH in the cuvettes were comprised between 9.74 and 9.90. For titration samples, 18 different combinations of EDTA and water volumes were explored, the total volume of the sample being kept constant at 3,926  $\mu\text{L}$ . The codes of titration series can be used to retrieve the specific data in the provided datasets.

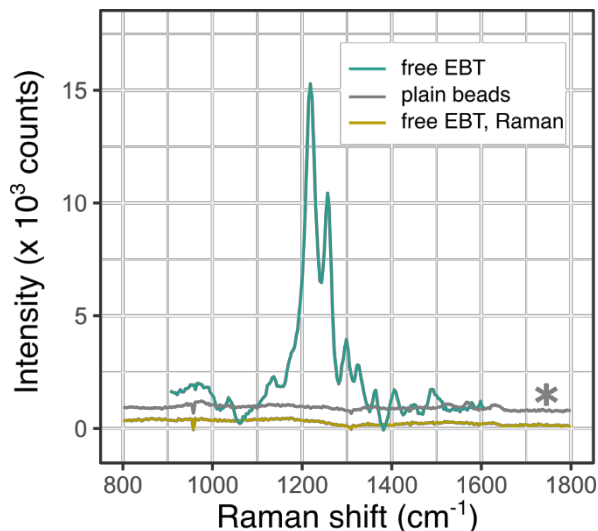


**Figure S6:** SERS spectra of free EBT-labelled beads and plain beads, along with normal Raman spectrum of free EBT. The pH is 10 for all samples. Where applicable, EBT concentration is 3.7  $\mu\text{M}$  and Ag concentration is 0.46 mM. Note that the SERS spectrum of plain beads (\*) has been offset for clarity.

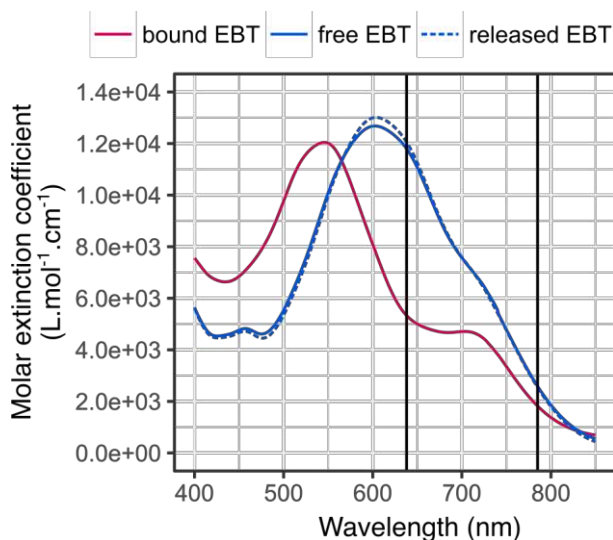


**Figure S7:** Visible absorption spectra at pH 10 of EBT (33  $\mu\text{M}$ ) in the as a free species, as a bound species (in the presence of 0.18 mM  $\text{Mg}^{2+}$  and 0.33 mM  $\text{Ca}^{2+}$ ) and again as a free species upon release of  $\text{Mg}^{2+}$  through addition of 6 metal equivalents of EDTA. The vertical lines indicate the excitation wavelengths of the Raman spectrometers used for SERS acquisition (638 and 785 nm).

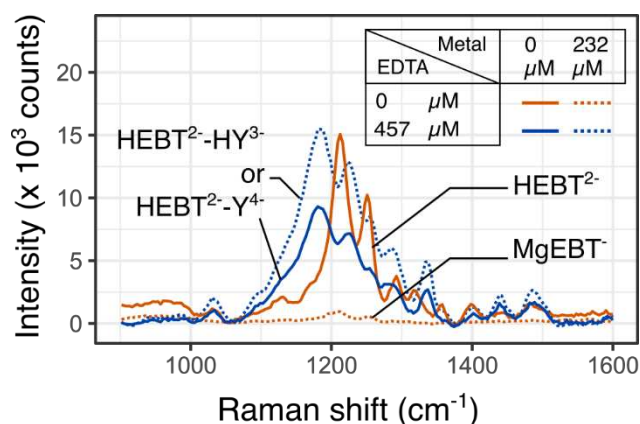


**Figure S8:** Tentative assignment of spectral contribution to species adsorbed on the surface of the SERS-active aggregates. According to speciation analysis at pH 10, over the course of the titration, EBT can exist as  $\text{MgEBT}^-$ ,  $\text{CaEBT}^-$  and  $\text{HEBT}^{2-}$  and EDTA exists as  $\text{CaY}^{2-}$ ,  $\text{MgY}^{2-}$ ,  $\text{HY}^{3-}$  and  $\text{Y}^{4-}$ . In the absence of metal, EBT likely adsorbs on the surface of NPs as  $\text{HEBT}^{2-}$ . Upon addition of EDTA, still in the absence of metal, we hypothesize that EDTA adsorbs onto the NPs as  $\text{HY}^{3-}$  but also as  $\text{Y}^{4-}$  since it accounts for 10% of dissolved EDTA at this pH. These deprotonated forms of EDTA could engage into hydrogen bonding with  $\text{HEBT}^{2-}$  on the surface of the NPs, driving the partial deprotonation of the last exchangeable proton of EBT. In the presence of a saturating amount of divalent cations, EBT adsorbs as complexes, mostly as  $\text{MgEBT}^-$  since it accounts for 87.5% of all dissolved EBT. After addition of 2 eq. of EDTA, the spectrum of the hypothesized hydrogen-bonded complexes of  $\text{HEBT}^{2-}\text{-Y}^{4-}$  or  $\text{HEBT}^{2-}\text{-HY}^{3-}$  is restored. More detailed investigations would be needed to support such tentative species assignment, in

particular through acquisition of spectra at well-resolved pH steps, but were beyond the scope of the present study.

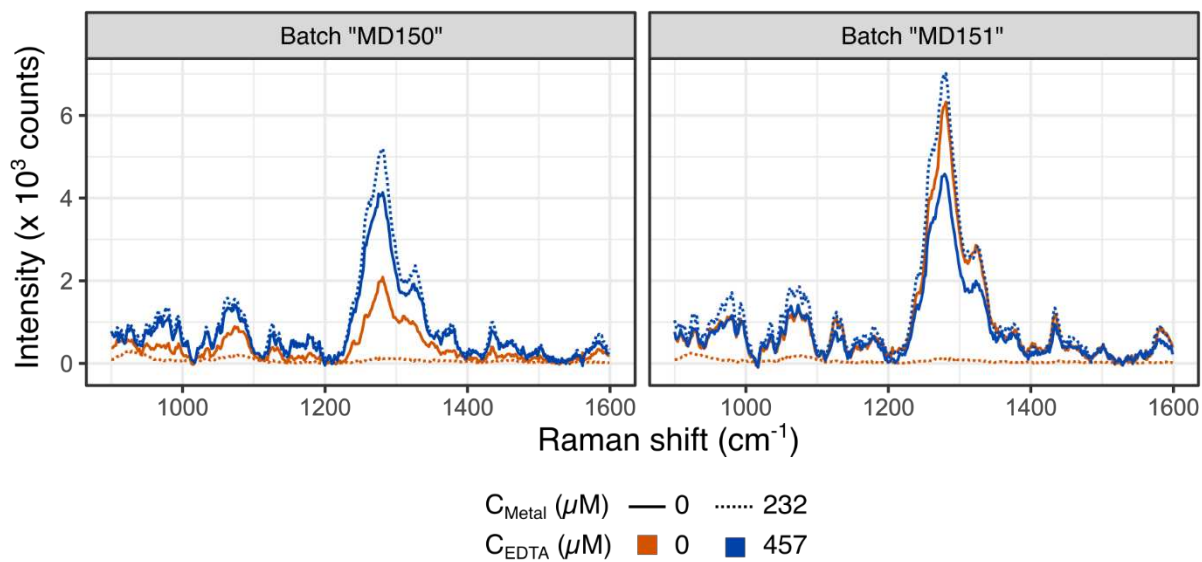


**Figure S9:** SERS spectra of free and bound EBT, in the presence or absence of an excess of EDTA, acquired under 785 nm irradiation. The analytical concentration of EBT is 3.7 μM in each condition. Complexation of the indicator occurs in the presence of 82 μM Mg<sup>2+</sup> (and 150 μM of Ca<sup>2+</sup>). The spectra have been acquired from two distinct batches of nanoparticles.

# Water hardness titration of Evian

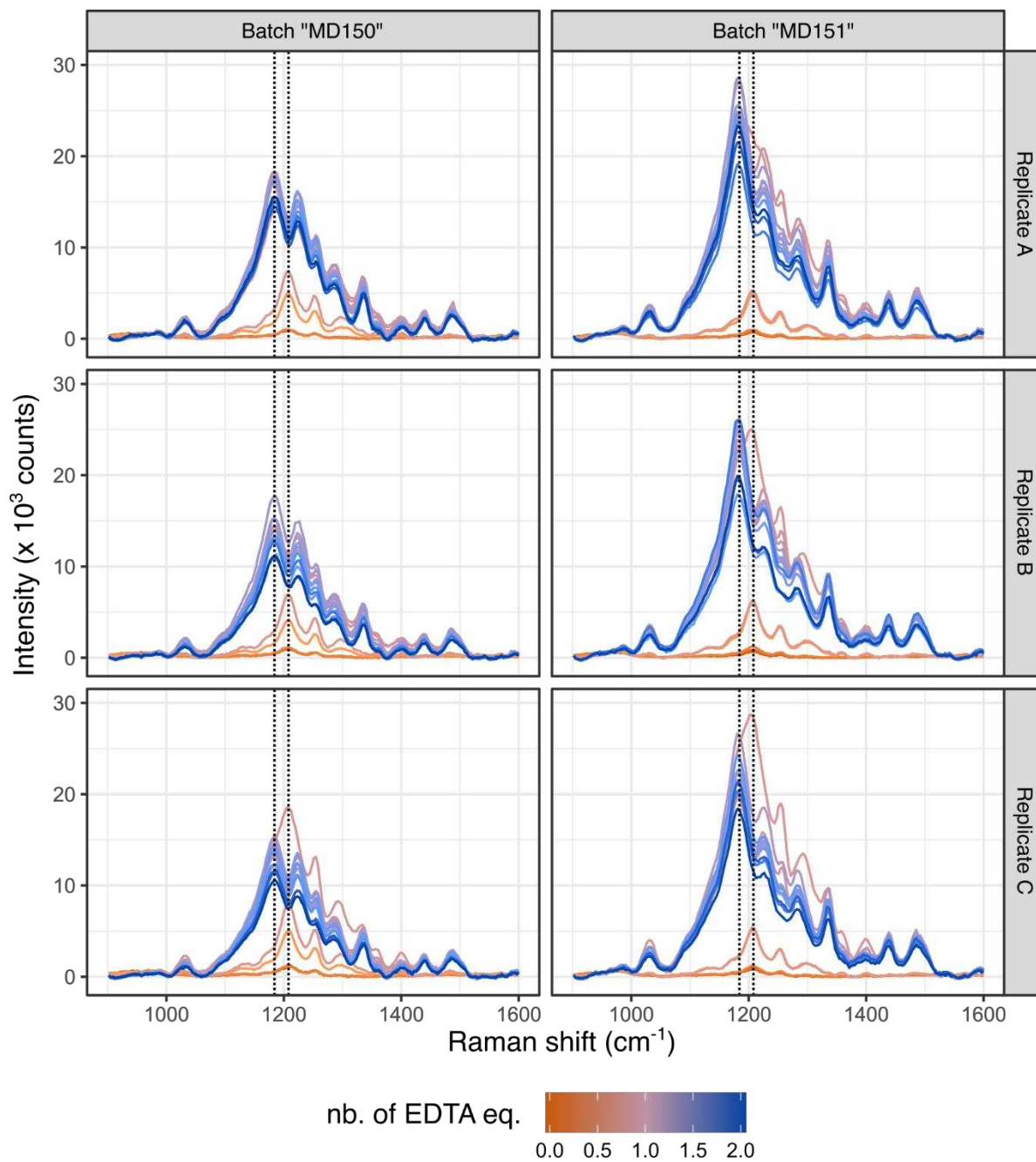


**Figure S10:** Replicates of Evian hardness titration monitored in SERS under 638 nm excitation as described in Figure S5. Three titration series (A, B, C) of 18 EDTA concentrations were performed using two distinct NP batches.

## Titration of Evian under 638 nm irradiation - 1184 $\text{cm}^{-1}$ peak

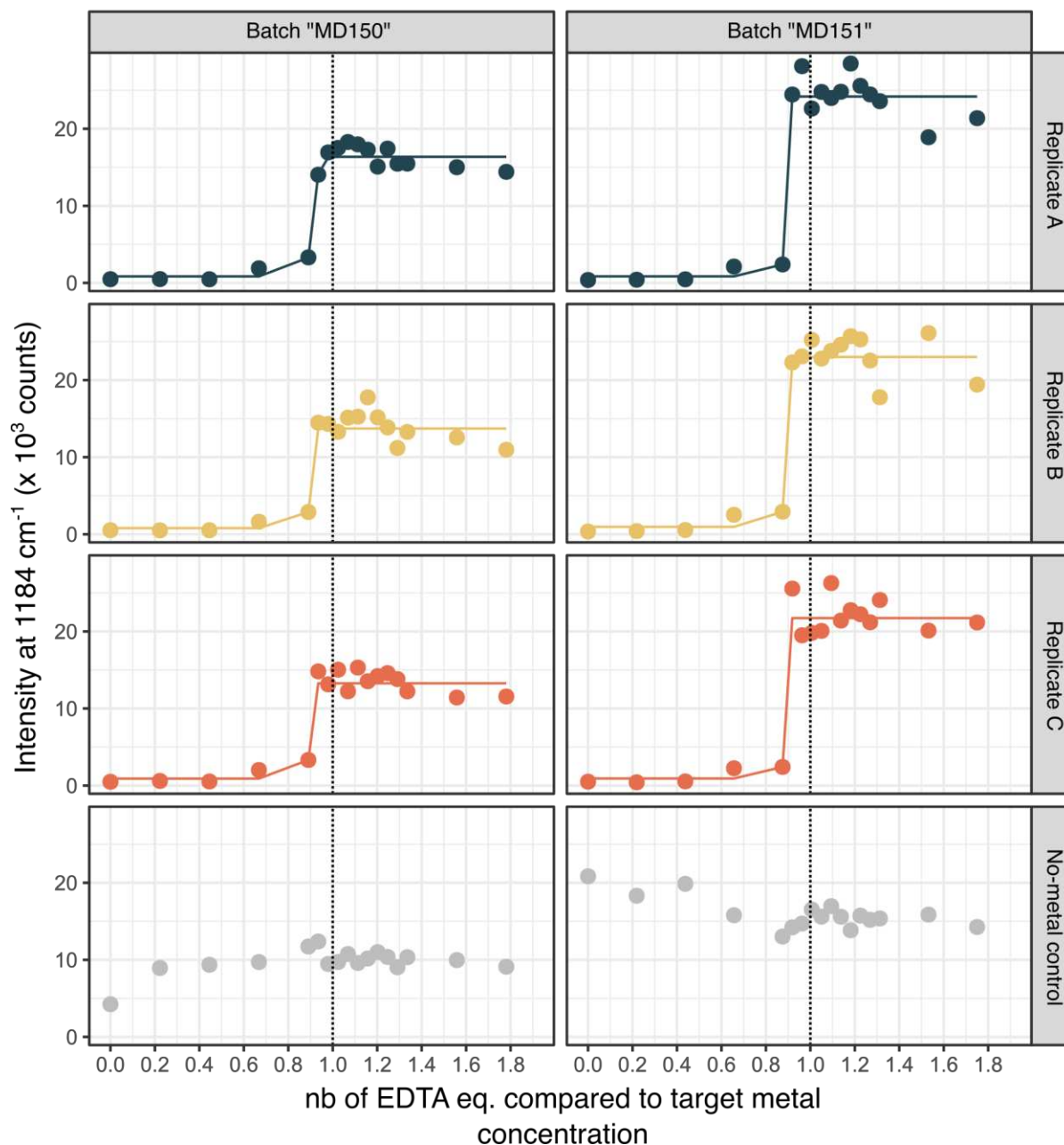


**Figure S11:** Evian hardness titration curves obtained from the tracking of the 1184  $\text{cm}^{-1}$  peak intensity under 638 nm excitation. A blank titration was performed as a control by substituting ultrapure water for Evian.

## Titration of Evian under 638 nm irradiation - 1208 $\text{cm}^{-1}$ peak

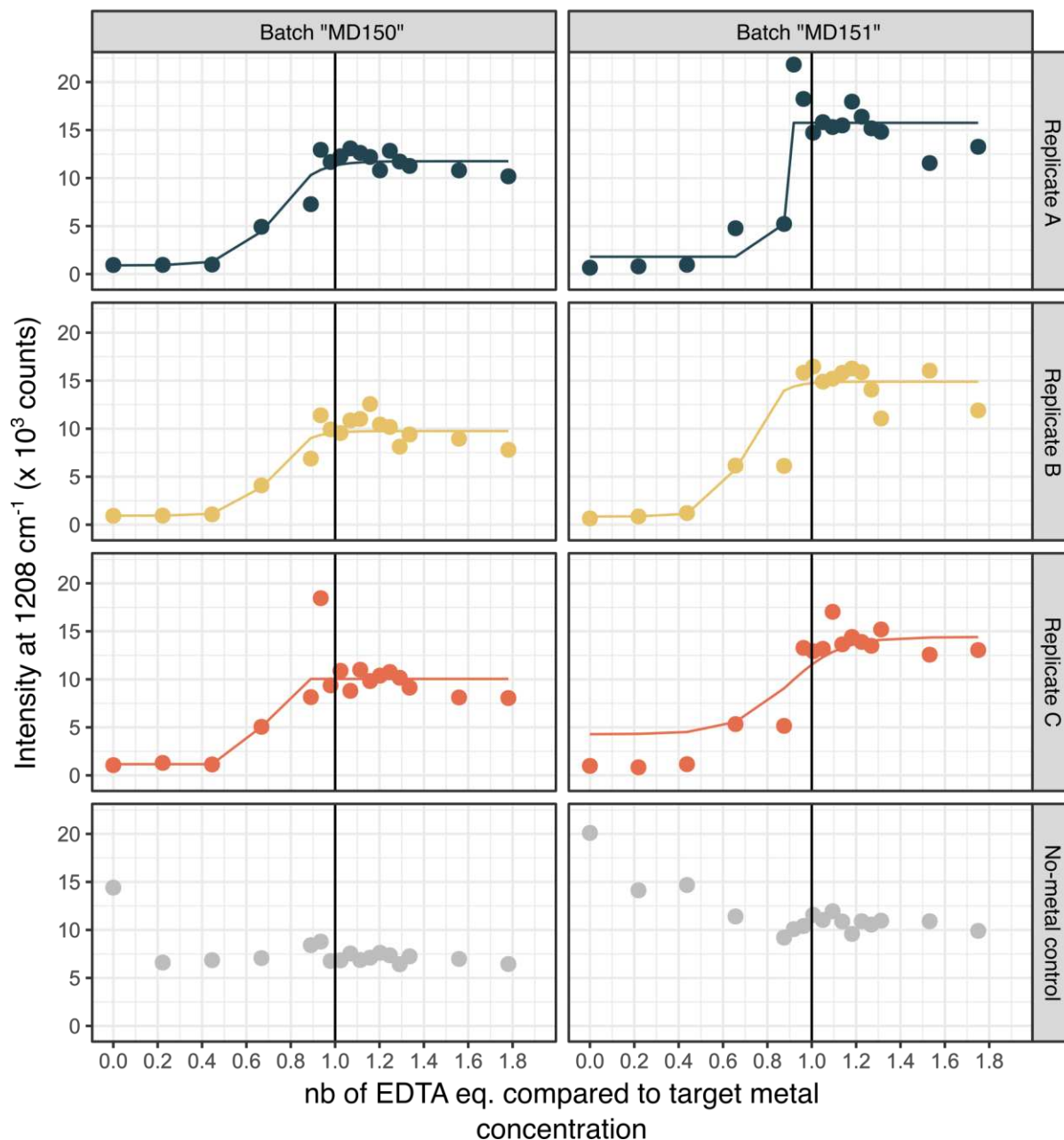


**Figure S12:** Evian hardness titration curves obtained from the tracking of the 1208  $\text{cm}^{-1}$  peak intensity under 638 nm excitation.

Titration of Evian under 638 nm irradiation -  
ratio of 1184  $\text{cm}^{-1}$  and 1208  $\text{cm}^{-1}$  peak intensities

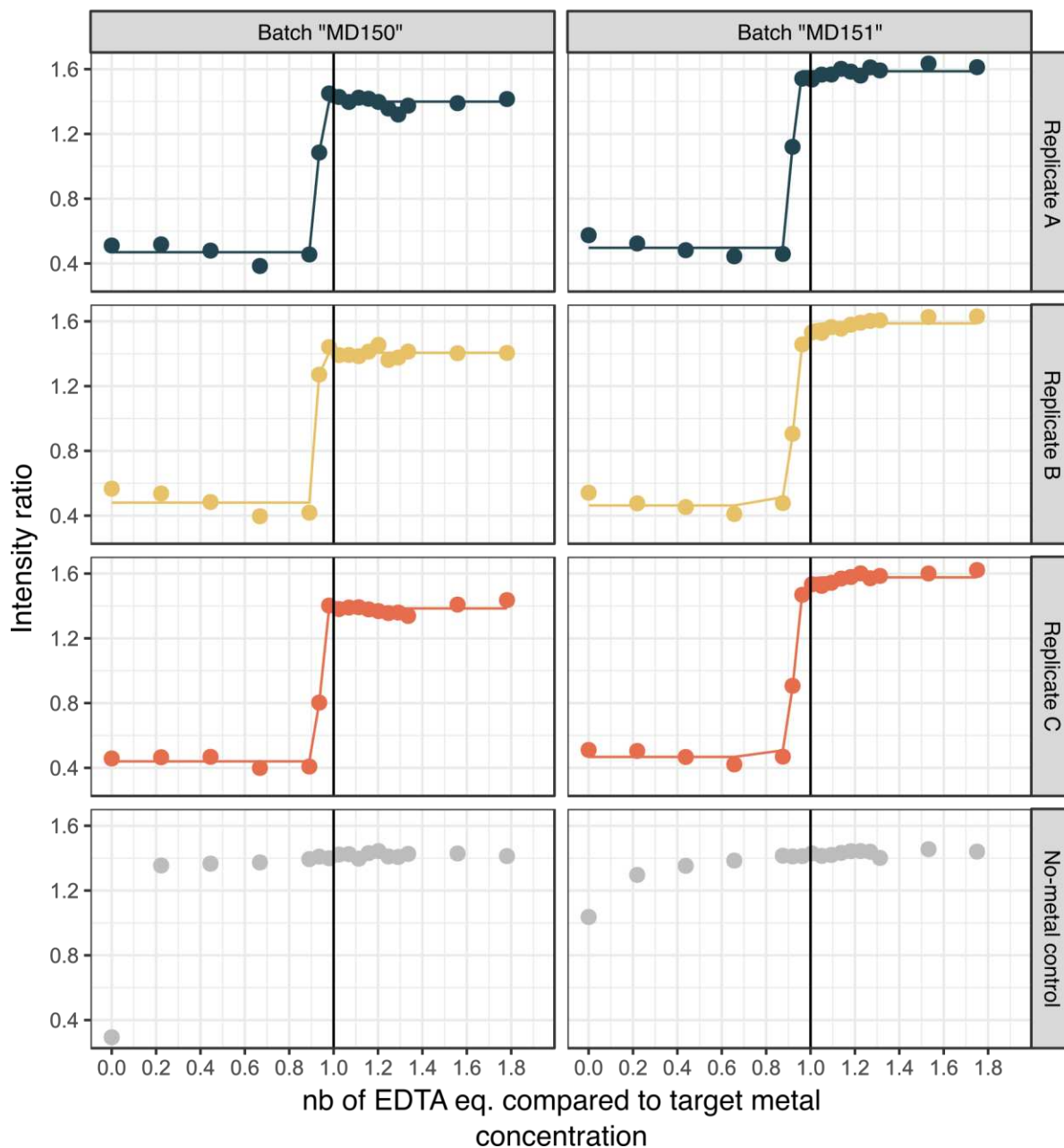


**Figure S13:** Evian hardness titration curves obtained from the ratio of the intensities of the 1184 and 1208  $\text{cm}^{-1}$  peaks, under 638 nm excitation.

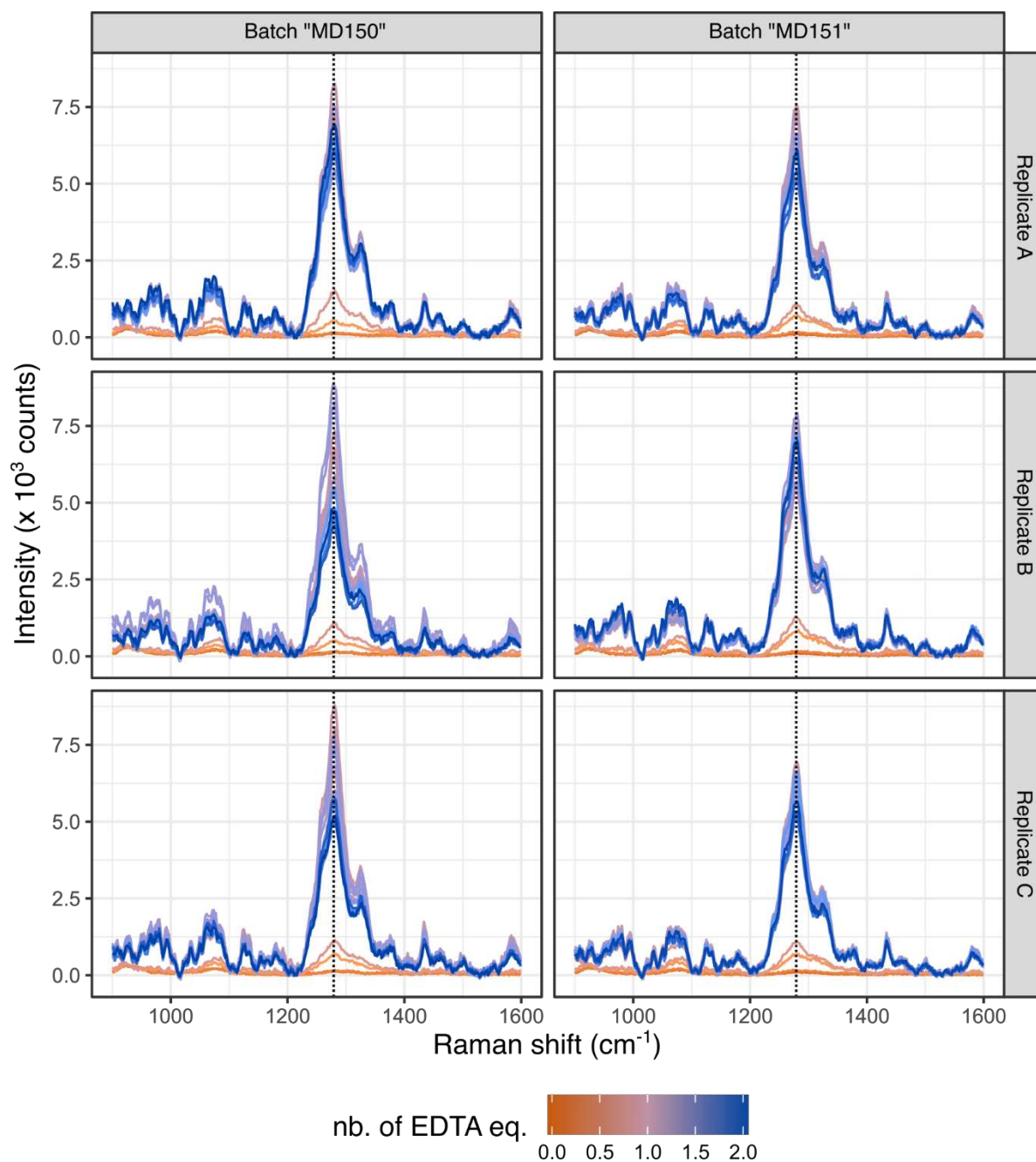


**Figure S14:** Replicates of Evian hardness titration monitored in SERS under 785 nm excitation as described in Figure S5. Three titration series (A, B, C) of 18 EDTA concentrations were performed using two distinct NP batches.

## Titration of Evian under 785 nm irradiation - 1279 $\text{cm}^{-1}$ peak

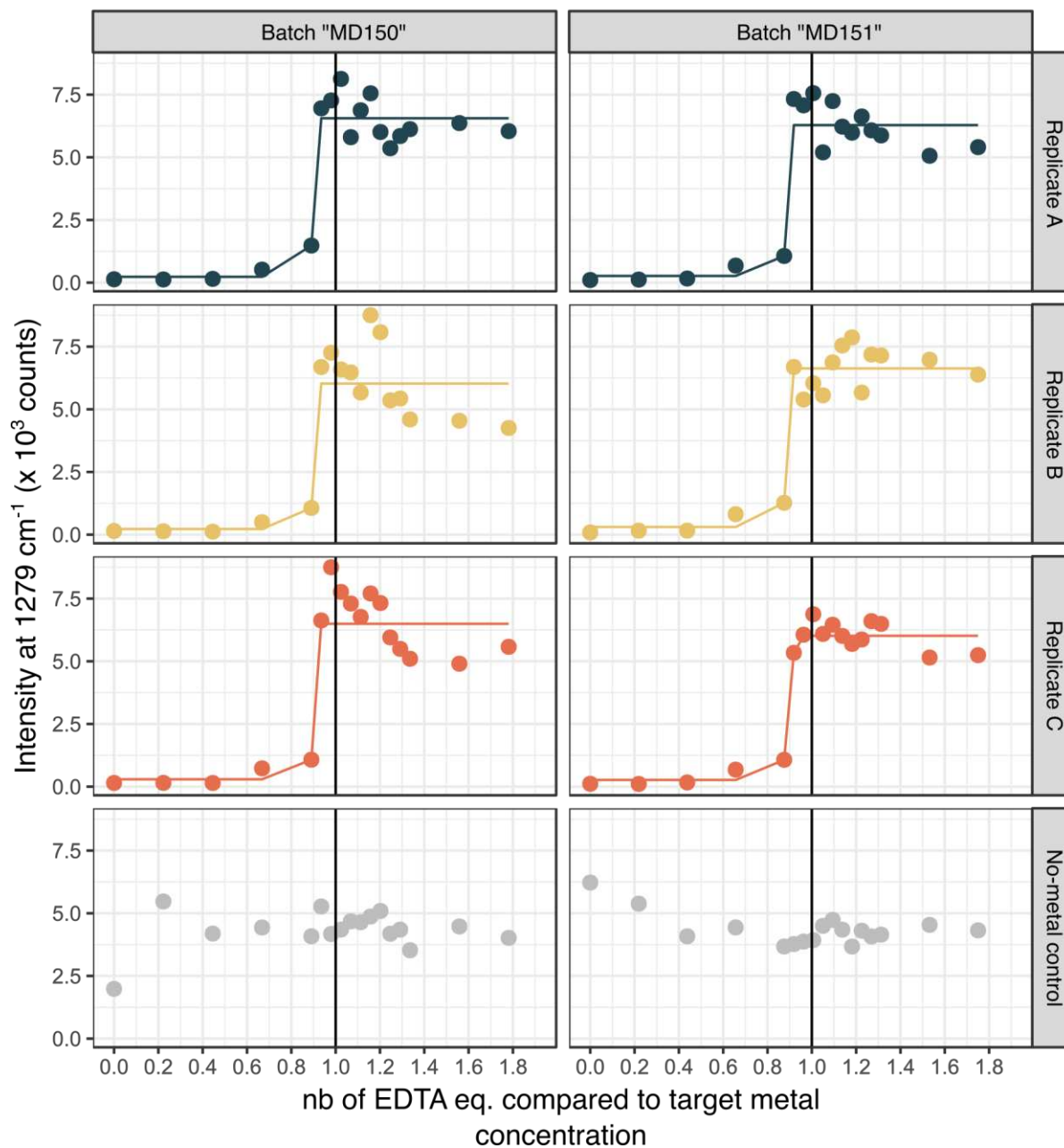


**Figure S15:** Evian hardness titration curves obtained from the tracking of the 1279  $\text{cm}^{-1}$  peak intensity under 785 nm excitation.

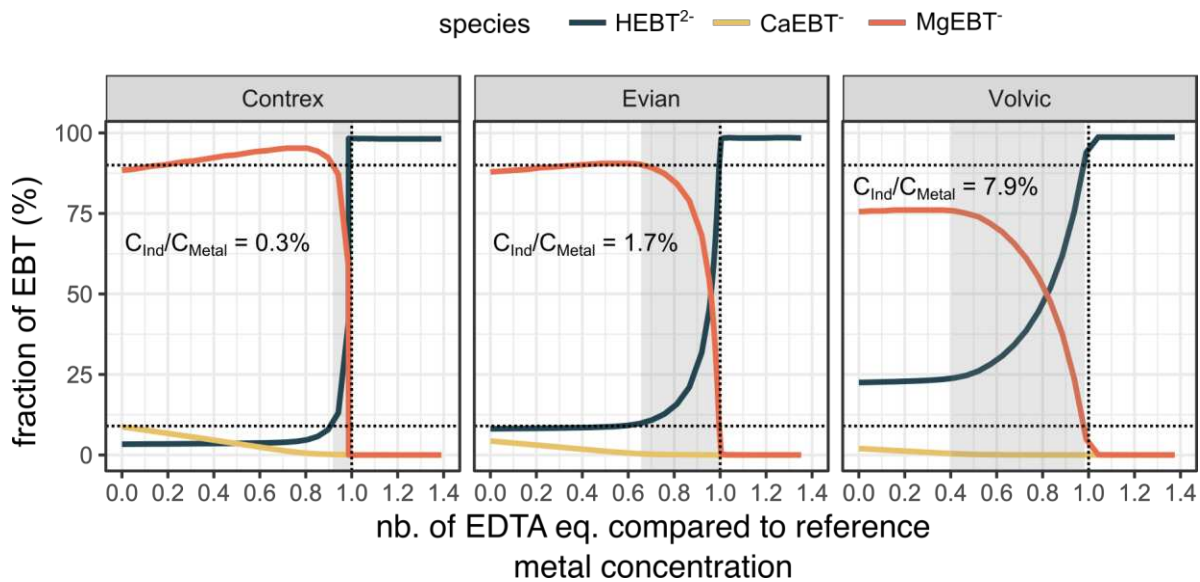


**Figure S16:** Speciation analysis of EBT over the course of the titrations of Contrex, Evian and Volvic.  $C_{Ind}/C_{Metal}$  refers to the ratio of indicator to metal concentrations within the cuvettes.

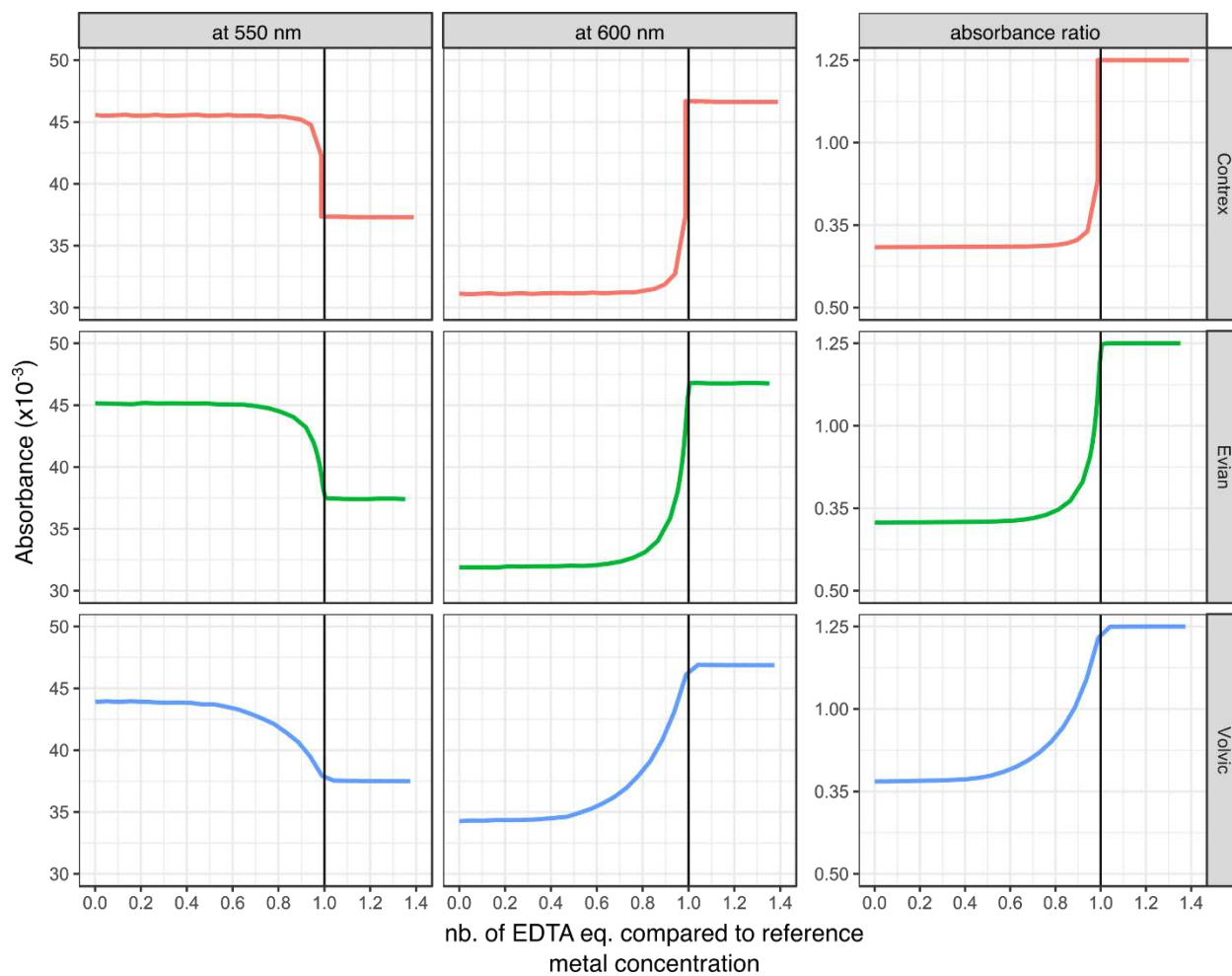


**Figure S17:** Simulation of absorption-based titration curves of Evian, Volvic and Contrex water in the concentration conditions used for the SERS titrations (*i.e.* 3.7  $\mu\text{M}$  EBT). The simulations are based on the molar extinction coefficients determined in Fig. S6.

## Water hardness titration of Volvic

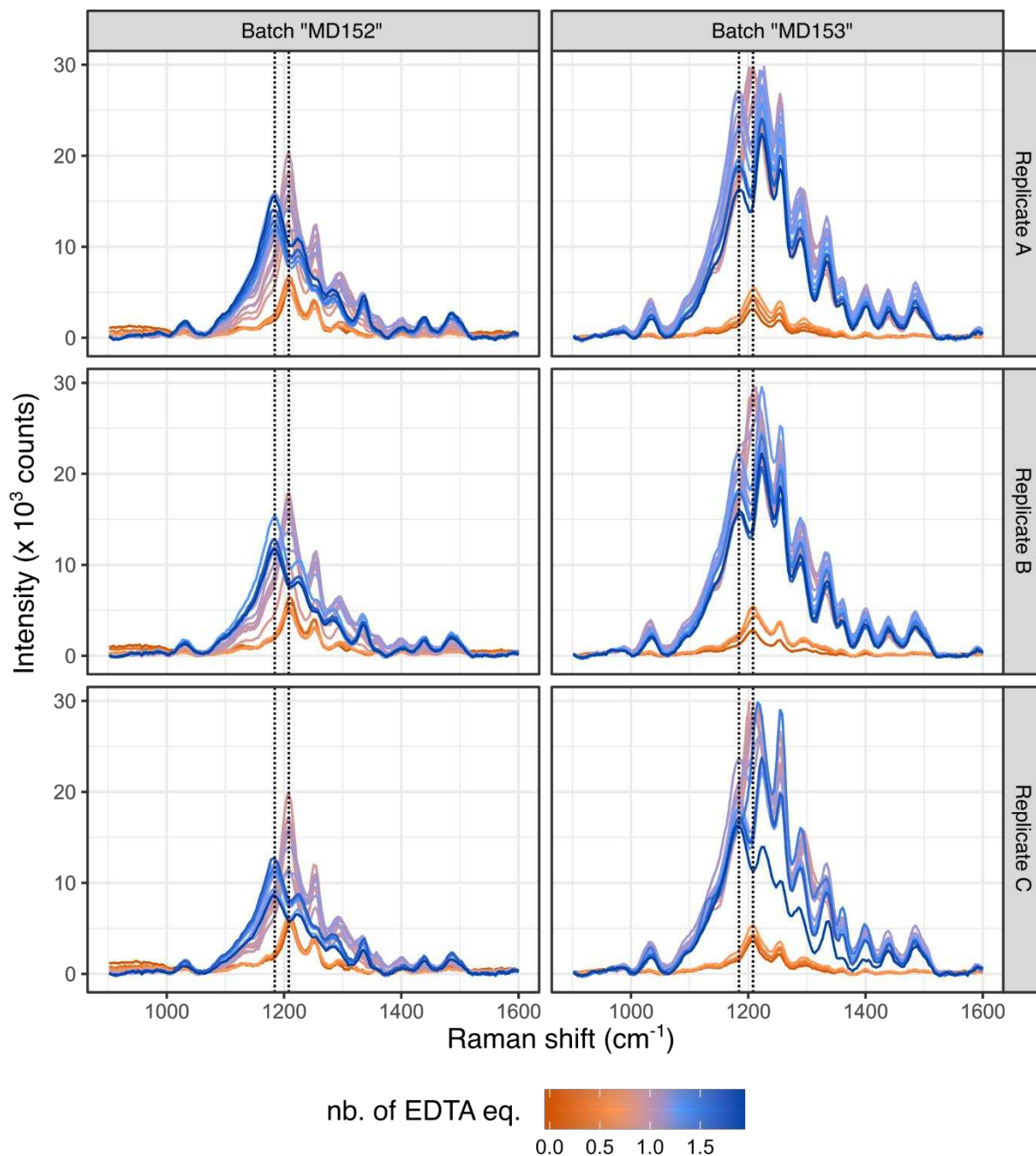


**Figure S18:** Replicates of Volvic hardness titration monitored in SERS under 638 nm excitation as described in Figure S5. Three titration series (A, B, C) of 18 EDTA concentrations were performed using two distinct NP batches.

# Titration of Volvic under 638 nm irradiation - ratio of 1184 $\text{cm}^{-1}$ and 1208 $\text{cm}^{-1}$ peak intensities

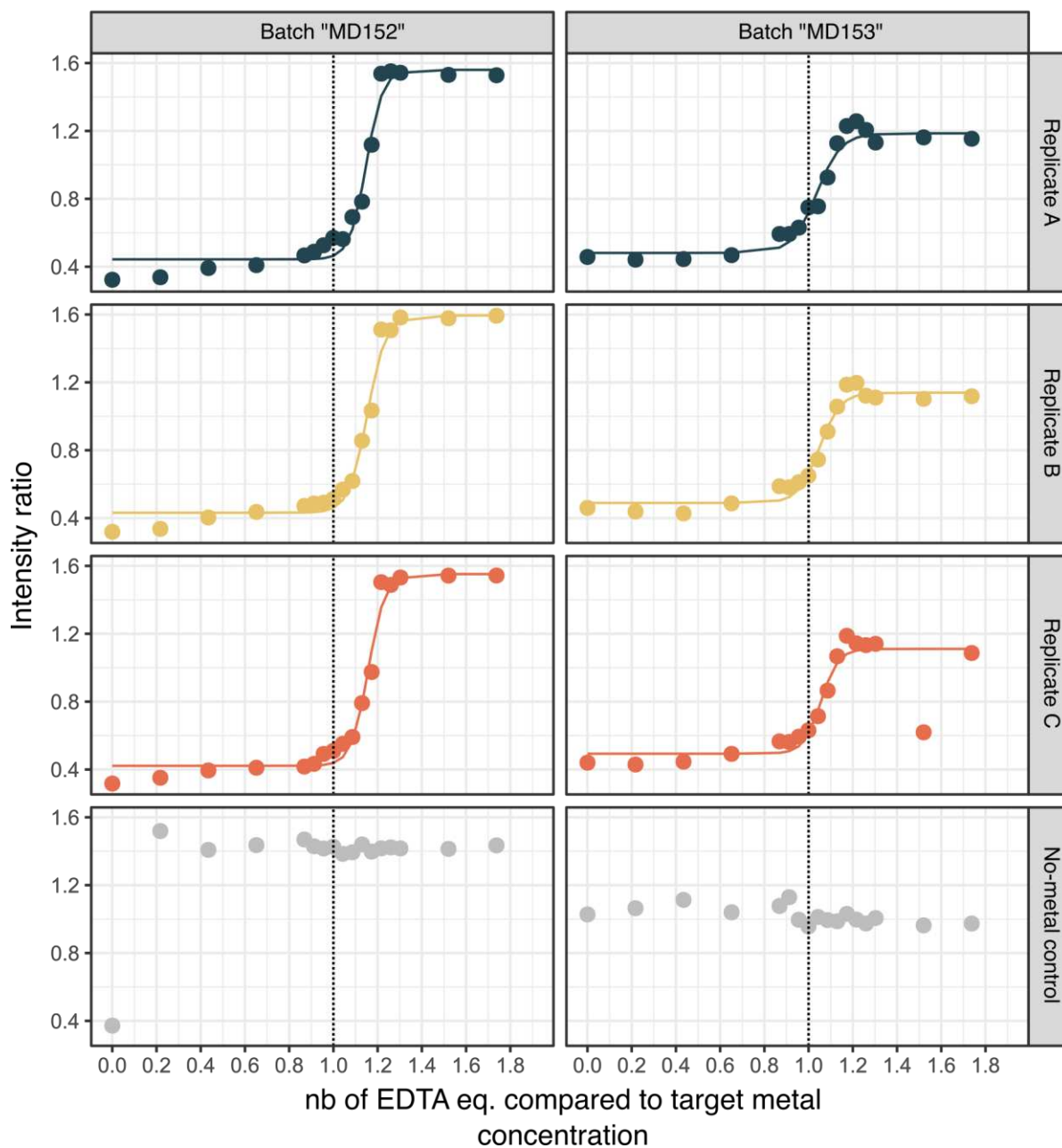


**Figure S19:** Volvic hardness titration curves obtained from the ratio of the intensities of the 1184 and 1208  $\text{cm}^{-1}$  peaks, under 638 nm excitation.

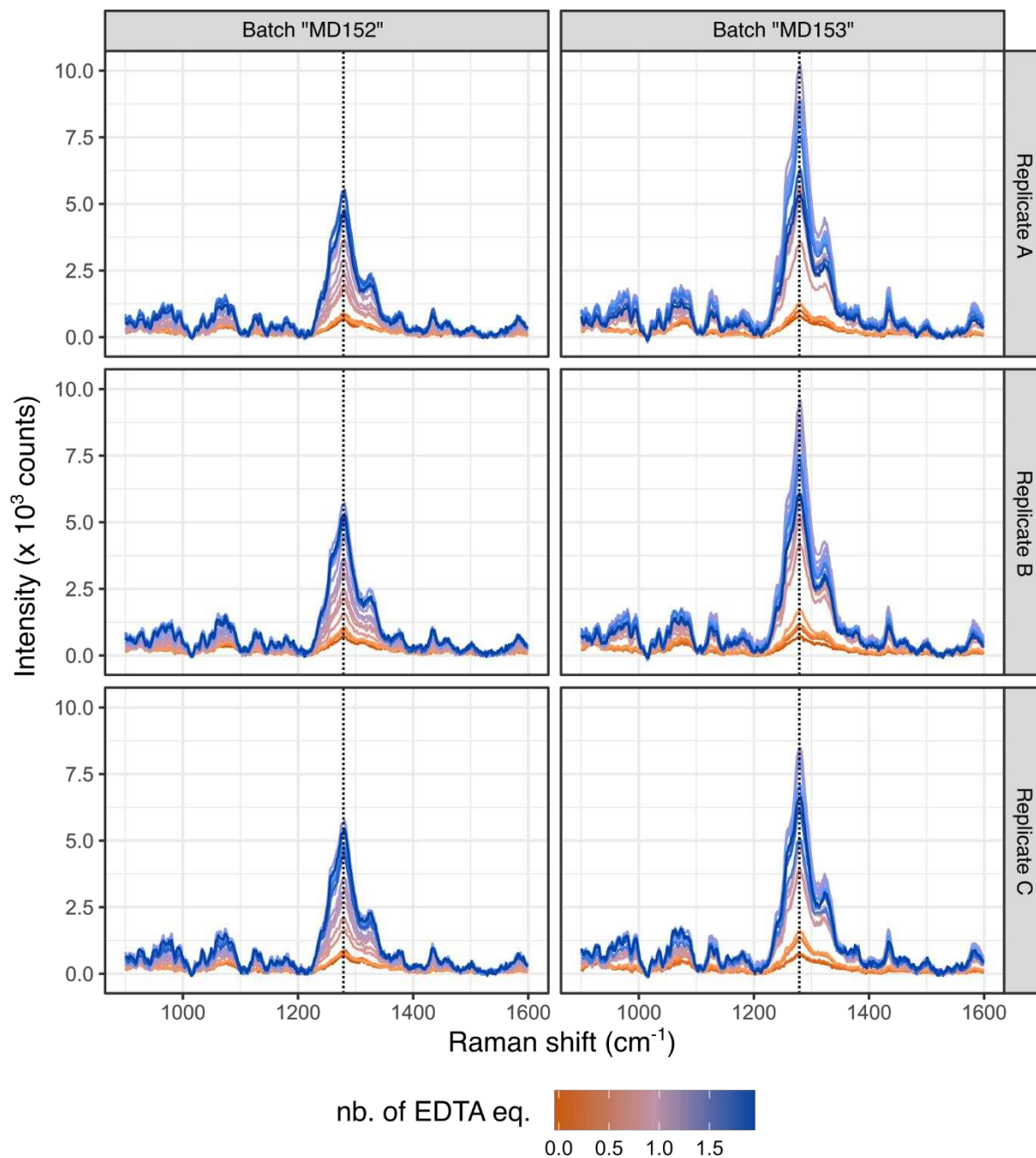


**Figure S20:** Replicates of Volvic hardness titration monitored in SERS under 785 nm excitation as described in Figure S5. Three titration series (A, B, C) of 18 EDTA concentrations were performed using two distinct NP batches.

# Titration of Volvic under 785 nm irradiation - 1279 $\text{cm}^{-1}$ peak

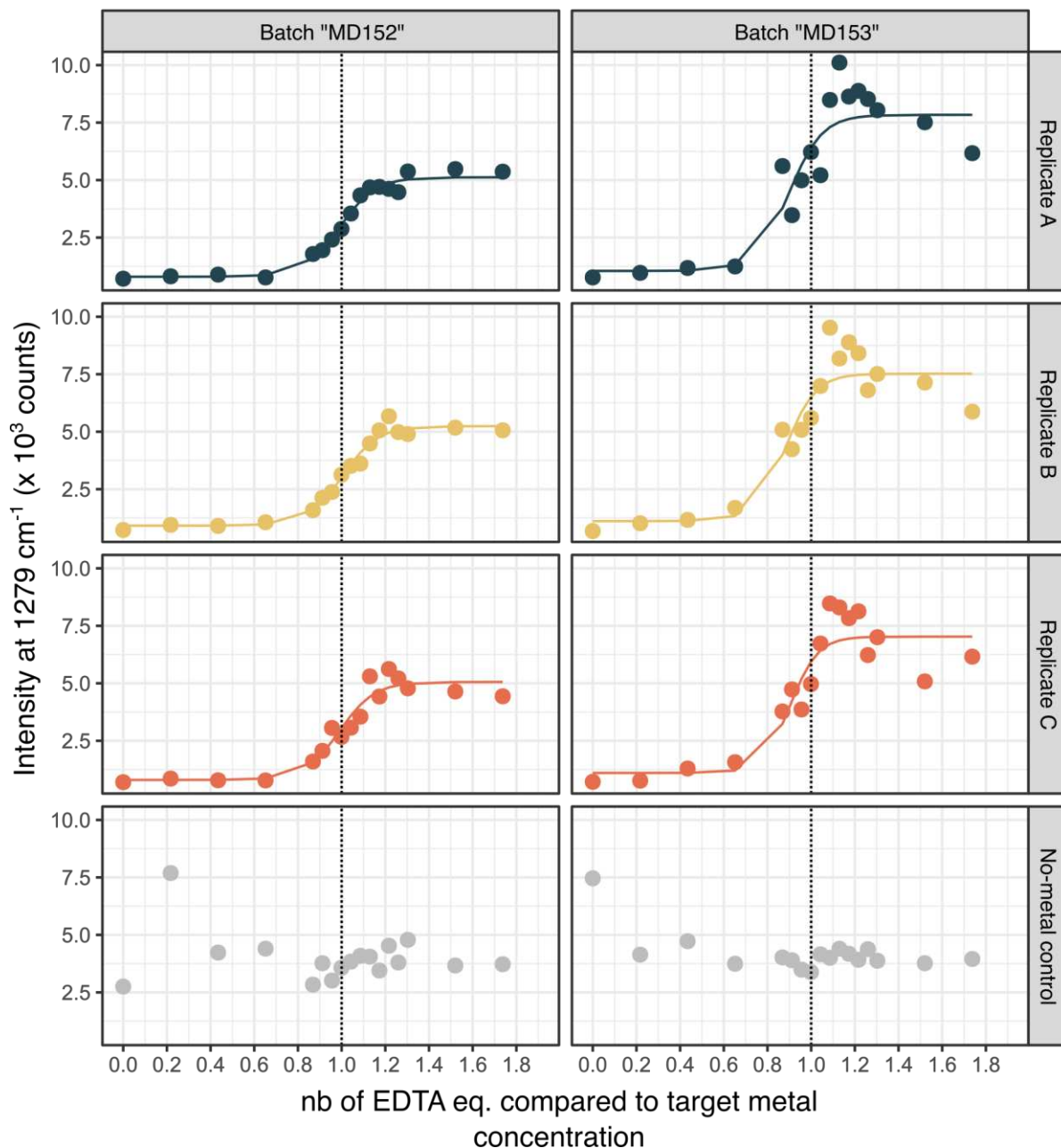


**Figure S21:** Volvic hardness titration curves obtained from the tracking of the 1279  $\text{cm}^{-1}$  peak intensity under 785 nm excitation.

# Water hardness titration of Contrex

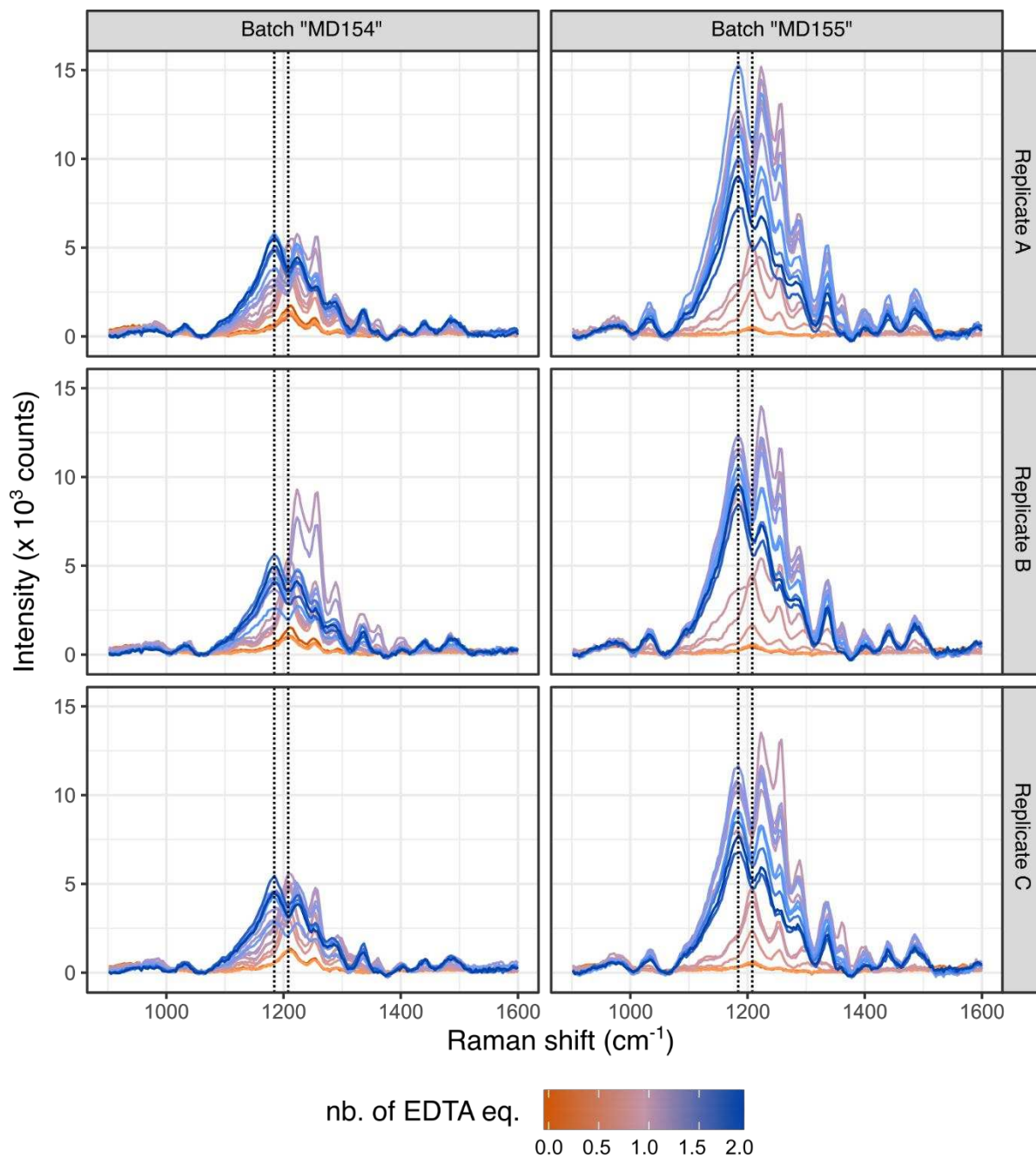


**Figure S22:** Replicates of Contrex hardness titration monitored in SERS under 638 nm excitation as described in Figure S5. Three titration series (A, B, C) of 18 EDTA concentrations were performed using two distinct NP batches.

## Titration of Contrex under 638 nm irradiation - ratio of 1184 $\text{cm}^{-1}$ and 1208 $\text{cm}^{-1}$ peak intensities

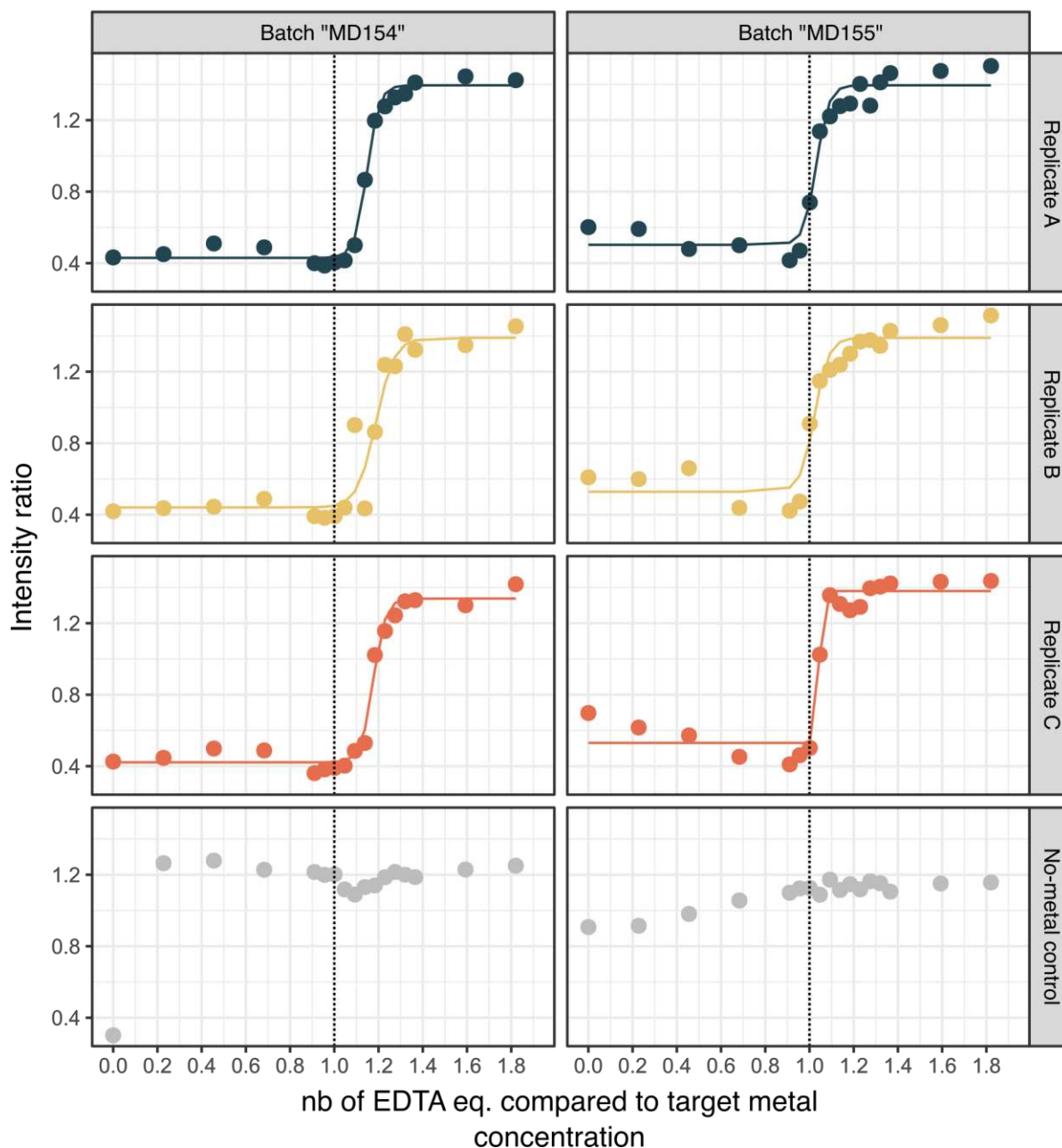


**Figure S23:** Contrex hardness titration curves obtained from the ratio of the intensities of the 1184 and 1208  $\text{cm}^{-1}$  peaks, under 638 nm excitation.

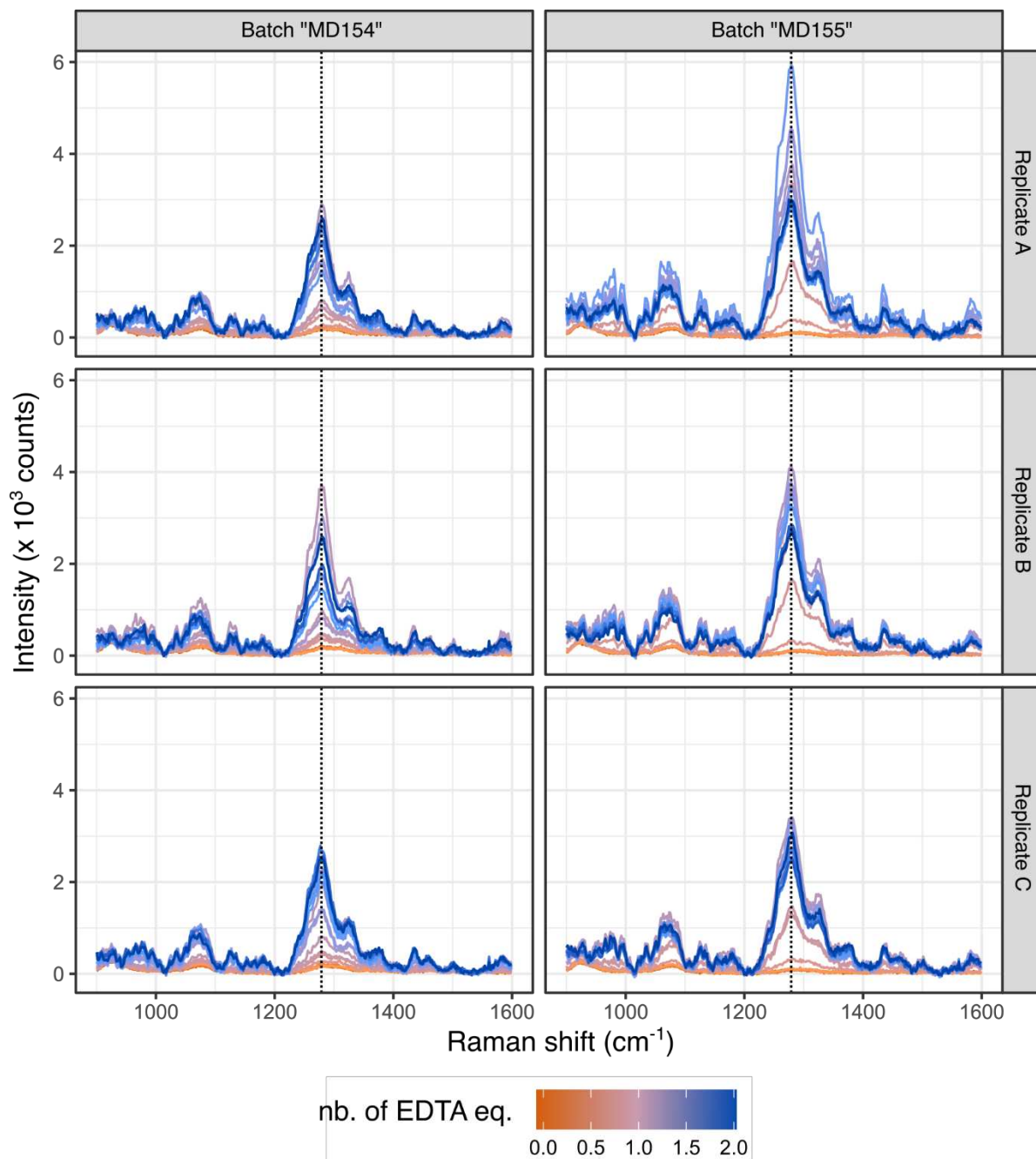


**Figure S24:** Replicates of Contrex hardness titration monitored in SERS under 785 nm excitation as described in Figure S5. Three titration series (A, B, C) of 18 EDTA concentrations were performed using two distinct NP batches.

## Titration of Contrex under 785 nm irradiation - 1279 $\text{cm}^{-1}$ peak

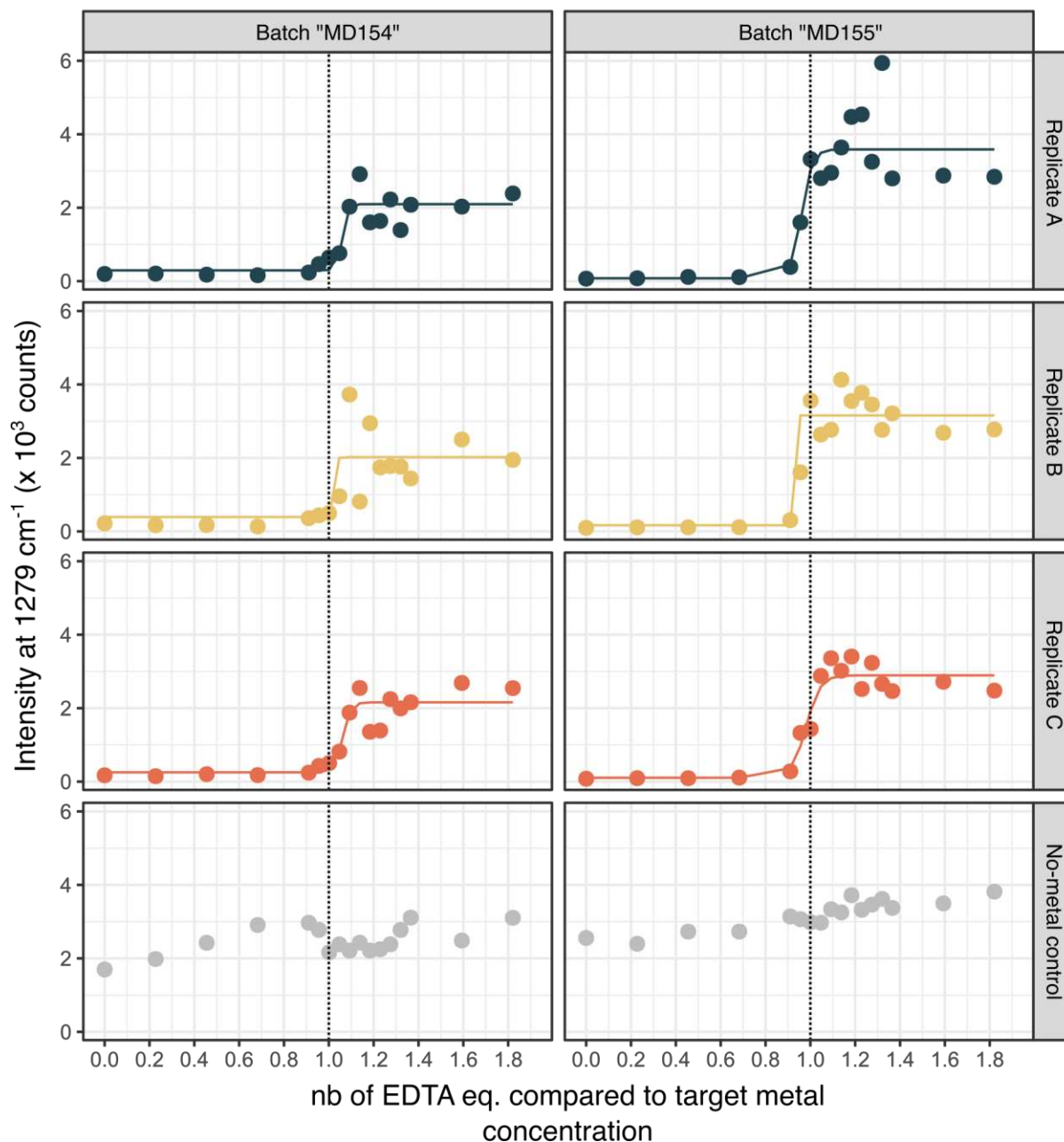


**Figure S25:** Contrex hardness titration curves obtained from the tracking of the 1279  $\text{cm}^{-1}$  peak intensity under 785 nm excitation.

## References

1. Munro, C. H., Smith, W. E., Garner, M., Clarkson, J. & White, P. C. Characterization of the Surface of a Citrate-Reduced Colloid Optimized for Use as a Substrate for Surface-Enhanced Resonance Raman Scattering. *Langmuir* **11**, 3712–3720 (1995).
2. Stewart, A., Murray, S. & Bell, S. E. J. Simple preparation of positively charged silver nanoparticles for detection of anions by surface-enhanced Raman spectroscopy. *Analyst* **140**, 2988–2994 (2015).
3. Cheng, K. L., Ueno, K. & Imamura, T. *CRC Handbook of Organic Analytical Reagents, Second Edition*. (CRC Press, 1992).
4. R Core Team (2016). *R: A language and environment for statistical computing*. (R Foundation for Statistical Computing).
5. Welcome to Python.org. *Python.org* <https://www.python.org/>.
6. Lieber, C. A. & Mahadevan-Jansen, A. Automated method for subtraction of fluorescence from biological Raman spectra. *Appl. Spectrosc.* **57**, 1363–1367 (2003).
7. Eilers, P. & Boelens, H. Baseline Correction with Asymmetric Least Squares Smoothing. Internal report from *Leiden University Medical Centre* (2005).



# Microfluidic Methods

---

## Contents

---

<b>3.1 SERS and microfluidics</b> . . . . .	<b>28</b>
<b>3.2 A typical microfluidic system</b> . . . . .	<b>30</b>
3.2.1 Fabrication of a microfluidic chip . . . . .	30
3.2.2 Flow control instruments . . . . .	32
<b>3.3 Droplet-based microfluidics</b> . . . . .	<b>34</b>
<b>3.4 Mixing in microfluidic systems</b> . . . . .	<b>37</b>
<b>3.5 Generation of concentration gradients</b> . . . . .	<b>37</b>

---

As discussed in chapter 1, SERS irreproducibility and time-consuming protocols for preparing SERS measurement samples are among the factors that hinder SERS from routine analyses. The previous work of our group on the quantitative detection of  $\text{Zn}^{2+}$  showed that the labour involved in obtaining a large data set for building a reliable calibration curve dominated the analysis cost [29]. In chapter 2, we presented the SERS-based titration method that required a smaller number of measurement samples. With a measurement duration of 30 – 60 minutes carried out by an analysis technician, this method is acceptable for punctual measurements, but it is still cumbersome for daily analysis. It is also not practical for environmental monitoring on a large scale or at high frequency. To move further to a real-world application, automatizing the SERS-based measurement procedures for both calibration and titration-based methods is our next goal.

Microfluidics, in brief, is the science of manipulating fluids in a network of fabricated microchannels. Since the 1990s, microfluidics has continuously contributed to improvements in life science and chemistry by providing precise manipulation of fluids at micrometric scales and a significant reduction in reagent consumption [63, 64]. Some local conditions can be controlled better on microscales thanks to a short diffusion path and fast heat transfer stemming from a high surface-to-volume ratio [65]. For instance, Tatsuro Asai et al. 2011 [66] reported a microreactor able to switch the reaction pathways to select one product over another through high-resolution residence-time and temperature control. Alexander D. Beaton et al. 2011 [67] reported an automated microfluidic colourimetric sensor for nitrite determination with reagent consumption in  $\mu\text{L}$  per sample that was able to operate in situ for 57 *h* and made 375 discrete measurements.

SERS-based analyses can also benefit from microfluidic technologies because microfluidics can reduce the consumption of plasmonic nanomaterials and allow one to automate sample preparation and analysis. Based on abilities brought from microfluidics, our strategy is to develop an automated microfluidic platform for SERS-based measurements to reduce labour work. In addition, scaling down the material consumption in microfluidic devices also benefits environmental monitoring on a large scale because one would not have to reload the reagent reservoirs regularly.

To name a few works on SERS-integrated microfluidics for proof-of-concept, Eunsu Chung et al. 2013 [68] reported a SERS-integrated microfluidic platform for mercury (II) ions trace analysis whose simplicity makes it suitable and promising to use on-field. Rongke Gao et al. 2010 [69] also reported a fast and reproducible analysis of herbicide paraquat using their developed SERS-microfluidic platform.

In section 3.1, we discuss the combination of SERS and microfluidics. Then, in section 3.2-3.5, we present the fundamentals of the main elements that constitute the microfluidic platform that we developed in chapter 4. Each section is accompanied by justifications for the specific choices made for developing our microfluidic system.

### 3.1 SERS and microfluidics

The combination of SERS and microfluidics brings a synergistic effect on both sides. On one side, microfluidic systems provide a fixed and reproducible procedure to manipulate SERS materials and chemical reactions. Therefore, the variation of SERS signal that is prone to human manipulation error can be avoided, improving SERS reproducibility [70]. Moreover, microfluidic systems can be automated to harvest SERS spectra at high throughput, facilitating the chemometrics analysis to extract the meaning information from informative finger-print Raman spectra. On the other side, SERS is a highly sensitive technique originating from metallic nanostructures. Therefore, integrating SERS into microfluidic systems would help to improve the measurement sensitivity [70].

The use of microfluidics for SERS can be classified into two categories: continuous flow [71, 72, 73] and dispersed flow fluidics [68, 74, 75]. Continuous-flow microfluidics evolve manipulating a single phase of fluids within microchannels without breaking their continuity. Segmented-flow microfluidics, also known as droplet-based microfluidics, consist in manipulating discrete volume of fluids dispersed in immiscible phases. Water-in-oil droplets is a popular example for droplet-based microfluidic in which the dispersed phase is water droplets, and the continuous phase is the oil. In each category, SERS can be implemented to fabricate in-situ SERS substrates [76, 77] or for (bio)chemical analyses [78, 79]. Based on the objective of this thesis project, the later target is of our interest.

For (bio)chemical analyses, continuous flow microfluidics was first implemented for SERS analysis with the purpose of less reagent consumption and increasing the measurement throughput [70]. However, because the sample continuously wet the microfluidic chip, it can lead to a gradual deposition of nanoparticles and chemical compounds onto the sidewalls, the so-called memory effect [69, 70]. This effect can lead to inaccurate quantitative measurement because the sidewall is contaminated after launching for a while. Moreover, in the case of using NPs aggregates, they can merge and grow to bigger aggregates under a continuous shear flow, causing clogging issues.

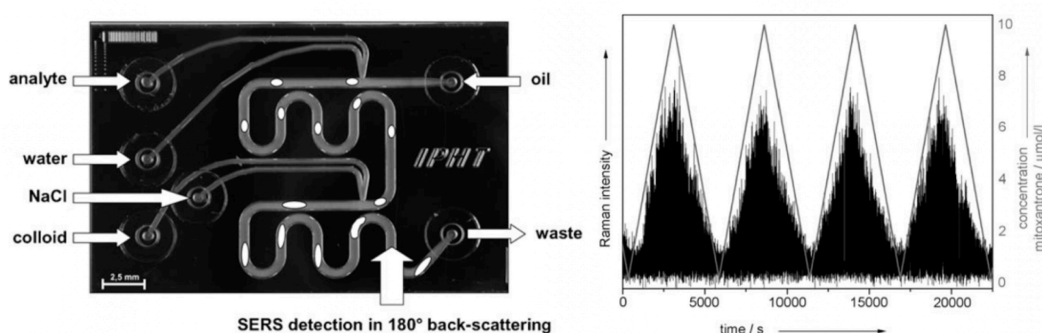


Figure 3.1: a) Segmented flow LoC-SERS system for quantitative detection of low concentrated drugs. Four ports on the left side were used for the injection of analyte of interest, water for dilution of analyte, sodium chloride NaCl for SERS activation and NPs colloids. Oil was injected in the main channel to create droplets. SERS measurement was acquired on the channel segment near the outlets. b) Fluctuation of SERS spectra (the integrated Raman intensity in the wavenumber region from  $1566$  to  $1598\text{ cm}^{-1}$ , presented as clusters of black bars) acquired from the LoC-SERS system in panel (a) over time when the concentration of the target analyte (mitoxantrone) was varied (black solid lines making triangles with the x-axis). Raman intensity is the integrated Raman intensity in the wavenumber region from  $1566$  to  $1598\text{ cm}^{-1}$ . (Adapted from [80]).

For this reason, recently, droplet-based microfluidics is popularly used as it can eliminate the contact between the sample and the channel walls. Droplet-based microfluidics also offer a high flexibility for complex analysis as droplets can be mixed, split, merged, or sorted in a predefined order [81]. Fig 3.1 shows an example of a lab-on-a-chip SERS (LoC-SERS) system for quantitative detection of low-concentrated drugs. In this work, droplets were formed from the flow streams of analyte solution and water for dilution of analyte, then they were merged with NPs colloids and sodium chloride NaCl for SERS activation (Fig 3.1a). The SERS signal was acquired online at high throughput (1 spectrum/sec) and their intensity fluctuated accordingly to the variation of analyte concentration (Fig 3.1b).

For this thesis project, we also chose to work with droplet-based microfluidics because of its advantages like avoiding memory effect and clogging, especially here we use SERS aggregates substrates. The SERS-based complexometric titration presented in chapter 2 is actually a complex chemical procedure. It includes aggregating SERS aggregates from precursor materials and scanning the ratio of titrant/analyte for titration. The following sections will present the basics of elements needed to understand the microfluidic platform that we developed in chapter 4. It comes first with the basics needed, like the main elements of a microfluidic system and droplet formation mechanism. Then the basics of necessary functions for the SERS-based titration like microfluidic mixing and concentration gradient generation are presented.

## 3.2 A typical microfluidic system

A typical microfluidic system often consists of a microfluidic chip and a flow control instrument, which generates fluid flows inside the chip. Then, the microfluidic chip, made of a microchannel network, manipulates fluids by, for instance, merging, mixing or sorting different fluids, and creating droplets. Besides these two main elements, other instruments can be integrated for a higher-level fluid control, like flow-rate meters, reservoir switchers or microvalves. In this section, we introduce in more detail the two main elements of a microfluidic system.

### 3.2.1 Fabrication of a microfluidic chip

A typical microfluidic chip can be made of different materials such as silicon, glass, polymers [82]. Among them, PDMS (Polydimethylsiloxane) is the most widely used because it is cheap, easy, and rapid in fabrication. Besides, PDMS is optically transparent, has a high gas permeability and is biocompatible. Fig. 3.2 shows the photograph of a PDMS microfluidic chip for mixing two fluids dyed in blue and yellow. They flow through a channel network to generate a color gradient from yellow to green and blue.

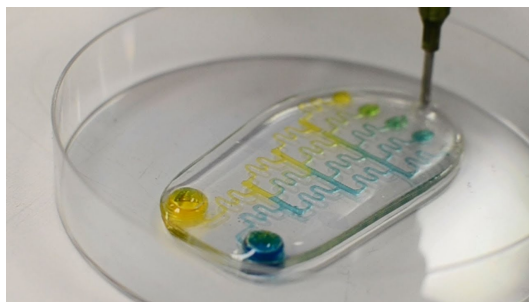


Figure 3.2: PDMS microfluidic chip that mixes a blue and a yellow fluids. The two fluids flow through a channel network forming a yellow-green-blue gradient [83].

To fabricate a PDMS chip, one often starts by fabricating a negative master mold, which is a rigid substrate containing micropatterns in a convex shape. Master molds can be fabricated by different techniques, namely photolithography, micro-3D-printing or micro-milling.

Photolithography is a process that uses light to generate micropatterns onto a substrate through a photosensitive material, i.e., photoresist. The scheme of the method is shown in Fig. 3.3a. The main procedure can be described as follow. First, the photoresist, SU-8 as an example, is uniformly deposited onto a silicon wafer thanks to a spin-coating, followed by a soft bake to become more solid. Then part of the photoresist is exposed to an intense UV light through a photomask containing micropattern, activating the cross-linking process. The cross-linked SU-8 part gets further activated and fully polymerized through a post-exposure bake. The wafer goes through a constant agitation in a developer agent to dissolve unpolymerized SU-8, leaving a solid micropattern remaining on the wafer. This technique allows for generating complex patterns at nanometric precision; however, it requires dedicated protocols in cleanrooms to ensure dust-free on the silicon wafer and photomask.

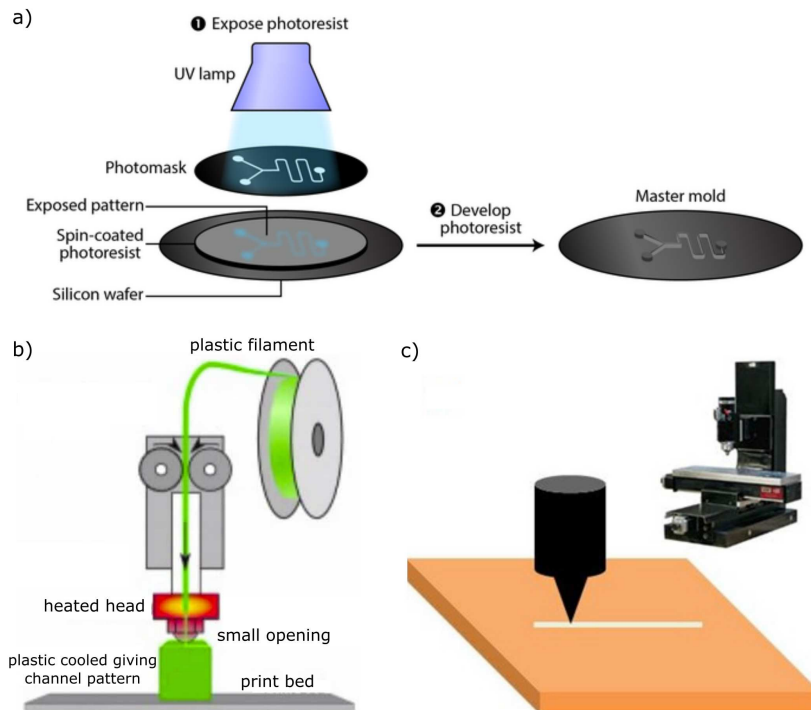


Figure 3.3: a) Scheme of the photolithography method (adapted from [84]). b) Scheme of Micro-3D-printer with fused deposition (adapted from [85]). c) Scheme of Micro-miller with a micro-mill (adapted from [86]).

The methods like micro-3D-printing or micro-milling can be more convenient in practice because they are simple, less expensive, and efficient. Fig. 3.3b shows a schematic of a 3D printing process. Briefly, a plastic filament is melted in a heated head, pushed through a small opening, then deposited on the print bed, and cooled down to generate a micropattern. Fig. 3.3c shows a schematic of a micro-milling process. Briefly, a micromachine mechanically carves on a substrate material by rotating a drum with multiple cutting teeth and leave a micropattern on top of the substrate.

Once the master mold is fabricated, many PDMS chips can be produced from the same master mold. Soft lithography is the most common technique to transfer the micropatterns from a master mold to a PDMS chip. Fig. 3.4 shows a schematic of this process. First, a mixture of PDMS and curing agent is poured onto the master mold. Next, this mixture is degassed under vacuum and cured at the temperature of  $65^{\circ}\text{C}$  for at least one hour to solidify it. Finally, the PDMS is peeled away from the master mold and sealed on a cover glass after a vacuum plasma treatment for both.

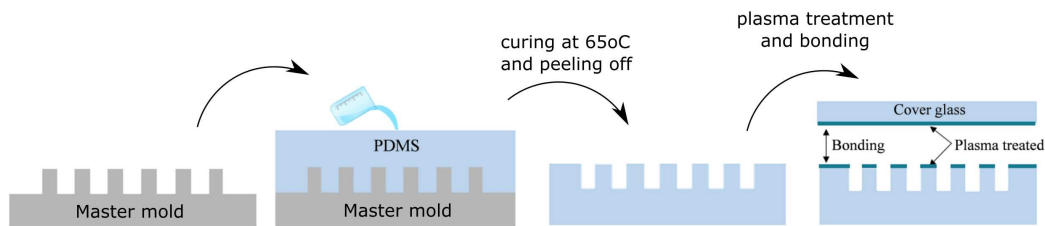


Figure 3.4: Scheme of soft lithography method to fabricate a PDMS microfluidic chip from a master mold. (Adapted from [87]).

### 3.2.2 Flow control instruments

The injection of fluids into a microfluidic chip is achieved by creating a pressure difference between the inlet port and the outlet port, which is normally open to atmosphere. Syringe pumps and pressure controllers are among the most commonly used instruments for generating fluid flows in microfluidic systems. In practice, the choice of flow control instrument is based on researcher's habit, experiment requirements, and equipment availability. Below, I will briefly present the working principle, advantages, and drawbacks for each of these instruments.

In syringe pumps, a motor pushes a piston of a syringe that contains a fluid inside (Fig. 3.5a). The flow rate ( $Q$ ) of the fluid depends on the speed of the piston ( $v$ ) and its cross-section area ( $S$ ),  $Q = v \times S$ . One of the main advantages of syringe pumps is that they are easy to setup and use. In addition, this instrument can both inject fluid and read the flow rate accordingly. However, the movement

of the piston can induce flow fluctuations at low flow rates and affect the stability of the flow. Nowadays, high precision syringe pumps have been developed with high performance of motor engine and smooth piston movement. The volume of fluid in syringe pumps is typically in the range from 1  $mL$  to 100  $mL$ , with exceptional cases of 0.01  $mL$  minimum and 250  $mL$  maximum. However, to obtain a pulse-free flow, the volume of syringe always depends on the desire flowrate value. For example, a 50  $mL$  syringe brand Cetoni can afford a minimum pulse-free flow rate of 8.4  $\mu L/min$ , corresponding to 4 days running continuously.

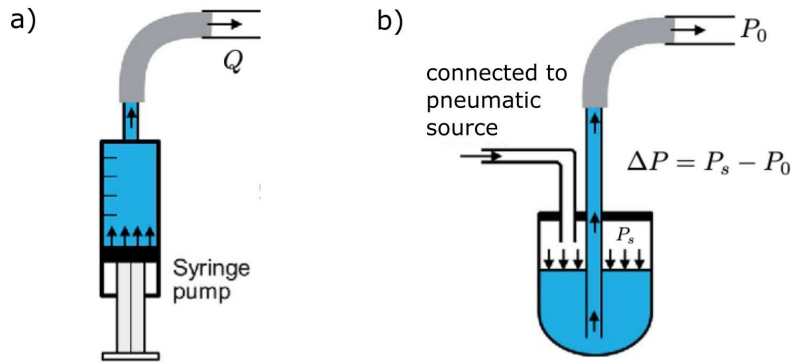


Figure 3.5: Working principle of (a) syringe pump and (b) pneumatic pump for injection of fluid into microfluidic system.  $Q$  is the flowrate,  $P_s$  and  $P_0$  are the pressures in the tank and in the outlet of the system (adapted from [88]).

In pressure controllers, a controlled pneumatic source pressurizes a fluid reservoir; then, as a consequence, the fluid inside the reservoir is pushed toward the microfluidic chip (Fig. 3.5b). The flow rate of the fluid ( $Q$ ) depends linearly on the pressure drop between the inlet and outlet of the system ( $\Delta P$ ) and the hydrodynamic resistance ( $R$ ) of the microfluidic chip,  $\Delta P = Q \times R$ . The hydrodynamic resistance is a parameter that measures the resistance of a fluid to flow in a channel and depends on the fluid viscosity and the channel geometry. In contrast to syringe pumps, the fluid containers that are used in pressure controllers have a wide range of volumes from milliliters to liters, and independent from the desire flow rate value. Besides, the fluid flow induced by pressure controllers is pulseless and highly responsive to changes of pressure. This instrument allows to generate a wide range of stable flows independently of the reservoir volume. However, the two main drawbacks of pressure controllers are the need of a pneumatic source and flow-rate meters to measure the actual flow rate of the fluid if needed.

My thesis project aims at a practical platform for environmental monitoring; thus, the microfluidic system should be designed to be easy to operate and affordable to low-income countries. Therefore, to fabricate the microfluidic master mold, we selected the micro-milling method because it is user-friendly as no cleanroom is

required. For the flow control system, we implemented pressure controllers and flow rate meters. As mentioned previously, the pressure controllers provide high flexibility in the fluid container volume. Thus, it is appropriate for continuous monitoring because one does not need to refill the fluid reservoirs regularly, especially when the platform is located in rural areas.

### 3.3 Droplet-based microfluidics

As briefly introduced previously in section 3.1, droplet-based microfluidics has several advantages over continuous flow microfluidics like avoiding memory effect caused by gradual deposition of analyte onto side wall and its flexibility in fluid manipulation. It becomes more and more popularly used. Each droplet can be considered as a micro-reactor in which the sample is confined and transported on the whole along the system. In further, droplet generation is usually fast and efficient (one droplet every second or every milli-second).

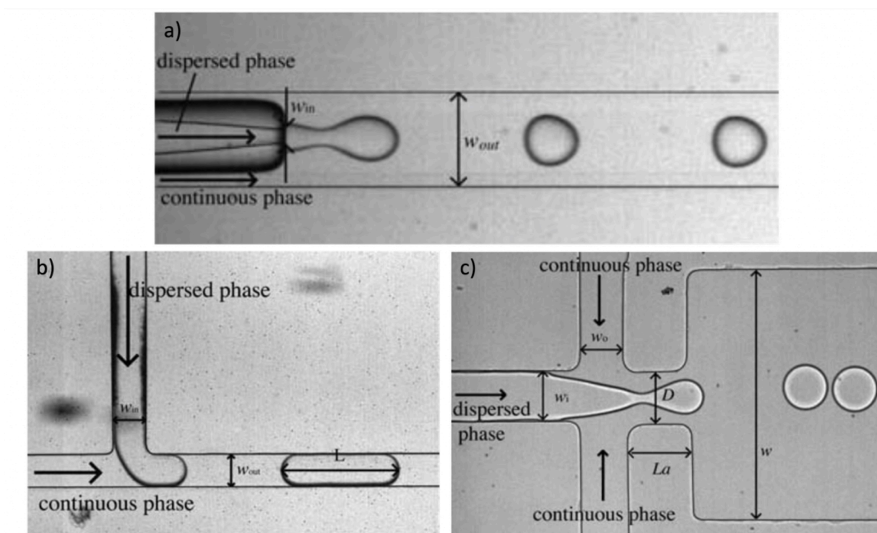


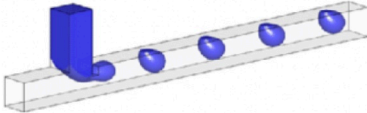
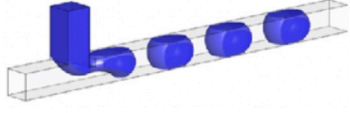
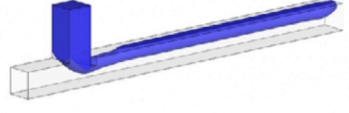
Figure 3.6: Examples of geometries for droplet formation. a) Co-axial injection b) T-junction and c) Flow-focusing. Adapted from ref. [89]. The dispersed and continuous phase are indicated in each panel. The rest of variables are related to geometrical characteristics of the microfluidic chips.

When working with droplet-based microfluidics, the main manipulation tasks are droplet formation and transport. Among them, creating droplets with a desired and highly monodispersed size is the first task needed to be handled. In general, to form droplets, two immiscible fluids are brought into a junction. Here, there is a competition between the viscous shear stress applied by the continuous phase on to the interface of the dispersed phase versus the interfacial tension acting to resist the deformation [89]. Depending on several factors such as the geometry of the

junction, the flow rate, and the physical properties of fluids like interfacial tensions and viscosity of fluids, droplet formation can happen.

There are three main geometries that have been commonly implemented for droplet formation, namely co-flowing, T-junction and flow focusing (Fig. 3.6). This section focuses on the T-junction geometry as it is simple to design, fabricate and manipulate fluids. For those reasons, we also chose this geometry to tackle the problem in this thesis project. T-junction includes two orthogonal channels bringing two immiscible fluids to meet, the continuous phase is injected straight to the main channel while the dispersed phase is injected perpendicular to the main channel (Fig. 3.6b). Depending on the factors mentioned above (geometry, flow rates and physical properties of fluids), three main regimes can occur: dripping, squeezing and parallel flowing. Tab. 3.1 lists the influences of some dimensionless numbers on the droplet formation regime; however, those dimensionless numbers are in fact dependent, therefore, this table just serves as quick guidelines to adjust the microfluidic system in order to obtain a desired outcome. In this thesis work, we chose to work with squeezing regime because we need to acquire the SERS signal from droplets. Therefore, a larger volume ratio of droplets and the continuous phase will produce a stronger signal.

Table 3.1: Control droplet formation in T-junction.  $w$  refers to the width of the channel,  $\mu$ : dynamic viscosity,  $v$ : fluid velocity,  $\sigma$ : surface tension (reproduced from [89]).

	<b>Dripping</b>	<b>Squeezing</b>	<b>Parallel flowing</b>
Simulation of droplet formation (*)			
Ratio of channel widths $x = \frac{w_{dispersed}}{w_{continuous}}$	$x \ll 1$	$x \sim 1$	
Capillary number $Ca = \frac{\mu v}{\sigma}$	High	Low	
Mechanism	Viscous shear stress overcomes the interfacial tensions, creates interfacial instability (so-called Plateau-Rayleigh instability).	The droplet grows and obstructs the channel, inhibit the flow of the continuous phase → the dynamic pressure upstream of the droplet is dramatically increased → the interface at the junction is deformed to a neck, then pinch off into a droplet	The viscous shear stress is not large enough to win interfacial tension.
Flow rate ratio $q = \frac{Q_{dispersed}}{Q_{continuous}}$	Droplet's size increasing with the flow rate ratio, but always in spherical shapes as they are emitted before they can block the channel.	Droplets of pancake shape with the length increasing linearly with the flow-rate ratio.	More likely to happen when flow rate ratio is large enough.

## 3.4 Mixing in microfluidic systems

At small scale, viscosity dominates inertia, thus the flow of fluids in microchannels is laminar (i.e., fluid flows in parallel layers) and characterized by a low Reynolds number which is often less than 1. The Reynolds number ( $Re$ ) is defined as the ratio of inertial forces to viscous forces:  $Re = \rho Ul/\mu$ , where  $\rho$  is the fluid density ( $kg/m^3$ ),  $U$  is the fluid velocity ( $m/s$ ),  $l$  is the characteristic length scale ( $m$ ), and  $\mu$  is the dynamic viscosity ( $Pa.s$ ). Considering a typical case in microfluidic systems, an aqueous solution (viscosity water =  $10^{-3}$   $Pa.s$  density  $10^3$   $kg/m^3$  (1  $g/mL$ )) flows inside a channel of  $10^{-4}$   $m$  (100  $\mu m$ ) width at a speed of  $10^{-3}$   $m/s$  (1  $mm/s$ ), the Reynolds number is in the order of 0.1.

In laminar flow, fluid particles flow in parallel trajectories, thus the mixing is mainly governed by molecular diffusion between lateral layers which is a slow process. Nevertheless, a thorough and rapid mixing in microscale devices is important for many chemical systems. Many efforts have been made by either passive or active approaches. In active micromixers, to accelerate the mixing, external energy besides the one that generate fluid flows is required, for instance: temperature, acoustics, electrohydrodynamic, dielectrophoretic, magnetohydrodynamics [90]. Active micromixers are often robust but in turn, they are expensive and complicated to develop. On the other side, passive micromixers are often a preference choice for most of researchers because they do not require external energy. The strategy is to accelerate the diffusion by increasing the contact area between fluids and decreasing the diffusion path between them. A practical approach consists in creating chaotic advection by designing special geometries for mixing channels, [91]. Another efficient and simple approach is to mix inside droplets. After being generated, the droplets travel through a curvy channel, they are deformed, leading to internal flows of sketching and folding fluid streams [92].

For my thesis project, we applied passive mixings in both continuous phase and in droplets to mix several reagents in a certain order. Chapter 4 presents our mixing design and implementation.

## 3.5 Generation of concentration gradients

In titration methods, scanning the titrant concentration versus the analyte concentration is essential to identify the endpoint. In classical titrations such as acid-base, redox and complexometric titrations, this concentration variation is traditionally carried out using a volumetric burette to add titrant to the sample gradually. Along with the development of microfluidic engineering, Jesse Greener et al. 2012 [93] demonstrated an adaptation of acid-base titrations in a continuous flow microfluidic platform. Scanning of the acid/base concentration ratio was carried out by varying the flow rate ratios of the two solutions injected from two inlets while remaining their total flow rate constant, Fig. 3.7a. After mixing in a

serpentine channel, the pH was measured through a pH microelectrode at point  $P_1$ , Fig. 3.7a. Fig. 3.7b shows reproducible titration curves obtained.

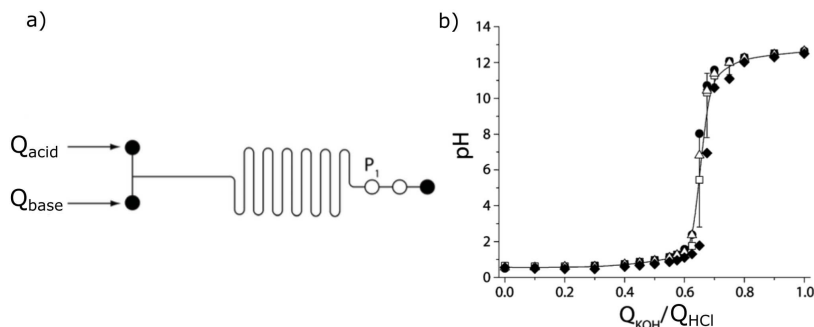


Figure 3.7: a) Schematic of the microfluidic reactor for acid-base titration. Acid and base solutions are injected from two inlets at flow rates  $Q_{acid}$  and  $Q_{base}$ . Then they are merged to a serpentine channel for mixing and neutralisation reactions. The pH is measured through a microelectrode integrated at the points  $P_1$ . b) The titration curves of 4 microfluidic experiments carried out in two different days using stock solutions of HCl 0.075 M, and KOH 0.05 M. Adapted from [93].

Regarding the SERS-based complexometric titration presented in chapter 2 for microfluidic adaption, we note that the concentration gradient was achieved in a series of separate cuvettes with a stepwise variation of titrant concentration. This is because the in-situ formation of SERS active colloidal aggregates and the interaction between analyte molecules and SERS active aggregates is generally perceived to be out of equilibrium. Therefore, each standard sample corresponding to different titration composition needs to be prepared independently from the next one. Otherwise, the speciation of the sample is unlikely to readjust itself to the new composition and/or SERS-active colloidal particles could age in an uncontrolled, unpredictable, and irreproducible manner.

For adapting this SERS-based titration method to a microfluidic system, each cuvette can be transformed into a droplet. Therefore, we need to generate a chain of droplets with varied compositions. A straightforward approach for concentration gradient generation is similar to the continuous microfluidic titration, using several inlets to inject different components with controlled flow rate variation [94]. Then they are merged into a single channel and meet with another immiscible phase for droplet formation.

Fig. 3.8 illustrates a simple microfluidic configuration for generating concentration gradient in droplets. Three components  $i = 1, 2$  and 3 with the initial concentration  $C_{(i,feedstock)}$  are injected from three inlets at controlled flow rates  $Q_i$ .

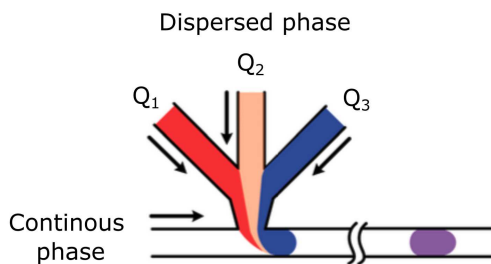


Figure 3.8: A simple configuration for generating concentration gradient in droplets from three components with controlled flowrates ( $Q_1$ ,  $Q_2$  and  $Q_3$ ). The continuous and dispersed phase are indicated in the panel. Adapted from [94].

The composition inside a droplet is linked to the flow rate by the formula:

$$C_{(i,\text{droplet})} = \frac{C_{(i,\text{feedstock})}Q_i}{\sum_i Q_i} \quad (3.1)$$

where  $C_{(i,\text{droplet})}$  is the concentration of component  $i$  within the droplet,  $C_{(i,\text{feedstock})}$  is the original concentration of component  $i$  in its feedstock, and  $Q_i$  is the flowrate of component  $i$ .

In chapter 4, we will detail our implementation of concentration gradient generation in droplets for SERS-based complexometric titration. In principle, this method can also be applied for SERS-based calibration methods.



# Microfluidic platform for SERS-complexometric titration

---

## Contents

---

<b>4.1</b>	<b>Introduction</b>	<b>41</b>
<b>4.2</b>	<b>Results and discussion</b>	<b>43</b>
4.2.1	Chemical principle of the SERS-based titration of water hardness	43
4.2.2	Overview of the automated SERS titrator	45
4.2.3	Microfluidic set-up	45
4.2.4	SERS readout	47
4.2.5	Injection system for controlling the progression of the titration	48
4.2.6	Operation of the platform python program	50
4.2.7	Evian titration	51
4.2.8	Volvic and contrex titrations	54
4.2.9	Critical reviewing of the analytical performances of platform	55
4.2.10	Operating cost	56
<b>4.3</b>	<b>Conclusion</b>	<b>57</b>
<b>4.4</b>	<b>Experimental section</b>	<b>58</b>

---

## 4.1 Introduction

Surface Enhanced Raman scattering (SERS) has emerged as an extremely sensitive chemical analysis in the past decades. Its sensitivity stems from the giant amplification of Raman signals that takes place at the surface of metallic nanostructures displaying sharp tips or steep grooves. Excitation of the surface plasmons of these so-called hot spots results in orders of magnitude large enhancements of the local electric field, which in turn amplifies the Raman processes of close-by molecules [42, 28, 95]. These hot spots can be fabricated on solid wafers or engineered as colloidal particles. Sensitivities in the sub-micromolar range are the norm in the SERS dedicated literature, which makes the technique especially attractive for environmental monitoring of trace contaminants. In spite of this, there is no SERS application in routine quantitative analysis yet to the best of our knowledge. SERS-based sensing is often hindered by time-consuming sample

## 42 Chapter 4. Microfluidic platform for SERS-complexometric titration

---

preparation procedures, for instance when sample solutions have to be dried out on solid SERS substrates [96, 53], complex measurements samples need to be prepared [29, 97], possibly with the use of costly precursors [98] such as when colloidal SERS particles of high synthetic value are used. Both factors are critical because SERS is highly irreproducible and therefore requires many readouts to achieve a satisfactory prediction power.

In SERS-based quantitative analysis, the concentration of the targeted molecule is usually determined from a calibration curve which ties the SERS signal to the concentration of the analyte [95, 99, 100]. Building a reliable and robust SERS-based calibration model is challenging [29], (see Chapter 2) due to the inherent irreproducibility of SERS signals. SERS enhancement factors are strongly sensitive to structural and compositional inhomogeneities between hot spots at the nanoscale. As a consequence, building a SERS calibration curve requires more data than other common spectroscopic techniques (c.a. fluorescence, absorption) do since these enhancement factors need to be averaged out. Moreover, the validity of any given SERS calibration model is short-lived because of aging of the SERS materials or significant disparities between batches of SERS-active materials. The calibration task needs to be carried afresh any other day or using any other SERS-active particle batch or set of solid SERS-active substrates. Meanwhile, many replicate readings of a sample need to be performed to give an accurate estimate of its concentration, again because of the significant dispersion of the SERS signals. We have shown earlier that the labour involved in acquiring such large data sets dominates the consolidated cost per analysis [29].

In recent work, we demonstrated that the need for calibration could be alleviated by implementing SERS-based titrations in the presence of an end-point indicator (see Chapter 2). The principle relies on reacting the analyte with a standardized titrant while monitoring the SERS signal of the indicator. The abrupt switch in this SERS signal upon approaching the equivalence acts as a proxy for the determination of the endpoint. In this method, the workload of calibration is therefore transferred from the construction of a large training spectral dataset to using various amounts of a standardized titrant. The method was successfully applied to the complexometric determination of the hardness of several mineral waters. This shrank the number of data needed to achieve an accurate estimate of concentration compared to using a calibration model. The time per concentration reading was about 40 min, which is acceptable for punctual measurements but still is too cumbersome when frequent readouts or large measurement sets are needed.

A significant improvement of practicality, for both calibration and titration-based methods, could be achieved upon automatizing the preparation of the SERS samples. Automated titrators can be bought from commercial suppliers. They generally rely on controlled volumetric additions of reagents into a reaction mixture which is probed throughout the additions, either optically or electrochemically.

However, their design makes them unsuitable for SERS measurements. Obviously, such mode of operation precludes their use with solid SERS substrates. But even when focusing on colloidal SERS active materials, the progressive addition of titrant into a single reaction mixture could prove problematic. Indeed, the *in-situ* formation of SERS active colloidal aggregates or the interaction between analyte molecules and SERS active particles is generally perceived to be out of equilibrium. Each standard sample or each titration composition needs to be prepared independently from the next one since the speciation of the sample is unlikely to readjust itself to the new composition and/or SERS-active colloidal particles could age in an uncontrolled, unpredictable, and irreproducible manner.

The present study aims at building an automated platform to conduct SERS-based titrations. We demonstrate the validation of this platform on the specific case of water hardness titration. Briefly, the platform can repeatedly and autonomously perform the tasks of preparing the SERS-active measurement samples, of reading the advancement of the reaction through a SERS measurement and of screening the proportions of analyte and titrant to identify the equivalent point. In the following, the conception and performance of the blocks composing the titrator will be sequentially described. Then, the operation of the full prototype will be critically assessed on three mineral waters by comparison with our previous manual SERS-based titrations.

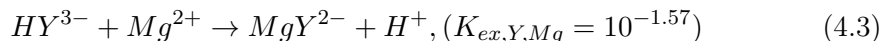
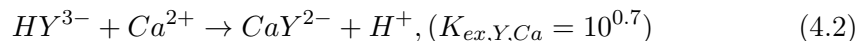
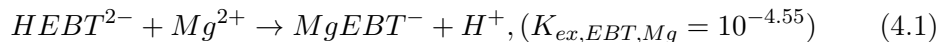
## 4.2 Results and discussion

### 4.2.1 Chemical principle of the SERS-based titration of water hardness

Water hardness refers to the total concentration of dissolved calcium and magnesium in a water sample. Before the advent of modern instrumental analysis, c.a. chromatography or atomic spectroscopies, water hardness was routinely measured by complexometric titration using a strongly absorbing indicator, such as Eriochrome Black T (*EBT*), that changed colour upon reaching the equivalence. A typical procedure proceeds as follows. First, *EBT* is introduced to the water sample in large default compared to the foreseen divalent metal content. It binds to a tiny fraction of free magnesium ions, forming  $MgEBT^-$  complexes having a pink colour (Eq. 4.1). Then, the titrant ethylenediaminetetraacetic acid (*EDTA*, referred to  $H^4Y$  in (Eqs. 4.1- 4.4), an hexadentate ligand with high affinity for divalent metal ions, is gradually added and sequentially binds to  $Ca^{2+}$  and  $Mg^{2+}$  ions in the water sample (Eq. 4.2, 4.3). Once *EDTA* has consumed all free  $Ca^{2+}$  and  $Mg^{2+}$  ions, newly added *EDTA* steals magnesium away from  $MgEBT^-$  and *EBT* is released as the unbound  $HEBT^{2-}$  species with a blue colour (Eq. 4.4). The colour switch from pink to blue can be used as a titration endpoint to estimate the total concentration of  $Ca^{2+}$  and  $Mg^{2+}$  from the amount of added *EDTA*. The titration should

## 44 Chapter 4. Microfluidic platform for SERS-complexometric titration

be conducted at a pH of at least 10.0 to ensure quantitative complexation of  $Mg^{2+}$  by  $EBT$ .



In our previous work presented in chapter 2, we re-exploited this titration procedure by using the SERS signal of the indicator as an end-point marker instead of relying on the classic colour switch probed by naked-eye. To do so, we performed the titration in the presence of SERS-active micrometric beads assembled *in-situ* from spherical silver nanoparticles (Ag NPs) and a polyamine aimed at bridging the NPs together. Practically, on top of the chemicals necessary to conduct the classic colorimetric titration, namely the indicator, buffer and titrant, the water sample was also mixed with precursors of the SERS-active beads: Ag NPs, polyethyleneimine (PEI) as the polyamine cross-linker and a polymeric screening agent (polyethylene glycol, PEG) (Fig. 4.1). The screening agent served to slow down the kinetics of nanoparticle aggregation to help achieve reproducible spherical aggregates and a reproducible insertion of the indicator into the aggregates.

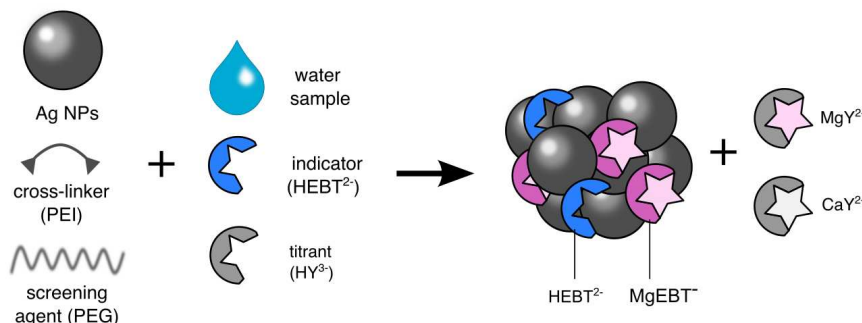


Figure 4.1: Scheme of the formation of active SERS substrates for water hardness measurement. Ag NPs are aggregated using cross-linkers in the presence of water sample, indicator, and titrant. EBT in different forms (free form  $HEBT^{2-}$  and metal-bound form  $MgEBT^{-}$ ) were entrapped within NPs aggregates during this process. Thus, they can give rise to SERS signal under laser excitation.

Our procedure for running the titration was similar to running the classic colorimetric titration but for one point: instead of adding the titrant by incremental additions into a single test portion of the water sample, increasing amounts of titrant were added into separate test portions of the water sample. This procedure was needed because the aggregation process runs out of equilibrium. Thus, incremental additions of the titrant onto preformed aggregates are unlikely to result

in the change of speciation of the indicator that would be observed if it was not trapped within nanoparticle aggregates.

### 4.2.2 Overview of the automated SERS titrator

To automate the running of this chemical titration scheme, the automated titrator must therefore perform three main tasks: (i) autonomously preparing complex measurement samples containing test portions of the water sample, the necessary precursors of the SERS-active aggregates and the titrant and indicator; (ii) acquiring the SERS spectra of the resulting mixtures and (iii) varying the analyte/titrant ratio in order to pinpoint the end of reaction.

The prototyped titrator consists of three functional blocks that perform these tasks: (i) a microfluidic chip designed to prepare independent measurement samples as water-in-oil droplets from all the necessary feedstocks, (ii) an optical measurement chamber set-up to acquire the SERS spectra of droplets in line and (iii) a controllable injection system to control and sweep the proportions of the sample and titrant to conduct a titration (Fig. 4.2). In addition, we developed a python program (accessible on GitHub [101]) that controls the various instruments involved in the preparation of the droplets and the Raman spectrometer in order to autonomously run titrations.

### 4.2.3 Microfluidic set-up

A PDMS microfluidic chip is used to continuously prepare SERS-active measurement samples. Upon manipulating colloidal nanoparticles in microfluidic channels, one is confronted with the problem of gradual deposition of nanoparticles and chemical compounds onto to sidewalls. This may lead to cross-contamination, for instance between compositions explored at the beginning and at the end of a titration run. Moreover, NPs aggregates under a continuous shear flow can merge and grow to bigger aggregates, causing clogging issues. To keep the composition of each investigated titration step independent from the previous one, and to ensure long running times, we chose to encapsulate each reaction mixture into water droplets segmented into an oil flow. This alleviates both clogging and cross-contamination problems.

Six chemical components need to be brought together within droplets for each step of the titration: the water sample, the titrant, the indicator, the NPs, the screening agent, and the cross-linker. To simplify the design of the chip and ensure robust droplet formation, the screening agent, cross-linker, and indicator, which are inert towards one another and need to be added into the reaction mixture into fixed proportions, were combined as a single pseudo-unitary EBT-PEI-PEG feedstock.

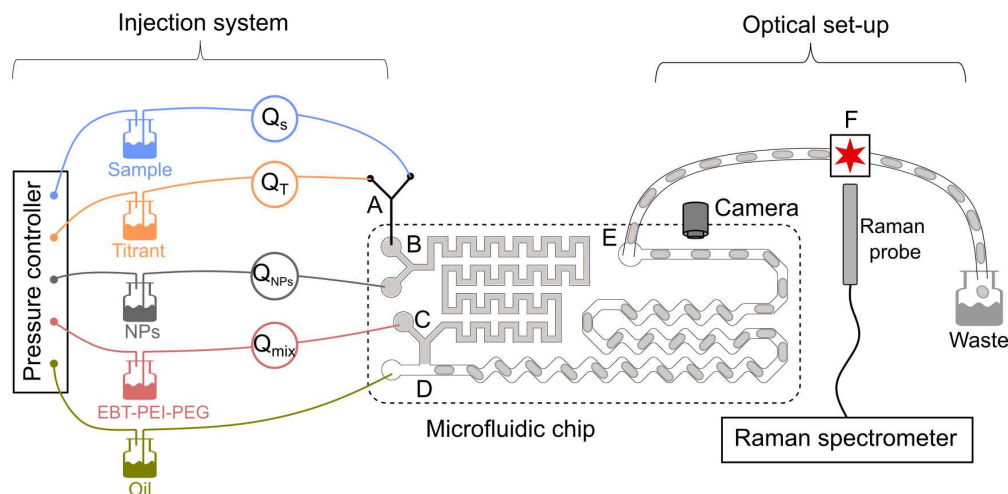


Figure 4.2: The schematic of the microfluidic platform includes three main parts: an injection system, a microfluidic chip, and an optical set-up. The injection system consists of a pressure controller, five reservoirs, and four flow rate sensors. Five reservoirs are water sample (blue), titrant EDTA (orange), Ag NPs (grey), a mixture of PEG, PEI, and indicator EBT (pink), and mineral oil (dark green). The outlets of the pressure controller are connected to the reservoirs which then push fluids into tubings and towards flowrate sensors ( $Q$ ). The tubings are connected to the inlets on the chip. A camera is placed on top of the channel segment near the microfluidic chip's outlet for monitoring droplet movement. The optical setup includes a Raman spectrometer whose Raman dual probe focuses within droplets travelling through a glass capillary nested inside a dark chamber.

The other feedstocks were sequentially combined using serial Y junctions. All feedstocks were connected upstream to two pneumatic devices to push onto the fluids towards the microfluidic chip. Each of the feedstock but for the oil one passes through a flowrate sensor before entering the chip.

First, the titrant and water sample are combined using a commercial Y-junction upstream of the chip (Fig. 4.2, junction A). The binary solution is fed to the microfluidic chip through one branch of a Y junction (junction B), the other branch being fed by the NP solution. The now ternary mixture is homogenized thanks to a square-wave serpentine mixer, which ends onto a third Y junction (junction C). The second branch of that junction is fed by the EBT-PEI-PEG pseudo-unitary feedstock. The full reaction mixture exits the Y junction into a perpendicular stream of oil injected through a dedicated inlet (junction D). This aqueous mixture grows at this T-junction, until it pinches off into a droplet.

The droplets travel through a second serpentine segment, which facilitates inner mixing through stretching and folding the liquid streams [102, 92]. Because

of the screening agent slows down the interaction between NPs and cross-linker, assembly of the SERS-active beads significantly starts only once the reaction mixture is encapsulated into droplets. The SERS-active beads are matured for about 5 minutes after exiting the chip (at junction E) by travelling through a 130 cm-long tubing towards the optical readout chamber. Images of the flow at different locations of the microfluidic chip are provided in supporting information (Fig. 4.12).

Droplet volume and speed were determined by recording movies of the flow within the chip. Under typical conditions for forming droplets and conducting a titration using the platform, the mean volume is  $2.51 \pm 0.17 \mu\text{l}$  (three droplets measured out of 8 independent launches) and its mean speed next to junction E is  $4 \pm 0.1 \text{ mm/s}$ . The aqueous/oil segment ratio is  $0.88 \pm 0.05$ . See section 4.9 for measurement details.

#### 4.2.4 SERS readout

SERS measurement set-up. Raman spectra were acquired using a compact fiber optic high-resolution spectrometer paired with a 638 nm laser excitation source. In order to acquire the SERS spectra of a train of droplets away from ambient light, an optical measurement chamber was built by passing a glass capillary within a commercial 4-window cuvette holder. The outlet of the capillary was connected to another piece of tubing to transport droplets to the waste bin. See section 4.10 for more details of the set-up.

We performed SERS measurements of droplets prepared in excess of titrant compared to alkaline earth ions (11 eq. titrant with respect to metal, see Fig. 4.17 for composition details). Under this composition, the indicator, which is the only significant contributor to the SERS spectrum is in its free form and should display an intense SERS signal according to our previous manual SERS titrations. The integration time for the Raman spectrometer was always set to 15 seconds. Given the afore estimated droplet speed and aqueous/oil segment ratio, this duration accumulates the Raman signal from about a dozen of droplets. Fig. 4.18 compares the SERS spectra from the microfluidic system and the manual test in cuvettes that used the same stocks and component proportions, under the same integration times.

In the range which formed the basis of quantification in our previous manual titration method ( $850 - 1600 \text{ cm}^{-1}$ ), they display high similarity in spectral patterns, (Fig. 4.18). Remarkably, there is no prominent contribution from mineral oil that alters the peaks of interest from  $1100 - 1300 \text{ cm}^{-1}$ . In droplets, the spectral intensity of the most prominent peak is 76% of the that in cuvettes. This was unexpected since the segment ratio between aqueous and oil was previously measured from recorded videos of  $0.88 \pm 0.05$  or 44/56%, and one would therefore have expected a 44% drop in intensity compared to that in cuvette. The % excess

## 48 Chapter 4. Microfluidic platform for SERS-complexometric titration

---

of signal intensity could be due to the disappearance in droplet of some inert filter effect present in cuvettes [103]. The optical path being longer in cuvette, some scattered photons might be reabsorbed by the sample and therefore not be collected by the Raman probe. The spectra measured in the microfluidic mode therefore were of suitable quality to monitor SERS-based titrations.

Similarly, we acquired in line SERS spectra of droplets in excess of metal ions (0.2 eq. titrant compared to metal), a composition in which the indicator is bound to magnesium. Like we observed in cuvette, the spectra were much less intense than when the indicator was free, although its bound signal was more intense in droplets than in cuvettes having the same composition. Nevertheless, the difference between both bound and free spectra were significant enough to read the indicator speciation from the SERS signal.

**Reproducibility of SERS spectra.** The formation of in-situ SERS-active aggregates generally proceeds under kinetic control. Therefore, their SERS activity depends on the mass transfer rate, namely on the rate and order of addition of reagents and the rate of homogenization. Those are the factors that often cause the SERS signal irreproducibility. In our manual titration method, the irreproducibility was partially tamed by slowing down the kinetics of bead formation through the use of PEG as a screening agent: it gave the operator enough time to add and adequately homogenize reagents. In droplet microfluidics, the mass transfer rates are standardized by the microfluidic chip and flow rates. Therefore, we expected the reproducibility of the SERS acquisition to improve upon generating SERS-active beads in droplets compared to preparing manual measurement samples at 3 mL scale in tubes. Indeed, when comparing spectra acquired in cuvettes and droplets at similar composition proportions, we observed a decrease in the relative standard deviation of the maximum peak intensity from 10 – 14% to 2.2 – 2.3%, depending on the batch of NP precursor (4.20).

### 4.2.5 Injection system for controlling the progression of the titration

For the automaton to run a titration, the system needs to incrementally vary the proportions between the target analytes in the sample and the titrant and to quantitatively link those proportions to the collected SERS spectra, in a manner equivalent to reading a volume on the burette when observing a change of colour in the classic colorimetric titration.

**Monitoring droplet composition.** The two pneumatic pressure control devices push onto the liquid feedstocks to tune the flow rates imposed on each channel. The outlets of all feedstocks but for the oil reservoir are connected to flow rate sensors to monitor in real-time the effective flow rates and, therefore, the

effective proportions of the reagents co-injected as droplets. Between the flow rate sensors and the chip, a significant length of tubing ( $\sim 50\%$  of total circuit length, 2 m) was added to increase the hydrodynamic resistance, thereby damping flow rate fluctuations induced by pressure fluctuations [104].

Fig. 4.3a shows that the monitored flow rates closely mirror any newly defined pressure set point, evidencing correct synchronization between the microfluidic devices and the absence of leaks. The flow rates are stable during each pressure plateau's duration with the average relative standard deviation of 1.5%.

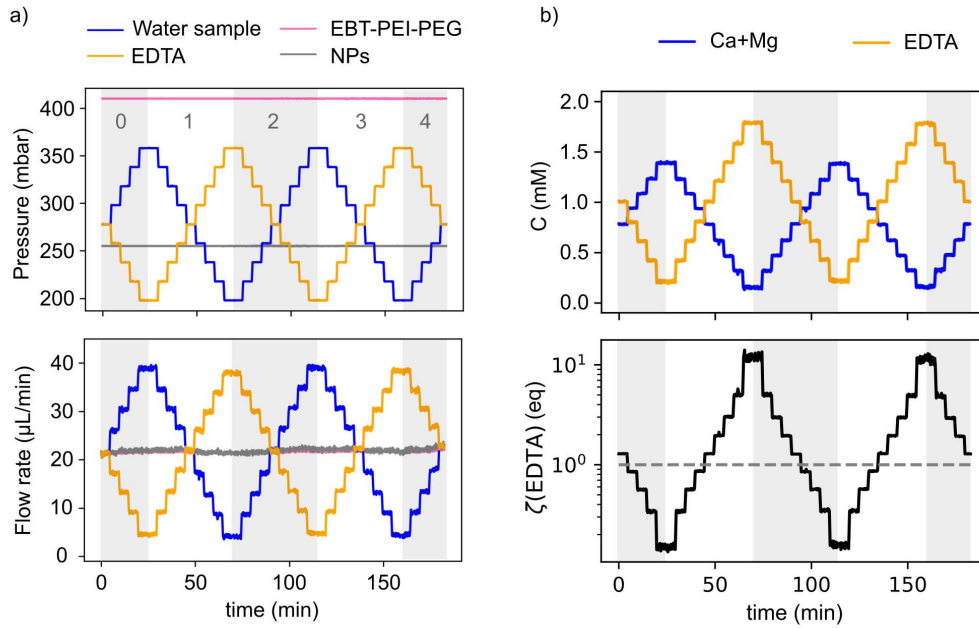


Figure 4.3: Composition control in a microfluidic experiment (experiment MD162\_14h10). a) Pressure and flow rate trajectories over time in water sample (blue), titrant (orange), Ag NPs (gray) and PEG-PEI-Ind (pink) inlets. b) the upper panel: total concentration of calcium and magnesium ions (blue) and EDTA concentration (orange) within droplets over time; the bottom panel: number of EDTA equivalents,  $\xi(\text{EDTA})$ , over time in log scale. The gray dashed horizontal line serves as visual guide of the equivalence.

The composition of the droplets can be inferred from the various aqueous flowrates as:

$$C_{i,\text{droplet}} = \frac{C_{i,\text{feedstock}} \times Q_i}{\sum_i Q_i} \quad (4.5)$$

where  $C_{i,\text{droplet}}$  is the concentration of component  $i$  within the droplet (in  $\mu\text{M}$ ),  $C_{i,\text{feedstock}}$  is the original concentration of component  $i$  in its feedstock (in  $\mu\text{M}$ ), and  $Q_i$  is its flowrate (in  $\mu\text{L}/\text{min}$ ).

**Sweeping the proportions of analyte and titrant.** The ratio between titrant and analyte was varied by sweeping the pressures in the water sample and titrant channels in opposite directions, while the pressures in other channels were maintained constant. This kept the total flow rate of all droplet components at a fixed value to enable stable droplet formation throughout a titration. This approach is commonly used in microfluidic systems [56, 93].

Fig. 4.3b shows representative trajectories of total divalent metal ions ( $\text{Ca}^{2+}$ ,  $\text{Mg}^{2+}$ ) concentration and EDTA titrant concentration throughout serial titrations of Evian water. The intersection between both trajectories marks the equivalence, namely the point at which the titrant has been introduced in the droplet in stoichiometric proportions compared to the divalent metal content.

In the following, we defined the number of EDTA equivalents as:

$$\xi(\text{EDTA}) = \frac{C_{\text{EDTA}}}{C_{\text{Ca}} + C_{\text{Mg}}} \quad (4.6)$$

Thus, at the equivalence point,  $\xi(\text{EDTA}) \equiv 1$ . The evolution of  $\xi(\text{EDTA})$  over the series of titrations of Evian water depicted in Fig. 4.3b is worth a comment. In a typical complexometric titration, and also in our previous manual implementation of a SERS-read determination of water hardness, the volume of the test portion is fixed throughout the titration and only the volume of titrant is varied, with  $\xi$  generally varying from 0 to 2. Here, due to the constraints of droplet formation, the volume of the test portion of sample varies over the course of the titration while the volume of droplets remains the same. Therefore, the volume of titrant varies in the opposite direction. As a consequence, the range of explored  $\xi(\text{EDTA})$  values extend over a much larger range than usual, from 0 to 13.

**Linking the SERS readouts to the flow rate readouts.** Because the flow rate sensors and the spectral readout point are placed nearly 2 m apart (Figs.4.2, 4.10), there is a time lag ( $t_{lag}$ ) between the flow rate and spectral data readouts. This lag time reflects the time it takes for a fluid particle to travel from the flow rate sensors to the focal point of the Raman probe, through the chip and tubings. Section 4.14 details this calculation based on the fluid traveling time in each segment. However, in our system, the lag time can be also estimated numerically by taking advantage of the periodic sweeping pattern applied to the spectral data (see section 4.2.7 about Evian titration below). We applied this numeric method to all the experiments because it is systematically fast and efficient.

#### 4.2.6 Operation of the platform python program

A dedicated Python program was developed to run several titrations in a row autonomously. The program starts after the platform has been manually primed to

generate droplets with equivalent flow rates in all the aqueous channels. The program then controls the pneumatic device to sweep the pressures so as to screen ratios between analyte and titrant. The program sweeps the pressures in one direction and then automatically finds the point where a new sweep in the reverse direction needs to start. It takes as arguments the height of the pressure steps ( $\Delta P$ ), their duration ( $t_{\text{step}}$ ), and the number of sweeps (equivalent to number of titration series) to be performed. It also stops the automaton progressively when the appropriate number of sweeps has been run to avoid backflows in the channels. During the sweep, the program records the flow rates for aqueous inlets and the spectral signals with time stamps. The spectral intensities, pressures and flow rates and time stamps are periodically assembled into a single data frame. The framerate for collecting data equals the integration time for the spectrometer. The data is saved on an external hard disk drive after completion of every pressure step to avoid data loss. For more details on the program, we refer the reader to the section 4.13. The code is accessible on GitHub [101]. We found that the program was robust because it was able to run eight independent launches on four different days, with uninterrupted runs lasting up to 2.5 hours.

#### 4.2.7 Evian titration

We tested the performances of the automatic titration platform on Evian water which has a moderate hardness ( $C_{Ca^{2+}} + C_{Mg^{2+}} = 3.1 \text{ mM}$ ). An EDTA solution having a  $4.06 \text{ mM}$  concentration was used as the titrant feedstock. The titration only works if the pH is of  $\sim 10$  or above. Control measurement samples were prepared in cuvettes to check that the compositions imposed in the droplets had an appropriate pH. Across a composition sweep, the pH was comprised between 9.5 and 10.4.

A sequence of titration series was launched using a pressure increment  $\Delta P$  of 20 mbar. The time stamps, pressure, flow rate and spectral intensities were recorded. In the first full series, the program generated 9 steps, starting from the excess EDTA pole, equivalent to 9 titration increments. Each step lasted 5 minutes over which 20 spectra were acquired. After baseline removal (see section 4.15 for data processing), the 180 collected spectra cluster into two distinct high and low-intensity groups, in a similar manner to what we observed in our previous manual protocol in cuvettes (Fig. 4.24). The time evolution of the most intense peak, at  $1191 \text{ cm}^{-1}$ , displays a periodic sigmoidal pattern (Fig. 4.26-bottom panel), consistently with a speciation switch between the free and bound forms of the complexometric indicator upon lowering the EDTA to metal ratio. The SERS signal sigmoidal pattern lags behind the imposed flow rate pattern due to the travelling time of the droplets from the flow rate sensors and to the focal point of the Raman probe. Therefore, the SERS readouts actually correspond to composition readouts made a certain lag time before. To estimate the time lag, we take advantage of the symmetry of flowrate profiles between two consecutive titration series. As these pro-

## 52 Chapter 4. Microfluidic platform for SERS-complexometric titration

---

files are symmetric, the SERS intensities should be symmetric about the very same dates once the time stamps of the SERS spectra have been corrected so that SERS readouts and composition readouts are correctly matched (Fig. 4.26-bottom panel).  $t_{lag}$  is then determined as the translation in time needed to match the middle points of the SERS intensity plateaus and of the extreme flowrate plateaus. Over eight independent experiment launches in this work, time lags ranged from 348 to 385 sec. These values are in the same order of magnitude with a rough estimate based on flow rate readings, speed of droplets and overall length of fluidic circuit (see section 4.14).

The resulting time-corrected SERS spectra cluster into low intensity ones below the equivalence and high intensity ones above, just as in the manual titration protocol, Fig. 4.4a. The temporal profile SERS intensity at  $1191\text{ cm}^{-1}$  shows that this low/high-intensity transition is sharp for each of the 5 recorded titration series. The inflexion points of the SERS intensity sigmoids are slightly time-shifted compared to the equivalence inferred from the flow rate readings, Fig. 4.4b. This corresponds to the analytical bias of the method. To quantitatively determine the titration endpoints, the intensity at  $1191\text{ cm}^{-1}$  was plotted versus the number of EDTA equivalents,  $\xi(\text{EDTA})$ , for each series, Fig. 4.4c. A sigmoid function was then fitted to the data and its inflexion point was used as the endpoint. The trueness is defined as the percentage ratio between the endpoint and the equivalence. The mean trueness over the four consecutive titration series represented in Figure 4.4 is  $64 \pm 3\%$ . This result proved reproducible on another independent launch of the platform using the same NP batch, giving the trueness of  $65 \pm 3\%$  (Fig. 4.32).

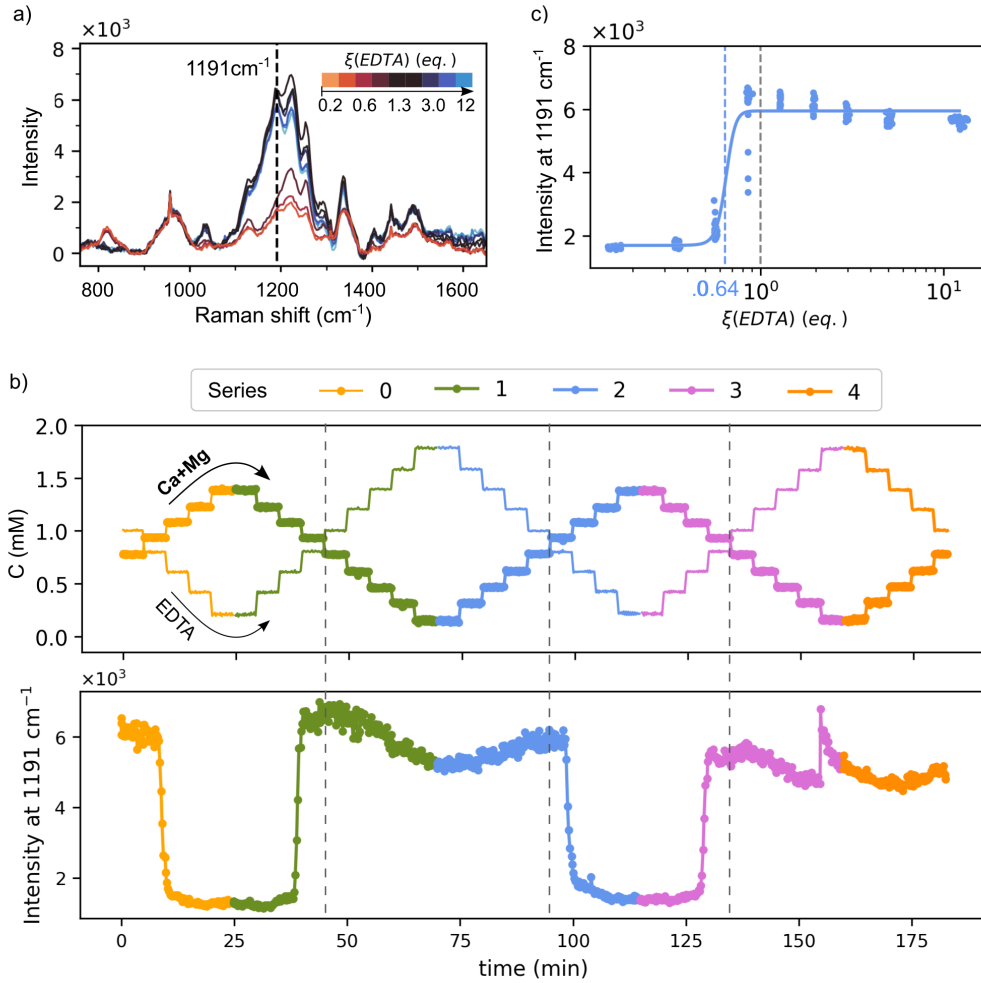


Figure 4.4: Evian titration results acquired under  $638\text{ nm}$  irradiation (experiment *MD162\_14h01* in Tab. 4.3). Its corresponding pressure and flowrate trajectories are shown in Fig. 4.3). a) Baseline-corrected SERS spectra over one full titration series (the 2nd series, blue data in panel b). For clarity, only the 10th spectrum of each step (the middle one) is shown, resulting in 9 spectra in total. The dashed line marks the position of the highest peak at  $1191\text{ cm}^{-1}$ . Legend: number of EDTA equivalents,  $\xi(\text{EDTA})$  in Eq. 4.6). b) The intensity of the  $1191\text{ cm}^{-1}$  peak over time throughout the whole experiment (upper panel) and the corresponding titrant-analyte concentrations (bottom panel). Each series was colored differently. The thick trajectory in the bottom panel is the concentration of the total  $\text{Ca}^{2+}$  and  $\text{Mg}^{2+}$ . In the same panel, the thin trajectory corresponds to the concentration of EDTA. The cross section point of the two trajectories is the equivalence. Each series except the 4th one has a jump in the signal which is the signature of the titration endpoint. c) Intensity of the  $1191\text{ cm}^{-1}$  peak within the 2nd series as a function of number of EDTA equivalents. Dots: experimental data. Solid lines: sigmoidal fits. The gray dashed line: the theoretical equivalence point. Blue dashed line: the experimental endpoint, which is the maximum of the 1st derivative of the fitting, at 0.64. The titration curves of the other series are plotted overlapped in Fig. 4.30.

The rather poor trueness could reflect an unsuitable choice of complexometric indicator. For instance, when the indicator over metal ratio is too high, the endpoint occurs significantly before the equivalence. To verify this assumption, we ran speciation simulations involving only the metal ions, titrant and indicator (Fig. 4.29). They show that with the compositions explored over our titrations, the endpoint precedes the equivalence by at most 4%. Therefore, unsuitable choice of indicator can be ruled out. Insufficient resolution around the equivalence can also degrade the trueness. Indeed, when performing classic colorimetric titrations with a burette, one increases the resolution of the volumetric additions close to the expected equivalence to pinpoint the endpoint with precision. Therefore, the platform was relaunched with a pressure increment half of the initial one,  $\Delta P = 10 \text{ mbar}$  (Fig. 4.33). Each titration series comprised 19 steps, in which 7 steps are in the range from 0.5 to 2 eq., compared to 4 steps within this range at  $\Delta P = 20 \text{ mbar}$  increments. The duration of each pressure step was lowered from 5 min to 2 min to prevent doubling the duration of each titration series. Eight spectra were recorded per step instead of twenty, without increasing of the dispersion of the data points in the titration plot. The mean trueness over 4 consecutive titration series increased to 78%. A higher trueness could certainly be obtained by programming a pressure sweep with lower pressure increments close to the equivalence point. This would only require software development, which was considered beyond the scope of the present demonstration.

### 4.2.8 Volvic and contrex titrations

The robustness of the platform was investigated further by titrating Volvic and Contrex, which have hardnesses 5 times smaller and 5 times larger than Evian respectively. The molarity of the titrants was adapted to be roughly match that of the total calcium and magnesium ions, so that equivalence is crossed around the middle of a titration series (see Fig. 4.6 for details of the compositions of measurement samples). Again, the pH of measurement samples having extremal compositions were tested in cuvettes to check that the pH did not deviate too much from the recommended value of 10. Volvic measurement samples had a suitable pH range of 9.8 – 10.3. For Contrex, the pH ranged from 8.4 to 10.6. However, according to speciation simulations (Fig. 4.38), the lowest value of the pH did not significantly shift the speciation switching point of the indicator compared to the more optimal pH value of 10.6. This is most probably because the indicator is in very strong default compared to magnesium ions, which forces the coordination reaction despite the unfavourable pH.

Three and two independent launches of the platform were run for Volvic and Contrex respectively, each with a pressure increment of  $\Delta P = 20 \text{ mbar}$  and variable step durations from 2 to 5 minutes (sections 4.18, 4.19). Each launch gave rise to periodic sigmoidal patterns of the highest intensity peak at  $1191 \text{ cm}^{-1}$ . After lag time adjustment, they lead to canonical titration plots. That of Volvic was smoother

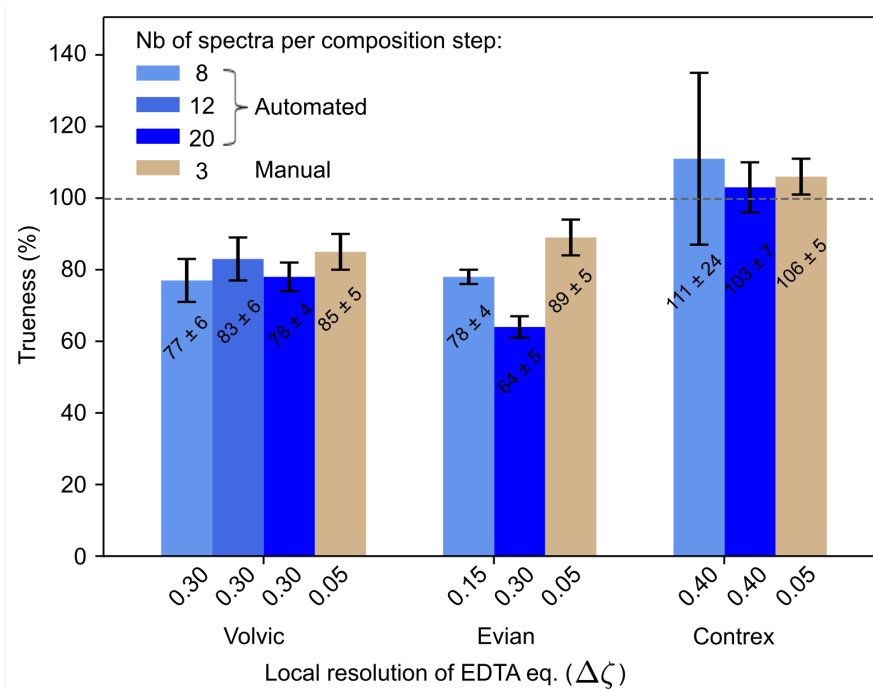


Figure 4.5: Overview of the titration trueness from the microfluidic systems (blue bars) in comparison to ones carried in cuvettes (brown bars).  $\Delta\xi$  is the distance between the two consecutive compositions in terms of EDTA equivalents near the endpoint. It refers to the local resolution of the titration curve near the endpoint.

than that of Evian, consistently with the indicator being introduced in larger proportion (0.14% of alkaline earth content near the equivalence) than for Evian (0.03% of alkaline earth content near the equivalence) and as expected from the titration simulations. The mean trueness was  $79 \pm 6\%$  (three independent launches, each comprising 4 titration series,  $N = 3, n = 4$ ) for Volvic, and  $107 \pm 17\%$  ( $N = 2, n = 5$ ) for Contrex (Fig. 4.5). These figures are close to what we observed when running the titrations manually in cuvettes. Together with the Evian titration data, these results evidence the robustness of the automated platform for titrating water samples from soft to very hard.

#### 4.2.9 Critical reviewing of the analytical performances of platform

For Evian and Volvic, the trueness of the automated titrations is lower than the ones determined from manually acquired titrations series (Fig. 4.5). The effect is only marginal for Volvic and more pronounced for Evian. We attributed the moderate trueness of  $69 \pm 7\%$  ( $N=3, n=3$ ) observed for Evian under  $\Delta P = 20 \text{ mbar}$  pressure increment to an insufficient density of compositional steps around the equivalence. Indeed, in those experiments, the switching range is only covered by two compositional points separated by  $\Delta\xi = 0.3 \text{ eq.}$ , six times the local resolution near the endpoint of the manual titration series. At

that same resolution  $\Delta\xi = 0.3$  eq., incidentally, three compositional steps were explored within the switching range of the SERS signal in the Volvic automated titrations and therefore, the trueness was not as impaired as for Evian compared to the manual titrations. Upon increasing the resolution about the endpoint using a smaller pressure increment  $\Delta P = 10$  mbar, the absolute trueness of the automated titration of Evian increased by 10%. The resolution could in principle be furthered lowered. Because the flow rate relative standard deviation on each plateau is  $\delta Q = 0.33$   $\mu\text{L}/\text{min}$ , the minimal flow rate step should be 3 times of that,  $\Delta Q_{\text{min}} = 1$   $\mu\text{L}/\text{min}$ , to be able to differentiate 2 compositions. This flow rate step corresponds to  $\Delta P_{\text{min}} \sim 5$  mbar, giving the minimal resolution of  $\Delta\xi_{\text{min}} = 0.075$  eq.

From the various runs of automated Volvic titrations using different step durations, it appears that the trueness is not significantly affected by the number of spectra recorded per step, at least as far as this number is within 8 to 20 spectra. Therefore, a step duration of 2 min, corresponding to 8 spectra per step, could be imposed to save time when increasing the resolution about the endpoint without altering the analytical performances.

### 4.2.10 Operating cost

Overall, the use of the automated platform saves a significant amount of time, effort, and consumables.

**Reagent consumption.** In manual protocol in cuvettes, the reagent cost is 0.405€/spectrum, included the chemical purchase and labour work for preparing stock solutions (see section 4.20.3 for details of calculations). In our previous manual protocol featuring a resolution close to the endpoint of  $\Delta\xi = 0.05$  eq., each measurement of 3 replicates, 18 increments corresponding to 54 spectra, it costs about 22 €/measurement. In a typical automated microfluidic run, the reagent cost is 0.005 €/spectrum, which is 81 times less than in cuvette (see section 4.20.3 for details of calculations). For a shortest measurement that includes one complete series (10 increments with the endpoint resolutions of about  $\Delta\xi = 0.30$ , 8 spectra/increment, corresponding to 80 spectra), it costs 0.4€/measurement that gives comparable trueness to that in manual protocol. Therefore, using the platform to conduct a titration measurement lowers the cost of feedstock consumption 55 folds.

### Costs of preparation of measurement samples and acquisition of spectra.

In our previous manual version, one titration measurement including 18 step titration series with three replicates, it takes 120 min of labour work, including preparing measurement samples and spectral acquisition (see section 4.20.5 for details of calculations). For microfluidic platform, it takes a little less than

30 minutes of labour work to set up to set up the platform, namely, to plug the reservoirs, to mount a new chip and a new glass capillary, and to prime the system so as to pinpoint initial pressure inputs. After that, the platform run the titration automatically without any labour need. Therefore, the longer using the microfluidic platform, the more gaining in labour time by at least 4 times.

**Instrumental costs.** The platform comprises several pieces of instrument: the Raman optical set-up (including laser, spectrometer, Raman probe, optical fibers, and sample holder), the pneumatic injection apparatus, the flowrate sensors, the imaging set-up (microscope and camera). In total, the instrumental cost of the platform is about 33 k€ (section 4.20.7). This cost does not result from any minimization attempt and rather reflects the equipments already available in the lab. It could be shrunked by using a lower resolution spectrometer, which would still enable seeing the intensity switch of the SERS signal of the indicator, by using a single 8-port pneumatic device instead of two 4-port ones and by downgrading the droplet imaging module.

Overall, the operating costs amounts to 10 – 14 € per analysis. The automation has reduced the cost by more than 5 times compared to the manual protocol that costs 58 €/analysis. Moreover, this compares favourably with the golden standard for analysing alkaline earth content: an ICP-AES analysis costs 23 € per sample at the French national center for scientific research (CNRS) analysis facility. Moreover, these operating costs relate to a platform that costs about 30 – 50% of the price of an ICP-AES spectrometer, without any attempt at price optimization, and does not need as much qualification to operate. Indeed, ICP-OES analysis require using compressed argon cylinders and concentrated strong acids, while our platform used compressed air and a mild reagent. Although the instrumental cost of our platform is presently too high for large scale deployment in low-income countries, it offers a viable alternative to build analytical facilities where there are none. It could also generate the interest of local public agencies or private sector stakeholders in water in middle- and high-income countries to empower the enforcement of water quality regulations.

### 4.3 Conclusion

A microfluidic platform has been developed to carry out SERS-based complexometric titrations automatically. The platform continuously and autonomously performed water hardness measurements for three mineral waters ranging from soft to very hard, and it did reliably on each of the 8 runs we launched. Overall, the platform provided mean trueness of 82% and precision 7%. For each launch, the trueness varies from 64% to 111% with their relative standard deviation of 17%. The trueness was improved with a higher resolution of the titration around the equivalence. Compared to the manual SERS titrations of water hardness demonstrated in our

previous work, these automated titrations brought several advantages. The automated preparation of the measurement samples as droplets lowered the fluctuations of the SERS signals by one order of magnitude, meanwhile lowering the preparation time per acquired spectrum by at least 4 times and the consumption of reagents by a factor 82. Moreover, the platform successfully ran for 2.5 hours without any intervention from the operator, thereby demonstrating its ability to perform continuous measurements. The platform is approachable for non-experts after just a few hours of training and less than 30 minutes for setting up. Its analytical performances and cost-effectiveness compared to the golden analytical standards for water hardness determination make it a credible opportunity for setting up analytical facilities where budgets cannot meet monitoring demands. Finally, we believe we provided a practical and realistic demonstration of how to turn SERS into a proper routine analysis method.

### 4.4 Experimental section

**Composition of feedstocks.** Each experimental launch in the microfluidic platform requires five stocks: 1) water sample, 2) titrant EDTA, 3) NPs, 4) a mixture of PEG, PEI and indicator EBT (EBT-PEI-PEG), and 5) Mineral oil. The later three stocks (stocks 3, 4 and 5) were the same for every experiment. The NP stock had the assumed Ag concentration as colloidal nanoparticles of 2.4 *mM*. Stock (4) is the mixture of PEG 5 %wt, PEI 100  $\mu\text{M}$ , EBT 1.65  $\mu\text{M}$  in BRB 20 *mM* at pH 10.5. Mineral oil in stock (5) was directly used as received. Three water samples, Volvic, Evian and Contrex, with the total calcium and magnesium ions are 0.6 *mM*, 3.1 *mM* and 14.7 *mM* were analyzed without pH adjustment. The molarity of EDTA in the titrant stock was adapted for each water sample according to the previous total divalent metal ions in each water sample, 0.81, 3.1 and 14.7 *mM*, respectively. The schematic of the set of stocks is shown in Fig. 4.5.3. Details about the composition and preparation of the feedstocks can be found in section 4.5.2.

**Microfluidic chip fabrication.** The microfluidic chip design was created in Autocad 2018. Then, its pattern was milled on a PMMA plate using a Minitch micro-miller to obtain a master mold. The disposable PDMS (polydimethylsiloxane)-on-glass chips were repeatedly fabricated. The PDMS elastomer base and curing agent were mixed in a weight ratio of 10:1, poured onto the PMMA master mold, degassed, and cured overnight at 55°C. The solidified PDMS wad was then peeled off, punched inlet holes, and sealed on a glass slide after plasma treatment. Finally, the microfluidic chip was gone through a wet-phase hydrophobic silanization. The detailed protocol for the microfluidic chip fabrication is also described in section 4.6. The full characteristics of the microfluidic chip and tubing can be found in Fig. 4.11. The images of the liquid flows in different segments of the microfluidic chip are shown in Fig. 4.12.

**Droplets characterization.** For estimations of droplets' volume, speed and aqueous/oil segment ratio, the camera was set to focus on the channel segment near the outlet of the microfluidic chip to record a video of about 1 minute. Three droplet dimensions (height, width and length) were extracted from the video frames for droplet volume calculation. In eight videos corresponding to eight independent launches, three droplets in each video were measured. We obtained the average volume of  $V_{\text{droplets}} = 2.51 \pm 0.17 \mu\text{l}$  (N=8, n=3). The droplet speed is calculated from the displacement of the front and the back interface of the droplet over time. About 20 droplets with 40 speeds were measured and averaged in each video. Over eight independent launches, the average droplet speed is  $4 \pm 0.1 \text{ mm/s}$  (N=8, n=40). The aqueous/oil segment ratio was calculated as the ratio of effective lengths of aqueous and oil segments,  $\delta_{\text{aqueous/oil}} = 0.88 \pm 0.05$  (N=8, n=3). The detail of these characterizations are described in section 4.9.

**Custom-built optical measurement chamber.** A commercial 4-window sample holder was tailored for microfluidic measurements. One window was equipped with a combined excitation and collection Raman probe. Two parallel windows were shut but for two pinholes through which a glass capillary was nested, with the axis of the capillary crossing the optical path of the laser beam right at its focal point. The remaining window was sealed off. The inlet of the capillary was connected to the outlet tubing from the chip to receive droplets for SERS acquisition. The outlet was connected to another piece of tubing to transport droplets to the waste bin. The detail of this setup is described in section 4.10.



# Supplementary information for chapter 4

## Contents

---

<b>4.5 Feedstock preparation</b> . . . . .	<b>62</b>
4.5.1 Chemicals . . . . .	62
4.5.2 Protocol for stock preparation . . . . .	62
4.5.3 Stock selection for microfluidic launches . . . . .	64
<b>4.6 Microfluidic chip fabrication</b> . . . . .	<b>64</b>
<b>4.7 Full microfluidic platform set-up</b> . . . . .	<b>67</b>
<b>4.8 Imaging the flows in the microfluidic chip</b> . . . . .	<b>70</b>
<b>4.9 Droplet characterization</b> . . . . .	<b>72</b>
4.9.1 Droplet volume . . . . .	72
4.9.2 Droplet speed . . . . .	73
4.9.3 Aqueous/oil segment ratio . . . . .	73
<b>4.10 SERS measurement set-up</b> . . . . .	<b>74</b>
<b>4.11 Comparison between spectra acquired in cuvettes and in-line in droplets</b> . . . . .	<b>76</b>
4.11.1 Preparation of test cuvettes and microfluidic set-up for spectral and pH check. . . . .	76
<b>4.12 SERS signal reproducibility</b> . . . . .	<b>78</b>
<b>4.13 Python program &amp; automated experiment procedure description</b> . . . . .	<b>78</b>
<b>4.14 Estimation of lag time from fluidic circuit</b> . . . . .	<b>81</b>
<b>4.15 Data processing</b> . . . . .	<b>84</b>
4.15.1 The raw data structure . . . . .	84
4.15.2 Baseline correction . . . . .	84
4.15.3 Lag time estimation by metrical calibration method . . . . .	85
4.15.4 Lag time correction for spectral data . . . . .	88
4.15.5 Endpoint identification . . . . .	88
<b>4.16 Comparison between the microfluidic system and manual protocol</b> . . . . .	<b>89</b>
<b>4.17 Evian titrations</b> . . . . .	<b>90</b>
<b>4.18 Volvic titrations</b> . . . . .	<b>95</b>
<b>4.19 Contrex titrations</b> . . . . .	<b>99</b>
<b>4.20 Estimation of cost of the platform</b> . . . . .	<b>103</b>
4.20.1 Cost per liter of chemical stock solutions . . . . .	103
4.20.2 Labour for the preparation of the stock solutions . . . . .	103

4.20.3 Reagent cost per spectrum . . . . .	104
4.20.4 Cost for microfluidic chip fabrication . . . . .	104
4.20.5 Time and costs of preparation of measurement samples and acquisition of spectra . . . . .	105
4.20.6 Total cost per spectrum . . . . .	105
4.20.7 Instrument cost for the microfluidic platform . . . . .	106

---

## 4.5 Feedstock preparation

### 4.5.1 Chemicals

Ethylenediamine tetraacetic acid, di sodium salt dihydrate (99% purity as per titration, CAS 6381-92-6r), Eriochrome Black T (Reagent specification as per European Pharmacopoeia, #CAS 1787-61-7), polyethylene glycol (MW 20 kDa, BioUltra grade, CAS 25322-68-3), polyethyleneimine (branched, MW 25 kDa by light scattering, 13000 – 18000 mPa.s viscosity, CAS 9002-98-6), silver nitrate (ACS reagent, >99.0%, CAS 7761-88-8), sodium citrate tribasic dihydrate (p.a.,  $\geq 99.0\%$ , CAS 6132-04-3) and tetrasodium borate (99%, BioUltra, CAS1330-43-4) were purchased from Aldrich. Glacial acetic acid (100%, NormaPur, CAS 64-19-7) and disodium hydrogen phosphate dodecahydrate (102% assay, NormaPur, CAS 7558-79-4) were purchased from VWR. Mineral oil (light oil, Sigma aldrich CAS 8042-47-5). All pH adjustments were performed using a 1N sodium hydroxide standardised solution from Aldrich. All chemicals were used as received without further purification. Evian, Volvic and Contrex waters were stocked as 1.5 L bottles from a supermarket.

### 4.5.2 Protocol for stock preparation

All stock solutions were prepared using volumetric glassware (glass pipettes and flask) and scales with a 1 mg or 0.1 mg precision under our experimental conditions.

**Britton and Robinson buffer (BRB).** An equimolar mixture of acetic, phosphoric, and boric acid 40 mM in boron at pH 8 was prepared from glacial acetic acid, disodium hydrogen phosphate and sodium tetraborate. This mother buffer was then diluted to give rise to BRB 20 mM and BRB 4 mM in boron. Then they were adjusted to pH 10.5 using NaOH 1N.

**PEI solution.** 43 mg PEI was dissolved in 10 mL BRB 4 mM pH 8 to give a 10 mM (monomeric unit) stock.

**EBT solution.** 23.3 mg of EBT were dissolved in 10 mL ultrapure water to give a 5.05 mM stock.

**EDTA solutions.** 379 mg EDTA disodium salt were introduced in a volumetric flask and dissolved in approximately 250 mL BRB 4 mM pH 10.5. The pH was monitored and adjusted to 10.5 through addition of approximately 1.7 mL NaOH 1 N. The flask was topped up to the mark using BRB 4 mM pH 10.5. The pH can drift by  $\sim 2\%$  overnight. On the day of SERS acquisition, the pH was adjusted to 10.5 using NaOH 1N. The final EDTA titer was 4.06 mM. Following the same protocol, 1861 mg of EDTA disodium salt were introduced in a 250 mL volumetric flask along with 250 mL BRB 4 mM pH 10.5 and approximately 8 mL of a NaOH 1N. The pH was measured and adjusted to 10.5 before topping up the flask to the mark with BRB 4 mM pH 10.5. Overnight, the pH had dropped to 10.35 and was adjusted back to 10.5 to give a 19.97 mM stock. The 4.06 mM solution was diluted 5 times with BRB 4 mM pH 10.5 to give a 0.81 mM solution.

**Mixture of EBT-PEI-PEG.** First, 2 g of PEG 20 kDa was dissolved in 40 mL buffer BRB 20 mM pH 10.5 to get PEG 5 %wt. Then, 420  $\mu$ L PEI 10 mM and 14  $\mu$ L EBT 5.05 mM was mixed in turn with the above PEG solution. We got the final mixture of PEG 5 %wt, PEI 100  $\mu$ M, EBT 1.65  $\mu$ M in BRB 20 mM at pH 10.5.

#### Synthesis of Lee-Meisel silver nanoparticles.

*Apparatus for the synthesis process.* A 250 mL triple-neck round bottom flask was washed using 100 mL (1 volume) aqua regia (a mixture of 80 mL hydrochloric acid (37 %wt) and 20 mL nitric acid (69 %wt)) prior to synthesis, rinsed with 10 equivalent volumes of miliQ water, then with 0.5 volume of 70 % ethanol afterwards and finally dried overnight in a 55 °C stove. The flask was nested within a silicon oil bath on top of a magnetic heating plate. The temperature was controlled through a thermocouple inserted in the oil bath and a temperature controller. The flask was equipped with an oval stir bar and a condenser.

*Synthesis.* To synthesize 100 mL silver nanoparticle 1.2 mM Ag, 20 mg silver nitrate were inserted into the flask along with 100 mL ultrapure water. The solution was brought to reflux under stirring using a 130 °C set point for the oil bath. 2 mL of trisodium citrate 34.0 mM were quickly injected using a syringe into the reaction mixture through one of the side necks. The temperature was set and maintained at 100°C for 1 hour. Over time, the solution turns yellow then grey to reach a final milky green-grey colour. After cooling, the solution is stored in a closed glass bottle at 2-5°C for months and used assuming a concentration of 1.2 mM Ag concentration as colloidal nanoparticles (assuming a 100 % reaction yield).

*Removal of surface citrates.* In order to get rid of the citrate residuals and obtain more active surfaces, the Lei-Meisel silver NPs synthesized previously were supplemented with sodium chloride at a final concentration of 0.2 mM and incubated for 10 minutes. The solution was then aliquoted as 12.5 ml fractions into 15 mL falcon tubes, centrifuged at 6000 rpm for 25min on a Hettich EBA

21 centrifuge. The supernatant was discarded to leave a 0.5 mL NP-rich fraction which was resuspended in ultrapure water to reach half of the initial volume, and homogenized using a vortex mixer and then by ultrasonication for 4 min. All aliquots were then merged into a single stock which was stored in a closed glass bottle at 2-5°C. The assumed Ag concentration as colloidal nanoparticles is 2.4 mM. At most, the free citrate concentration is 0.03 mM and the chloride concentration is 0.2  $\mu$ M. The NPs are ideal to be used after at least one night of aging and up to a few days stored in these conditions.

### 4.5.3 Stock selection for microfluidic launches

Each experiment launch in microfluidic platform requires 5 stocks: 1) water sample, 2) titrant, 3) NPs, 4) a mixture of PEG, PEI and indicator EBT (EBT-PEI-PEG), and 5) Oil. The later three stocks (stocks 3, 4 and 5) are the same for every experiment. Three water samples, Volvic, Evian and Contrex with the total calcium and magnesium ions are 0.6 mM, 3.1 mM and 14.7 mM respectively were analyzed. The molarity of the titrant EDTA was adapted for each water sample accordingly to its total Calcium and Magnesium ions as shown in Fig. 4.6.

Sets of five stock solutions			
① Water sample	Evian ( $C_{Ca+Mg} = 3.1$ mM)	or	Volvic ( $C_{Ca+Mg} = 0.6$ mM)
	EDTA 4.06 mM in BRB 4 mM pH 10.5		EDTA 0.81 mM in BRB 4 mM pH 10.5
			Contrex ( $C_{Ca+Mg} = 14.7$ mM)
② Titrant			EDTA 19.97 mM in BRB 4 mM pH 10.5
③ NPs	Lee-Meisel Ag Cl-NPs 2.4 mM		
④ EBT-PEI-PEG	Mixture of PEG 5 %wt, PEI 100 mM, EBT 1.65 $\mu$ M in BRB 20 mM, pH 10.5		
⑤ Oil	Mineral oil		

Figure 4.6: Schematic of the 5 stock solutions for microfluidic titration experiments. For each water sample (Evian, Volvic and Contrex), the molarity of titrant was adapted accordingly to its total Calcium and Magnesium ions in that water sample.

## 4.6 Microfluidic chip fabrication

**Design.** The main steps of the microfluidic chip fabrication are shown in Fig 4.7. First, the microfluidic chip was designed in AutoCAD 2018. The chip has a uniform height of 1000  $\mu$ m; its 2D configuration and dimensions are detailed in Fig 4.8a. Then, the design in 3D was exported to STL file to be compatible with the micro-miller machine (MiniTech, model Mini-Mill/3).

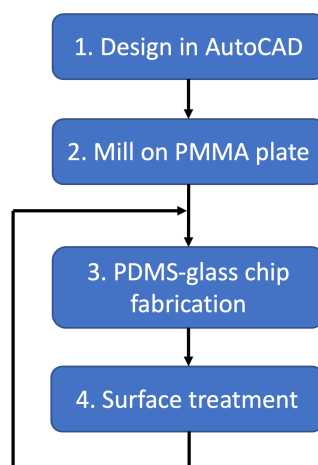


Figure 4.7: Main steps of the microfluidic chip fabrication. Steps 1 and 2 were done once. Steps 3 and 4 were repeated over for every disposal PDMS-glass chip.

**Milling of the master mold.** Then, the micro-miller was set up to mill the designed pattern on a polymethyl methacrylate (PMMA) plate using a drill bit of 500  $\mu\text{m}$  in diameter. The PMMA plate had already in advance the pool of 5 mm depth which was served as the container for polymer reagents in later steps, Fig 4.8c. The PMMA plate after milling is called the master mold. This mold was fabricated once and re-used as many times as needed to fabricate the disposable microfluidic chips. The photograph of the master mold is in Fig 4.8d.

**Chemicals.** Sylgard 184 silicone elastomer kit from DOW, including elastomer base and curing agent. Trichloro(octadecyl)silane from Sigma-Aldrich, CAS 112-04-9.

**Molding.** Next, disposal polydimethylsiloxane (PDMS)-on-glass chips were fabricated. First, a mixture of PDMS base and curing agent with a weight ratio of 10:1 was poured into the pool in the master mold. The PDMS in the mold was degassed in a vacuum chamber and then cured in an oven at 65°C overnight. The next day, the PDMS was peeled off the mold, and punched holes in the inlets and the outlet using the puncher of 1.2 mm in diameter. Then this PDMS plate was sealed on the glass slide 76x26x1 mm (Marienfeld, Germany) after a plasma activation for 5 minutes using Harrick plasma generator. Note that before bonding, to increase tightness, the glass slides were cleaned thoroughly three times in turn with ultra-pure water, ETOH 70%, and ultra-pure water under ultrasonication, then got dried in the oven at 55°C overnight. After sealing, the microfluidic chip was cured on the oven at 55°C for at least 1 hour.

**Hydrophobization of the channels.** Finally, the chips were gone through the hydrophobic surface treatment for the main channel from the inlet 4 to the outlet

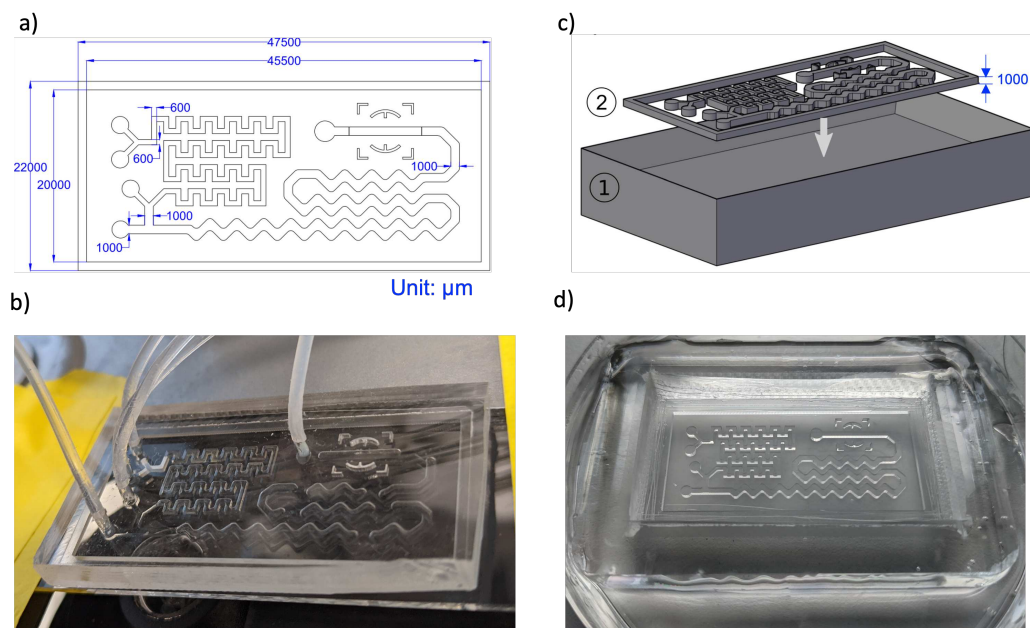


Figure 4.8: a) The microfluidic chip design with its 2D dimension and b) its photograph. c) 3D microfluidic chip is milled on top of a PMMA plate that had a containing pool and d) its photograph.

5, Fig. 4.9a. To do so, the inlets 1 to 3 were closed by using a piece of tubing in which one edge was sealed. For chemical injections, the inlet 4 was connected to a syringe 1mL using needle G21 and tubing. The outlet 5 was extended through tubing to transport the chemicals to the waste bin. All the tubing used in this step was the liquid flows Tygon tubing 0.02" ID x 0.06" OD. This is because it fits the microfluidic chip's inlets, and it is flexible for inserting the syringe needle. The following steps for chemical injections were as follows:

- (i) Filled up the channels of the chip with NaOH 1M for 24 hours. To avoid the evaporation of NaOH solution during a whole day long, the chips stayed in a closed chamber with a saturated humidity ambient (Fig. 4.9b).
- (ii) In the next day, flushed NaOH away by air, ultra-pure water, air, isopropanol, and air in turn.
- (iii) Incubated the channels with Trichloro(octadecyl)silane 2.5% *v/v* in isopropanol for 15 minutes.
- (iv) Flushed the channels with air, isopropanol, air, ultra-pure water, and air in turn.
- (v) Dried the chip in the oven at 55°C overnight. Fig. 4.8b shows a photograph of the final fabricated microfluidic chip.

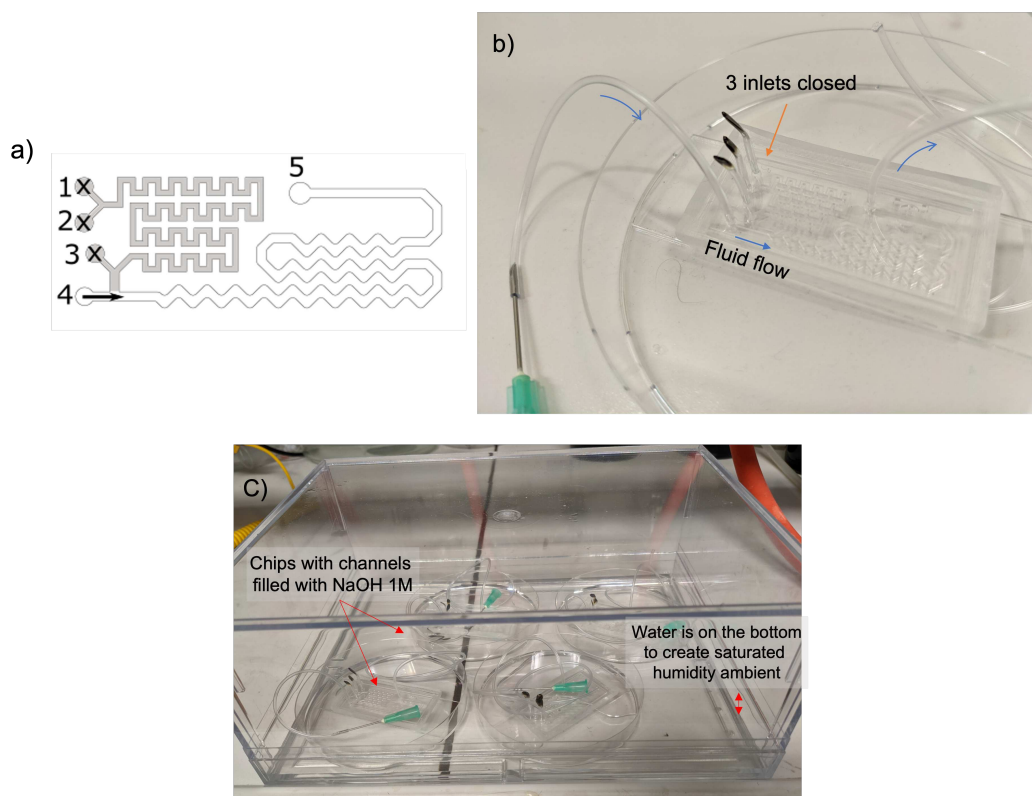


Figure 4.9: Preparation for the surface treatment for microfluidic chips a) in schematic and b) in reality. Three inlets 1 to 3 were closed using a piece of tubing that sealed on one edge, the fluids therefore flow along the arrows from the inlet 4 to the outlet 5. This is the segment needed to become hydrophobic. (c) The setup for NaOH incubation: to prevent the evaporation of NaOH for 24 hours of incubation, the chips that were filled with NaOH 1M were kept inside a close chamber where water was put on the bottom to create a saturated humidity ambient.

## 4.7 Full microfluidic platform set-up

Five stock solutions were contained in 5 glass bottles GL45 100 mL. Each bottle was closed by a microfluidic cap with two threaded ports; one port was connected with compressed air input, and the other port was connected to tubing prolonged until the bottom of the bottle to suck fluid. Two pressure controllers (Fluigent MFCS<sup>TM</sup>-EZ) with 4 outlets in each were used to feed the fluids from 5 bottle reservoirs into the microfluidic system. Four flow rate sensors were plugged between the reservoirs and the microfluidic chip's inlets. Here, due to our instrument availability limitation, we used three Fluigent Flow Unit size M (range  $0 \pm 80 \mu\text{L}/\text{min}$ ) for measuring flow rates of water sample ( $Q_S$ ), titrant ( $Q_T$ ) and EBT-PEI-PEG mixture ( $Q_{\text{EBT-PEI-PEG}}$ ); and one Fluigent Flow Unit size L (range  $0 \pm 1 \text{ mL}/\text{min}$ ) for measuring the flow rates of Ag NPs ( $Q_{\text{NPs}}$ ). The outlet of the chip was extended to a 130-cm-long tubing to generate about 5 minutes of

## 68 Chapter 4. Microfluidic platform for SERS-complexometric titration

incubation time. This tubing was connected to a glass capillary for measurement in the optical chamber. See Fig. 4.10 for the photograph of the whole platform in the laboratory and Fig. 4.11 for the characteristics of the tubing network such as the length, internal and external diameter (ID, OD).

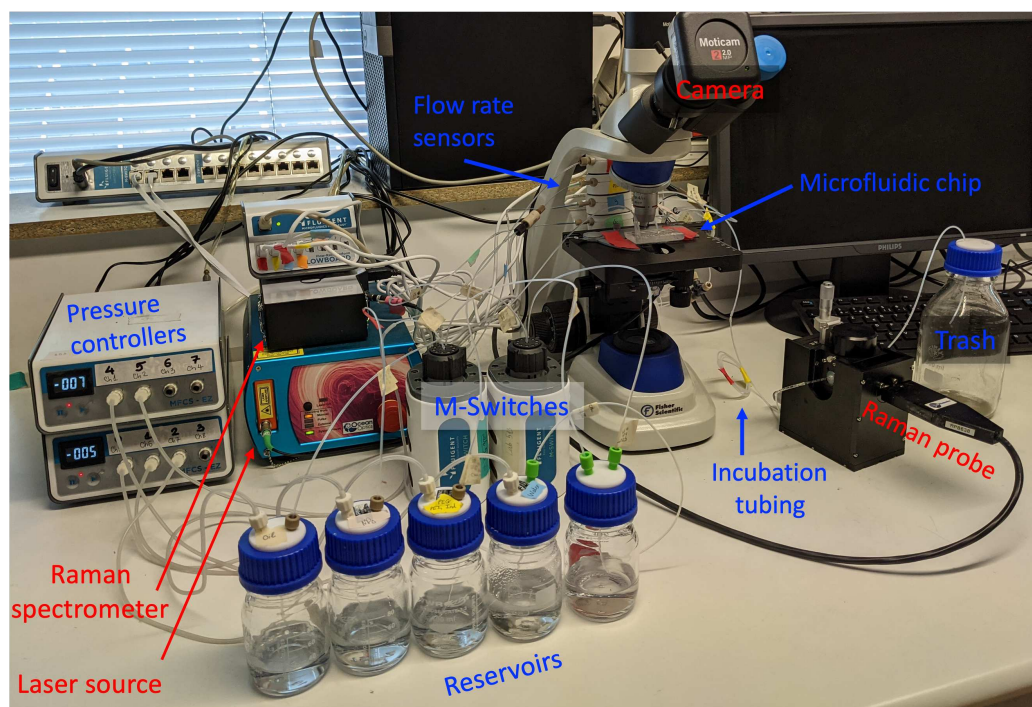


Figure 4.10: Photograph of the full microfluidic system in the laboratory. The fluidic components are labeled in blue, and the optical components are in red. Note that 2 M-switches, electric manifolds that can accommodate 10 different reservoirs and select one of them to connect to the system, were integrated but only a single reservoir was plugged, and the selection mode was fixed at this reservoir position in all experiments in this work.

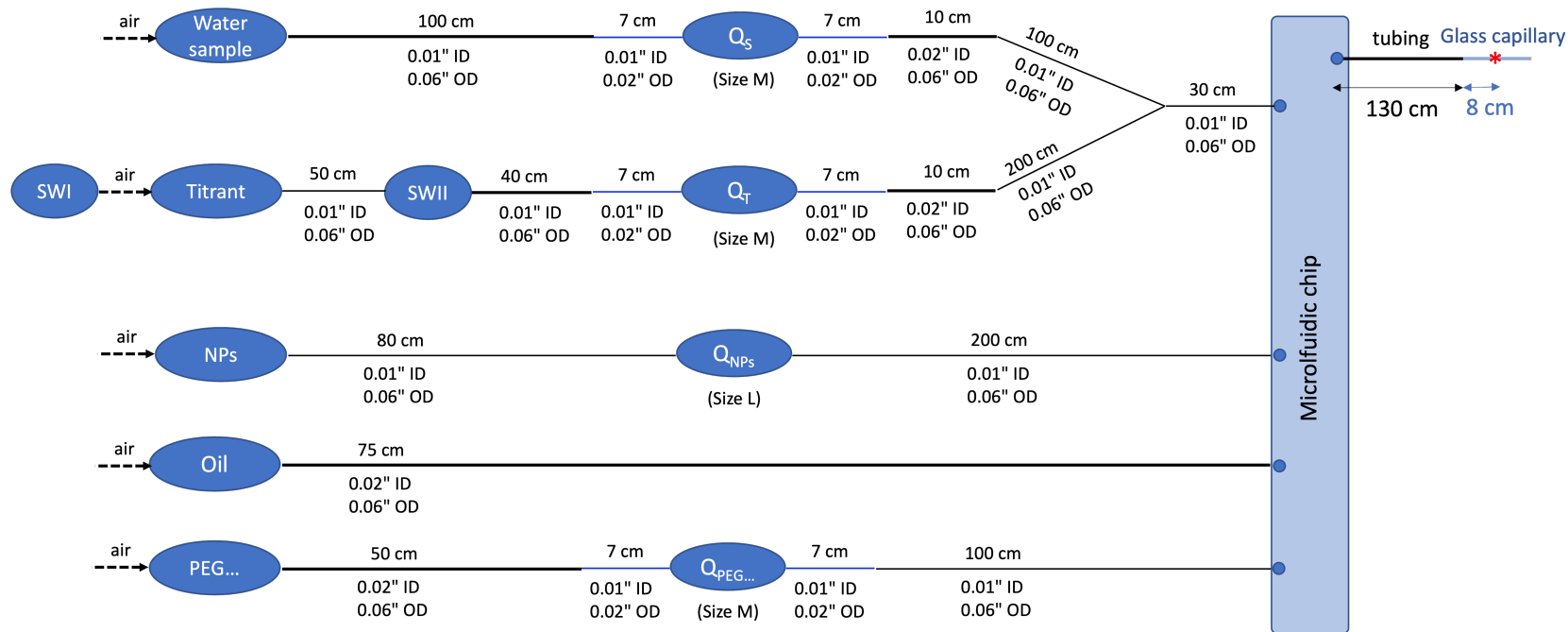


Figure 4.11: Schematic of the full connection of the microfluidic system together with details of the tubing characteristics (length, internal and external diameter (ID, OD)).

## 4.8 Imaging the flows in the microfluidic chip

The flows of fluids in both continuous and dispersed phases in the microfluidic chip were monitored using a 4x objective lens. Fig. 4.12 shows different channel segments of the microfluidic chip. Frames number 1 to 5 show the mixing progression of NPs (grey) with a water sample and EDTA (transparent) from the entering Y-junction to the second Y-junction. In one branch of the second Y-junction, the mixture, called NPs-Water-EDTA, was well mixed and ready to merge with the mixture of EBT-PEG-PEI in another branch. Once EBT-PEG-PEI and NPs-Water-EDTA met, a droplet was quickly formed at the T-junction. Frame 5 shows the droplet formation process. First, the whole aqueous mixture (EBT-PEG-PEI and NPs-Water-EDTA) was injected into a perpendicular stream of oil. It grew up at this T-junction and then was bent due to the push from the oil flow. Quickly later, it obstructed the channel and inhibited the oil's flow. The oil kept flowing and pushed the interface between the two immiscible fluids, deformed it to a neck shape, and then pinched off into a droplet. After being formed, EBT-PEG-PEI and NPs-Water-EDTA were not yet well mixed; we still see the stripe pattern within the droplet in frame 6. While the droplet travelled through the second serpentine mixer, the liquid streams were continuously stretched and folded. In the segment at the end of the microfluidic chip, frame 7, the final mixture was presented in a grey colour with multiple fine stripes at a closer look, showing the mixing improvement. Later, the droplet got out of the chip and started the incubation period of about 5 minutes in a 130-cm-long tubing.

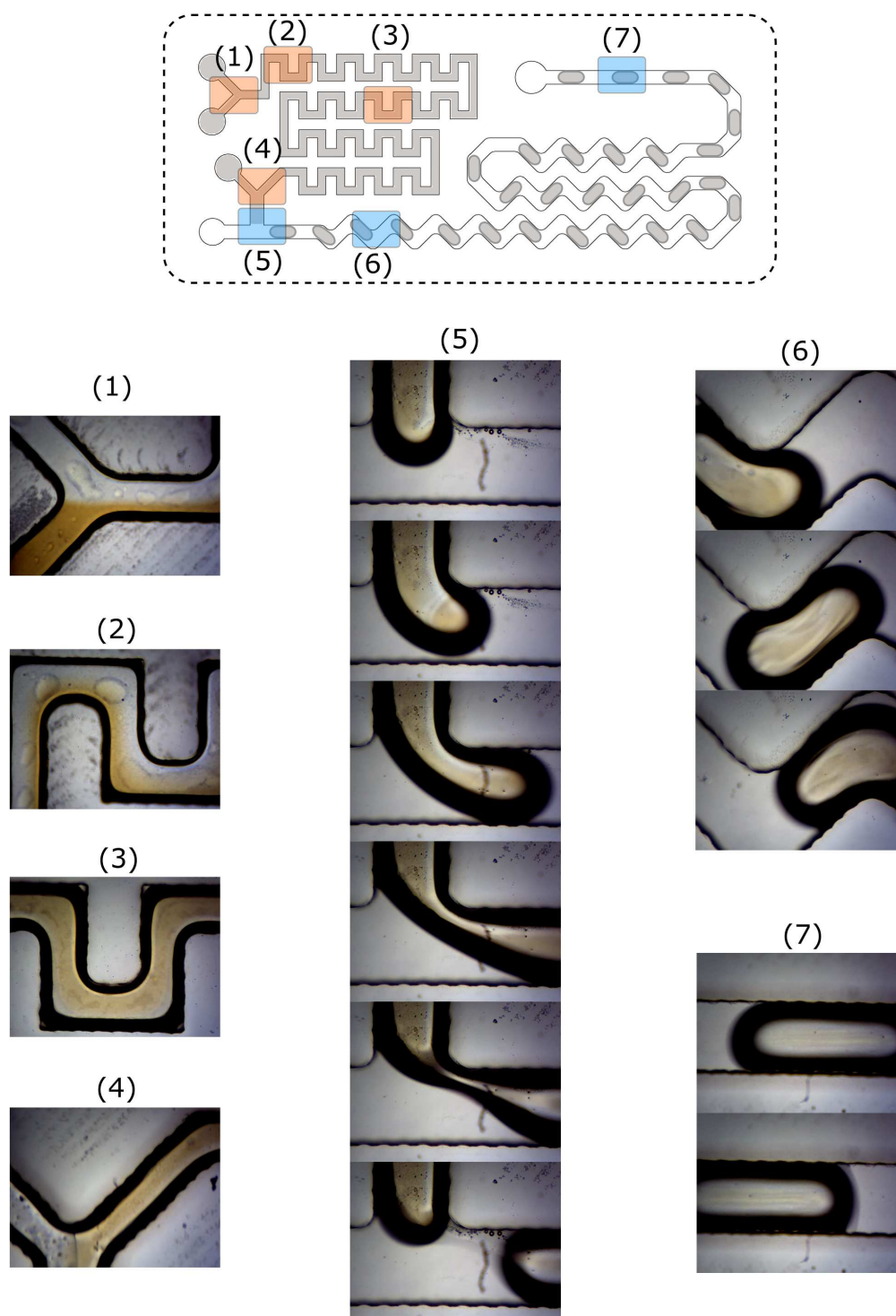


Figure 4.12: Images of different channel segments in the microfluidic chip during the titration experiment. Frames (4) and (7) evidence that mixing after passing through the square-wave serpentine and the round serpentine leads to homogeneous water phases.

## 4.9 Droplet characterization

For droplet characterizations such as droplets' volume and speed, and aqueous/oil segment ratio, the camera was set to focus on the channel segment near the outlet of the microfluidic chip to record a video of about 1 minute.

### 4.9.1 Droplet volume

The approximated volume of a droplet in a rectangular channel is calculated as:

$$V = \left[ HW - (4 - \pi) \left( \frac{2}{H} + \frac{2}{W} \right)^{-2} \right] \left( L - \frac{W}{3} \right),$$

where  $H$  is the droplet height,  $W$  is the droplet width,  $L$  is the length of the droplet between two poles on the front and back interfaces [106].

In our case, the droplet height and width were taken as the height and width of the microfluidic channel,  $H = W = 1000 \mu\text{m}$ . Because the droplets are usually longer than the length of the window frame, the length  $L$  is calculated as:

$$L = L_{\text{front}} + L_{\text{body}} + L_{\text{back}},$$

where  $L_{\text{front}}$ ,  $L_{\text{back}}$  are the lengths of the front and back droplet caps, marked in Fig. 4.13 for the dark regions up-front and back-end of the droplet.  $L_{\text{body}}$  is the length of the droplet body part, which is marked along the bright region in the middle of the droplet.

The volumes of three droplets at the beginning, the middle and the end of each video were measured. In eight videos corresponding to eight independent launches, we obtained the average volume of  $V_{\text{droplets}} = 2.51 \pm 0.17 \mu\text{l}$  ( $N=8$ ,  $n=3$ ).

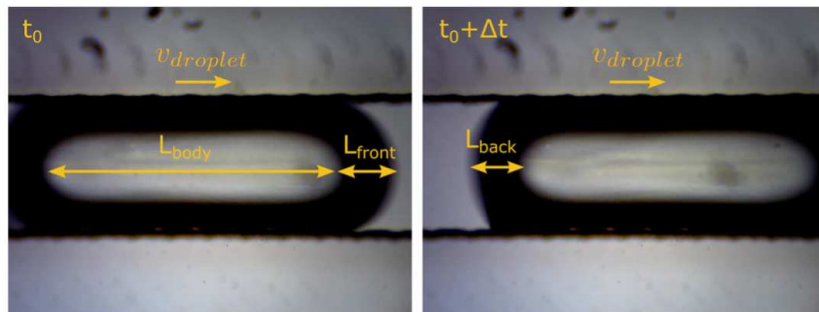


Figure 4.13: The length of the droplet is divided into the front the back and the body parts.

### 4.9.2 Droplet speed

The speed of the droplet is also the speed of the front or back interface of the droplet. After a time  $\Delta t$ , this interface moves a distance of  $\Delta l$  (Fig. 4.14); thus, its speed is calculated as:

$$v_{\text{droplet}} = \frac{\Delta l}{\Delta t}$$

For each droplet in the recorded video, the speeds of its front and back interfaces were measured. About 20 droplets with 40 speeds were measured and averaged in each video. Over eight independent launches, the average droplet speed is  $4 \pm 0.1$  mm/s ( $N=8$ ,  $n=40$ ).

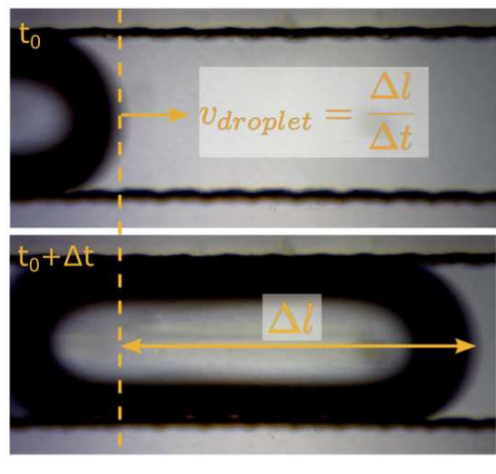


Figure 4.14: The length of the droplet is divided into the front the back and the body parts.

### 4.9.3 Aqueous/oil segment ratio

Because in our experiments, the oil segments are usually longer than the length of the window frame, we divide this segment into several segments that can be measured in different frames.

We consider two consecutive droplets A and B having oil filling in the space between the back interface of A and the front interface of B (Fig. 4.15). After a time  $\Delta t$ , the back interface of A moves a distance of  $\Delta l$ :

$$\Delta l = v\Delta t,$$

where  $v$  is the droplet speed calculated previously in section 4.9.2.

The distance between the back interface A and the front interface of B is the sum of  $\Delta l$  and their distance when overlapping two frames,  $\Delta x$  (Fig. 4.15).

## 74 Chapter 4. Microfluidic platform for SERS-complexometric titration

Because the droplet interface is curved in the front and back caps, the effective oil segment is considered as:

$$L_{\text{oil}} = \Delta x + \Delta l + \frac{l_{\text{cap A}}}{2} + \frac{l_{\text{cap B}}}{2},$$

where  $l_{\text{cap A}}$  and  $l_{\text{cap B}}$  is the length of the caps of droplet A and B respectively (Fig. 4.15).

We therefore apply the same principle to the effective aqueous segment:

$$L_{\text{aqueous}} = L_{\text{droplet}} - \frac{l_{\text{cap A}}}{2} - \frac{l_{\text{cap B}}}{2},$$

where  $L_{\text{droplet}}$  is the total length of droplet measured in section 4.9.1.

Finally, the aqueous/oil segment ratio is:

$$\delta_{\text{aqueous/oil}} = \frac{L_{\text{aqueous}}}{L_{\text{oil}}},$$

Three aqueous/oil segment ratios were measured at the beginning, the middle, and the end of each video. In eight videos corresponding to eight independent launches, we obtained the average volume of  $\delta_{\text{aqueous/oil}} = 0.88 \pm 0.05$  (N=8, n=3), ranging from 0.80 to 0.95.

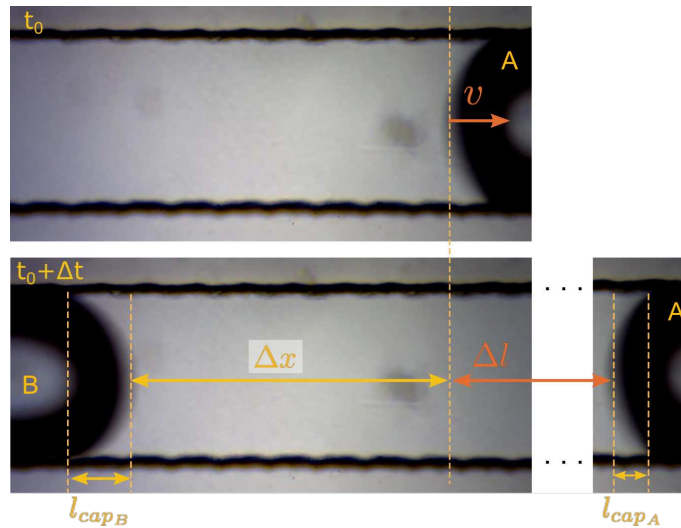


Figure 4.15: Schematic for aqueous/oil segment ratio measurement.

### 4.10 SERS measurement set-up

**Portable Raman spectrometer.** The optical fiber-based set-up from Ocean Optics comprising a QE Pro spectrometer, a 638 nm laser module (I0638SL0050MA)

with power within 50-100 mW and a coaxial Raman probe for measurement in backscattering configuration.

Custom-built optical measurement chamber. Raman signal was acquired under a high elimination of the ambient light through tailoring a commercial 4-window sample holder. One window was equipped with a combined excitation and collection Raman probe. Two parallel windows were shut but for two pinholes through which a glass capillary was nested. This glass capillary was the 16-cm tip part of the disposable glass Pasteur pipettes 230 mm. The capillary axis was fixed, crossing the optical path of the laser beam right at its focal point. The remaining window was sealed off. The inlet of the capillary was connected to the outlet tubing from the chip to receive droplets for SERS acquisition. The outlet was connected to another piece of tubing to transport droplets to the waste bin. See Fig. 4.16 for the photographs of this chamber.

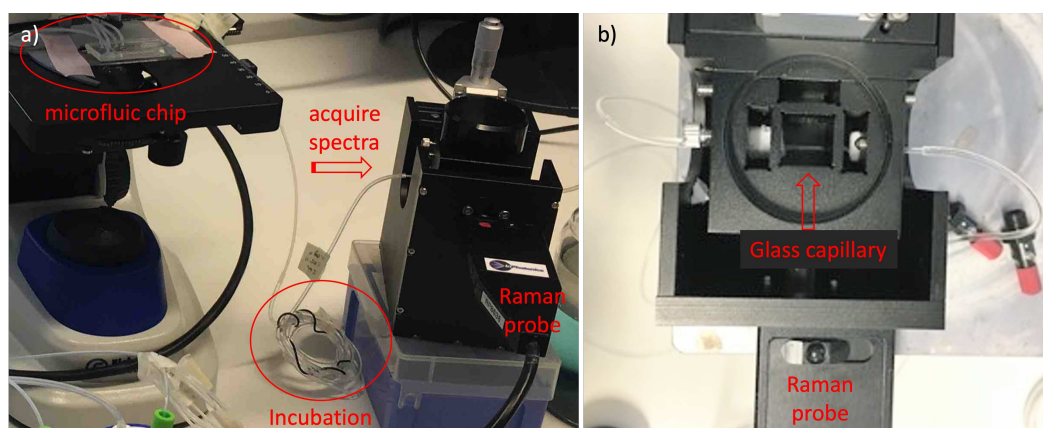


Figure 4.16: The Raman measurement chamber from: a) side view, and b) from top view. A commercial 4-window cuvette holder was customized for nesting a glass capillary for receiving matured-active-SERS droplets from the microfluidic chip. A Raman probe was fixed on this holder to focus on the center of the glass capillary.

## 4.11 Comparison between spectra acquired in cuvettes and in-line in droplets

### 4.11.1 Preparation of test cuvettes and microfluidic set-up for spectral and pH check.

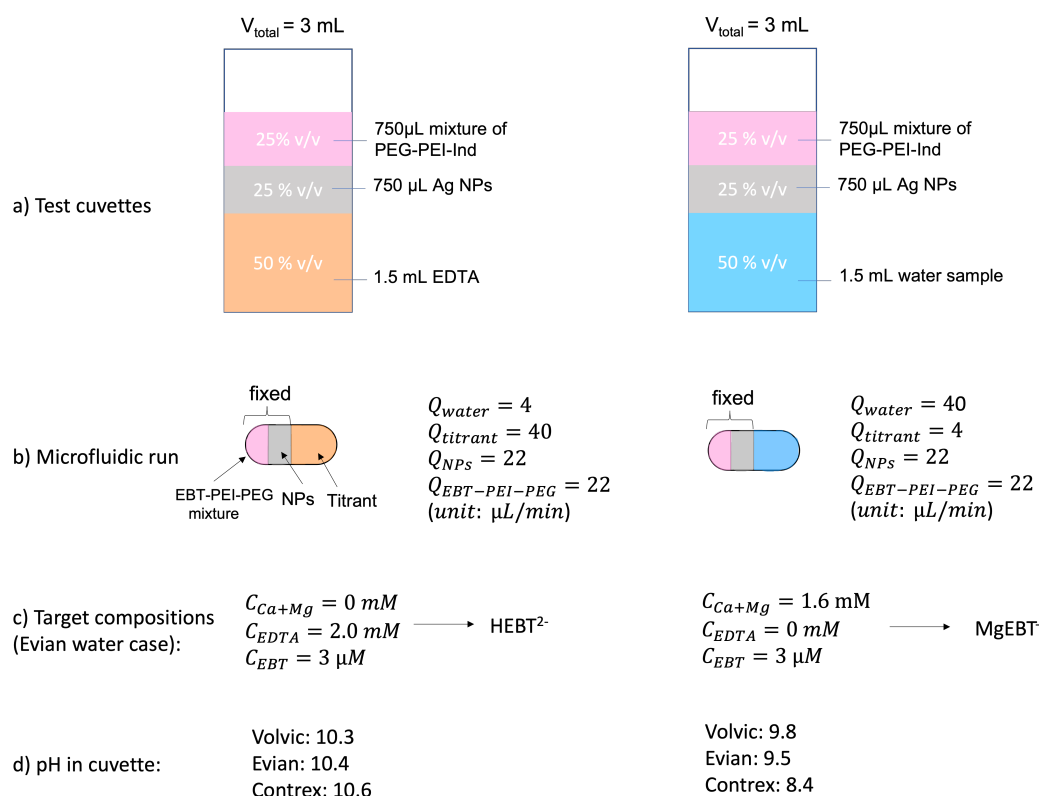


Figure 4.17: a) Preparation for two test cuvettes using the sets of feedstocks in Fig. 4.6. Each ingredient from the bottom to the top of the cuvette was added in turn and mixed thoroughly after each addition. The final mixtures were incubated for 5 minutes before measuring pH and acquiring SERS spectra. b) The target droplet compositions in the microfluidic runs which are the same as in cuvettes, and the actual generated flow rates values. These flow rates are maintained for 5 minutes to collect 20 spectra from droplets. c) The concentration compositions for Evian water case with relation to obtain the free or metal-bound EBT signals. d) pH measurements in test cuvettes for all three water samples.

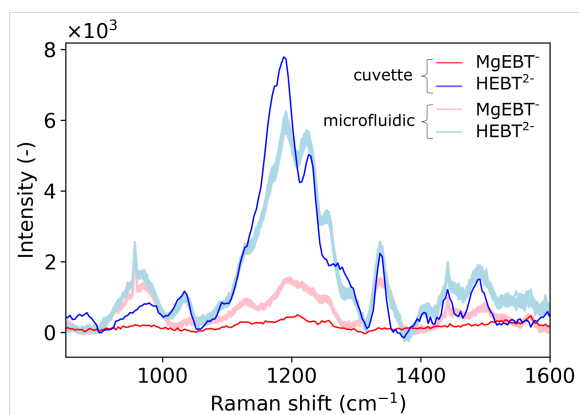


Figure 4.18: Representative SERS spectra of EBT in free and metal-bound forms from test cuvettes (thin blue and red curves) and from microfluidic system (blue and pink areas) that were prepared in Fig. 4.17 in the case for Evian water. The light blue and pink areas, each is the clusters of 20 spectra from droplets that are supposed to be the SERS signals of  $\text{HEBT}^{2-}$  and  $\text{MgEBT}^-$ , respectively. The black curve is the Raman spectrum of mineral oil, its full Raman spectrum is shown in Fig. 4.19. The spectral pattern of in-line measurements is similar to that from cuvettes.

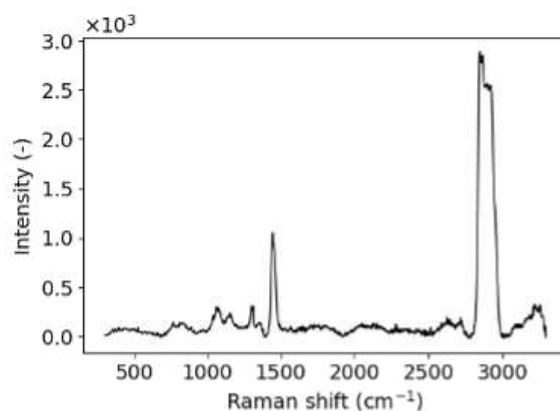


Figure 4.19: Raman spectrum of mineral oil with the integration time of 5 seconds. The spectrum displays a strong band near  $3000\text{ cm}^{-1}$  for C-H bonds and a few other bands from  $500$  to  $1500\text{ cm}^{-1}$

## 4.12 SERS signal reproducibility

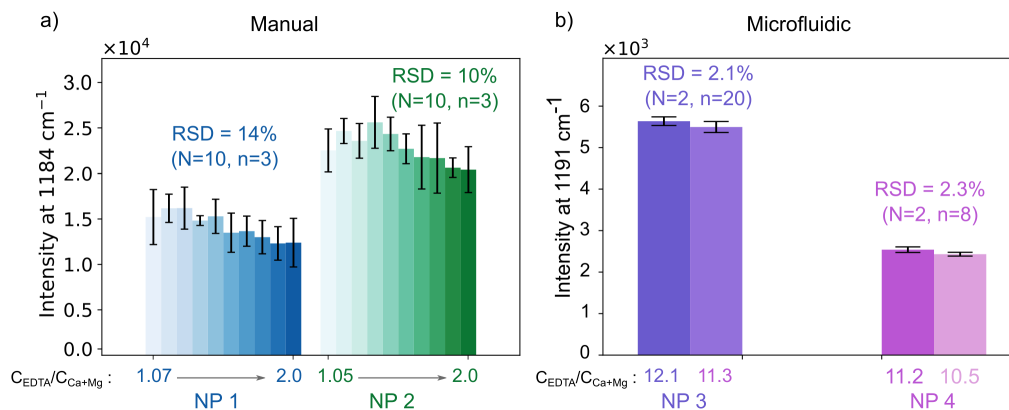


Figure 4.20: Averaged SERS signal intensities of  $\text{HEBT}^{2-}$  from four independent experiments carried out in four different days using four different NP batches and their standard deviations. (a) Two experiments using NP batch 1 (blue) and 2 (green) were carried out using the manual protocol. Each bar corresponds to the mean intensity of  $1184 \text{ cm}^{-1}$  peak and its standard deviation over 3 replicates ( $n = 3$ ) at 10 compositions ( $C_{\text{EDTA}}/C_{\text{Ca+Mg}}$  from 1.05 to 2.0,  $C_{\text{EBT}} = 4 \mu\text{M}$ ). These compositions give rise to the signal of free  $\text{HEBT}^{2-}$ . The relative standard deviations (RSD) over 10 compositions for each NP batch are 14 % and 10 % ( $N = 10$ ). (b) The experiments using NP batches 3 (purples) and 4 (pinks) were carried out using the automated microfluidic system. Each bar corresponds to the mean intensity of  $1191 \text{ cm}^{-1}$  peak and its standard deviation over 20 and 8 replicates ( $n = 20, 8$ ) at the similar compositions ( $C_{\text{EDTA}}/C_{\text{Ca+Mg}}$  from 10 to 12,  $C_{\text{EBT}} = 0.4 \mu\text{M}$ ). These compositions give rise to the signal of free  $\text{HEBT}^{2-}$ . The relative standard deviations (RSD) over 2 compositions for each NP batch are 2.1 % and 2.3 % ( $N = 2$ ).

## 4.13 Python program & automated experiment procedure description

For the program to run, the user needs to determine the initial pressures to apply onto every aqueous inlet to give rise to 4 equal flow rates on the order of  $20 \pm 5 \mu\text{L}/\text{min}$ ; the deviation between flow rates in each channel is  $1 \mu\text{L}/\text{min}$ . The pressure in the oil inlet is adjusted to obtain droplets with slug shape; this corresponds to pressure typically 1.5 times the pressure in the water sample inlet. This step state ensures the sweep later on is symmetric. It is carried out manually takes just a few minutes. Once it is done, the program is launched. First, the program maintains the manually set state for 1 minute to stabilize the whole system before sweeping applied pressures.

The program starts to sweep stepwise the pressures of water sample and titrant in the opposite directions by setting the applied pressure in each of them a step of

#### 4.13. Python program & automated experiment procedure description 79

$\Delta P$  higher and lower than the current values (Fig. 4.21). The pressure step  $\Delta P$  is defined in the inputs. Usually with  $\Delta P = 20$  mbar, the platform generates about 10 steps for a full titration, equivalent to a series of data set. If  $\Delta P = 10$  mbar, the number of steps will be doubled to about 20 steps for a full titration. The step duration input  $t_{step}$  (min) determines the number of replicate SERS acquisition per step  $n$ , given the fixed integration time of 15 s. In this work, we launched the platform with  $t_{step} = 2, 3, 5$  min. The program continues the sweep until it reaches to an extreme state when the flow rate readout in either water sample or titrant channel is equal to  $2 \mu\text{L}/\text{min}$ , the lowest accessible value that does not generate back flow. Upon reaching that threshold, the program sweeps the pressure of water sample and titrant in the reverse direction, which marks the beginning of a new titration series (and acquisition of a new dataset). The number of series is defined in the inputs.

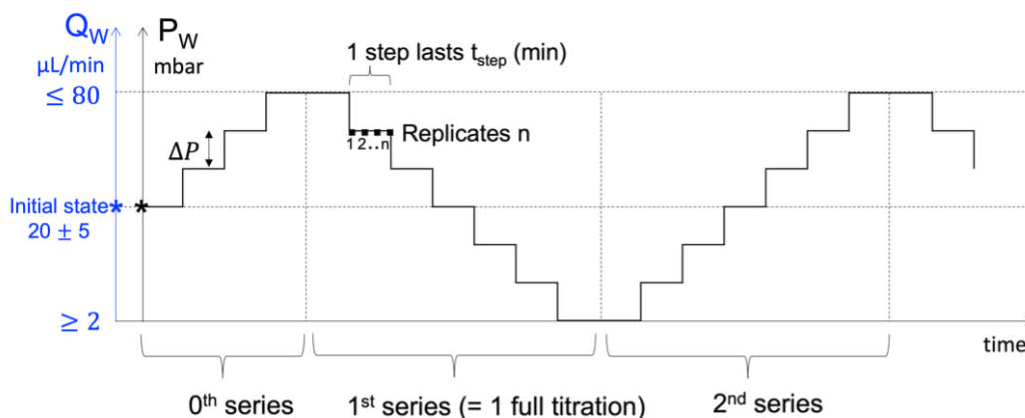


Figure 4.21: Schematic trajectory of the applied pressure ( $P_W$ ) and flow rate ( $Q_W$ ) in water channel. The trajectory in titrant channel is obtained by mirroring the trajectory in water channel through the horizontal axis that goes through the initial state. At the initial state, the pressure is set at which the flow rate is  $20 \pm 5 \mu\text{L}/\text{min}$ . Then the applied pressure is increased by  $\Delta P$  mbar and maintained at this pressure step for  $t_{step}$  minutes. As the integration time of the Raman spectrometer is always 15 seconds, there are 4 spectra acquired every minute, thus every pressure step there are  $n = t_{step} \times 4$  spectra acquired which is equivalent to  $n$  replicates. The applied pressure continues to sweep stepwise until the flow rate in water sample or titrant channel is equal to 2, it finishes 1 titration experiment and obtains 1 series of data set. Then, the applied pressure changes the sweeping direction, it continues until a number of series is reached.

Once the number of series is reached, the program stop sweeping and set the pressures in all inlets to 0 gradually within 1 minute, it runs the function `close()` (Fig. 4.22c). The reason for a dedicated `close()` function is because the oil and the mixture of PEG-PEI-Ind have different viscosity than other stock solutions. If the program immediately set the applied pressures in all the inlets to 0, the actual

## 80 Chapter 4. Microfluidic platform for SERS-complexometric titration

pressures in oil and PEG-based channels will decrease to 0 slower than in other inlets, leading to back flow of fluids from channels of higher pressures to the channels of lower pressures. The `close()` function helps to set the pressures in all the inlets reach to zero at the same time to avoid contaminating the chip for the next use.

Finally, the data that includes all information such as the series number, pressures, flow rates and spectra in real time is exported to an external file regularly after every pressure step to secure the data in case there is any disturbance during the experiment, such as electric shut or dry reservoir.

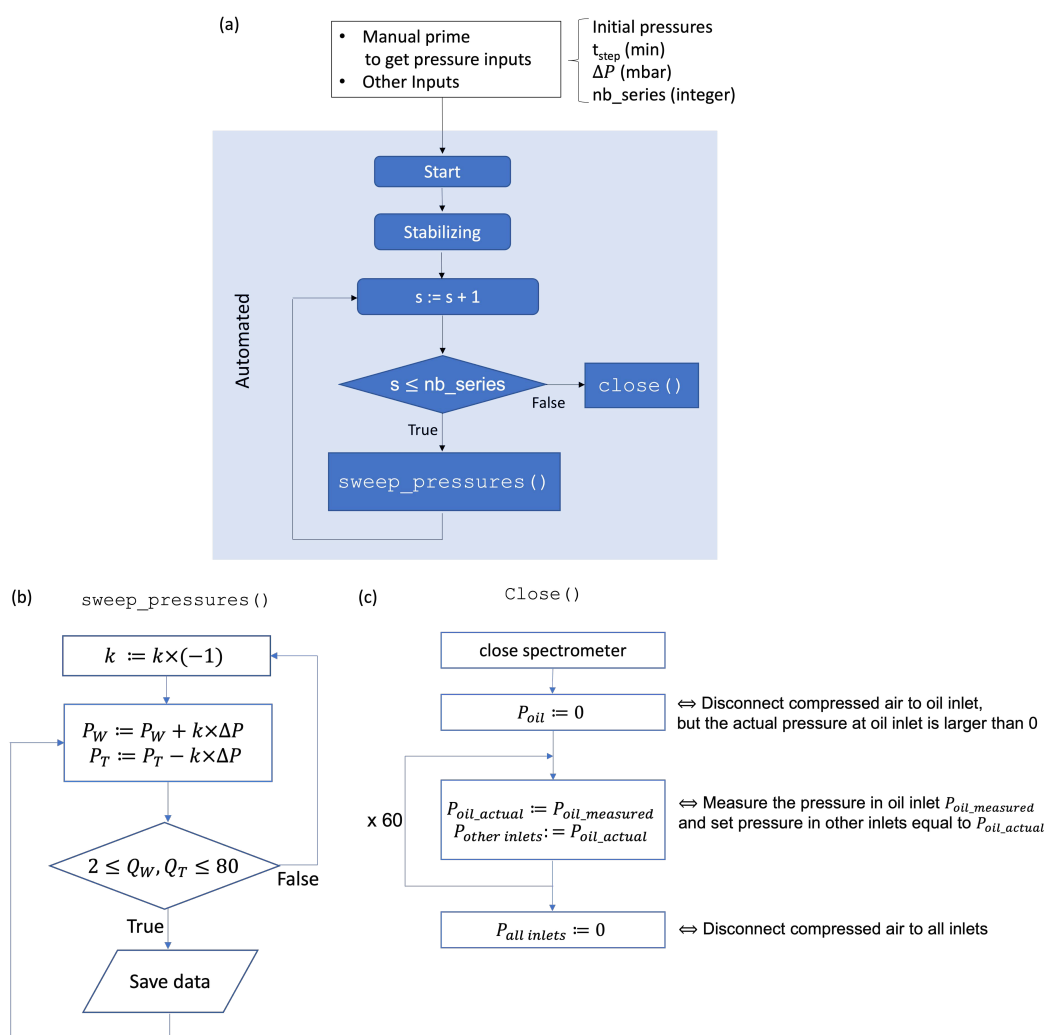


Figure 4.22: a) The full flow chart of the python program which contains 2 functions `sweep_pressures()` and `close()`. b) Flow chart of the function `sweep_pressures()`. c) Flow chart of the function `close()`.

## 4.14 Estimation of lag time from fluidic circuit

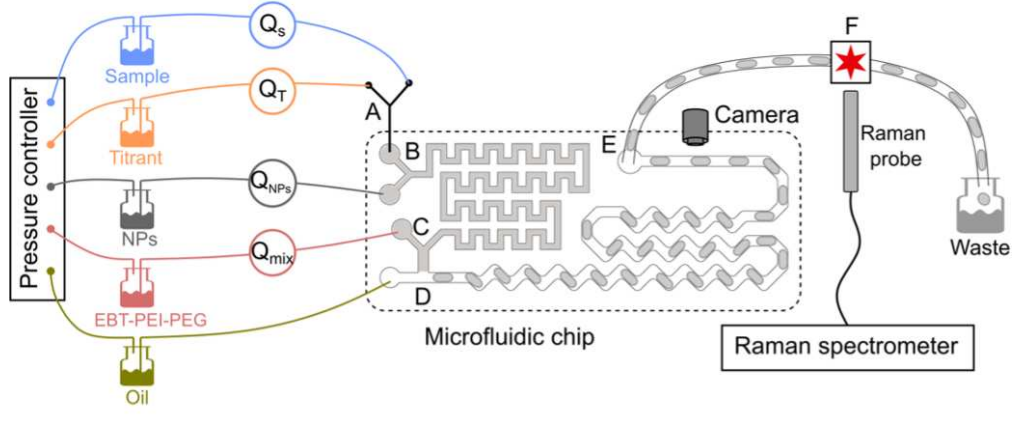


Figure 4.23: The schematic of the microfluidic platform showing different segments from A to F that contributes to the lag time between the flow rate readouts and spectral readout.

Because the flow rate sensors and the spectral readout point are placed nearly 2 m apart (Fig. 4.23), there is a time lag ( $t_{lag}$ ) between the flow rate and spectral data readouts. This lag time reflects the time it takes for a fluid particle to travel from the flow rate sensors to the focal point of the Raman probe, through the chip and tubings. Practically, it includes the travel time in the continuous phase from junction A to junction D (segment AD) and the travel time in droplets from junction D until the spectrometer focal point (segment DF). We neglected the travel time from the flow rate sensors  $Q_S$  and  $Q_T$  to the junction A because each stock solution in these segments is conserved, and the flow rate change in the upstream is instantly effective in the downstream. Because the pressure in NPs, mixture EBT-PEI-PEG and Oil inlets were maintained constant, their composition is unchanged throughout the experiment launch. Therefore, we also neglected the travel time of fluid particles in these channels. In the end, the lag time is calculated as:

$$t_{lag} = t_{AD} + t_{DF} = (t_{AB} + t_{BD}) + (t_{DE} + t_{EF}), \quad (4.7)$$

Based on the conservation of mass law for incompressible fluid, the same fluid in different cross section areas ( $S$ ) has different fluid velocities ( $v$ ), because the flux  $Q$  is constant,  $Q = vS = \text{const}$ . Therefore, their travel time depends on the cross-section area. The total lag time is then calculated as the sum of the lag times in 4 segments having different cross section areas (eq. 4.7). Here after, we detail the analytical calculation of lag time for each segment. Then, we calculate the value of lag time for a specific experiment, MD162\_14h01, by using the values of the flow rates and droplet speed in this experiment.

## 82 Chapter 4. Microfluidic platform for SERS-complexometric titration

(a) Lag time in segment AB ( $t_{AB} = t_1$ )

Some parameters of this segment are:

- The tubing length  $L_1 = 30$  cm, the cross section is circular of the internal diameter ID =  $D_1 = 0.0254$  cm (0.01",  $R = D_1/2$ ). We have the cross-section area:

$$S_1 = \pi \frac{D_1^2}{4}.$$

- The total flow rate:

$$Q_1 = Q_{\text{water}} + Q_{\text{titrant}} \left( \mu \frac{L}{\text{min}} \right).$$

- Exchange unit:  $1 \mu L/\text{min} = \frac{10^{-3}}{60} \text{ cm}^3/\text{sec}$ .

We have the speed of fluid in this segment:

$$v_1 = \frac{Q_1}{S_1}$$

The time for fluid travelling in this segment:

$$t_1 = \frac{L_1}{v_1} = L_1 \frac{S_1}{Q_1}.$$

$$t_1 = 15.10^3 \pi \frac{D_1^2 L_1}{Q_1} (\text{sec}) \quad (4.8)$$

where  $D_1$  and  $L_1$  are in cm,  $Q_1$  is in  $\mu L/\text{min}$ .

Apply eq. 4.8 for an experiment MD161\_14h01 in which  $Q_1 = 44 \mu L/\text{min}$ , we have  $t_{AB} = t_1 = 21$  sec.

(b) Lag time in segment BD ( $t_{BD} = t_2$ )

Some parameters of segment BD are:

- The channel length  $L_2 = 12$  cm, the cross section is rectangular with the height of  $h_2 = 1000 \mu m = 0.1$  cm, and the width  $w_2 = 600 \mu m = 0.06$  cm.
- The total flow rate:

$$Q_2 = Q_{\text{water}} + Q_{\text{titrant}} + Q_{\text{NPs}} \left( \mu \frac{L}{\text{min}} \right)$$

We have the speed of fluid in this segment:

$$v_1 = \frac{Q_2}{S_2} = \frac{Q_2}{h_2 w_2}$$

The time for fluid travelling in this segment:

$$t_2 = \frac{L_2}{v_2} = \frac{L_2}{\frac{Q_2}{h_2 w_2}} = \frac{h_2 w_2 L_2}{Q_2}$$

$$t_2 = 60.10^3 \frac{h_2 w_2 L_2}{Q_2} \quad (4.9)$$

Apply eq. 4.9 for an experiment MD161\_14h01 in which  $Q_2 = 66 \mu L/min$ , we have  $t_{BD} = t_2 = 66$  sec.

(c) Lag time in segments of droplet phase, DE and EF

Some parameters of segment DE are:

- The channel length  $L_1 = 11$  cm, the cross section is rectangular with the height and width of  $h_3 = w_3 = 1000 \mu m = 0.1$  cm.
- Speed of droplet  $v_3$  was measured in section 4.9.2,

$$v_3 = 4 \pm 0.1 mm/s \simeq 0.4 cm/s.$$

For the experiment MD162\_14h01,  $v_3 = 0.3861$  cm/s.

The parameters in segment EF:

$$v_1 = \frac{Q_2}{S_2} = \frac{Q_2}{h_2 w_2}.$$

- The channel length  $L_4 = 138$  cm, the cross section is circular of the internal diameter  $ID = D_4 = 0.03'' = 0.0762 cm$ .

$$S_4 = \pi \frac{D_4^2}{4}.$$

- Speed of droplet  $v_4$  is unknown and is calculated as follows.

In this dispersed phase segment, the oil is the continuous phase. We apply the conservation of mass law for oil. We take the approximation that the speed of droplets is equal to the speed of oil in squeezing regime [107]. We have:

$$Q_{oil} = S_3 v_3 = S_4 v_4.$$

$$v_4 = \frac{S_3 v_3}{S_4}.$$

$$v_4 = \frac{4h_3w_3}{\pi D_4^2} \cdot v_3 = \frac{4 \times 0.1 \times 0.1}{\pi \times 0.0762^2} \cdot v_3 \simeq 2.2 \times v_3$$

$$\Rightarrow t_3 = \frac{L_3}{v_3} = \frac{11}{v_3} (sec). \quad (4.10)$$

$$\Rightarrow t_4 = \frac{L_4}{v_4} = \frac{138}{2.2 \times v_3} (sec). \quad (4.11)$$

Applying eq. 4.10, eq. 4.11 for the experiment MD162\_14h01 where  $v_3 = 0.3861 cm/s$ , we have:

$$t_{DE} = t_3 = 28 sec,$$

$$t_{EF} = t_4 = 162 sec.$$

The total lag time for the experiment MD162\_14h01 is:

$$t_{lag\_MD162\_14h01} = 278 sec.$$

## 4.15 Data processing

### 4.15.1 The raw data structure

The raw dataset exported from the python program contains 2 main parts: information and spectra, both were labeled with a time stamp in real time when they were measured. The information part contains all the conditions of the experiment such as: number of titration series, applied pressures, measured pressures, and measured flow rates. The spectral part contains the intensity of the spectra in which the column names are the wavelength,  $\lambda$  from 642.09 nm to 808.76 nm. The Raman shift ( $\Delta\omega$ ) were then converted from the wavelength by the formula:

$$\Delta\omega [cm^{-1}] = 10^7 \left( \frac{1}{\lambda_{laser}} - \frac{1}{\lambda} \right); \lambda [nm]$$

### 4.15.2 Baseline correction

SERS spectra in the spectral part of the full data frame were truncated from the Raman shift 300 to 3300  $cm^{-1}$  before doing baseline subtraction. The baselines were generated using the algorithm published in "Baseline correction with asymmetric least squares smoothing" by P. Eilers and H. Boelens in 2005 [108]. The python code was adapted from StackOverFlow forum [109]. The implemented parameters values were asymmetry  $p = 0.001$  and smoothness  $\lambda = 10000$ . Fig. 4.25 illustrates the baseline correction for two representative spectra with low and high intensity, at minute 27 and 67 of an microfluidic launch, respectively. The spectra after baseline

correction between these time stamps are plotted in Fig. 4.24 with a zoom in the fingerprint region.

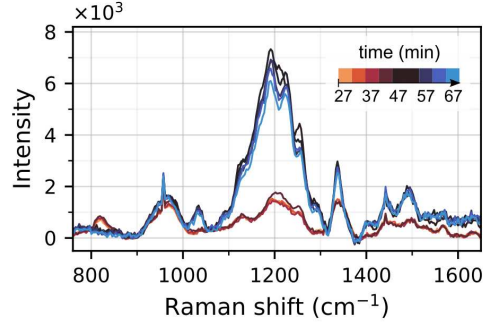


Figure 4.24: Spectra data of a full series after baseline correction.

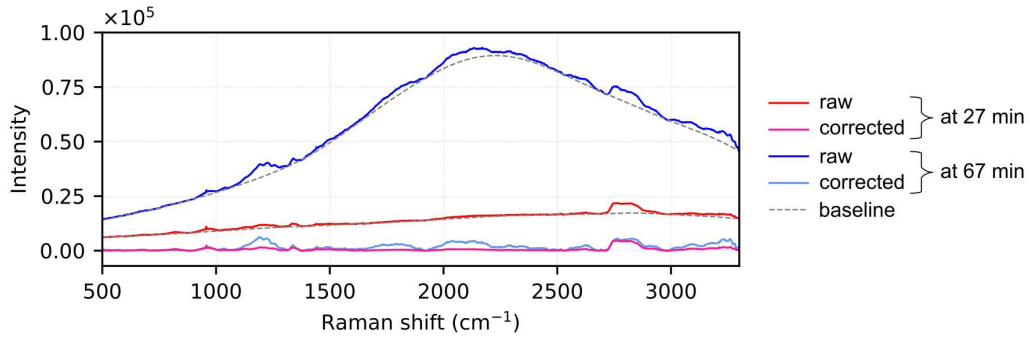


Figure 4.25: Spectra before and after baseline correction at minute 27th and 67th showed in Fig. 4.24.

### 4.15.3 Lag time estimation by metrical calibration method

After baseline correction for the raw spectral data, the intensity of the  $1191.4\text{cm}^{-1}$  peak over time was extracted and marked in different colours for different series that were defined in the flow rate data, Fig. 4.26. Note that the time tag in this dataset is still incorrect; it is shifted a lag time  $t_{\text{lag}}$ . Because two first consecutive series are reversed titrations, their titration curves after lag time correction need to be symmetric through the vertical red dashed line that goes through the middle point between  $t_1$  and  $t_2$ . Thus,  $t_{\text{lag}}$  is the shift between the middle point between  $t_1$ ,  $t_2$  and the first point of the first series.

$t_1$  and  $t_2$  are numerically determined as the maximum of the 1st derivative of the sigmoid function that fits the data of each series.

$$f(x) = \frac{L}{1 + e^{-k(x-x_0)}} + y_0,$$

where

$$f(x) \equiv y_{\text{data}} \equiv \frac{I_{1191}}{1000},$$

$$x \equiv x_{\text{data}} \equiv t.$$

The initial parameters for each data for fitting iteration is:

$$p_0 = [L, x_0, k, y_0] = [\max(y_{\text{data}}), \text{median}(x_{\text{data}}), 1, \min(y_{\text{data}})]$$

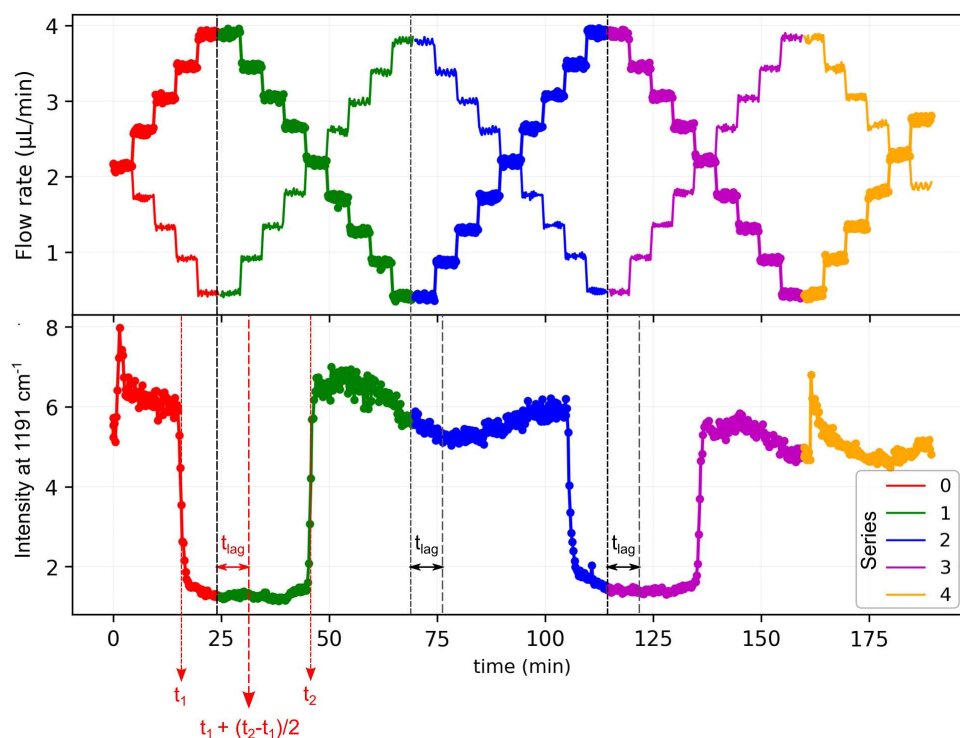


Figure 4.26: Upper panel: the intensity of the  $1191.4 \text{ cm}^{-1}$  peak overtime of the experiment MD162\_14h01. Each series were marked in different colours based on the series defined in the flow rate data (bottom panel, only the flow rate profiles in aqueous channels are displayed for clarity's sake). Note that the time tag in this spectral dataset is incorreced.  $t_1$  and  $t_2$  are the inflection points of the 0th and 1st series.  $t_{lag}$  is the shift between the middle point of  $t_1, t_2$  and the first point of the first series.

Table 4.1: Lag times estimated in 8 independent launches in the microfluidic platform.

Independent launch	Lag time (sec)
MD162_12h45	363
MD162_14h01	348
MD168_12h36	370
MD163_12h10	355
MD163_14h17	385
MD163_17h14	362
MD166_13h42	376
MD166_17h25	369
	366 $\pm$ 12

Commenting on the lag time analytically estimation from fluidic circuit (section 4.14) and from numerical calibration.

In section 4.14, we calculated the lag time from fluidic circuit for the experiment MD162\_14h01,  $t_{\text{lag\_MD162\_14h01}} = 278 \text{ sec.}$  Even though this value is 70 sec different than the value calculated by numerical method in Tab. 4.1, 348 sec, they are in the same order of magnitude.

Examining the intensity of the  $1191 \text{ cm}^{-1}$  peak after adjusting the lag time for both cases, we obtained that the lag time obtained from the numerical calibration method gave a better symmetric match between the titration curves than from analytical method, Fig. 4.27. For better visualization, we flipped the intensity of the odd series, then overlapped all the series. Therefore, we selected the numerical method for lag time estimation for all the experiments.

We think the unprecise lag time estimation from the fluidic circuit can be generated from several approximations. For instance, we neglected the error of droplet speed, and the flow in the droplet segment (two-phase flow) is complex to infer the exact lag time.

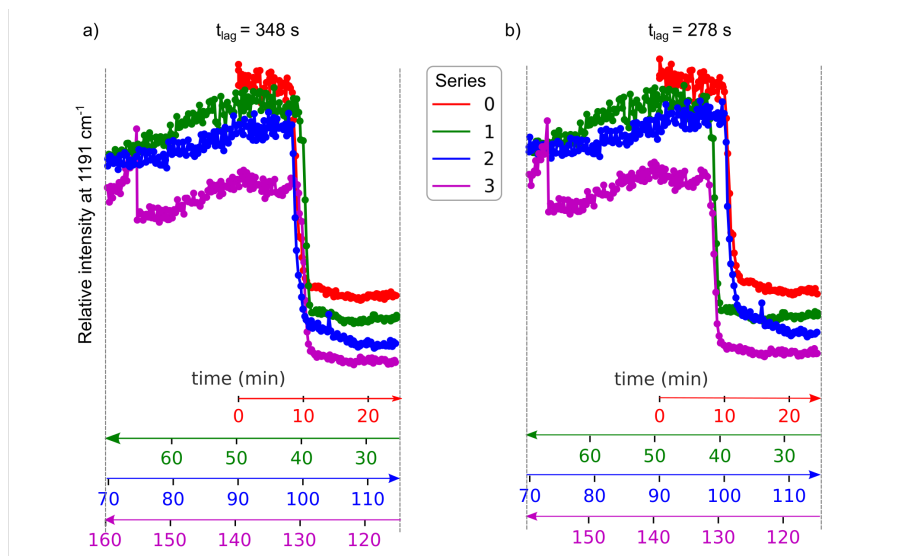


Figure 4.27: The intensity of the  $1191\text{ cm}^{-1}$  peak after adjusting the lag time from a) numerical calibration by matching periodic sweeping spectral pattern, and b) analytical calculation from fluid circuit. The intensity of the odd series was flipped  $180^\circ$ , then all series are plotted overlapping for easier comparison.

#### 4.15.4 Lag time correction for spectral data

To correct the time lag  $t_{lag}$  between the time point of droplet formation and the time point of spectra acquisition of the same droplet, the part of the spectra in the data set was shifted in time by  $-t_{lag}$ , while the rest of the data set was unchanged, see Fig. 4.28.

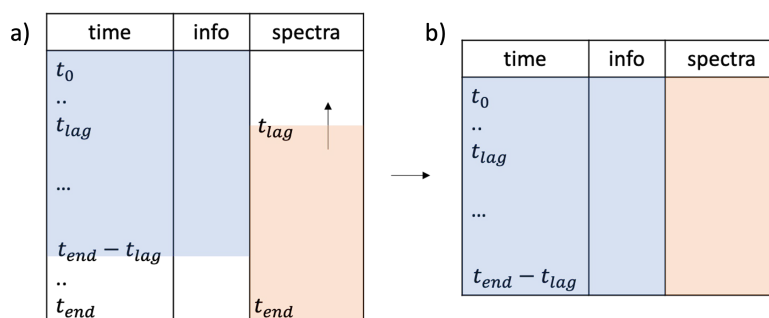


Figure 4.28: Raw data frame structure before and after lag time adjustment.

#### 4.15.5 Endpoint identification

From the known concentration of divalent metal ions and EDTA in stocks and the recorded flow rates, the concentration of a compound A in the microfluidic

#### 4.16. Comparison between the microfluidic system and manual protocol

system is

$$C_{A \text{ in microsystem}} = \frac{C_{A \text{ in stock}} \times Q_A}{Q_{\text{total}}}.$$

The number of EDTA equivalents is defined as:

$$\xi(EDTA) = \frac{C_{EDTA}}{C_{Ca} + C_{Mg}}.$$

To identify the end point of the titration, the intensity of the  $1191.4 \text{ cm}^{-1}$  peak was plotted versus the number of  $\xi(EDTA)$ . Then, the data was fitted to a sigmoidal function with the analytical formula as follows:

$$f(x) = \frac{L}{1 + e^{-k(x-x_0)}} + y_0,$$

where,

$$f(x) \equiv y_{\text{data}} \equiv \frac{I_{1191}}{1000},$$
$$x \equiv x_{\text{data}} \equiv \xi(EDTA).$$

The initial parameters for each data for fitting iteration is:

$$p_0 = [L, x_0, k, y_0] = [\max(y_{\text{data}}), \text{median}(x_{\text{data}}), 1, \min(y_{\text{data}})]$$

The end point of the titration is then identified at the deepest slope of the sigmoid curve, which is also the maximum of the 1st derivative of  $f(x)$ .

#### 4.16 Comparison between the microfluidic system and manual protocol

Below, we summarize the typical range of chemical parameters for titration experiments on the microfluidic system and for the manual protocol, see Tab. 4.2.

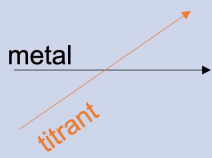
	Manual protocol	Microfluidic system
Titrating manner		
pH	~ 10	8.4 ÷ 10.6
Range of $\zeta(\text{EDTA})$	0 ÷ 2	0 ÷ 13
$\Delta\zeta(\text{EDTA})$ near endpoint	0.05	0.30 (N=7) 0.15 (N=1)
EBT concentration	~ 3 $\mu\text{M}$	~ 400 nM

Table 4.2: Comparison of some titration parameters in the microfluidic system and by the manual protocol in cuvettes.

#### 4.17 Evian titrations

Here, we add the experimental details of the titration experiments with Evian samples, Tab. 4.3.

Water sample	Evian	Evian	Evian
Experiment (independent launch)	MD162_12h45	MD162_14h01	MD168_12h36
Step duration (min)	5	2	2
Pressure step $\Delta P$ (mbar)	20	20	10
Nb of titration increments	9	9	19
Time per titration series (min)	45	45	38

Table 4.3: Details of the 3 Evian titration experiments on the microfluidic platform.

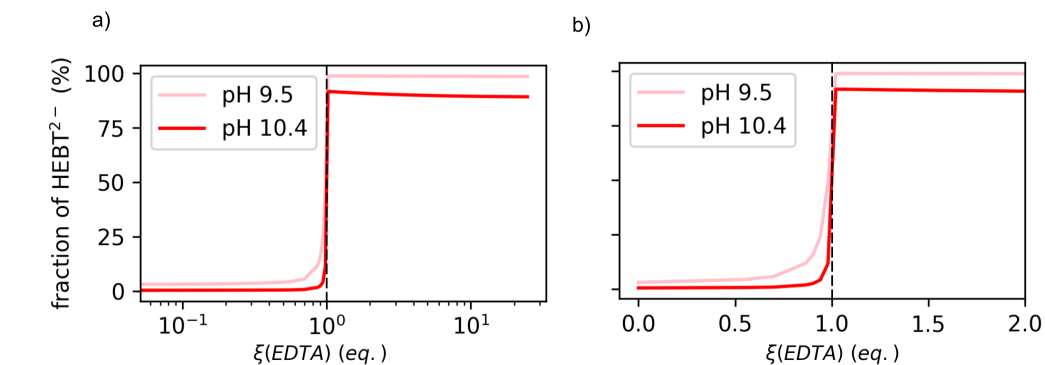


Figure 4.29: Speciation analyses of EBT at two extreme pH value during Evian titration in a) log scale, and b) zoom in linear scale from 0 to 2 eq..

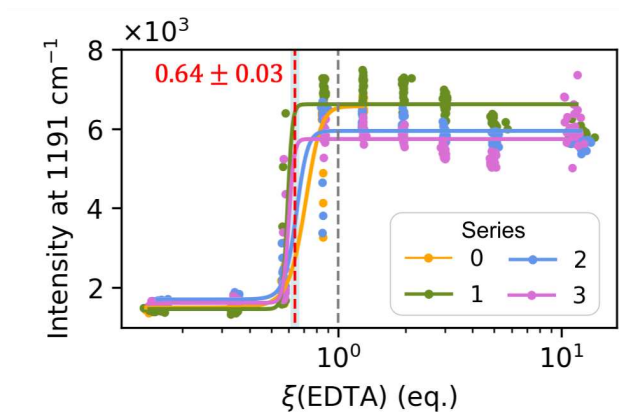


Figure 4.30: Titration curves of the Evian titration, MD162\_14h01 with  $\Delta P = 20$  mbar,  $t_{\text{step}} = 5$  minutes.

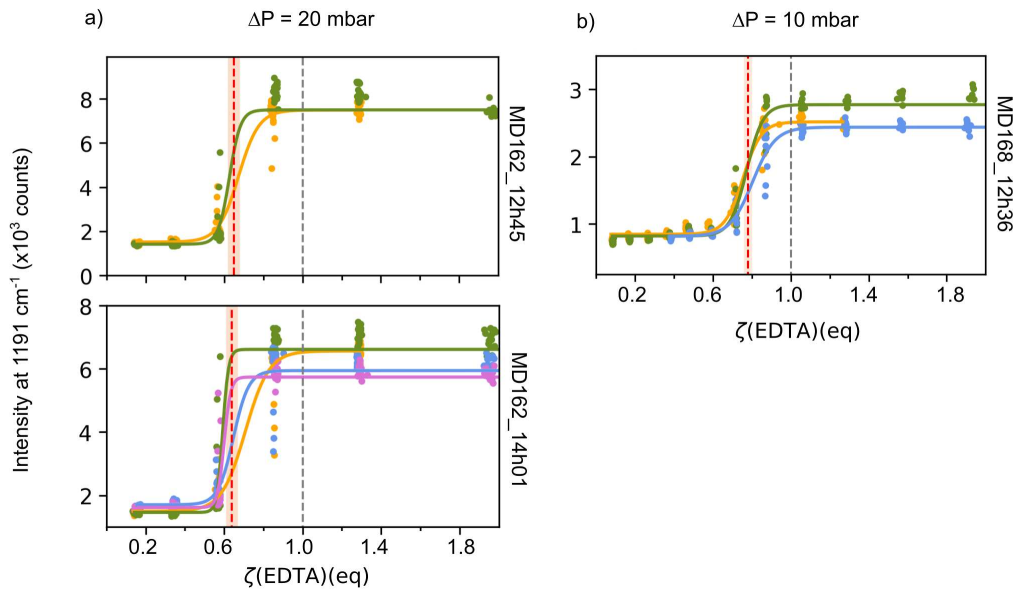


Figure 4.31: Spectral titration curves of Evian titrations at (a)  $\Delta P = 20 \text{ mbar}$  from two different launches using the same NP batch, and (b) at  $\Delta P = 10 \text{ mbar}$  using another NP batch. We observed that a closer endpoint to the equivalence was obtained in the higher resolution titration experiment.

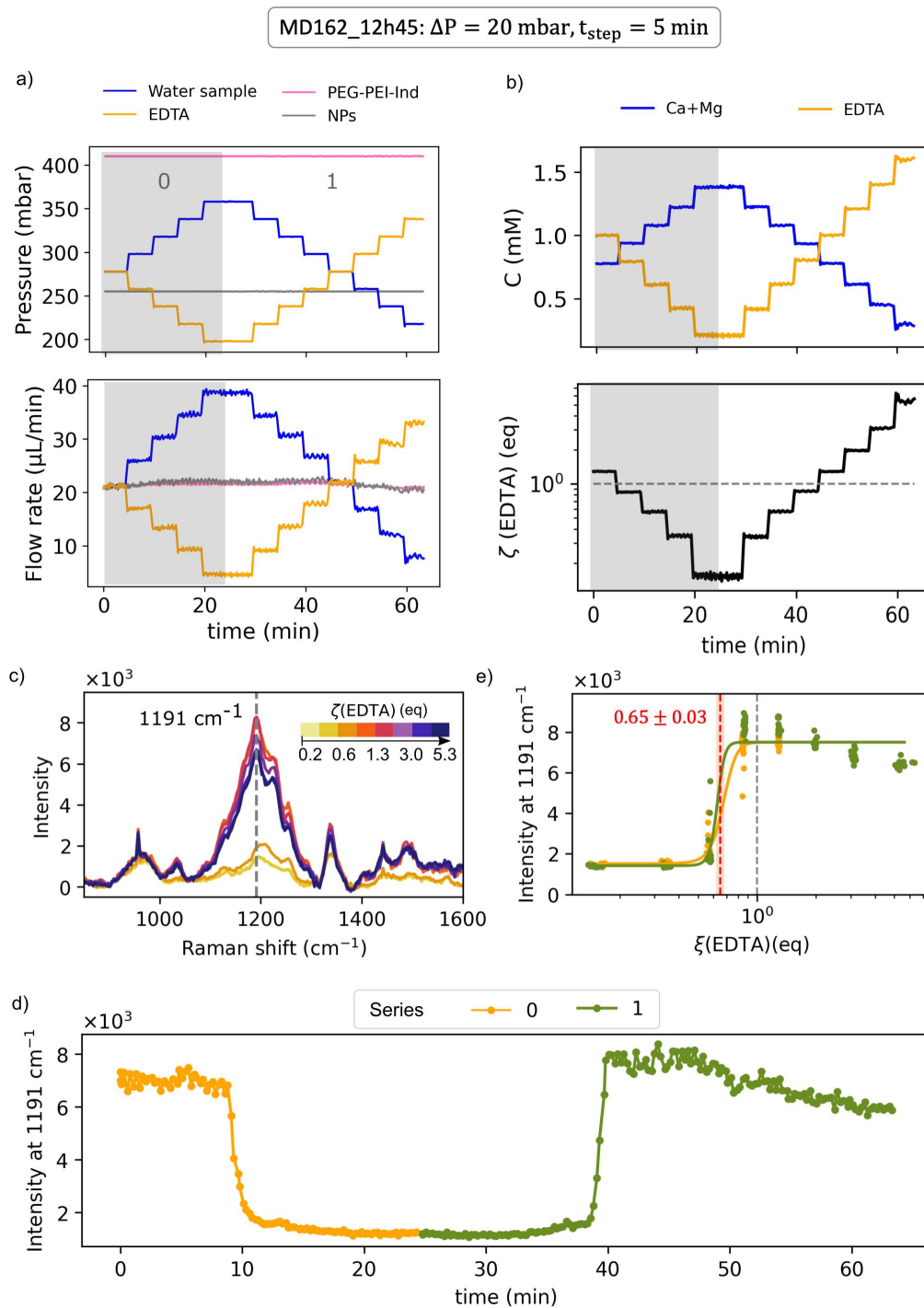


Figure 4.32: a, b) Composition control and c, d) spectral data analysis of Evian titration experiment MD162\_12h45 with  $\Delta P = 20$  mbar,  $t_{\text{step}} = 5$  minutes.

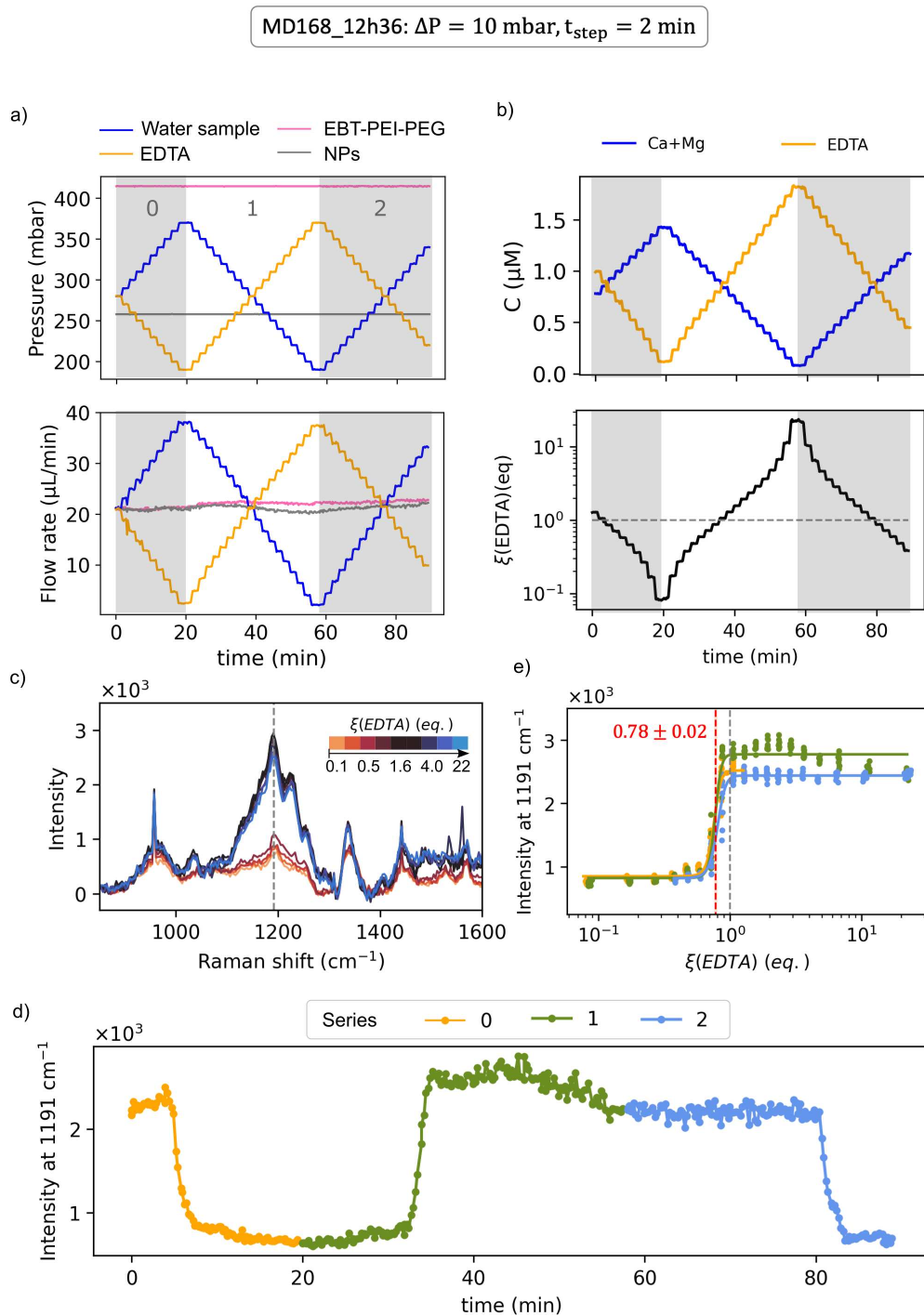


Figure 4.33: a, b) Composition control and c, d) spectral data analysis of Evian titration experiment MD168\_12h36 with  $\Delta P = 10$  mbar,  $t_{\text{step}} = 2$  minutes.

## 4.18 Volvic titrations

Here, we add the experimental details of the titration experiments with Volvic samples, Tab. 4.4.

Water sample	Volvic	Volvic	Volvic
Experiment (independent launch)	MD163_12h10	MD163_14h17	MD163_17h14
Step duration (min)	3	5	2
Pressure step $\Delta P$ (mbar)	20	20	20
Nb of titration increments	10	9	10
Time per titration series (min)	30	45	20

Table 4.4: Details of the 3 Volvic titration experiments on the microfluidic platform

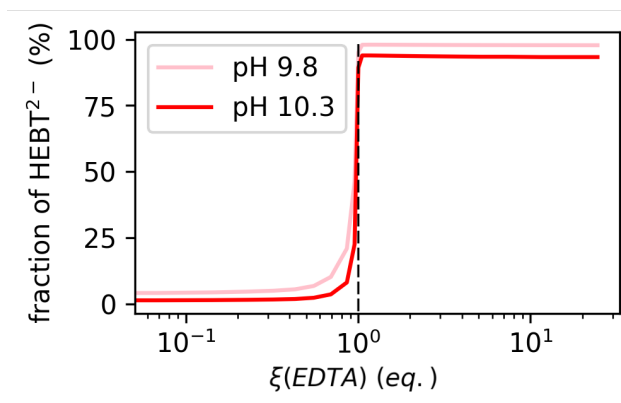


Figure 4.34: Speciation analyses of EBT at two extreme pH value during Volvic titration in log scale.

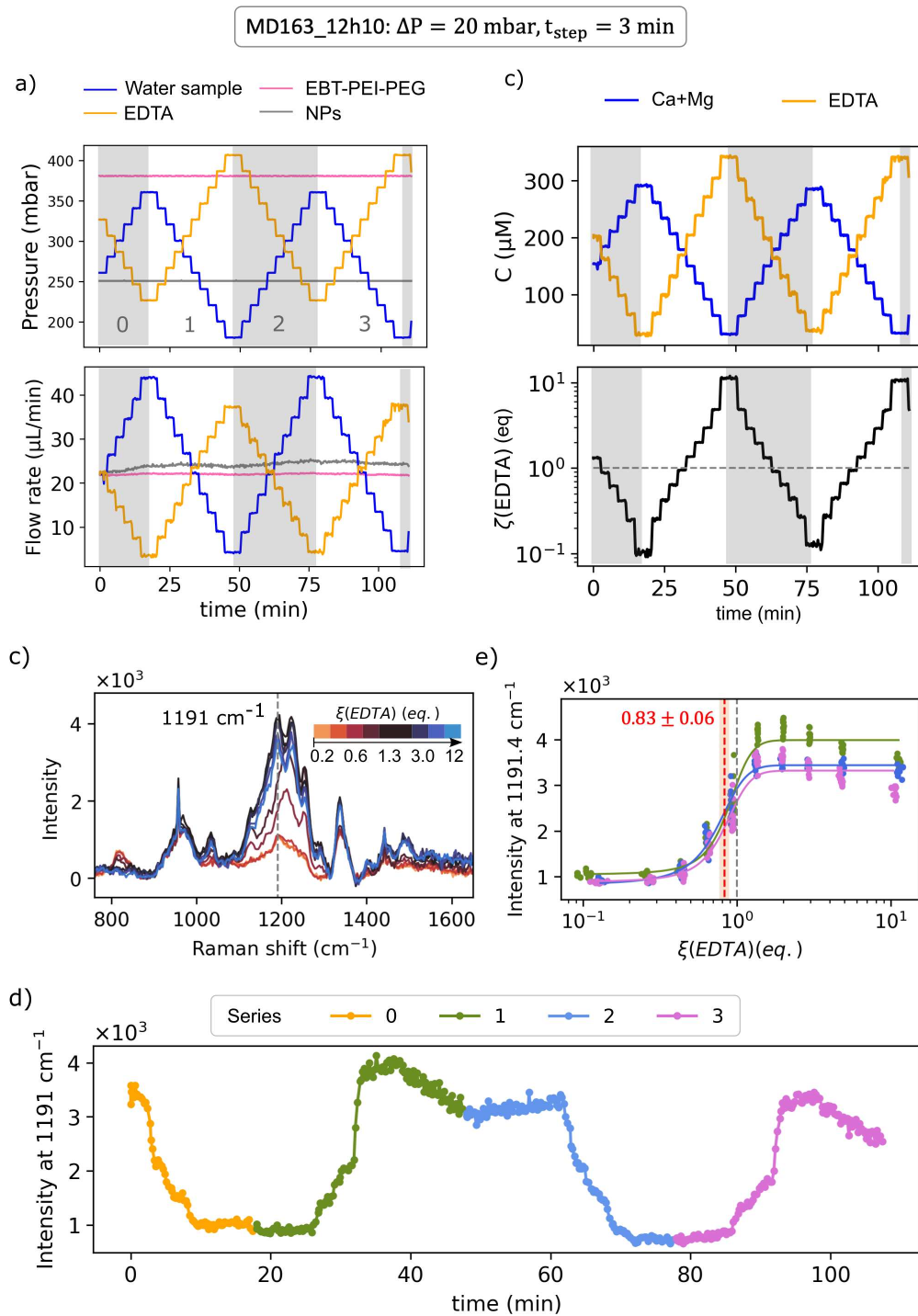


Figure 4.35: a, b) Composition control and c, d) spectral data analysis of Volvic titration experiment MD163\_12h10 with  $\Delta P = 20$  mbar,  $t_{\text{step}} = 3$  minutes.

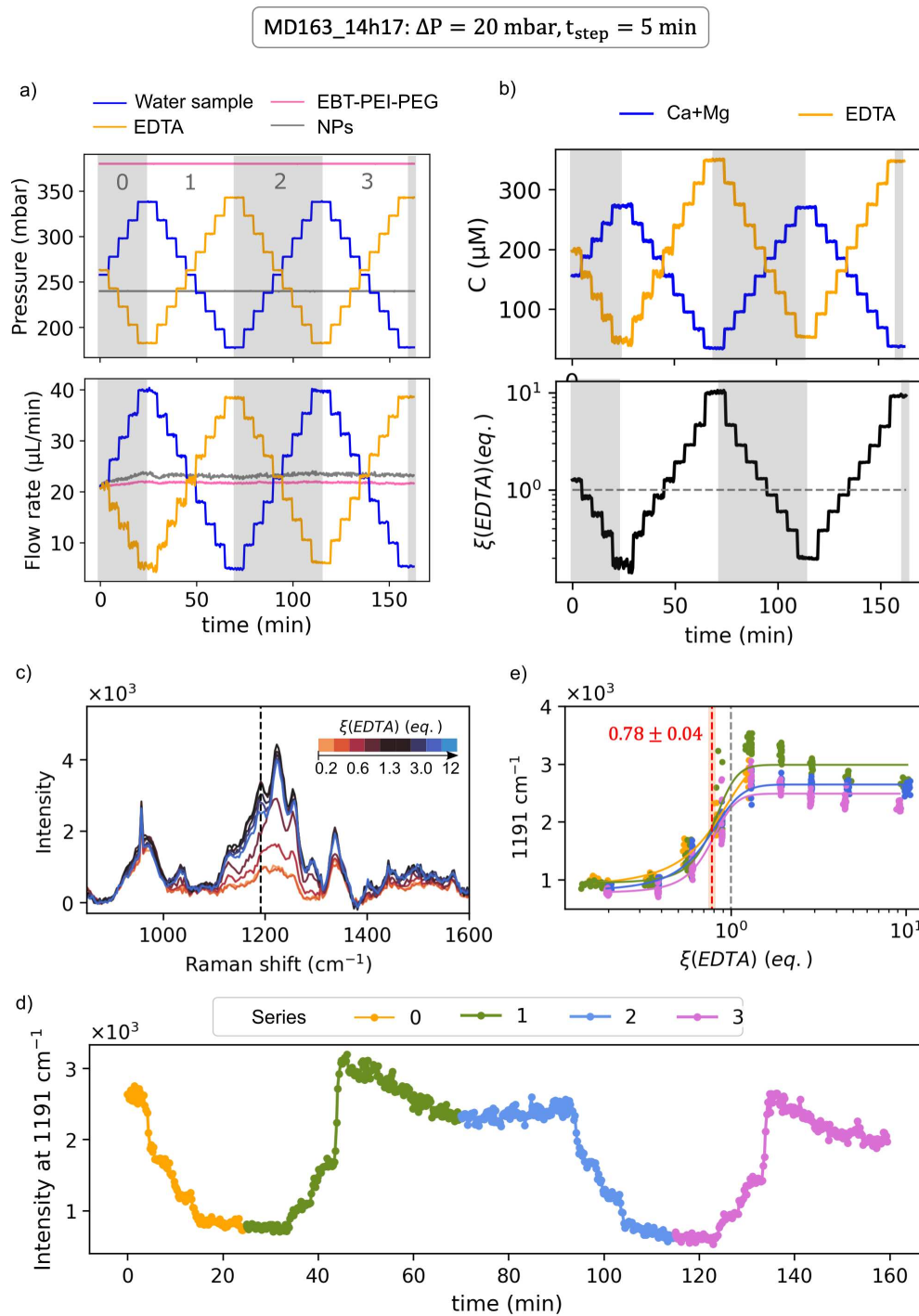


Figure 4.36: a, b) Composition control and c, d) spectral data analysis of Volvic titration experiment MD163\_14h17 with  $\Delta P = 20$  mbar,  $t_{\text{step}} = 5$  minutes.

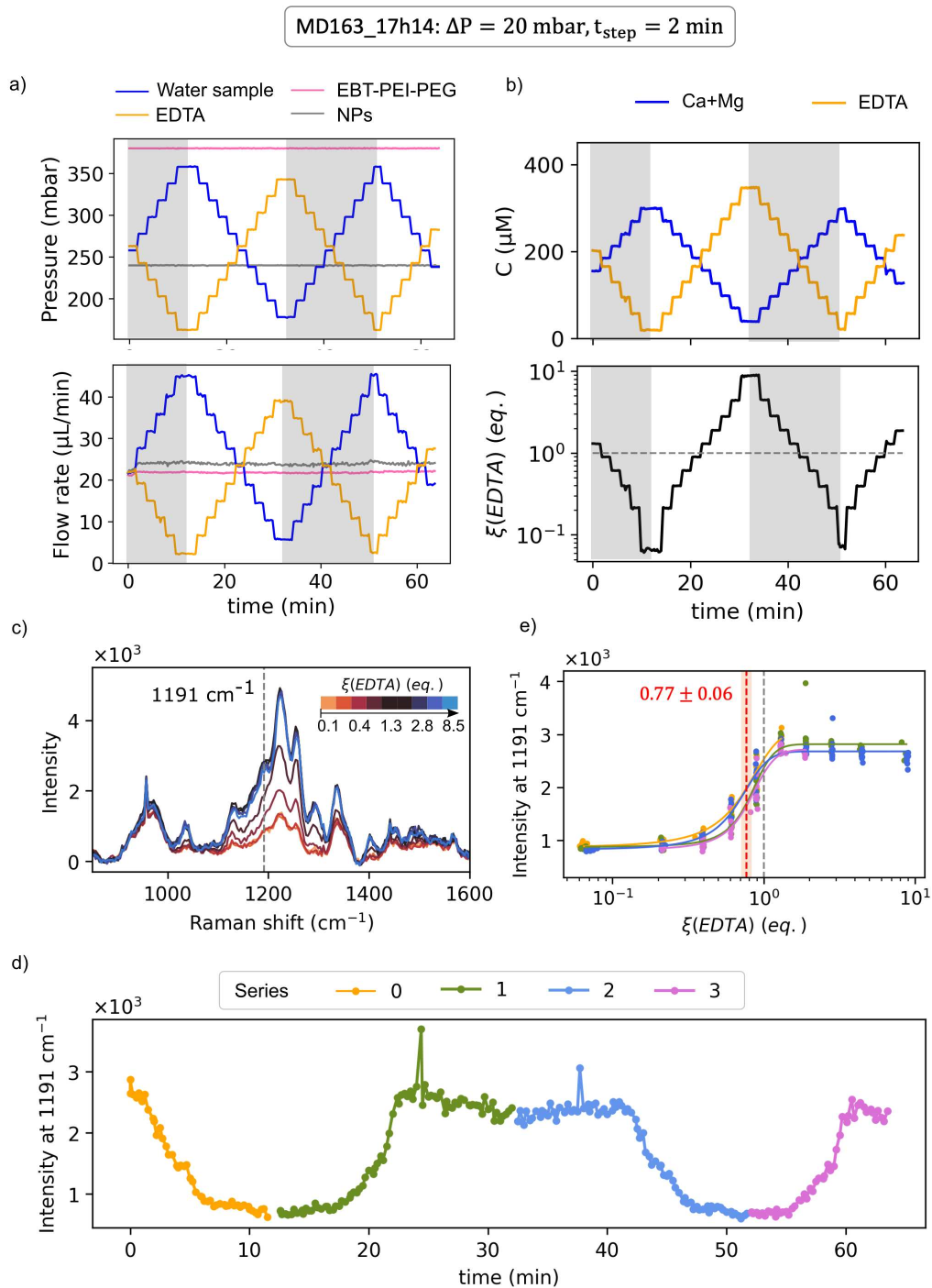


Figure 4.37: a, b) Composition control and c, d) spectral data analysis of Volvic titration experiment MD163\_17h14 with  $\Delta P = 20$  mbar,  $t_{step} = 2$  minutes.

## 4.19 Contrex titrations

Here, we add the experimental details of the titration experiments with Contrex samples, Tab. 4.5.

Water sample	Contrex	Contrex
Experiment (independent launch)	MD166_13h42	MD166_17h25
Step duration (min)	5	2
Pressure step $\Delta P$ (mbar)	20	20
Nb of titration increments	9	9
Time per titration series (min)	45	18

Table 4.5: Details of the 2 Contrex titration experiments on the microfluidic platform

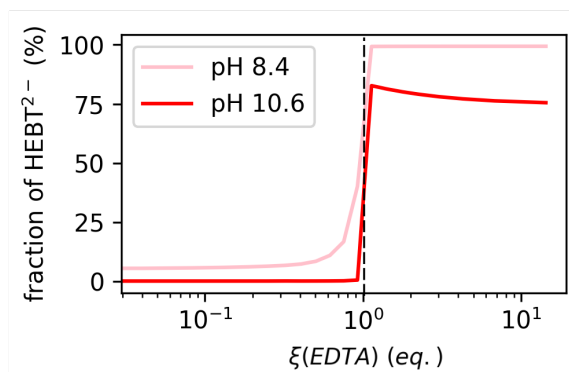


Figure 4.38: Speciation analyses of EBT at two extreme pH value during Contrex titration in log scale.

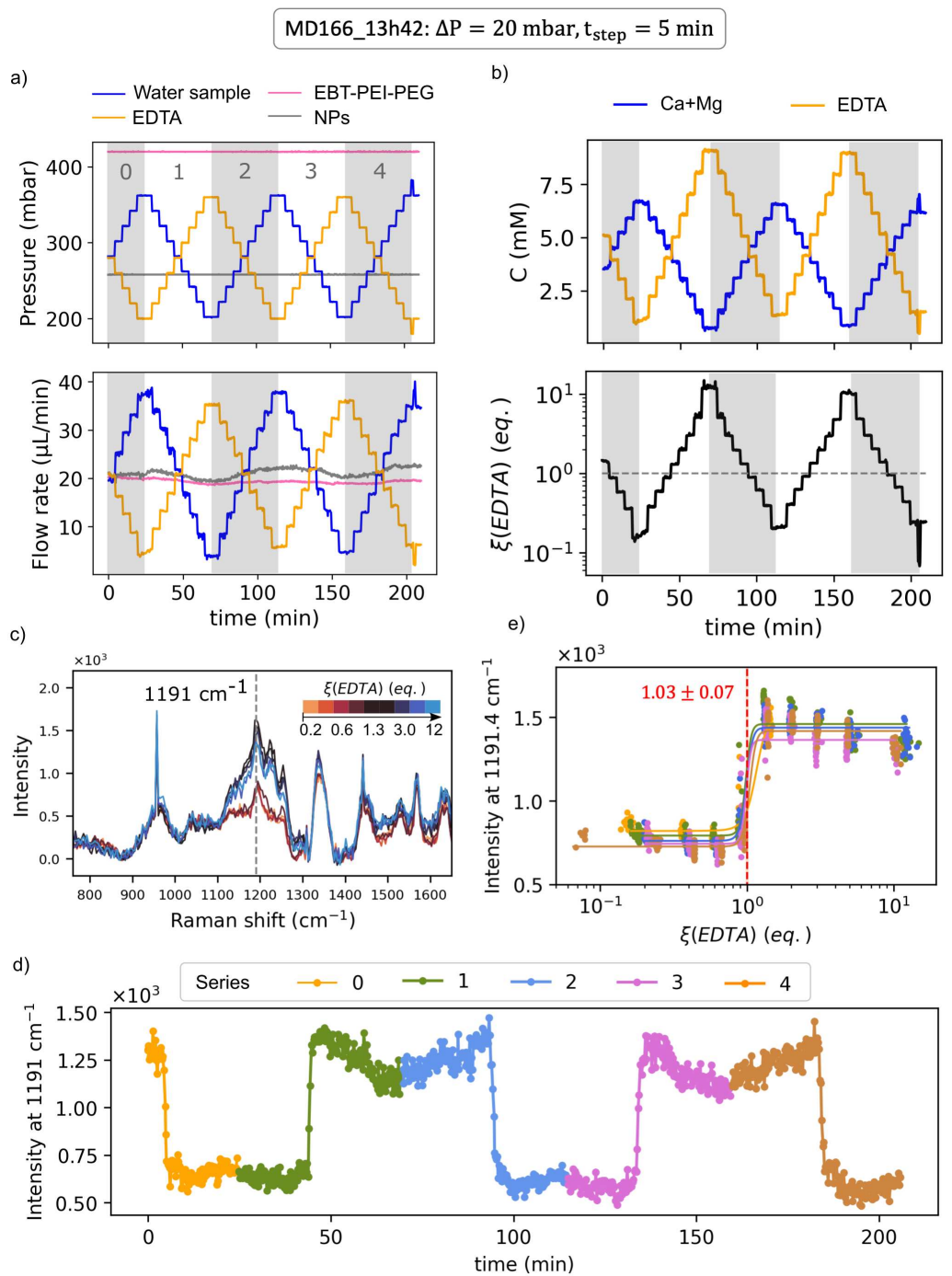


Figure 4.39: a, b) Composition control and c, d) spectral data analysis of Contrex titration experiment MD166\_13h42 with  $\Delta P = 20$  mbar,  $t_{step} = 5$  minutes.

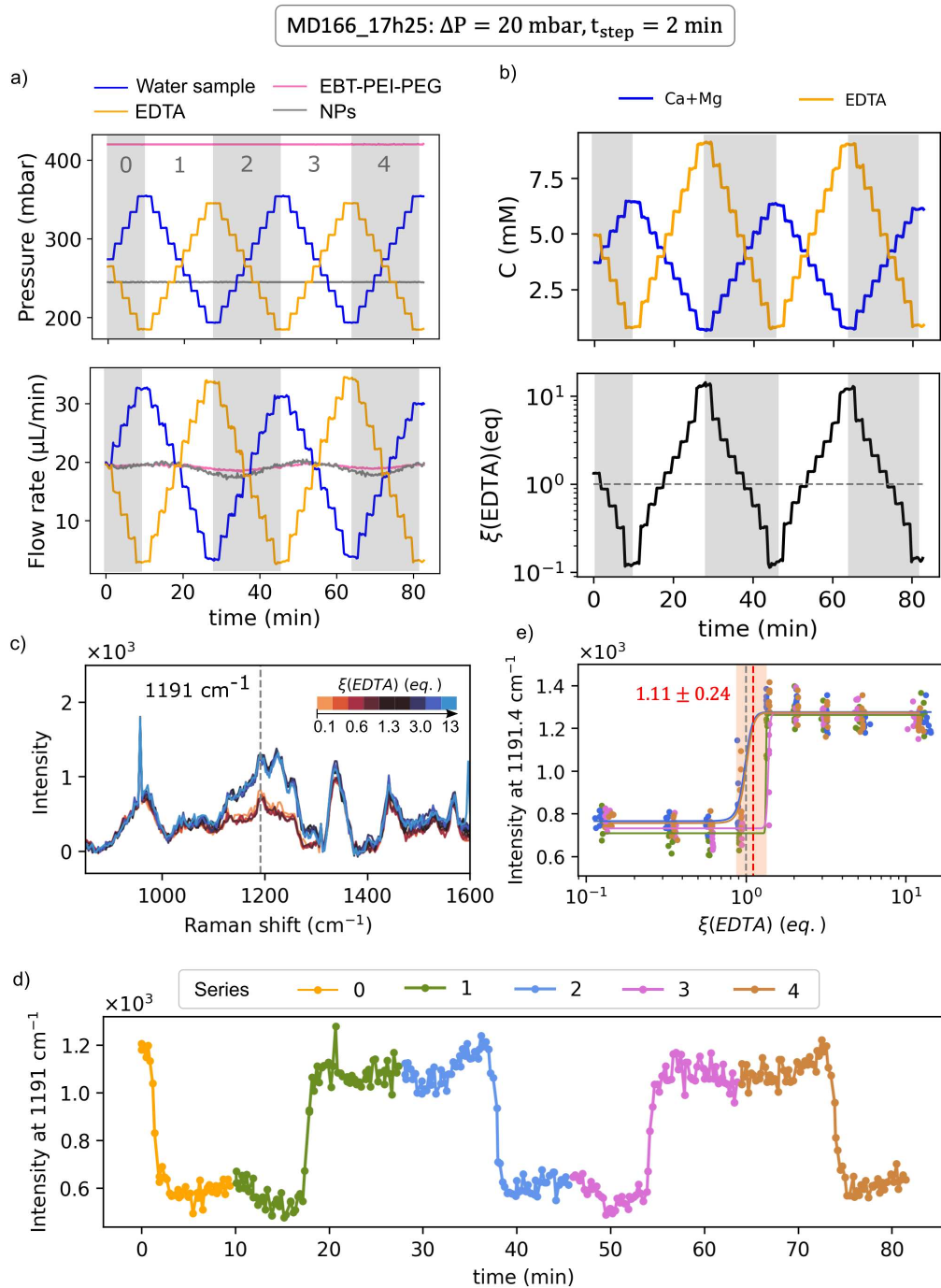


Figure 4.40: a, b) Composition control and c, d) spectral data analysis of Volvic titration experiment MD166\_17h25 with  $\Delta P = 20$  mbar,  $t_{\text{step}} = 2$  minutes.

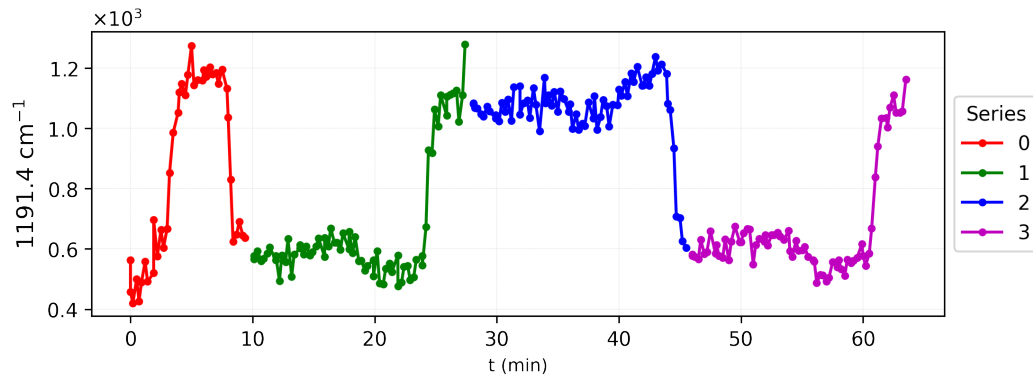


Figure 4.41: The intensity of the  $1191.4 \text{ cm}^{-1}$  of the titration experiment MD166\_17h25 before lag time adjustment. An usual signal was observed at the beginning of the experiment (red data points). In this experiment, the first two switching in intensity was supposed to be too close.

## 4.20 Estimation of cost of the platform

### 4.20.1 Cost per liter of chemical stock solutions

Here, we estimate the cost per liter of the chemical stock solutions and the labour time and cost in Tab. 4.6.

Chemical	Chemical purchased	Raw material (mg/L)	Material cost (€/L)	Material cost percentage in final mixed sample (%)	Labour time (h/L)	Labour cost (€/L)
Silver NPs 2.4 mM in Ag	Silver nitrate (54.5€/25gr)	400	0.87	17	30	540
	Trisodium citrate dihydrate (121€/500gr)	40	0.01			
Mixture of PEG, PEI, EBT	PEG 20kDa (64.7€/1kg)	50.10 <sup>3</sup>	3.24	63		
	PEI 25kDa (103€/100mL)	90	0.09			
	EBT (52.8€/100gr)	1.6	8.10 <sup>-4</sup>			
EDTA 0.8, 4 and 20mM	EDTA (89.1€/250gr)	3 088	1.10	20		
<b>Total</b>			<b>5.31</b>			<b>540</b>

Table 4.6: Table of cost per litre of chemical stock solutions and estimation of labour time and cost.

### 4.20.2 Labour for the preparation of the stock solutions

Silver nanoparticles stock used for the microfluidic system (2.4 mM in Ag) was produced in 50 mL batch at a time. It takes 1 hour to fabricate 100 mL citrate-NP, then 30 minute to generate Chloride-NPs. Within these 1.5 hour, there are 50 min for waiting citrate-NP growth, the operator prepares the other stocks and adjusts pH. The PhD labour cost is 18€/hour. Therefore, it cost 27€/50 mL NPs stock solution. For 1 L of NPs and other chemical stock solutions, it costs 540€ in labour.

### 4.20.3 Reagent cost per spectrum

In manual protocol in cuvettes, 1 L of each stock solution can produce 1333 cuvettes = 1333 spectra (750  $\mu\text{L}$  NPs/cuvette). From the price per liter calculated in section 4.20.1 of 543.5€/hour, the reagent cost per spectrum is 0.409 €/spectrum.

In the microfluidic system, one typical titration series (10 increments, 8 spectra/increment) needs 10 minutes automated priming before starting complete titrations for measurement readout. Each complete titration lasts 20 minutes, produces 80 spectra (4 spectra/min because spectra integration time is 15 sec). The mean flow rate is 25  $\mu\text{L}/\text{min}$  for each stock.

- Case of 1 complete titration per launch: 10 min + 20 min = 30 min, it consumes 750  $\mu\text{L}$  reagent in each stock for producing 80 spectra. 1 L of reagent produces 106.667 spectra.

Reagent cost per spectrum is  $545.3 \text{ €}/106.667 = 0.005 \text{ €/spectrum}$ .

- Case of 4 complete titrations per launch: 10 min + 20 x 4 min = 90 min, it consumes 2250  $\mu\text{L}$  reagent in each stock for producing 320 spectra. 1 L of reagent produces 142.222 spectra.

Reagent cost per spectrum is  $545.3 \text{ €}/142.222 = 0.004 \text{ €/spectrum}$ .

By using the microfluidic system, reduced the reagent consumption by 82 times per spectrum.

### 4.20.4 Cost for microfluidic chip fabrication

Component	Quantity/chip	Cost/chip (€)
Glass slip (20€/144 pieces)	1	0.14
PDMS reagent (223€/kg)	10 g	2.23
Silanization (107€/25g)	0.025 mL (2.5%v/v of 1 mL)	0.11
Glass capillary (76€/1000pieces)	1	0.076
Total		2.56

Table 4.7: Details of the cost for the fabrication of our microfluidic chip

For PDMS-on-glass microfluidic chip, it takes 15 minutes for mixing PDMS and put in vacuum chamber to degassing. Then 8 minutes for sealing on glass. Most of the time is waiting for curing agents, it does not need labour work. In total, 23 min/chip.

The silanization takes 20 minutes for prepare and insert tubing onto the chip for chemical injection, then inject NaOH for incubation. The next day, 10 minutes

for preparing silane solutions, 15 minutes for silane incubating and 15 minutes for flushing. Usually, we do 4 chips at a time, in total it takes 60 minutes for 4 chips.

For 4 chips,  $23 \text{ min} \times 4 \text{ (fabricate)} + 60 \text{ min (silane)} = 152 \text{ min}/4 \text{ chips}$  In average, labour duration 38 min /chip. Labour cost per chip 11.4€/chip.

In total 14€/chip, including both material and labour cost.

One chip can be used for a whole day titration running, which is equivalent to about 5 hours of total continuous running (apply for MD163 in Tab. 4.4). This 5 hour produces 1200 spectra. Therefore, the chip cost per spectrum is 0.012 €/spectrum.

#### 4.20.5 Time and costs of preparation of measurement samples and acquisition of spectra

In our previous manual version, one titration measurement including 18 step titration series with three replicates (54 spectra), it takes 120 min of labour work, including preparing measurement samples and spectral acquisition. The time for 133 sec/spectrum, 0.667 €/spectrum.

For microfluidic platform, it takes a little less than 30 minutes of labour work to set up to set up the platform, namely, to plug the reservoirs, to mount a new chip and a new glass capillary, and to prime the system so as to pinpoint initial pressure inputs. After that, the platform run the titration automatically without any labour need.

In the case of obtaining 1 titration series/launch, in addition to 30 min of labour work for setting up, it needs 30 min waiting for automatic acquiring of 80 spectra, therefore it takes 45 sec/spectrum. However, the cost per spectrum remains low of 0.113 €/spectrum because no extra labour cost.

In the case of obtaining 4 titration series/launch, in addition to 30 min of labour work for setting up, it needs 90 min waiting for automatic acquiring of 320 spectra, therefore it takes 22.5 sec/spectrum. Again, the cost per spectrum is even lower because no extra labour cost, 0.028 €/spectrum.

#### 4.20.6 Total cost per spectrum

Manual protocol in cuvettes:

- $0.409 \text{ € reagent} + 0.667 \text{ € measurement} = 1.076 \text{ €/spectrum}$

For a measurement (3 replicates, 18 increments = 54 spectra), it costs 58 €/measurement.

Microfluidic platform:

- The case of 1 titration series/launch:  
 $0.005 \text{ € reagent} + 0.012 \text{ € chip} + 0.113 \text{ € measurement} = 0.130 \text{ €/spectrum}$ .  
 For a short measurement (1 complete series of 10 increments, 8 spectra each = 80 spectra), it costs 10.4 €/measurement.
- The case of 4 titration series/launch:  
 $0.004 \text{ € reagent} + 0.012 \text{ € chip} + 0.028 \text{ € measurement} = 0.044 \text{ €/spectrum}$ .  
 It costs 14 € in this case.

#### 4.20.7 Instrument cost for the microfluidic platform

Here, we estimate the total cost per spectrum, Tab. 4.8.

Instrument	Quantity	Price per unit (k€)	Total price (k€)
Pressure controller	2	2.0	4.0
Flow rate sensors	4	1.6	6.4
Portable Raman spectrometer	1	23.0	23.0
Microscope + camera	1	1.0	1.0
Total			34.4

Table 4.8: Details of the instruments cost for the microfluidic platform

# Conclusions and perspectives

---

This thesis project aimed at developing an on-field platform for monitoring freshwater quality. We achieved this goal in two parts: (i) establishing a protocol to perform SERS-based complexometric titration, and (ii) developing a microfluidic platform to automatize the previous chemical method. Hereafter, we summarize our main results, critical reviews, and perspectives of each part.

## a) SERS-based complexometric titration

*Achievements.* We first reported the SERS-based complexometric titration in manual procedure to determine water hardness. This method involves monitoring the SERS signal of a complexometric indicator while titrating the alkaline earth ions with a chelating titrant. During the process, the SERS signal of the indicator abruptly jumps upon switching from the complex form to the free form. This behaviour was used as an endpoint marker. Three mineral waters spanning alkaline earth metal concentrations varying by a factor of 25 were successfully titrated using two different NP batches, giving the satisfactory mean trueness of 93% and mean precision of 2%. For each triplicate measurement, the trueness varies from 78% to 111%, with their relative standard deviation of 12%. An estimate of the concentration can be obtained from triplicate measurements in about two hours and about 30 minutes for a single measurement without the need for calibration.

*Advantages.* In this method, because the abrupt jump in the titration curve dominates the fluctuation of the SERS signal, there is no need to build a calibration curve. Therefore, this method significantly reduced the measurement time, material consumption and labour work compared to SERS quantitative analyses based on calibration curves. Indeed, in the group's previous work, a calibration curve of 8 increment data points was built from 10 replicates due to the dispersion of SERS signal. In total, at least 86 standard and sample measurements were carried out, giving the trueness of 97% and precision of 4%. In SERS based complexometric titration, the titration curve of 18 increments was built from 3 replicates, and the concentration readout is direct from it. In total, 54 sample measurements were carried out, giving the comparable trueness and precision as in the calibration method. This roughly demonstrates that the material, time and labour load were reduced by about 40%. This shrank in number of data has brought SERS closer to routine and practical uses.

*Limitations.* This manual protocol can be acceptable for punctual measurements. However, it is still challenging for environmental monitoring that needs high frequency and measurements of large libraries of samples. A dramatic improvement in practicality could be achieved upon automatizing the analysis procedure. This was the second task of this thesis.

*Perspectives.* This work has demonstrated the working principle of SERS-based titration on an easy target, water hardness measurement. In this case, the total concentration of dissolved calcium and magnesium ions is generally high, in the mM scale in fresh waters. However, exploring the method for other metal ion determination should be feasible because complexometric titration was established for virtually every metal cation. The selectivity can be achieved by adjusting to an appropriate pH. For instance, the indicator zincon (2-Carboxy-2'-hydroxy-5'-sulfoformazylbenzene) forms stable complexes with zinc ions over the pH range from 8.5 to 9.5, and with copper ions over the pH range from 5.0 to 9.5 [105]. Moreover, because SERS is a highly sensitive technique, this method is promising for heavy metal determination, usually displayed at sub- $\mu$ M in freshwaters. These perspectives of exploring other metal ions at low concentrations are the scope of another doctoral candidate in our group.

### **b) Automated microfluidic platform**

*Achievements.* We developed the automated microfluidic platform for SERS-based analysis to automatize the previous SERS-based titration procedure. We assembled various microfluidic and optical instruments and developed the python program to perform all the experimental tasks, from preparing the SERS measurement samples to collecting the spectral data. The platform could successfully implement continuous water hardness titrations for up to 2.5 hours on four different days without any human intervention. Three mineral waters, same as in the manual protocol, were titrated in 8 independent launches, giving the comparable mean trueness and precision as in the manual protocol, 82 % and 7 %, respectively. For each launch, the trueness varies from 64 % to 111 % with their relative standard deviation of 17%. Through automation and fluidic manipulation at small scale, the platform reduced the measurement time by at least 4 times and the reagent consumption by a factor of 82.

*Advantages.* The platform needs only 30 minutes of labour work for initial setup; then it runs titrations automatically. Therefore, the longer using the platform, the more benefits it brings in terms of labour work. For instance, when increasing the number of spectra 4 times from 80 to 320 spectra, the labour time per acquired spectrum reduced exponentially from 45 to 6 sec/spectrum. In contrast, the labour time increases linearly with the number of acquired spectra. The microfluidic platform considerably reduces labour load, which is the analysing part that dominates the consolidated cost in the manual protocol. In addition, with low reagent

consumption ( $25 \mu\text{L}/\text{min}$ ), the platform is highly appropriate for environmental monitoring in large scale and at high frequency. For instance, a 50 mL NP batch is enough for 33 hours of continuously monitoring, producing 8000 spectra, whereas this amount is just enough to produce 66 spectra in the manual protocol. Moreover, the platform's operation is user-friendly for non-expert after just a few hours of training. These features are critical to bringing SERS analysis to real-world applications where the users have no training in chemistry and time to prepare the samples. This work has built a solid foundation for an on-field environmental monitoring station. The total instrumental cost is 35 k€, which is 30 – 50% of the price of an ICP-AES spectrometer usually used to analyse alkaline earth content.

*Limitations.* The current platform needs about 10 minutes to prime the initial pressure inputs manually. Even though this step can be easily done by a non-expert, it is not convenient for monitoring in weeks and months. However, this can be achieved by deploying a feedback loop between pressures and flowrates at the beginning of the python program (Fig. 5.1a).

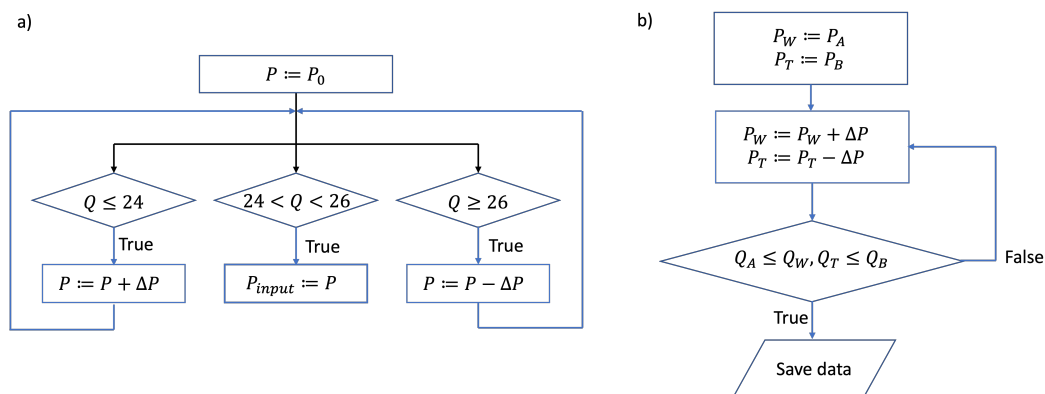


Figure 5.1: a) Proposed flow chart of feedback loop to automatically find the initial pressures ( $P$ ) at which the flow rate ( $Q$ ) in each channel is about  $25 \mu\text{L}/\text{min}$ . This flow chart applies to each channel in which  $P_0$  can be set to 300 mbar which is close to the expected values. b) Proposed flow chart for zoom-in titration region A-B around the equivalence.  $P_A$ ,  $P_B$ ,  $Q_A$  and  $Q_B$  are pressures and flow rates defined from a previous skimming titration to define roughly the equivalence. W and T stand to water and titrant channels, respectively.

*Perspectives.* Thanks to its automation, user-friendliness, and robustness, the developed microfluidic platform can be considered a solid foundation for an on-field environmental monitoring station. The platform is ready to test with unknown freshwaters for water hardness measurement and apply to large scale measurements. Hardness determination is one of the most important and frequent analyses performed by many water-using facilities. This is because hardness can cause complications in the water treatment process if a stream or river is used

as a source of drinking water. For instance, it facilitates the formation of scale, especially when heating up.

With the main functions of automatically generating concentration gradient and acquiring spectra, the current platform can implement other metal ion determination by just changing the reservoirs. It should also be applicable for building calibration methods. Further, multi-analyte analysis can be integrated into the platform by inserting two switchers in the titrant channel before and after the titrant reservoir. These switchers can connect up to 10 reservoirs. Each reservoir contains different indicators selective to specific metal ions. The scheme of this configuration is presented in Fig. 5.2. In fact, the current hardware configuration of the platform and the Python programming are already integrated with these switchers and used in single mode. However, implementing multiple reservoirs has not been experimentally accomplished yet.

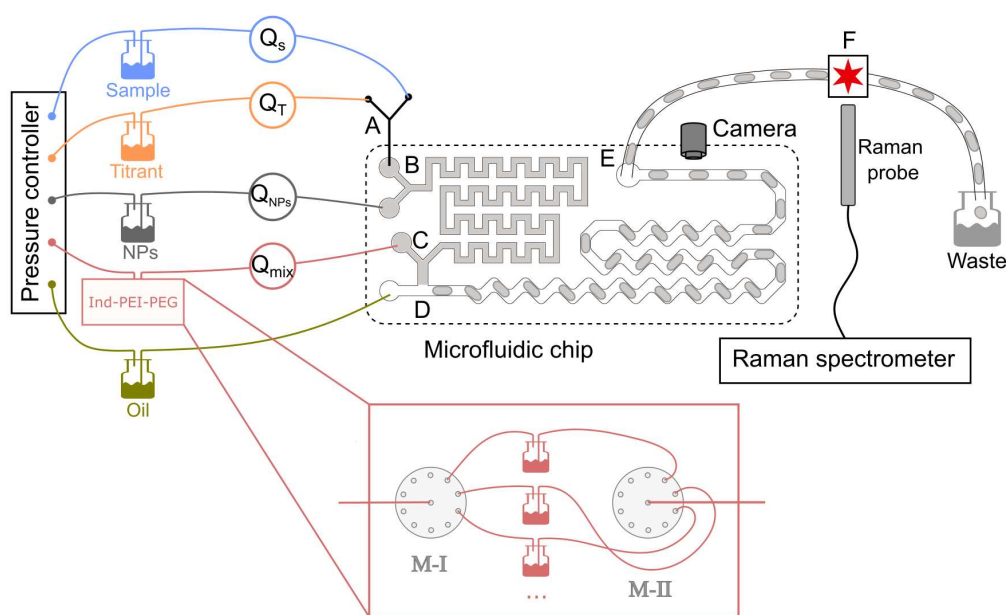


Figure 5.2: Scheme of the microfluidic platform with an upgrade in the indicator channel (Ind-PEI-PEG) in pink. Two switchers (M-I and M-II) are inserted in this channel giving possibility to plug up to 10 reservoirs. The switchers can select the gates corresponding to a wanted reservoir to inject into the microfluidic system.

Another upgrade to obtain a higher accuracy measurement is to run the titration at a higher resolution near the equivalence. This can be done by inputting a range of pressures and flow rates around the equivalence that is identified after a full skim as programming right now (Fig. 5.1b). This function is helpful in practice because the analyte concentration in fresh waters can vary a wide range from pM to mM. Thus, confining the titration range near the equivalence after a quick

skimming will save time by avoiding scanning at high resolution for a complete titration.

In summary, with open possibilities of upgrading to full automation and multi-analyte analysis, the developed microfluidic platform is a solid foundation for developing a versatile environmental monitoring instrument.



# Bibliography

- [1] Colin N Waters, Jan Zalasiewicz, Colin Summerhayes, Anthony D Barnosky, Clément Poirier, Agnieszka Gałuszka, Alejandro Cearreta, Matt Edgeworth, Erle C Ellis, Michael Ellis, et al. The anthropocene is functionally and stratigraphically distinct from the holocene. *Science*, 351(6269), 2016. (Cited on page 1.)
- [2] G. Charron. Quantitative chemistry of nanomaterials. from fundamewntal studies and towards a practical application. *HDR at Université Paris Diderot*, 2018. (Cited on pages 1, 7, 10, 11 and 13.)
- [3] World Water Assessment Programme WWAP. The united nations world water development report 2020: Water and climate change, 2020. (Cited on page 1.)
- [4] EU Commission for Environment. Evaluation of eu water legislation concludes that it is broadly fit for purpose but implementation needs to speed up. <https://ec.europa.eu/info/news/evaluation-eu-water-legislation-concludes-it-broadly-fit-purpose-implementation-n-en>, 2019. Accessed: 2021. (Cited on page 1.)
- [5] L’association UFC-“Que Choisir”. Préservation de la ressource aquatique: L’ufc-que choisir lance un s.eau.s! <https://www2.assemblee-nationale.fr/static/15/commissions/CDD/Synth%C3%A8se%20S%20eau%20S%20-%20UFC-Que%20Choisir.pdf>, 2017. Accessed: 2022. (Cited on page 1.)
- [6] A. Brault A. Kieffer and V. Rebeyrotte. Radiofrance. Guadeloupe: vivre avec le chlordécone. <https://www.franceculture.fr/emissions/grand-reportage/guadeloupe-vivre-avec-le-chlordecone>, 2021. Accessed: 2021. (Cited on pages 1 and 2.)
- [7] Philip J Landrigan, Richard Fuller, Nereus JR Acosta, Olusoji Adeyi, Robert Arnold, Abdoulaye Bibi Baldé, Roberto Bertollini, Stephan Bose-O’Reilly, Jo Ivey Boufford, Patrick N Breyse, et al. The lancet commission on pollution and health. *The lancet*, 391(10119):462–512, 2018. (Cited on page 2.)
- [8] Water-pollution.org.uk. Dangers of water pollution. <https://www.water-pollution.org.uk/dangers-of-water-pollution/>. Accessed: 2021. (Cited on page 2.)
- [9] A Afal and SW Wiener. Metal toxicity. *Medscape.org*, 2014. (Cited on page 2.)
- [10] Californians for Pesticide Reform. Pesticides and human health. <https://www.pesticidereform.org/pesticides-human-health/>. Accessed: 2021. (Cited on page 2.)

- [11] David M Borrok, David A Nimick, Richard B Wanty, and W Ian Ridley. Isotopic variations of dissolved copper and zinc in stream waters affected by historical mining. *Geochimica et Cosmochimica Acta*, 72(2):329–344, 2008. (Cited on page 2.)
- [12] Kelsey J Pieper, Min Tang, C Nathan Jones, Stephanie Weiss, Andrew Greene, Hisyam Mohsin, Jeffrey Parks, and Marc A Edwards. Impact of road salt on drinking water quality and infrastructure corrosion in private wells. *Environmental science & technology*, 52(24):14078–14087, 2018. (Cited on page 2.)
- [13] Kelsey J Pieper, Rebekah Martin, Min Tang, LeeAnne Walters, Jeffrey Parks, Siddhartha Roy, Christina Devine, and Marc A Edwards. Evaluating water lead levels during the flint water crisis. *Environmental science & technology*, 52(15):8124–8132, 2018. (Cited on pages 2 and 4.)
- [14] R McKinlay, JA Plant, JNB Bell, and N Voulvoulis. Endocrine disrupting pesticides: implications for risk assessment. *Environment international*, 34(2):168–183, 2008. (Cited on page 3.)
- [15] Francis Albarède. *Geochemistry: an introduction*. Cambridge University Press, 2009. (Cited on page 3.)
- [16] Leo ML Nollet and Leen SP De Gelder. *Handbook of water analysis*. CRC press, 2000. (Cited on pages 3 and 4.)
- [17] Ted Roelofs. Bridge Magazine. Issues at deq cited years before flint crisis. <https://eu.detroitnews.com/story/opinion/2016/02/17/issues-deq-cited-years-flint-crisis/80532786/>. Accessed: 2021. (Cited on page 4.)
- [18] WA House and Ziqing Ou. Determination of pesticides on suspended solids and sediments: Investigations on the handling and separation. *Chemosphere*, 24(7):819–832, 1992. (Cited on page 4.)
- [19] Steve Wilbur. A comparison of the relative cost and productivity of traditional metals analysis techniques versus icp-ms in high throughput commercial laboratories. *Agilent Technologies Application Note*, 2005. (Cited on page 5.)
- [20] WHO/UNICEF Joint Water Supply and Sanitation Monitoring Programme. *Progress on sanitation and drinking water: 2015 update and MDG assessment*. World Health Organization, 2015. (Cited on page 5.)
- [21] International Water Resources Association. Why focus on water quality? <https://www.iwra.org/waterquality/>. Accessed: 2021. (Cited on page 5.)
- [22] Haibin Tang, Chuhong Zhu, Guowen Meng, and Nianqiang Wu. Surface-enhanced raman scattering sensors for food safety and environmental monitoring. *Journal of the Electrochemical Society*, 165(8):B3098, 2018. (Cited on page 6.)

- [23] Rebecca A Halvorson and Peter J Vikesland. Surface-enhanced raman spectroscopy (sers) for environmental analyses, 2010. (Cited on pages 6 and 14.)
- [24] Katrin Kneipp, Harald Kneipp, Irving Itzkan, Ramachandra R Dasari, and Michael S Feld. Ultrasensitive chemical analysis by raman spectroscopy. *Chemical reviews*, 99(10):2957–2976, 1999. (Cited on page 6.)
- [25] Eric C Le Ru, Johan Grand, Idrissa Sow, Walter RC Somerville, Pablo G Etchegoin, Mona Treguer-Delapierre, Gaëlle Charron, Nordin Félidj, Georges Lévi, and Jean Aubard. A scheme for detecting every single target molecule with surface-enhanced raman spectroscopy. *Nano letters*, 11(11):5013–5019, 2011. (Cited on page 6.)
- [26] David I Ellis, Victoria L Brewster, Warwick B Dunn, J William Allwood, Alexander P Golovanov, and Royston Goodacre. Fingerprinting food: current technologies for the detection of food adulteration and contamination. *Chemical Society Reviews*, 41(17):5706–5727, 2012. (Cited on page 6.)
- [27] William Cheung, Iqbal T Shadi, Yun Xu, and Royston Goodacre. Quantitative analysis of the banned food dye sudan-1 using surface enhanced raman scattering with multivariate chemometrics. *The Journal of Physical Chemistry C*, 114(16):7285–7290, 2010. (Cited on page 6.)
- [28] Dana Cialla, Anne März, René Böhme, Frank Theil, Karina Weber, Michael Schmitt, and Jürgen Popp. Surface-enhanced raman spectroscopy (sers): progress and trends. *Analytical and bioanalytical chemistry*, 403(1):27–54, 2012. (Cited on pages 6, 14 and 41.)
- [29] Gwennaëlle Brackx, Damien Guinoiseau, Ludovic Duponchel, Alexandre Gélabert, Victoria Reichel, Samia Zrig, Jean-Marc Di Meglio, Marc F Benedetti, Jérôme Gaillardet, and Gaëlle Charron. A frugal implementation of surface enhanced raman scattering for sensing zn 2+ in freshwaters—in depth investigation of the analytical performances. *Scientific reports*, 10(1):1–11, 2020. (Cited on pages 6, 18, 19, 20, 27 and 42.)
- [30] Eric C Le Ru, Evan Blackie, Matthias Meyer, and Pablo G Etchegoin. Surface enhanced raman scattering enhancement factors: a comprehensive study. *The Journal of Physical Chemistry C*, 111(37):13794–13803, 2007. (Cited on pages 7, 12 and 13.)
- [31] Alan Champion and Patanjali Kambhampati. Surface-enhanced raman scattering. *Chemical society reviews*, 27(4):241–250, 1998. (Cited on page 7.)
- [32] Ewen Smith and Geoffrey Dent. *Modern Raman spectroscopy: a practical approach*. John Wiley & Sons, 2019. (Cited on pages 7 and 9.)
- [33] Anton Paar. Basics of raman spectroscopy. <https://wiki.anton-paar.com/en/basics-of-raman-spectroscopy/>. Accessed: 2021. (Cited on page 8.)

- [34] Alan G Ryder, Gerard M O'Connor, and Thomas J Glynn. Quantitative analysis of cocaine in solid mixtures using raman spectroscopy and chemometric methods. *Journal of Raman Spectroscopy*, 31(3):221–227, 2000. (Cited on page 9.)
- [35] María Á Carmona, Fernando Lafont, César Jiménez-Sanchidrián, and José R Ruiz. Raman spectroscopy study of edible oils and determination of the oxidative stability at frying temperatures. *European Journal of Lipid Science and Technology*, 116(11):1451–1456, 2014. (Cited on page 9.)
- [36] Jean-Claude Tinguely, Gaëlle Charron, Stéphanie Lau-Truong, Andreas Hohenau, Johan Grand, Nordin Félidj, Jean Aubard, and Joachim R Krenn. Template-assisted deposition of ctab-functionalized gold nanoparticles with nanoscale resolution. *Journal of colloid and interface science*, 394:237–242, 2013. (Cited on pages 11 and 14.)
- [37] Ramon A Alvarez-Puebla and Luis M Liz-Marzan. Traps and cages for universal sers detection. *Chemical Society Reviews*, 41(1):43–51, 2012. (Cited on page 14.)
- [38] Rebecca S Golightly, William E Doering, and Michael J Natan. Surface-enhanced raman spectroscopy and homeland security: a perfect match? *ACS nano*, 3(10):2859–2869, 2009. (Cited on page 14.)
- [39] Katrin Kneipp, Yang Wang, Harald Kneipp, Lev T Perelman, Irving Itzkan, Ramachandra R Dasari, and Michael S Feld. Single molecule detection using surface-enhanced raman scattering (sers). *Physical review letters*, 78(9):1667, 1997. (Cited on page 14.)
- [40] Shuming Nie and Steven R Emory. Probing single molecules and single nanoparticles by surface-enhanced raman scattering. *science*, 275(5303):1102–1106, 1997. (Cited on page 14.)
- [41] Meikun Fan, Gustavo FS Andrade, and Alexandre G Brolo. A review on the fabrication of substrates for surface enhanced raman spectroscopy and their applications in analytical chemistry. *Analytica chimica acta*, 693(1-2):7–25, 2011. (Cited on page 14.)
- [42] Pamela A Mosier-Boss. Review of sers substrates for chemical sensing. *Nanomaterials*, 7(6):142, 2017. (Cited on pages 15 and 41.)
- [43] Widsanusan Chartarrayawadee, Phattaraporn Charoensin, Juthaporn Saenma, Thearum Rin, Phichaya Khamai, Pitak Nasomjai, and Chee On Too. Green synthesis and stabilization of silver nanoparticles using lysimachia foenum-graecum hance extract and their antibacterial activity. *Green Processing and Synthesis*, 9(1):107–118, 2020. (Cited on page 15.)

- [44] Xiaoyi Ma, Xinyue Kou, Yuanyuan Xu, Dawei Yang, and Peng Miao. Colorimetric sensing strategy for heparin assay based on pdda-induced aggregation of gold nanoparticles. *Nanoscale Advances*, 1(2):486–489, 2019. (Cited on page 15.)
- [45] Furong Tian, Franck Bonnier, Alan Casey, Anne E Shanahan, and Hugh J Byrne. Surface enhanced raman scattering with gold nanoparticles: effect of particle shape. *Analytical Methods*, 6(22):9116–9123, 2014. (Cited on page 15.)
- [46] Ziyu Chen, Hongwei Dai, Jiaming Liu, Hui Xu, Zixuan Li, Zhang-Kai Zhou, and Jun-Bo Han. Dipole plasmon resonance induced large third-order optical nonlinearity of au triangular nanoprism in infrared region. *Optics express*, 21(15):17568–17575, 2013. (Cited on page 15.)
- [47] Wolfgang Kiefer. *Surface enhanced Raman spectroscopy: analytical, biophysical and life science applications*. John Wiley & Sons, 2011. (Cited on page 15.)
- [48] Rogelio Rodríguez-Oliveros and José A Sánchez-Gil. Gold nanostars as thermoplasmonic nanoparticles for optical heating. *Optics express*, 20(1):621–626, 2012. (Cited on page 15.)
- [49] Isabel Pastoriza-Santos and Luis M Liz-Marzán. Reduction of silver nanoparticles in dmf. formation of monolayers and stable colloids. *Pure and Applied Chemistry*, 72(1/2):83–90, 2000. (Cited on page 15.)
- [50] PC Lee and D Meisel. Adsorption and surface-enhanced raman of dyes on silver and gold sols. *The Journal of Physical Chemistry*, 86(17):3391–3395, 1982. (Cited on page 15.)
- [51] Hui Wang, Carly S Levin, and Naomi J Halas. Nanosphere arrays with controlled sub-10-nm gaps as surface-enhanced raman spectroscopy substrates. *Journal of the American Chemical Society*, 127(43):14992–14993, 2005. (Cited on pages 16 and 17.)
- [52] Angela Capocéfalo, Daisy Mammucari, Francesco Brasili, Claudia Fasolato, Federico Bordi, Paolo Postorino, and Fabio Domenici. Exploring the potentiality of a sers-active ph nano-biosensor. *Frontiers in chemistry*, 7:413, 2019. (Cited on pages 16 and 17.)
- [53] Vlastimil Peksa, Martin Jahn, Lucie Stolcova, Volker Schulz, Jan Proska, Marek Prochazka, Karina Weber, Dana Cialla-May, and Jurgen Popp. Quantitative sers analysis of azorubine (e 122) in sweet drinks. *Analytical chemistry*, 87(5):2840–2844, 2015. (Cited on pages 17, 18 and 42.)
- [54] Vitor M Zamarion, Ronaldo A Timm, Koiti Araki, and Henrique E Toma. Ultrasensitive sers nanoprobe for hazardous metal ions based on trimercaptotriazine-modified gold nanoparticles. *Inorganic chemistry*, 47(8):2934–2936, 2008. (Cited on pages 16 and 17.)

- [55] Siegfried Schneider, Harald Grau, Peter Halbig, and Ulrich Nickel. Kinetic effects in surface-enhanced raman spectroscopy: does it have potential as an analytical tool? *Analyst*, 118(6):689–694, 1993. (Cited on page 16.)
- [56] Anne März, Katrin R Ackermann, Daniéll Malsch, Thomas Bocklitz, Thomas Henkel, and Jürgen Popp. Towards a quantitative sers approach—online monitoring of analytes in a microfluidic system with isotope-edited internal standards. *Journal of biophotonics*, 2(4):232–242, 2009. (Cited on pages 16, 18 and 50.)
- [57] Evelyn Kämmer, Konstanze Olschewski, Thomas Bocklitz, Petra Rösch, Karina Weber, Dana Cialla, and Jürgen Popp. A new calibration concept for a reproducible quantitative detection based on sers measurements in a microfluidic device demonstrated on the model analyte adenine. *Physical Chemistry Chemical Physics*, 16(19):9056–9063, 2014. (Cited on page 17.)
- [58] Agnieszka Kaminska, Obianuju Inya-Agha, Robert J Forster, and Tia E Keyes. Chemically bound gold nanoparticle arrays on silicon: assembly, properties and sers study of protein interactions. *Physical Chemistry Chemical Physics*, 10(28):4172–4180, 2008. (Cited on page 18.)
- [59] Steven EJ Bell and Narayana MS Sirimuthu. Rapid, quantitative analysis of ppm/ppb nicotine using surface-enhanced raman scattering from polymer-encapsulated ag nanoparticles (gel-colls). *Analyst*, 129(11):1032–1036, 2004. (Cited on page 18.)
- [60] Jiaji Zhu, Akwasi Akomeah Agyekum, Felix YH Kutsanedzie, Huanhuan Li, Quansheng Chen, Qin Ouyang, and Hui Jiang. Qualitative and quantitative analysis of chlorpyrifos residues in tea by surface-enhanced raman spectroscopy (sers) combined with chemometric models. *Lwt*, 97:760–769, 2018. (Cited on page 18.)
- [61] Shi Xuan Leong, Li Keng Koh, Charlynn Sher Lin Koh, Gia Chuong Phan-Quang, Hiang Kwee Lee, and Xing Yi Ling. In situ differentiation of multiplex noncovalent interactions using sers and chemometrics. *ACS Applied Materials & Interfaces*, 12(29):33421–33427, 2020. (Cited on page 18.)
- [62] László Szabó, Krisztian Herman, Nicolae Leopold, Claudia Buzumurgă, and Vasile Chiş. Surface-enhanced raman scattering and dft investigation of eriochrome black t metal chelating compound. *Spectrochimica Acta Part A: Molecular and Biomolecular Spectroscopy*, 79(1):226–231, 2011. (Cited on pages 20 and 21.)
- [63] Patrick Tabeling. *Introduction to microfluidics*. OUP Oxford, 2005. (Cited on page 27.)

- [64] Nam-Trung Nguyen, Steven T Wereley, and Seyed Ali Mousavi Shaegh. *Fundamentals and applications of microfluidics*. Artech house, 2019. (Cited on page 27.)
- [65] Klaus Jähnisch, Volker Hessel, Holger Löwe, and Manfred Baerns. Chemistry in microstructured reactors. *Angewandte Chemie International Edition*, 43(4):406–446, 2004. (Cited on page 27.)
- [66] Tatsuro Asai, Atsushi Takata, Yousuke Ushioji, Yoshiharu Iinuma, Aiichiro Nagaki, and Jun-ichi Yoshida. Switching reaction pathways of benzo [b] thiophen-3-ylithium and benzo [b] furan-3-ylithium based on high-resolution residence-time and temperature control in a flow microreactor. *Chemistry letters*, 40(4):393–395, 2011. (Cited on page 27.)
- [67] Alexander D Beaton, Vincent J Sieben, Cedric FA Floquet, Edward M Waugh, Samer Abi Kaed Bey, Iain RG Ogilvie, Matthew C Mowlem, and Hywel Morgan. An automated microfluidic colourimetric sensor applied in situ to determine nitrite concentration. *Sensors and actuators B: Chemical*, 156(2):1009–1014, 2011. (Cited on page 27.)
- [68] Eunsu Chung, Rongke Gao, Juhui Ko, Namhyun Choi, Dong Woo Lim, Eun Kyu Lee, Soo-Ik Chang, and Jaebum Choo. Trace analysis of mercury (ii) ions using aptamer-modified au/ag core-shell nanoparticles and sers spectroscopy in a microdroplet channel. *Lab on a Chip*, 13(2):260–266, 2013. (Cited on page 28.)
- [69] Rongke Gao, Namhyun Choi, Soo-Ik Chang, Seong Ho Kang, Joon Myong Song, Seong In Cho, Dong Woo Lim, and Jaebum Choo. Highly sensitive trace analysis of paraquat using a surface-enhanced raman scattering microdroplet sensor. *Analytica chimica acta*, 681(1-2):87–91, 2010. (Cited on pages 28 and 29.)
- [70] IJ Jahn, O Žukovskaja, X-S Zheng, K Weber, TW Bocklitz, D Cialla-May, and J Popp. Surface-enhanced raman spectroscopy and microfluidic platforms: challenges, solutions and potential applications. *Analyst*, 142(7):1022–1047, 2017. (Cited on pages 28 and 29.)
- [71] Hyundoo Hwang, Dongsik Han, Young-Jae Oh, Yoon-Kyoung Cho, Ki-Hun Jeong, and Je-Kyun Park. In situ dynamic measurements of the enhanced sers signal using an optoelectrofluidic sers platform. *Lab on a Chip*, 11(15):2518–2525, 2011. (Cited on page 28.)
- [72] Yunbo Guo, Maung Kyaw Khaing Oo, Karthik Reddy, and Xudong Fan. Ultrasensitive optofluidic surface-enhanced raman scattering detection with flow-through multihole capillaries. *Acs Nano*, 6(1):381–388, 2012. (Cited on page 28.)

- [73] Soroush H Yazdi and Ian M White. Optofluidic surface enhanced raman spectroscopy microsystem for sensitive and repeatable on-site detection of chemical contaminants. *Analytical chemistry*, 84(18):7992–7998, 2012. (Cited on page 28.)
- [74] Lei Wu, Zhuyuan Wang, Shenfei Zong, and Yiping Cui. Rapid and reproducible analysis of thiocyanate in real human serum and saliva using a droplet sers-microfluidic chip. *Biosensors and Bioelectronics*, 62:13–18, 2014. (Cited on page 28.)
- [75] Izabella J Hidi, Martin Jahn, Karina Weber, Thomas Bocklitz, Mathias W Pletz, Dana Cialla-May, and Juergen Popp. Lab-on-a-chip-surface enhanced raman scattering combined with the standard addition method: toward the quantification of nitroxoline in spiked human urine samples. *Analytical chemistry*, 88(18):9173–9180, 2016. (Cited on page 28.)
- [76] Bin-Bin Xu, Ran Zhang, Xue-Qing Liu, Huan Wang, Yong-Lai Zhang, Hao-Bo Jiang, Lei Wang, Zhuo-Chen Ma, Jin-Feng Ku, Feng-Shou Xiao, et al. On-chip fabrication of silver microflower arrays as a catalytic microreactor for allowing in situ sers monitoring. *Chemical Communications*, 48(11):1680–1682, 2012. (Cited on page 28.)
- [77] Juyoung Leem, Hyun Wook Kang, Seung Hwan Ko, and Hyung Jin Sung. Controllable ag nanostructure patterning in a microfluidic channel for real-time sers systems. *Nanoscale*, 6(5):2895–2901, 2014. (Cited on page 28.)
- [78] Rongke Gao, Namhyun Choi, Soo-Ik Chang, Eun Kyu Lee, and Jaebum Choo. Real-time analysis of diaquat dibromide monohydrate in water with a sers-based integrated microdroplet sensor. *Nanoscale*, 6(15):8781–8786, 2014. (Cited on page 28.)
- [79] Rongke Gao, Ziyi Cheng, Andrew J Demello, and Jaebum Choo. Wash-free magnetic immunoassay of the psa cancer marker using sers and droplet microfluidics. *Lab on a Chip*, 16(6):1022–1029, 2016. (Cited on page 28.)
- [80] Katrin R Ackermann, Thomas Henkel, and Jürgen Popp. Quantitative online detection of low-concentrated drugs via a sers microfluidic system. *ChemPhysChem*, 8(18):2665–2670, 2007. (Cited on page 29.)
- [81] Shia-Yen Teh, Robert Lin, Lung-Hsin Hung, and Abraham P Lee. Droplet microfluidics. *Lab on a Chip*, 8(2):198–220, 2008. (Cited on page 29.)
- [82] Elvys brand S. Momeniazandariani. Chemical resistance of microfluidic materials. <https://www.elveflow.com/microfluidic-reviews/general-microfluidics/chemical-resistance-of-microfluidic-materials/>, 2021. Accessed: 2021. (Cited on page 30.)

- [83] SE3D. Bioprinting 101: How to make microfluidic chips. [https://www.youtube.com/watch?v=dxz10In1774&ab\\_channel=SE3D](https://www.youtube.com/watch?v=dxz10In1774&ab_channel=SE3D), 2018. Accessed: 2021. (Cited on page 30.)
- [84] CMBL. Photolithography. <http://biomechanicalregulation-lab.org/photolithography>. Accessed: 2021. (Cited on page 31.)
- [85] Elvsys brand. Microfluidic 3d printer: Fused deposition modeling. <https://www.elveflow.com/microfluidic-reviews/soft-lithography-microfabrication/microfluidic-3d-printer/>. Accessed: 2021. (Cited on page 31.)
- [86] Minitex CNC. Mini-mill. <https://www.elveflow.com/microfluidic-reviews/soft-lithography-microfabrication/microfluidic-3d-printer/>, 2021. Accessed: 2021. (Cited on page 31.)
- [87] Anas Mohd Noor, Taisuke Masuda, and Fumihito Arai. Microfluidic device for rapid investigation of the deformability of leukocytes in whole blood samples. *ROBOMECH Journal*, 7(1):1–11, 2020. (Cited on page 32.)
- [88] Kwang W Oh, Kangsun Lee, Byungwook Ahn, and Edward P Furlani. Design of pressure-driven microfluidic networks using electric circuit analogy. *Lab on a Chip*, 12(3):515–545, 2012. (Cited on page 33.)
- [89] Charles N Baroud, Francois Gallaire, and Rémi Dangla. Dynamics of microfluidic droplets. *Lab on a Chip*, 10(16):2032–2045, 2010. (Cited on pages 34 and 36.)
- [90] Nam-Trung Nguyen and Zhigang Wu. Micromixers—a review. *Journal of micromechanics and microengineering*, 15(2):R1, 2004. (Cited on page 37.)
- [91] Valery Rudyak and Andrey Minakov. Modeling and optimization of y-type micromixers. *Micromachines*, 5(4):886–912, 2014. (Cited on page 37.)
- [92] Liguang Jiang, Yan Zeng, Hongbo Zhou, Jianan Y Qu, and Shuhuai Yao. Visualizing millisecond chaotic mixing dynamics in microdroplets: A direct comparison of experiment and simulation. *Biomicrofluidics*, 6(1):012810, 2012. (Cited on pages 37 and 46.)
- [93] Jesse Greener, Ethan Tumarkin, Michael Debono, Andrew P Dicks, and Eugenia Kumacheva. Education: a microfluidic platform for university-level analytical chemistry laboratories. *Lab on a Chip*, 12(4):696–701, 2012. (Cited on pages 37, 38 and 50.)
- [94] Xiang Wang, Zhaomiao Liu, and Yan Pang. Concentration gradient generation methods based on microfluidic systems. *RSC advances*, 7(48):29966–29984, 2017. (Cited on pages 38 and 39.)

- [95] Steven EJ Bell, Gaëlle Charron, Emiliano Cortés, Janina Kneipp, Marc Lamy de la Chapelle, Judith Langer, Marek Procházka, Vi Tran, and Sebastian Schlücker. Towards reliable and quantitative surface-enhanced raman scattering (sers): from key parameters to good analytical practice. *Angewandte Chemie International Edition*, 59(14):5454–5462, 2020. (Cited on pages 41 and 42.)
- [96] Xiaofeng Ding, Lingtao Kong, Jin Wang, Fang Fang, Dandan Li, and Jinhui Liu. Highly sensitive sers detection of hg<sup>2+</sup> ions in aqueous media using gold nanoparticles/graphene heterojunctions. *ACS Applied Materials & Interfaces*, 5(15):7072–7078, 2013. (Cited on page 42.)
- [97] Dionysia Tsoutsi, Luca Guerrini, Jose Manuel Hermida-Ramon, Vincenzo Giannini, Luis M Liz-Marzán, Alexander Wei, and Ramon A Alvarez-Puebla. Simultaneous sers detection of copper and cobalt at ultratrace levels. *Nanoscale*, 5(13):5841–5846, 2013. (Cited on page 42.)
- [98] Dionysia Tsoutsi, Jose Maria Montenegro, Fabian Dommershausen, Ulrich Koert, Luis M Liz-Marzan, Wolfgang J Parak, and Ramon A Alvarez-Puebla. Quantitative surface-enhanced raman scattering ultradetection of atomic inorganic ions: the case of chloride. *Acs Nano*, 5(9):7539–7546, 2011. (Cited on page 42.)
- [99] Charlotte De Bleye, Elodie Dumont, Eric Rozet, P-Y Sacré, P-F Chavez, Lauranne Netchacovitch, Géraldine Piel, Ph Hubert, and Eric Ziemons. Determination of 4-aminophenol in a pharmaceutical formulation using surface enhanced raman scattering: From development to method validation. *Talanta*, 116:899–905, 2013. (Cited on page 42.)
- [100] Li-Jia Xu, Zhi-Chao Lei, Jiuxing Li, Cheng Zong, Chaoyong James Yang, and Bin Ren. Label-free surface-enhanced raman spectroscopy detection of dna with single-base sensitivity. *Journal of the American Chemical Society*, 137(15):5149–5154, 2015. (Cited on page 42.)
- [101] Mai Ngoc Duong et al. Python program for sers-based complexometric titration in microfluidic platform. <https://github.com/maingduong/UnivSERS.git>, 05-2021. Accessed: 2022. (Cited on pages 45 and 51.)
- [102] Nam-Trung Nguyen. *Micromixers: fundamentals, design and fabrication*. William Andrew, 2011. (Cited on page 46.)
- [103] Alexander V Fonin, Anna I Sulatskaya, Irina M Kuznetsova, and Konstantin K Turoverov. Fluorescence of dyes in solutions with high absorbance. inner filter effect correction. *PloS one*, 9(7):e103878, 2014. (Cited on page 48.)
- [104] Elvesys brand. Flow control in microfluidics device. <https://www.elveflow.com/microfluidic-reviews/microfluidic-flow-control/>

- [flow-control-in-microfluidics-device/](#). Accessed: 2021. (Cited on page 49.)
- [105] Richard M Rush and John H Yoe. Colorimetric determination of zinc and copper with 2-carboxy-2-hydroxy-5-sulfoformazylbenzene. *Analytical Chemistry*, 26(8):1345–1347, 1954. (Cited on page 108.)
- [106] Michiel Musterd, Volkert van Steijn, Chris R Kleijn, and Michiel T Kreutzer. Calculating the volume of elongated bubbles and droplets in microchannels from a top view image. *RSC advances*, 5(21):16042–16049, 2015. (Cited on page 72.)
- [107] Fabien Jousse, Guoping Lian, Ruth Janes, and John Melrose. Compact model for multi-phase liquid–liquid flows in micro-fluidic devices. *Lab on a Chip*, 5(6):646–656, 2005. (Cited on page 83.)
- [108] Paul HC Eilers and Hans FM Boelens. Baseline correction with asymmetric least squares smoothing. *Leiden University Medical Centre Report*, 1(1):5, 2005. (Cited on page 84.)
- [109] Python baseline correction code source. <https://stackoverflow.com/questions/29156532/python-baseline-correction-library>. Accessed: 2022-06-04. (Cited on page 84.)



